Influence of advanced unsteady aerodynamic models on the aeroelastic response of an offshore wind turbine

Félix Barnaud

Normandie Université

THÈSE

Pour obtenir le diplôme de doctorat

Spécialité Energétique

Préparée au sein de l'INSA de Rouen Normandie

INFLUENCE OF ADVANCED UNSTEADY AERODYNAMIC MODELS ON THE AEROELASTIC RESPONSE OF AN OFFSHORE WIND TURBINE

présentée et soutenue par

FÉLIX BARNAUD

Thèse soutenue publiquement le 18 Décembre 2019 devant le jury composé de		
N.N. Sørensen	Professeur, DTU Wind Energy, Danemark	Rapporteur
C.J. Simão Ferreira	Professeur, TU Delft, Pays-Bas	Rapporteur
L. David	Professeur, Université de Poitiers	Examinateur
G. Balarac	Maître de conférence, LEGI	Examinateur
L. Danaila	Professeur, Université de Rouen	Directeur de thèse
V. Moureau	Chargé de recherche, CORIA	Co-encadrant de thèse

Thèse dirigée par Luminita DANAILA et Vincent MOUREAU, laboratoire CORIA (UMR 6614 CNRS) et co-dirigée par Boris DESMORAT, Institut Jean Le Rond d'Alembert (UMR 7190 CNRS).

INSA INSTITUT NATIONAL DES SCIENCES APPLIQUÉES ROUEN NORMANDIE

ED PSIME

UMR 6614 CORIA COMPLEXE DE RECHERCHE INTERPROFESSIONNEL EN AEROTHERMOCHIMIE

SIEMENS Gamesa RENEWABLE ENERGY

Abstract : Influence of advanced unsteady aerodynamic models on the aeroelastic response of an offshore wind turbine

The size of modern offshore wind turbine rotors has reached very large dimensions and keeps increasing in order to reduce the cost of electricity. More challenging designs are thus needed to improve the aerodynamic performances and reduce the structural loads. The state-of-the-art tools such as Blade Element Momentum Theory (BEMT) used to predict the loads and performances of wind turbines have been designed for much smaller rotors in standard operating conditions. Load cases in specific conditions such as yaw misalignment are a priori out of the validity range for such tools. The goal of the thesis is to investigate more advanced aerodynamic models in order to assess the differences in load predictions compared to state-of-the-art tools. In particular, this work focuses on unsteady flows which represent a challenge for engineering tools. For this purpose, a panel method code including viscous effects such as dynamic stall is compared to a BEMT code in realistic wind conditions with large yaw misalignment. The calculations are performed in the framework of aero-servo-elasto coupling in order to be representative of the load calculations performed in industry following certification standards. The impact of the dynamic stall model is investigated in particular for both BEMT and panel method, for extreme and fatigue loading in cases of yaw misalignment. Differences have been observed between both codes and for several parametrizations of dynamic stall model. In addition, it has been noticed that including the servo-elasto coupling changes a lot the observations regarding aerodynamic loading. Large angles of attack are observed on wind turbine blades in yaw misalignment cases, and the flow around blade sections in such conditions is particularly affected by viscous effects such as dynamic stall or vortex shedding which are not inherently solved by panel methods nor BEMT but modeled with semi-empirical models. Alternative models such as Large Eddy Simulation (LES) that would capture these effects have to be considered. Wall-modeled LES (WMLES) is thus used in the second part of this thesis to investigate the flow around wind turbine dedicated airfoils, much thicker than airfoils used in aeronautics. Several cases are simulated, for attached and detached flows and in steady or oscillating cases. Angles of attack up to 90° are investigated at realistic Reynolds number. It appears that WMLES is able to capture correctly the main flow features in attached conditions and at very high angle of attack with coarse meshes. However, the near stall cases are more challenging to capture even with appropriate wall laws and require very fine meshes to be correctly solved. A comparison is also performed for motions with high reduced frequency and compared to other models, revealing the promising capacities of WMLES in such cases.

Keywords : Wind turbines - Panel Method - Dynamic stall - LES - Unsteady flows - Vortex shedding - Yaw misalignment

Résumé : Influence des modèles aérodynamiques instationnaires avancés sur la réponse aéro-élastique d'une éolienne offshore

Les éoliennes offshore modernes ont atteint ces dernières années de très grandes dimensions, qui ne cessent d'augmenter en vue de diminuer les coûts de production de l'électricité. Des designs innovants sont alors nécessaires afin d'améliorer les performances aérodynamiques et de réduire les charges structurelles. Les outils de l'état de l'art tels que la théorie de l'élement de pale couplée à la méthode de la quantité de mouvement (BEMT en anglais), utilisés pour la prédiction des charges et performances des rotors, ont été conçus pour des rotors de plus faibles dimensions et dans des conditions standards d'utilisation. Des conditions particulières comme les cas de désalignement du rotor par rapport à l'axe

du vent sont a priori hors du domaine de validité des outils de l'état de l'art. Le but de cette thèse est d'étudier des modèles aérodynamiques plus poussés et de les comparer avec les outils de l'état de l'art sur des cas spécifiques. Les écoulements instationnaires sont particulièrement intéressants puisque difficiles à simuler avec les méthodes standards. Ainsi, un code de méthode des panneaux prenant en compte les phénomènes visqueux tels que le décrochage dynamique est comparé à un code BEMT dans des conditions de vent réalistes et avec un fort désalignement du rotor. Les calculs sont réalisés dans le cadre d'un couplage aéro-servo-élastique de m-anière à être le plus représentatif possible des calculs de chargement effectués dans l'industrie et nécessaires pour la certification des machines. L'impact du modèle de décrochage dynamique est étudié avec les deux méthodes, pour des cas de chargement extrêmes et en fatigue avec désalignement du rotor. Des différences ont été observées entre les deux méthodes et avec plusieurs paramétrisations du modèle de décrochage dynamique. De plus, la prise en compte du couplage servo-élastique modifie les observations faites sur les comparaisons aérodynamiques. De plus, les angles d'attaque observés sur les pales en cas de fort désalignement sont très élevés. L'écoulement autour de profils dans ces conditions est dominé par des effets visqueux non capturés par les méthodes des panneaux ou de BEMT mais modélisés via des modèles semi-empiriques. Des modèles alternatifs doivent donc être utilisés pour mieux prédire de tels phénomènes. Dans la seconde partie de cette thèse l'écoulement autour de profils aérodynamiques d'éoliennes, plus épais que dans l'aéronautique, est étudié à l'aide de Simulation aux Grandes Echelles avec loi de paroi. Plusieurs cas d'écoulement attachés et détachés sont simulés, pour des profils fixes et oscillants. De très grands angles d'attaque sont également simulés, jusqu'à 90°, à un nombre de Reynolds réaliste. Dans les cas attachés et très fortement détachés, la Simulation aux Grandes Echelles avec loi de paroi est capable de capturer correctement l'écoulement avec des maillages peu raffinés. Cependant les cas proches du décrochage se sont révélés plus difficiles à obtenir, et nécessitent des maillages très fins même en utilisant des lois de paroi adéquates. Enfin, des cas oscillants avec fréquence réduite élevée sont également étudiés et comparés avec d'autres modèles. La Simulation aux Grandes Echelles est alors particulièrement adaptée et donne des résultats prometteurs.

Mots-clés : Eoliennes - Méthode des panneaux - Décrochage dynamique - Simulation aux grandes échelles - Ecoulement instationnaire - Détachement tourbillonaire - Défaut d'alignement

Acknowledgments (remerciements)

After some years spent on this work, I now fully understand that this *Acknowledgments* page we see on all theses is not just a formality. This thesis could not have been completed without the support of those mentioned in the next lines to whom I am deeply grateful.
I would like to thanks first Niels Sørensen and Carlos Simão Ferreira for accepting to review the following chapters made in an unknown remote location in France, and for attending to the defence in the same location despite the distance and the strikes. The discussions and remarks have been highly interesting, and the enthusiasm toward wind energy coming from two experts in the field is contagious. Thanks also to Guillaume Balarac and Laurent David for participating to the defence.
I also thank Luminita Danaila and Boris Desmorat for directing this thesis despite the industrial constraints that shifted the initial project to a field of expertise not fully in line with theirs.
Thank you to CORIA laboratory, CRIANN and INSA de Rouen for making the collaboration with Siemens Gamesa Renewable Energy possible, and for providing all support needed during these years. I felt honored to be part of this partnership which now continues and creates new vocations toward wind energy in the region.
Then comes the dream team to which I owe so much : Vincent Moureau, Ghislain Lartigue and Pierre Bénard from CORIA. Vincent, I guess that you know these were not easy years, and that without the human quality of yours things could have gone differently. Thank you so much for you wise advice, in life as much as science. Ghislain, I felt ashamed the first time we met during a YALES2 training session and that I dared asking : "What is *vi* ?", which I am now proudly using with delight on a daily basis. Thank you for all the Linux - and science - tips. Pierre, thank you for your patience. My coding skills in Fortran were starting from scratch, and without your help YALES2 would have seemed much less user friendly. Thanks also to the three of you for introducing the engineer that I was into your team and for sharing your knowledge with pleasure. Thanks also to the extended YALES2 team, PhD students met during these years that regularly helped me with becoming a student again : Nicolas, Yann, Patricia, Lancelot, Hakim, Francesco. I wished I could have participated more into the laboratory daily life, but despite that you always make me felt like a member of your team.
I am of course very grateful to Siemens Gamesa Renewable Energy for giving me the opportunity to do this PhD. At a time were as an engineer I felt that I needed to improve my knowledge in wind turbine physics, the company answered positively to my wish for such a project even in an uncertain context. Among the people who made it possible, my greatest thanks go to Christine de Jouëtte and Paul Deglaire. Christine, you created the "French team" and gave me the possibility to be part of the wind adventure when I was just of of school, which I am deeply grateful. Paul, thank you for trusting me during these years, and for creating the perfect work environment. I will also remember the many hours on the road to Rouen : always the right time to talk about ideas, results and next steps, a nice radio programming and no car accident ! Thank you also for giving so much energy into the other dream team that I am much

obliged. Norbert, Maths is you first language, thank you for teaching me a few words of it with patience. And sorry for the dirty engineering models I had to introduce in ARDEMA. Laurent, yes your thesis is the most quoted paper of this thesis, no it is not a translation of it. Mine is on real wind turbines. Thank you for your help reviewing these pages, and also for translating Norbert's words in the first years of this work. Panos, thank you for explaining the essence of controllers to guys who only understand the wind point of view. And do not forget to wait when Windows is installing updates. Bastien, without you I think I would still be coupling ARDEMA to a structural code, maybe for the rest of my life. You created an user friendly tool and I would recommend you as technical support for any IT issue. Thank you also to the more recent team members, Hendri, Valentin, Maxence and the countless interns that participated in the Rouen R&D center adventure for bringing new energy to the team. I shall also thanks my oldest colleagues in the company, Hortense and Boumedyen, for the many discussions we've had along the years.

One can not guess before finishing the amount of personnal investment a thesis represents. During that period, family and friends have been the ones that kept me in one piece and I can never thank them enough for that. First, my deepest thanks go to my parents. Thank you for always taking the time to hear, understand and help me if needed in any of my choices. As a child you taught me wind turbines were to be hated, and now I have gone to the ennemy: thank you for your forgiveness. Then come the friends who kept encouraging me during these years despite not understanding a word about physics for most of them : Philippe, Claire, Juliette, Gaëtan, Gwenn, Florestan. Your presence at the defense was heartwarming as I knew my performance would be judged with innocent eyes.

Thank you also to the other friends that I could not see as much as desired these last years : Pierre, Siméon, Hicham, Nicolas, Jean-Marie, Anaïs, Camille, Arthur. Some of you became parents while some others are still hangovered from last night, still I am glad to be back among you.

And of course, thank you to my dear Laurianne that kept her smile and love despite the never ending work of the last months.

Synthèse des travaux en français

Introduction

En 2019, la réalité du réchauffement climatique causé par l'activité humaine n'est plus réellement remise en question par la communauté scientifique. L'importance du phénomène et sa gravité ont amené la plupart des institutions à prendre en compte le phénomène et essayer d'en limiter l'impact. La Convention-cadre des Nations unies sur les changements climatiques (CCNUCC) est une des organisations intergouvernementales qui promeuvent la reconnaissance politique du changement climatique. Cette organisation a amené à la ratification du Protocole de Kyoto en 1997 qui vise à réduire les émissions de gaz à effet de serre. En 2015, les accords de Paris sont signés dans le but de limiter à 2°C l'augmentation de la température d'ici 2100. Les rapports du Groupe d'experts intergouvernemental sur l'évolution du climat (GIEC) font figure de référence, les rapports de 2018 suggérant de limiter à 1.5°C l'augmentation de température afin de limiter au mieux les dégâts sociaux-économiques. Parmi les solutions proposées par ces rapports, l'emploi massif des énergies renouvelables à la place des énergies fossiles est nécessaire afin de réduire les émissions de gaz à effets de serre. Ces derniers semblent en effet être fortement corrélés avec la hausse de température comme l'indique la Figure 1.1.
Les tendances qui se dessinent ces dernières années quant aux capacités de production électrique témoignent de l'intérêt que portent les industriels aux énergies renouvelables, en particulier aux énergies solaires et éoliennes. En Europe plusieurs engagements ont été pris par les pays membres entre 2007 et 2009 de porter à 20% la part de renouvelable dans leur production énergétique d'ici 2020. L'éolien offshore fait partie de cette tendance, comme l'illustre la Figure 1.3. La capacité totale en éolien offhsore installé fin 2018 s'élève ainsi à 18499MW. Historiquement le Danemark, l'Allemagne et le Royaume-Unis sont les pays ayant le plus développé cette technologie. Ceci s'explique d'abord par l'historique énergétique de ces pays peu désireux d'investir dans le nucléaire et fortement dépendants des énergies fossiles, ensuite par l'abondance de sites propices au développement de fermes éoliennes offshore. En France, l'éolien offshore prend désormais son envol suite au lancement de plusieurs appels d'offres en 2012 et 2013 pour au total six fermes de 500MW chacune, puis à la parution de la Programmation Pluriannuelle de l'Energie de 2019 qui planifie des appels d'offre réguliers jusqu'à 2030.
L'éolien offshore est différent de l'onshore par plusieurs aspects propres à l'environnement marin :

- Le coût des fondations pour les éoliennes posées est bien plus élevé que dans l'onshore
- L'installation et la maintenance des fermes éoliennes nécessitent l'utilisation de navires spécifiques qui n'ont accès aux sites que lorsque les conditions météorologiques le permettent.
- L'environnement salin implique des contraintes de conception afin d'éviter la corrosion des machines

- Les rotors sont moins contraints en taille que pour l'onshore. Ceci est lié à la fois à l'absence de contraintes de voisinage et aux contraintes moindre de transport lorsque les usines sont construites à proximité des zones de transport maritime.

L'une des principales conséquences de ces différences est que la taille des éoliennes offshore est en moyenne plus importante que celle des machines offhsore, avec une tendance nette à l'augmentation de la taille des rotors au fil des ans. Cette tendance est fortement liée à une diminution du coût final de l'électricité produite. L'optimisation des éoliennes est un champ d'étude multi-disciplinaire qui révèle qu'augmenter la taille des rotors ne diminue le coût de l'électricité que si des concepts innovants sont développés (optimisation, nouvelles technologies, etc...) [7, 9].

La réduction du coût de l'électricité fait en particulier intervenir deux principes antagonistes :

- Augmenter la production électrique des parcs éoliens en captant plus efficacement l'énergie du vent.
- Réduire les chargements générés par le vent sur la structure afin d'augmenter la durée de vie des machines et réduire les coûts matériaux.

Pour prédire à la fois la production électrique et les chargements, des outils numériques simulant l'interaction entre le vent et l'éolienne sont nécessaires, en particulier des modèles aérodynamiques. Les outils de l'état de l'art tels que la méthode de l'élément de pale couplée à un bilan de quantité de mouvement (Blade Element Momentum Theory ou BEMT en anglais) sont majoritairement utilisés dans l'industrie et nécessaires de la conception à la certification des machines. Le domaine de validité restreint de ces outils implique qu'il ont besoin de nombreux modèles empiriques afin de donner des résultats fiables dans des conditions usuelles de fonctionnement. Afin de concevoir des éoliennes plus optimisées, de nouveaux modèles aérodynamiques sont ainsi nécessaires pour mieux prédire les performances et charges structurelles. De nombreuses méthodes permettent de résoudre ce type de problème, mais les plus précises sont également les plus coûteuses en terme de capacité de calcul. Un compromis doit donc être trouvé entre précision et temps de calcul. C'est dans ce contexte que s'inscrit ce travail.
D'un point de vue industriel, cette thèse est issue d'un partenariat entre Siemens Gamesa Renewable Energy (SGRE), fabricant majeur d'éoliennes industrielles, et du CORIA, laboratoire situé à Rouen et spécialisé dans l'étude des écoulements réactifs et non réactifs en particulier via la simulation numérique. L'expertise du CORIA dans le domaine du calcul haute performance a suscité l'intérêt de SGRE pour ce partenariat. L'objectif de cette thèse est d'investiguer des modèles aérodynamiques avancés dans un contexte industriel qui nécessite la réalisation de nombreux cas de calculs. Les phénomènes instationnaires tels que le décrochage dynamique, particulièrement compliqués à capturer, seront un point central de ce travail. Les modèles utilisés dans cette thèse ont donc pour but de modéliser plus précisément ces effets. Les principaux objectifs sont les suivants :

- Intégrer un modèle de décrochage dynamique dans un code de méthode des panneaux dans le but d'obtenir un modèle aérodynamique avancé capable de simuler une éolienne entière dans des conditions environnementales complexes (prise en compte de la turbulence du vent, du cisaillement vertical, etc...)
- Évaluer la réponse aéro-élastique d'une éolienne offshore dans le cadre de calculs de charge représentatifs de ce qui est fait dans l'industrie.

- Déterminer les capacités de la Simulation aux Grandes Échelles (Large Eddy Simulation, ou LES en anglais) pour la prédiction du phénomène de décrochage dynamique. Le code YALES2 développé au CORIA est utilisé dans ce but.

Les chapitres 1 et 2 du manuscrit présentent un état de l'art et les problématiques de la simulation aérodynamique appliqué au domaine de l'éolien. Le chapitre 1 se concentre sur les phénomènes physiques tandis que le chapitre 2 traite des modèles utilisés. Le chapitre 3 présente la méthodologie ainsi que les résultats obtenus avec le code ARDEMA, un code de méthode des panneaux développé au sein de SGRE. Le chapitre 4 présente les résultats obtenus avec le code YALES2 sur le décrochage dynamique de sections de pale. Ce résumé en français synthétise l'état de l'art ainsi que les résultats obtenus présentés de manière plus détaillée dans le reste du manuscrit, en anglais.

L'aérodynamique d'une éolienne

L'une des principales difficultés dans la modélisation aérodynamique réside dans la pluralité des échelles physiques. En effet les phénomènes étudiés peuvent être à l'échelle de la couche limite comme par exemple la transition laminaire-turbulente ou à l'échelle du rotor comme la dynamique du sillage. Ainsi Le chapitre 1 définit les principaux phénomènes existants sur une éolienne. Ce chapitre présentent d'abord les concepts en 2-D, ainsi que certains phénomènes pouvant être définis sur des profils aérodynamiques. L'aspect tri-dimensionnel est ensuite intégré en considérant une aile de dimension finie. Enfin, les principes et définitions propres aux éoliennes sont présentées ainsi que les principales sources d'instationnarités.
L'écoulement 2-D autour d'une section de pale représente un intérêt car l'écoulement autour d'une pale d'éolienne se fait majoritairement dans un plan, la troisième dimension pouvant être négligée en première approximation. Dans ce cadre, un certains nombre de définitions sont rappelées comme les forces de portance et de trainée, ainsi que la notion d'angle d'attaque (Angle of Attack, ou AoA en anglais) entre le profil et la direction de l'écoulement. L'explication quant à l'origine de la portance via la condition de Kutta permet d'introduire le concept de circulation ainsi que le théroème de Kutta-Jukowski qui relie circulation et portance. Les notions d'angle d'attaque, portance et trainée sont illustrées Figure 2.3.
Les profils aérodynamiques spécifiques à l'éolien sont apparus dans les années 1980-90. Ces profils sont souvent plus épais que ceux rencontrés dans d'autres domaines, ceci pour satisfaire plusieurs critères [195]:

- Ratio portance/trainée élevé afin d'optimiser les performances aérodynamiques
- Décrochage progressif pour réduire la fatigue structurelle
- Épaisseur relative élevée afin de réduire le poids des pales
- Portance élevée pour réduire la longueur de la corde et donc les efforts à l'arrêt.
- Une faible variabilité des performances en cas de rugosité du bord d'attaque, en cas de détérioration ou de contamination des pales

Les séries de profils développés par le NREL [190] ou par les universités de Risøe [16] et Delft [194] font figure de référence et sont souvent étudiés dans les milieux académiques. La majorité du travail effectué dans cette thèse utilise ces profils. Les simulations aux grandes échelles en particulier sont réalisées sur

le profil FFA-W3-241 [18] (voir Figure 2.4) qui constitue en partie la pale de l'éolienne académique DTU 10MW [13]. Les performances de ces profils sont caractérisées par leurs polaires, qui correspondent usuellement aux forces de portance et de trainée adimensionnées (appelés coefficients de portance et de trainée) et présentées en fonction de l'angle d'attaque. Ces polaires sont données pour une valeur spécifique du nombre de Reynolds. Dans le cas des éoliennes, ce nombre de Reynolds est d'autant plus élevé que les éoliennes sont grandes. Pour les éoliennes industrielles actuelles, les nombres de Reynolds usuels sont de l'ordre de plusieurs millions, voir dizaines de millions pour des écoulements considérés comme incompressibles. Les données expérimentales sont donc rares pour de tels profils puisque les souffleries ne permettent que rarement d'atteindre de telles valeurs. Afin d'obtenir les performances de ces profils, l'industrie a ainsi de plus en plus recours à la simulation numérique.
Le décrochage apparait lorsque l'angle d'attaque du profil dépasse un seuil appelé angle de décrochage. Il se caractérise par une brusque perte de portance et une augmentation de la trainée, et doit donc être correctement prédit. Du point de vue de l'écoulement, le flux se décolle de la paroi sur l'extrados du profil alors que pour les plus faibles angles d'attaque le flux reste attaché au profil. Le décrochage est particulièrement difficile à obtenir en simulation numérique car il nécessite une bonne prédiction des bilans de forces en proche paroi. Il représente donc un challenge en terme de modélisation, en particulier lorsqu'à haut nombre de Reynolds la couche limite est fine. Différents types de décrochages peuvent être observés en fonction d'un certain nombre de paramètres, dont en particulier la forme du profil. Ainsi les profils épais au bord d'attaque arrondi sont caractérisés par un décrochage au bord de fuite, plus progressif que le décrochage de bord d'attaque caractéristique des profils minces. L'impact sur la portance est visible en Figure 2.7. Pour les profils épais avec décrochage de bord de fuite, plus l'angle d'attaque augmente plus le décrochage de la couche limite est important : le point de séparation remonte le long de l'extrados vers le bord d'attaque. Lorsque il atteint le bord d'attaque, on parle alors de décrochage profond.
Le phénomène de décrochage dynamique apparait lorsque l'angle d'attaque varie au cours du temps. Dans le cas d'écoulement autour de profils oscillants, différents phénomènes instationnaires sont observés. A faible angle d'attaque, l'écoulement est attaché et un retard sur les valeurs des coefficients de portance et trainée est observé par rapport aux valeurs statiques. L'étude se situe alors dans le cadre de la théorie de Theodorsen qui considère que les forces ont alors deux composantes dynamiques : une partie circulatoire et une partie impulsive. La partie circulatoire correspond à l'émission de vorticité associée à la variation de circulation autour du profil. La composante impulsive en écoulement incompressible correspond aux masses ajoutées dues au déplacement du fluide.
Lorsque l'angle d'attaque dépasse l'angle de décrochage statique, la portance dépasse la valeur maximale statique avec un retard du phénomène de décrochage. Une phénoménologie particulière est ainsi établie pour les profils minces décrite en Figure 2.11 en fonction du temps:

- Avant que l'angle d'attaque n'atteigne l'angle de décrochage statique, les caractéristiques de l'écoulement sont les mêmes que dans le cas statique, avec un retard sur les coefficients aérodynamiques.

- Quand l'angle d'attaque dépasse l'angle de décrochage statique, on observe peu de modifications de l'écoulement qui reste attaché. La portance maximale statique est dépassée.

- L'angle d'attaque augmente encore jusqu'à provoquer une séparation à partir du bord de fuite. Puis un tourbillon de bord d'attaque apparait, qui s'amplifie jusqu'à se détacher et à être emporté par l'écoulement vers le bord de fuite.

- Si l'angle d'attaque continue d'augmenter, une succession de tourbillons moindres peut se détacher du bord d'attaque.
- Enfin, lorsque l'angle d'attaque diminue, l'écoulement se recolle à la paroi, avec un retard par rapport au cas statique. La portance reste ainsi assez faible et la trainée importante jusqu'à retourner sur la courbe statique linéaire pour l'angle d'attaque minimum du cycle.

Ce comportement donne aux polaires une hystérésis typique du phénomène de décrochage dynamique.
Cette description du phénomène est typique de certains profils minces mais ne reflète pas la réalité de tous les cas de décrochage dynamique. Un certains nombre de paramètres tels que la forme du profil, la fréquence réduite k d'oscillation, le type de mouvement responsable de la variation d'angle, ainsi que l'amplitude et l'angle moyen du cycle peuvent changer l'apparition des phénomènes. Ainsi, le tourbillon de bord d'attaque n'apparait pas systématiquement, en particulier pour les profils épais typiques de l'éolien.
Si une description 2-D permet de comprendre un certains nombre de phénomènes observables sur une éolienne, une description 3-D est nécessaire pour prendre en compte d'autre phénomènes puisque la réalité de l'écoulement autour d'une éolienne implique, par exemple, qu'au bout d'une pale de dimension finie une description 2-D n'est pas suffisante. Ainsi, si l'on considère une pale de dimension finie dans un écoulement uniforme avec un angle d'attaque donné, il apparait un tourbillon de bout de pale. En reprenant le principe de la circulation autour d'un profil et en l'appliquant à une pale 3-D, on peut distinguer la vorticité émise, proportionnelle à la variation temporelle de circulation, de la vorticité transverse proportionnelle au gradient radial (dans la direction de la longueur de la pale) de circulation. Ainsi en bout de pale, le fort gradient de portance, et donc de circulation via le théorème de Kutta-Jukowski, implique qu'une forte vorticité est émise. Ce tourbillon génère des vitesses dites *induites* en bout de pale, modifiant localement l'écoulement et donc l'angle d'attaque. La Figure 2.16 illustre la différence entre l'angle d'attaque géométrique et l'angle d'attaque effectif qui prend en compte les vitesses induites locales. Les effets causés par le tourbillon de bout de pale ont tendance à diminuer l'angle d'attaque et donc la portance.
Plusieurs effets propres au décrochage sont également observés dans un cas en 3-D. Ainsi les cellules de décrochage correspondent à des motifs de l'écoulement sur l'extrados comme illustré Figure 2.19. Si l'envergure du profil est trop faible pour permettre à ces cellules de se développer correctement, le décrochage ne se développe pas de la même manière et les coefficients de portance et trainées ne sont pas alors les mêmes. Cette problématique est importante en particulier lorsqu'il s'agit d'effectuer des mesures expérimentales ou des calculs CFD car l'envergure du profil étudiée est limitée soit par la taille de la soufflerie dans le premier cas, soit par le temps de calcul qui augmente avec l'envergure dans le cas de la CFD.
Deux autres phénomènes qui se rapportent à l'impact d'un écoulement tri-dimensionnel sur les polaires aérodynamiques d'un profil apparaissent sur une éolienne : l'angle de flèche, et le retard au décrochage causé par l'augmentation rotationnelle. Le premier apparait lorsque l'écoulement a une composante radiale comme illustré Figure 2.20. L'écoulement attaché n'est pas modifié par cette composante, mais on observe un retard au décrochage qui implique une portance maximale plus élevée que dans le cas bidimensionnel. Le deuxième phénomène apparait pour une éolienne en rotation. Les forces centrifuges créent des flux radiaux qui modifient le décrochage. Le décrochage est alors d'autant plus retardé que la section considérée est proche de l'axe de rotation.
Afin de comprendre comment opèrent ces phénomènes tri-dimensionnels dans le cas d'une éolienne,

il est nécessaire de définir correctement le système dynamique qui compose une éolienne à axe horizontale telle que celles développées dans l'industrie, en opposition aux éoliennes à axe verticale moins fréquentes. La Figure 2.23 introduit ainsi les principaux axes de rotation : l'axe de rotation du rotor (constitué par les trois pales et le moyeu), l'axe de rotation de la pale sur elle-même qui définit l'angle de calage (*pitch axis* en anglais) et l'axe d'orientation de la nacelle par rapport au vent (*yaw axis* en anglais). L'angle d'orientation de la nacelle peut être défini comme positif ou négatif lorsqu'il n'est pas aligné avec l'axe du vent.
Lorsque le rotor est en mouvement, l'ensemble des vitesses induites par les vorticités émises et transverses des pales forment un sillage tel que représenté en Figure 2.24. L'angle incident effectif que fait l'écoulement avec le plan du rotor est alors constitué par les vitesses du vent incident, de la rotation du rotor et de l'ensemble des vitesses induites par le sillage. Ces dernières se décomposent habituellement en deux composantes : une composante axiale qui correspond à une diminution locale de la vitesse du vent incident, et une composante tangentielle qui augmente la vitesse rotationnelle. Cette dernière correspond à la rotation du sillage dans le sens opposé à la rotation du rotor. On obtient alors l'angle d'attaque effectif en prenant en compte l'ensemble des vitesses induites générées par le sillage. En projetant les forces de portance et de trainée suivant le plan du rotor et la normale au plan du rotation, on obtient respectivement les forces générant le couple rotatif et les forces de poussée du rotor comme illustré sur la Figure 2.25.
Le calcul des vitesses induites est au coeur de la modélisation aérodynamique d'une éolienne. Une première approche de modélisation consiste à considérer uniquement la composante axiale des vitesses induites et d'établir un bilan de quantité de mouvement dans la direction axiale. On peut ainsi obtenir la puissance et la poussée du rotor en fonction de la vitesse axiale induite et définir les coefficients de puissance et de poussée (voir les équations 2.12 et 2.14). Cette théorie permet d'introduire la notion de limite de Betz qui correspond à la puissance maximale que peut théoriquement extraire du vent une éolienne. Comme l'illustrent les Figures 2.26 et 2.27, la limite de Betz est atteinte pour une vitesse axiale induite correspondant à 1/3 de la vitesse du vent incident. A cette puissance correspond une force de poussée qui est responsable, dans une première hypothèse simplificatrice, des charges sur le rotor. Pour des faibles valeurs de vitesse induite, le rotor est considéré comme peu chargé tandis qu'il est fortement chargé pour les valeurs d'induction proches de la limite de Betz. La Figure 2.27 permet d'illustrer l'influence du coefficient de poussée sur l'intensité de la vitesse induite axiale. Ainsi une forte poussée implique un sillage plus étendu radialement et une forte réduction de la vitesse axiale afin de respecter le bilan de quantité de mouvement.
Un paramètre important du fonctionnement d'une éolienne est le ratio vitesse de rotation en bout de pale sur vitesse incidente (appelé *Tip Speed Ratio* ou TSR en anglais) défini par l'équation 2.15. En effet, l'angle de l'écoulement pour une position radiale donnée varie en fonction du TSR. Il est ainsi possible de mettre en relation coefficient de puissance et poussée avec le TSR. Pour des faibles TSR autour de 2-3, le rotor est peu efficace et peu chargé tandis que pour des TSR autour de 8-10 l'efficacité est maximale et le rotor fortement chargé.
Dans le cas d'un rotor tournant a vitesse constante et un angle de calage fixe, avec les pales dans un plan parfaitement vertical et pour une vitesse de vent donnée, l'angle d'attaque d'une section ne varie pas en fonction du temps et dépend uniquement de sa position radiale. Les charges sur le rotor sont alors constantes. Ces conditions ne sont cependant pas réalistes et différentes sources d'instationnarité existent. Elles sont pour la plupart complexes à modéliser et responsables des charges critiques. Leishman [109] distingue ainsi les phénomènes périodiques des phénomènes apériodiques:

Sources périodiques

- Vitesse moyenne du vent évoluant dans le temps
- Cisaillement du vent
- Désalignement du rotor avec l'axe du vent
- Interaction de la tour avec l'écoulement

Sources apériodiques

- Turbulence du vent
- Dynamique du sillage
- Interactions entre les pales et le sillage d'autres éoliennes

Les sources périodiques sont relatives à la vitesse de rotation du rotor et correspondent à des fluctuations liées à une position azimutale des pales.
Le travail effectué au cours de cette thèse a étudié plus particulièrement l'influence du désalignement du rotor par rapport à l'axe du vent dans des conditions réalistes, c'est à dire en prenant en compte la turbulence du vent ainsi que le cisaillement verticale. Une étude purement géométrique (sans prendre en compte les vitesses induites) permet d'analyser l'instationnarité causée par écoulement formant un angle non nul avec le plan du rotor. Ainsi les Figures 2.30 2.31 2.32 donnent un ordre de grandeur de ces variations d'angle d'attaque ainsi que des fréquences réduites caractéristiques de l'éolienne DTU 10MW. On remarque ainsi que les variations les plus fortes dans le cas d'un désalignement du rotor se trouvent proches de la racine de la pale car la vitesse liée à la rotation y est moindre. Les désalignements positifs et négatifs sont en opposition de phase pour l'angle d'attaque, ce qui est important puisque cela implique que les charges par section seront également en opposition de phase. Pour le cisaillement vertical les sections les plus proches du bout de pale subissent de plus grandes amplitudes d'angle d'attaque puisque plus les variations de hauteur d'une section sont importantes, plus le gradient vertical a un impact. Enfin on remarque également que les désalignements positifs et négatifs du rotor par rapport à l'axe du vent ne se superposent pas de la même manière avec le cisaillement vertical : le cisaillement accentue l'amplitude des angles d'attaque pour un désalignement négatif tandis qu'il le diminue au contraire pour un désalignement positif.
Si l'on étudie maintenant la même turbine mais en considérant un écoulement turbulent, le même signal périodique lié au cisaillement et au désalignement du rotor apparait clairement avec une composante supplémentaire aux fréquences plus élevées. Ces fréquences apériodiques ne peuvent se quantifier en terme de fréquence réduite ou d'amplitude. La vitesse angulaire est donc représentée ici afin d'avoir un ordre de grandeur de l'instationnarité des charges liées à la turbulence. On remarque ainsi que pour les cas sans désalignement de rotor, la vitesse angulaire est bien plus faible pour les cas avant vent uniforme que pour les cas turbulents tandis que cet écart est fortement réduit lorsqu'un fort désalignement est présent. Il est important de remarquer que les variations liées à la turbulence sont à de multiples échelles et qu'elles peuvent aussi bien jouer sur les performances du profil que sur des variations à l'échelle du rotor. L'approche consistant à utiliser des polaires et à calculer un angle d'attaque pour obtenir les charges ne permet donc pas de rendre compte de toutes ces échelles de turbulence. La multitude d'échelles spatiales et temporelles est ainsi l'une des principales difficultés dans la modélisation aérodynamique des éoliennes.

État de l'art de la modélisation aérodynamique d'une éolienne

Les différentes échelles spatio-temporelles ont toutes une importance pour la détermination des charges sur le rotor. Par exemple, à l'échelle de la couche limite, les forces visqueuses et cinétiques doivent être correctement estimées pour prédire correctement la séparation et donc le décrochage. Ce dernier est quant à lui représentatif de l'écoulement et des forces à l'échelle du profil. Les forces aérodynamiques appliquées sur le profil modifient les vitesses induites à l'échelle du rotor. On remarque ainsi que la dynamique des très petites échelles à un impact sur les plus grandes échelles via des phénomènes non linéaires tels que le décrochage.
Ce chapitre d'état de l'art sur la modélisation aérodynamique dans le domaine de l'éolien aborde trois grandes familles de modèles : la BEMT, les méthodes particulaires et les méthodes appartenant à la mécanique des fluides numériques.

BEMT : Théorie de l'élément de pale couplée au théorème de quantité de mouvement La BEMT est la méthode la plus utilisée dans l'industrie pour calculer les charges aérodynamiques sur le rotor. Le chapitre 3.1.1 présente les bases de la théorie ainsi que plusieurs références de travaux présentant des états de l'art exhaustifs de la méthode BEMT et des nombreux modèles correctifs utilisés afin d'avoir des estimations correctes des charges sur un rotor réaliste.
Le principe fondamental de la BEMT consiste à appliquer les théorèmes de conservation de la quantité de mouvement dans les directions axiales et tangentielles au rotor. Les volumes de contrôle utilisés correspondent à des tubes suivant les lignes de courant comme illustré sur la Figure 3.1. Pour chaque position radiale un volume de contrôle élémentaire est ainsi utilisé. Il est ainsi possible de relier la puissance élémentaire (quantité de mouvement angulaire) et la poussée élémentaire (quantité de mouvement axiale) générées par chaque volume de contrôle aux vitesses induites tangentielles et axiales. Or ces vitesses permettent également d'exprimer pour chaque position radiale l'angle de l'écoulement relatif à une section via les triangles de vitesse de la Figure 2.25. C'est ensuite la théorie de l'élément de pale qui entre en jeu. Cette dernière estime que la pale peut être discrétisée en plusieurs sections d'une envergure donnée chacune définie par un profil aérodynamique dont les polaires sont connues. Il est ainsi possible de déterminer les forces de portance et de trainée générées par chaque section si l'on connait l'angle de l'écoulement ainsi que sa vitesse. Ces forces correctement projetées donnent le couple (et donc la puissance) et la poussée générée par chaque section. On voit ainsi que puissance et poussée peuvent être estimées de deux manières différentes. La BEMT combine donc ces deux approches via un algorithme itératif.
On distingue la BEMT stationnaire de la BEMT instationnaire. Dans le premier cas le rotor est supposé à l'équilibre et un processus itératif permet de calculer successivement les puissances et poussées élémentaires en utilisant les deux méthodes décrites précédemment jusqu'à atteindre un critère de convergence (voir Figure 3.2). Dans le cas de la BEMT instationnaire, plusieurs modèles entrent en jeu avec des variables évoluant dans le temps. Dans ce cas, des schémas numériques temporels permettent d'estimer les vitesses induites. Il faut également s'assurer que le pas de temps utilisé soit bien plus faible que les constantes de temps des systèmes dynamiques considérés.
La BEMT repose sur de nombreuses hypothèses qui dans le cas d'un rotor réel ne sont pas réalistes et doivent donc être corrigées via des modèles spécifiques. Les plus communs sont les suivants:

- Modèle de pertes de bout de pale : il permet de prendre en compte le caractère fini du nombre de pales. En effet, les volumes élémentaires sur lesquels sont appliqués les théorèmes de quantité

de mouvement répartissent uniformément l'action des pales sur l'aire du rotor, ce qui n'est pas représentatif de la réalité. Le modèle de Prandtl est le plus connu.

- Correction de Glauert pour les hautes valeurs d'induction. En effet, l'expérience a prouvé que pour des valeurs d'induction supérieures à 1/3, la théorie n'est plus correcte. Le modèle permet alors de corriger l'équation du moment axial en modifiant la relation entre poussée et induction axiale.

- Modèle de sillage déformé, pour les cas où le rotor n'est pas parfaitement perpendiculaire à l'axe du vent. L'induction est alors dépendante de la position azimutale de la pale.

- Modèle de sillage dynamique afin de tenir compte du caractère instationnaire des variations d'induction. En effet une variation rapide des charges sur le rotor ne s'applique pas instantanément sur l'ensemble du sillage.

- Modèle de décrochage dynamique, qui permet de prendre en compte l'instationnarité des forces aérodynamiques. L'ensemble des phénomènes liés au décrochage dynamique décrits au premier chapitre est modélisé via des polaires dites *dynamiques* par opposition aux polaires dites *statiques*.

- Modèles de correction des polaires 2-D afin de prendre en compte l'augmentation rotationnelle présentée plus haut. Les polaires résultantes sont dites *polaires 3-D*.

Lorsque le rotor présente un fort désalignement avec l'axe du vent, il a été vu plus haut que l'angle de l'écoulement avec les sections de pale varie fortement, et donc que l'angle d'attaque varie également. Dans ces cas, le comportement du modèle de décrochage dynamique est critique pour l'estimation des charges exercées sur la turbine puisque l'écoulement autour des profils est fortement instationnaire. Plusieurs modèles de décrochage dynamique sont répertoriés dans le tableau 3.1. Trois modèles sont présentés plus en détail : le modèle d'Øye, le modèle de Beddoes-Leishman, et enfin les modèles de l'ONERA. Le modèle d'Øye prend uniquement en compte le retard à la séparation de l'écoulement au moyen d'une équation différentielle d'ordre 1 appliquée à la position du point de séparation (situé entre 0 et 1, respectivement bord d'attaque et bord de fuite). Ce point de séparation est défini comme une fonction pondérant la polaire réelle à l'aide d'une polaire pour un écoulement totalement attaché et d'une polaire pour un écoulement totalement détaché. Le modèle de Beddoes-Leishman est l'un des modèles les plus étudiés, avec de nombreuses publications proposant des améliorations au modèle original. Sa principale caractéristique est qu'il décompose le phénomène de décrochage dynamique à l'aide de plusieurs sous-modèles chacun représentant un phénomène particulier. Il permet ainsi de modéliser séparément plusieurs phénomènes physiques avec des constantes de temps propres à chacun. Les différents modèles sont suffisamment indépendants pour pouvoir être utilisés ou non, ce qui donne une grande souplesse d'utilisation et de validation. De plus, les constantes de temps utilisées dans le modèle sont relativement indépendantes du profil étudié. On distingue ainsi :

- Le sous-modèle pour l'écoulement attaché instationnaire. Basé sur la théorie de Theodorsen, on distingue une partie circulatoire d'une partie impulsive. La partie circulatoire correspond à l'émission de vorticité causée par une variation d'angle d'attaque et donc de portance. Cette vorticité émise modifie localement l'angle d'attaque qui est retardé par rapport à l'angle d'attaque statique. La partie impulsive dans le cas de l'éolien correspond principalement à des termes de masse ajoutée, comme modélisé dans le modèle de Risø qui est un modèle dérivé de Beddoes-Leishman.

- Le sous-modèle gérant le retard d'établissement de la pression pariétale, en particulier au bord d'attaque. Ce retard est traduit par un retard sur la portance.

- Le sous-modèle prenant en compte le retard sur la position du point de séparation par rapport au point de position statique. Le point de séparation peut être calculé soit suivant le même principe que le modèle d'Øye, soit en utilisant la loi de Kirchhoff pour les plaques planes, qui relie le coefficient normal à la position du point de séparation.

- Le sous-modèle de tourbillon de bord d'attaque. Il permet de modéliser l'impact sur les coefficients aérodynamiques de la création et émission du tourbillon de bord d'attaque. Le modèle de Risø ne contient pas ce sous-modèle compte tenu des observations faites sur les profils épais typiques de l'éolien avec séparation par remontée du point de séparation depuis le bord de fuite.

Toutes les fonctions de retard du modèle de Beddoes-Leishman sont basées sur des équations différentielles du premier ordre. La Figure 3.6 synthétise les différentes entrées, sorties et variables du modèle originel.

L'ONERA a developpé deux modèles de décrochage dynamique: le modèle EDLIN et le modèle BH. Le premier est basé sur une approche plus mathématique que le modèle de Beddoes-Leishman et propose de relier par des systèmes du second ordre les variations d'efforts au variations d'incidence. Les nombreuses constantes de temps nécessaires par profil sont déterminées en comparant le modèle à des résultats expérimentaux. Le modèle BH est davantage basé sur la physique puisqu'il propose de modéliser l'écoulement séparé par le même principe que le modèle de Beddoes-Leishman en considérant la position du point de séparation. De plus il intègre une composante évoluant périodiquement afin de prendre en compte le décrochage profond et l'apparition des détachements tourbillonnaires successifs. La différence majeur en terme de représentation physique tient au fait que cette oscillation est auto entretenue tandis que dans le modèle de Beddoes-Leishman une variation d'incidence est nécessaire pour que le modèle de tourbillon de bord d'attaque s'active.

Méthode des singularités Deux méthodes des singularités sont abordées ici : la méthode de la ligne portante avec sillage libre et la méthode des panneaux. Ceci permet d'introduire le code ARDEMA basé sur la méthode des panneaux qui est utilisée dans le chapitre 4. L'hypothèse principale derrière ces modèles est celle du fluide non visqueux et incompressible. Cette hypothèse permet de simplifier les équations de Navier-Stokes 3.31 et 3.32 pour obtenir les équations d'Euler 3.33 et 3.34. L'hypothèse d'irrotationnalité du fluide peut également se déduire des deux premières via le théorème de Kelvin, et la vitesse de l'écoulement peut alors s'exprimer comme le gradient d'une fonction potentielle. On aboutit ensuite à l'équation de Laplace 3.36 sur le potentiel. En définissant les conditions limites comme des singularités, il est possible de résoudre analytiquement l'équation de Laplace et ainsi de connaitre les caractéristiques de l'écoulement. Ces singularités peuvent être de différents types en fonction de ce que l'on cherche à modéliser. De plus, l'équation de Laplace étant linéaire, il est possible de sommer les contributions élémentaires de chaque singularité afin de représenter des environnements complexes. La complexité du système à résoudre n'est donc pas dépendante de la taille du domaine fluide à étudier, mais du nombre de singularités.
La principale limite concernant la méthode des singularités repose sur l'hypothèse du fluide non visqueux. A haut nombre de Reynolds cette hypothèse est valable sur une grande partie du domaine étudié. En proche paroi cependant les phénomènes visqueux sont dominants et la physique de l'écoulement n'est prise en compte que de façon limitée par les singularités. Le phénomène de décrochage par exemple

ne peut être prédit par ces modèles puisqu'il implique de connaitre les forces visqueuses et forces cinétiques.
La méthode de la ligne portante avec émission de sillage libre repose sur la modélisation d'une section de pale par une distribution de vorticité le long d'une ligne située généralement au quart de la corde du profil. Cette distribution de vorticité linéaire est reliée à la portance du profil via le Théorème de Kutta-Joukowski. En discrétisant la pale en un certain nombre de sections, on forme un système de plusieurs anneaux de vorticité comme schématisé Figure 3.12. Ces anneaux sont constitués de quatre lignes de vorticité constante d'une intensité proportionnelle à la portance du profil. Deux lignes appartenant à deux anneaux distincts sont superposées à la jonction entre deux sections. La différence d'intensité entre ces deux lignes constitue donc la vorticité transverse. A chaque pas de temps un nouvel anneau de vorticité est créé. Les deux lignes de vorticité à la jonction entre les deux anneaux créés à t et $t - \Delta t$ ont une différence d'intensité correspondant à la vorticité émise, donc proportionnelle à la différence de portance entre deux pas de temps. Le sillage ainsi émis forme un ensemble de plusieurs anneaux de vorticité dont le nombre augmente au cours du temps et convectés en fonction de l'écoulement. Chacune des lignes de vorticité est responsable d'une vitesse induite calculable en tout point du domaine. Pour connaitre le déplacement de chaque ligne à l'aide d'une équation de transport, il est donc nécessaire de calculer les vitesses induites de toutes les autres lignes émises à l'emplacement de la ligne en question.
Cette méthode présente l'avantage de ne pas reposer sur certains modèles empiriques de la BEMT comme les modèles de sillage dynamique ou de sillage déformé. Les effets de bout de pale sont également intrinsèquement pris en compte. Cependant ce modèle reste dépendant de polaires tabulées utilisées dans le théorème de Kutta-Joukovski. Du point de vue du temps de calcul, la complexité du système est relative au nombre de lignes de vorticités dans le sillage.
La méthode des panneaux a les mêmes problématiques concernant le sillage que la méthode de la ligne portante. La principale différence vient de la modélisation de la pale : au lieu d'une simple ligne de vorticité, la surface de la pale est discrétisées en singularités formant des panneaux. Dans le cas de la méthode des panneaux étudiées durant cette thèse, les panneaux sont constitués d'une distribution surfacique de type source et doublet. La distribution de type source permet d'assurer la condition de non-perméabilité de la surface tandis que la distribution de type doublet permet à la surface d'être portante. En prenant en compte l'influence réciproque de chaque panneau sur les autres, il est possible d'établir un système d'équations linéaires appelé *Matrices AIC* (pour Aerodynamic Influence Coefficients). Pour être résolu, ce système a besoin d'une condition supplémentaire appelé condition de Kutta : on suppose qu'au bord de fuite, la vitesse est finie. Une manière d'interpréter cette condition est de forcer la vorticité à zéro au bord de fuite. En résolvant ensuite le système, l'intensité de chaque panneau est connue et il est alors possible de calculer les vitesses induites en tout point du fluide (hors singularités). Le principale avantage de cette méthode par rapport à la méthode de la ligne portante est qu'elle permet d'obtenir la pression sur chaque panneau via le Théorème de Bernoulli, et donc de connaitre la force aérodynamique par intégration de tous les panneaux. Cependant cette force est dite *non visqueuse* à ce stade puisque les effets de la viscosité ne sont pas pris en compte. De plus du point de vue du temps de calcul, il est nécessaire de résoudre un système dont la taille est relative au nombre de panneaux (donc de la discrétisation surfacique de la pale et du sillage), ce qui est plus long que pour la méthode de la ligne portante.
Pour obtenir les forces réelles (incluant la viscosité) et modéliser certains phénomènes comme le décrochage il y a plusieurs possibilités :

- Méthodes avec couplage des équations de la couche limite : les équations de Navier-Stokes sont explicitées dans un faible volume autour du profil, puis couplées à la solution potentielle.

- Méthode avec double sillage : afin de gérer l'émission de vorticité à la fois au bord de fuite et au point de séparation lors du décrochage, deux sillages sont émis.
- Méthode avec correction par polaires tabulées. L'intensité du sillage ainsi que les forces non visqueuses peuvent être corrigées via des polaires tabulées.

La dernière solution a été choisie dans ce travail car plus simple à implémenter et offrant la possibilité d'une meilleure comparaison avec les méthodes BEMT via l'utilisation des mêmes polaires tabulées.

Mécanique des fluides numériques La mécanique des fluides numériques définie dans ce chapitre s'identifie à toutes les méthodes cherchant à résoudre un écoulement en utilisant les équations de Navier-Stokes discrétisées 3.50 et 3.51 spatialement sur un maillage du domaine fluide. Par rapport à la méthode des panneaux, la complexité du système à résoudre est relative au nombre de cellules du maillage volumique au lieu d'une résolution surfacique. Ces méthodes sont donc plus coûteuses en terme de temps de calcul mais permettent de prendre en compte la viscosité du fluide via le tenseur des contraintes visqueuses 3.52. Une attention particulière est portée à la Simulation aux Grandes Echelles (Large Eddy Simulation, ou LES) puisque cette méthode est utilisée au chapitre 5 via le code YALES2.
Trois grandes familles de méthodes sont souvent décrites dans la littérature : les méthodes RANS (pour Reynolds Averaged Navier-Stokes), LES et DNS (pour Direct Numerical Simulation). Ces trois méthodes se distinguent par leur manière de traiter la turbulence comme représenté sur la Figure 3.15. D'après le principe de la cascade énergétique de Richardson, il y a un transfert d'énergie des grandes structures énergétiques vers les petites structures jusqu'à atteindre l'échelle dissipative de Kolmogorov. Toute la turbulence est résolue dans la DNS, ce qui implique d'avoir un maillage suffisamment fin pour capturer toutes les structures tourbillonnaires. La LES agit comme un filtre qui ne résout que les plus grandes échelles et modélise les structures plus petites tandis que les méthodes RANS modélisent la totalité du spectre turbulent et ne permet donc que d'accéder à un écoulement moyen.
La modélisation de la turbulence en LES doit permettre de prendre en compte le transfert d'énergie des grandes structures résolues vers les structures plus petites dont le comportement est modélisé. La taille des plus petites structures résolues est proportionnelle à la taille des cellules du maillage qui dans la majorité des modèles de sous-maille joue le rôle de taille de filtre. Les modèles de Smagorinsky et de WALE présentés suivent l'hypothèse de Boussinesq qui postule que la turbulence non résolue a le même effet qu'une viscosité additionnelle. Dans le cas du modèle de Smagorinsky il y a équilibre entre la création et la dissipation d'énergie cinétique pour les structures de la taille du filtre. Cette hypothèse n'est pas valide en proche paroi où le modèle de WALE lui est préféré puisqu'il gère mieux la turbulence des écoulements cisaillés.
En proche paroi, la résolution de la couche limite pose problème pour les écoulements à haut Reynolds. En effet plus celle-ci est fine, plus il est nécessaire d'avoir un nombre de cellules importants pour la résoudre correctement. Les phénomènes de transition laminaire turbulente ou de séparation impliquent de prédire correctement les équilibres entre forces visqueuses et cinétiques. Afin de rester dans des temps de calcul raisonnables des modèles spécifiques appelés lois de paroi gèrent différemment l'écoulement en proche paroi. Dans le cadre de la LES, deux approches existent : soit par une approche combinant RANS en proche paroi et LES ailleurs, soit en appliquant la LES jusqu'à la paroi mais en appliquant un tenseur de cisaillement à la paroi calculé via d'autres modèles. Cette dernière option est utilisée dans le code YALES2. Deux modèles ont été utilisés dans cette thèse : le modèle de loi logarithmique classique qui fait l'hypothèse d'un équilibre entre termes convectifs et de gradient de pression à la paroi, et le modèle de Duprat qui introduit le gradient de pression longitudinal dans les équations du modèle.

Ce dernier semble ainsi plus adapté aux cas d'écoulements autour de profils pour lesquels les gradients longitudinaux de pression ne sont pas négligeables.

Étude à l'échelle du rotor

Ce chapitre présente une méthodologie de calculs de chargements sur une éolienne de type industrielle ainsi que les résultats obtenus sur certains cas critiques, en particulier lorsque un fort désalignement du rotor avec l'axe du vent est présent. Le code de méthode des panneaux ARDEMA et l'inclusion des effets visqueux sont introduits ainsi qu'une première étape de validation sur des profils extrudés simples. Le code ARDEMA développé au sein de SGRE est basé sur le travail de Dixon [44] : c'est une méthode des panneaux qui modélise la pale via une approche doublet/source et le sillage par des anneaux de vorticité. Chaque panneau est d'ordre 0 (intensité constante). Toutes les études présentées ici sont basées sur une discrétisation d'une section en 60 panneaux. La discrétisation radiale dépend de la pale : pour l'éolienne NREL 5MW étudiée ici, 22 sections sont définies. Le code est développé sous environnement Matlab, avec utilisation de cartes graphiques (GPU) et de la librairie OpenMP pour la parallélisation.
Afin de prendre en compte la viscosité dans les efforts et intensités de sillage non visqueux issus de la théorie potentielle, une correction basée sur des polaires tabulées est utilisée dans ARDEMA. Pour utiliser ces polaires, il est d'abord nécessaire de calculer un angle d'attaque par section. Trois différentes manières d'obtenir l'angle d'attaque sont explicitées :

- A partir des vitesses géométriques et induites.
- En utilisant la circulation autour du profil
- En utilisant l'intégration de pression autour du profil

La première pose le problème de la présence de la pale : celle-ci modifie localement l'écoulement. Pour obtenir les vitesses induites à un point donné ou est défini l'angle d'attaque, il faut faire abstraction du corps de la pale. Ceci est réalisé en remplaçant dans le calcul des vitesses induites le corps de la pale par une ligne portante. Les deux autres méthodes nécessitent d'inverser l'utilisation des polaires : à partir des valeurs de circulation et de pression, on remonte à l'angle d'attaque en utilisant des polaires non visqueuses générées préalablement. De ces trois méthodes, il apparait que la troisième donne les meilleurs résultats, donc en utilisant l'intégration de pression.
Les forces calculées sur le profil par intégration de pression ainsi que l'intensité du sillage émis sont basés sur l'hypothèse d'un fluide non visqueux. Afin d'obtenir les forces et sillage réels, ceux-ci sont corrigés à l'aide d'un facteur de réduction. Dans le cas de la force aérodynamique sur une section de pale, ce facteur de réduction correspond au ratio des coefficients de portance visqueux et non visqueux obtenus par les polaires tabulées. L'équation 4.5 donne la formulation de la force visqueuse à partir de la force non visqueuse. De même l'intensité du sillage émis est réduite à l'aide d'un facteur de réduction (voir l'équation 4.9).
La polaire visqueuse utilisée pour le calcul du facteur de réduction est une polaire dynamique issue d'un modèle de décrochage dynamique implémenté durant cette thèse et basé sur le modèle de Beddoes-Leishman. L'implémentation du modèle dans une méthode des panneaux est cependant différente que pour une méthode BEMT. En effet pour cette dernière les variations d'induction ne prennent pas en compte l'instationnarité locale dues aux variations de circulation autour du profil telle que décrite dans la théorie de Theodorsen. Dans le cas de la méthode des panneaux, cette dernière est intrinsèquement

résolue et prise ici en compte via la méthode de calcul de l'angle d'attaque. Le module d'écoulement attaché n'est donc pas utilisé dans le modèle implémenté. Seuls les retards sur la séparation et sur la pression sont considérés. De plus, comme dans le modèle de Risø, la modélisation du tourbillon de bord d'attaque n'est pas non plus implémentée car il est supposé que ce type de phénomène ne se produit pas dans les conditions de fonctionnement et sur les profils éoliens. Les polaires dynamiques obtenues en sortie du modèle sont ensuite utilisées à la fois pour les corrections visqueuses des forces et du sillage. Les polaires statiques introduites pour le calcul des polaires dynamiques sont préalablement modifiées à l'aide d'une correction pour les écoulements radiaux (modèle de retard au décrochage de Snel [181]).
Le code ARDEMA est utilisé à la fois seul et couplé au code FAST de NREL (voir Figure 4.2). Ce dernier est un code permettant d'effectuer des calculs de charge à l'aide d'un couplage aéro-servo-élastique. Le module aérodynamique de FAST est basé sur une méthode BEMT tandis que dans le cadre de cette thèse le couplage avec ARDEMA permet de réaliser soit un calcul par méthode des panneaux soit par la BEMT tout en conservant les autres modules de FAST tels que la modélisation structurelle et le contrôleur. Ce dernier est composé principalement de deux boucles de contrôle PI sur l'angle de calage des pales ainsi que sur le couple appliqué au moyeu principal. Les principales caractéristiques du code BEMT inclus dans FAST version 8.15 sont les suivantes:

- Modèle de décrochage dynamique type Beddoes-Leishman
- Modèle de sillage déformé
- Correction de Prandtl
- Correction de Glauert

Aucun modèle de sillage dynamique n'est disponible dans la version de FAST utilisée dans cette thèse contrairement à ce que l'état de l'art préconise d'utiliser dans les méthodes BEMT.

La validation du code ARDEMA est présentée en deux grandes étapes : la validation 2-D et la validation 3-D. La première a pour but de vérifier la validité des corrections visqueuses appliquées sur une aile droite suffisamment élancée pour que les effets 3-D soient négligeables. Le modèle de décrochage dynamique en particulier est comparé à des valeurs expérimentales. La validation 3-D se décompose en trois parties : d'abord une validation est effectuée sur une aile dans un écoulement uniforme afin de vérifier la bonne prise en compte des effets de bout de pale. Ensuite un rotor d'éolienne est modélisé et les résultats comparés à la méthode BEMT de FAST. Enfin le code couplé est utilisé et les deux modules aérodynamiques sont comparés.
La validation 2-D révèle une bonne prédiction des boucles d'hystérésis en écoulement attaché et décroché. Deux profils sont étudiés, le FFA-W3-241 typique des profils éoliens et un profil symétrique plus fin : le NACA0015. L'absence de module de tourbillon de bord d'attaque est plus handicapant pour ce profil qui dans les cas étudiés a une portance maximale plus élevée que ce que le modèle prédit, probablement due à la présence d'un tourbillon de bord d'attaque. Cela n'apparait pas sur le FFA-W3-241. La comparaison avec le modèle de décrochage dynamique inclus dans la BEMT de FAST donne des résultats assez semblables à ARDEMA une fois corrigé pour inclure les mêmes éléments théoriques en écoulement décroché. La validation 3-D sur une pale dans un écoulement uniforme a également permis de démontrer la pertinence de la méthode des panneaux : les effets de bout d'aile sont correctement pris en compte en écoulement attaché. Enfin la validation sur une éolienne de type industriel (la NREL 5MW) révèle que sur des cas théoriques (vent uniforme, pale rigide et vitesse de rotation constante) et pour trois

points de fonctionnement (TSR de 3.2, 5.3 et 7.0 ce qui correspond respectivement à des vitesses de vent de 25m/s, 15m/s et 11.4m/s), les deux codes donnent des résultats similaires. L'évolution radiale des forces axiales et tangentielles en particulier est similaire pour les deux méthodes. La validation du couplage avec FAST s'effectue alors en deux étapes : d'abord en considérant une structure élastique mais sans prendre en compte le contrôleur, puis en activant le contrôleur. Dans le premier cas, la vitesse de rotation et l'angle de calage sont donc imposés comme pour la validation purement aérodynamique. Dans le deuxième cas le contrôleur cherche à atteindre un point de fonctionnement donné et adapte le couple appliqué ainsi que l'angle de calage. Si la vitesse de rotation optimale est atteinte alors le contrôleur augmente l'angle de calage (ce qui diminue l'angle d'attaque) afin de réduire la puissance extraite du vent. Les déflections observées pour les deux modèles aérodynamiques sont très semblables sur les 3 points de fonctionnement. Pour un TSR de 7.0 proche du TSR optimal, la déflection est maximale et les différences de résultats entre les simulations avec pale rigide et pale élastique sont maximales. On observe alors plus de différences entre les deux codes aérodynamiques : dans le cas de la BEMT, l'élasticité de la pale modifie surtout les charges en bout de pale tandis que cela affecte l'ensemble de la pale sur ARDEMA. Cela peut s'expliquer par le fait que la déformation de la pale a le plus d'impact en bout de pale et que dans le cas de la BEMT, l'induction à une position radiale n'est pas affectée par les inductions des autres positions radiales. Dans le cas d'ARDEMA au contraire, l'induction va s'équilibrer sur toute la pale modifiant les valeurs d'angle d'attaque sur toute la longueur et pas uniquement en bout de pale. Tant que le contrôleur n'est pas actif, les puissances et poussées générées par les deux méthodes donnent des résultats jusqu'à 10% différents. Dans les simulations avec contrôleur et une fois que la puissance nominale est atteinte (ce qui est le cas sur les trois points de fonctionnement étudiés), les puissances obtenues sont proches à moins de 1% près tandis que la poussée présente au maximum 3% de différence entre les deux solveurs. La différence de puissance va être gérée par le contrôleur en modifiant légèrement l'angle de calage pour les deux codes. On voit donc clairement que les différences observées dans le cas d'une comparaison purement aérodynamique peuvent ne plus être présentes dès qu'on introduit le couplage aéro-servo-élastique. Cette notion est importante à prendre en considération puisque les calculs de charges effectués dans l'industrie se font obligatoirement avec des codes couplés.

Après la présentation et la validation du code ARDEMA, la dernière partie du chapitre aborde plusieurs cas d'étude centrés sur le désalignement du rotor de l'axe du vent. Une éolienne n'est en effet jamais parfaitement dans l'axe du vent puisque ce dernier est fluctuant, et l'angle peut atteindre plusieurs degrés. De plus de récentes études académiques ont été menées sur l'impact d'un désalignement volontaire afin de réduire les effets du sillage d'une éolienne sur l'autre. Les pertes de production d'une turbine à l'autre pouvant atteindre jusqu'à 40%, désaxer le rotor permet de dévier le sillage afin qu'il ne touche pas la turbine sous le vent. Il est cependant nécessaire de connaitre précisément l'impact d'un tel fonctionnement sur les chargements aérodynamiques. La BEMT n'est en effet à la base pas valide dans ce cas et nécessite une correction basée sur les modèles de sillage déformé et dynamique. De plus, comme vu au chapitre 1, ce désalignement provoque des variations d'angle d'attaque au cours d'une rotation qui ne sont pas négligeables. Un modèle de décrochage dynamique est donc également nécessaire. Le but de cette étude est donc de comparer la méthode BEMT ainsi que les sous-modèles correctifs avec la méthode des panneaux présentée dans des cas de chargement représentatifs des calculs de charges réalisés par l'industrie. En effet la méthode des panneaux modélise intrinsèquement les déformations de sillage, la dynamique du sillage ainsi que les variations de circulation autour du profil. Elle permet donc ici d'offrir une comparaison avec la BEMT afin de déterminer quels sous-modèles sont

sollicités et potentiellement inexacts dans des cas critiques. Des calculs avec vent uniforme puis avec vent cisaillé turbulent sont ainsi présentés, en analysant plus précisément l'impact des modèles de sillage déformé (pour la BEMT) et de décrochage dynamique (BEMT et méthode des panneaux).

Les cas avec vent uniforme sont d'abord présentés. Le tableau 4.9 synthétise les différents cas étudiés. Les désalignements positifs ou négatifs (voir Figure 2.23) sont étudiés pour deux valeurs d'angle différentes : 20° et 40°. L'aérodynamique uniquement est d'abord investiguée (structure rigide et pas de contrôleur), puis ensuite des cas avec élasticité et contrôleur. Pour les premiers, le modèle de déformation de sillage modifie très peu les forces axiales et tangentielles moyennes. Si l'on observe par contre l'évolution au cours d'une rotation, on observe des différences importantes : déphasage et amplitude varient fortement en utilisant le modèle de déformation de sillage. La phase est ainsi plus proche d'ARDEMA mais les amplitudes de variation sont surestimées. Au niveau des forces intégrées sur tout le rotor, les moments avant/arrière YawBrMyn, droite/gauche YawBrMxn et de rotation YawBrMzp (voir Figure 4.36) en haut de la tour révèlent également l'importance du modèle de déformation de sillage : le moment de rotation est largement sous-estimé par rapport à la méthode des panneaux lorsque il n'est pas activé. En utilisant le modèle on remarque cependant une surestimation de ce moment, qui est donc plus conservatif que la méthode des panneaux dans ce cas.
Les cas avec couplage aéro-servo-élastique sont réalisés pour des vents de 5m/s jusqu'à 25m/s afin de couvrir la quasi totalité de la plage de fonctionnement de la turbine. Lorsque la turbine fonctionne avec un fort désalignement, la perte de puissance est importante et la vitesse nominale est atteinte pour une plus haute vitesse de vent que sans désalignement. La figure 4.40 compare les moments moyens en haut de tour : là encore l'influence du modèle de sillage déformable est visible. Dans les cas avec fort désalignement, on remarque en effet que sans ce dernier, le moment de rotation est largement sous-estimé par rapport à la méthode des panneaux tandis qu'il est surestimé avec. La différence entre les différents codes est cependant minime quand il n'y a pas de désalignement. Le modèle a clairement une importance cruciale et permet donc ici à la BEMT d'être conservative par rapport à la méthode des panneaux.
L'impact du modèle de décrochage dynamique est ensuite étudié avec vent uniforme. Un angle de désalignement de -40° est utilisé avec une vitesse de vent de 25m/s, ce qui correspond à des cas où les angles d'attaques sont les plus élevés et subissent des variations importantes. Différentes paramétrisations du modèle de décrochage dynamique sont testées en modifiant les valeurs des constantes de temps du modèle. Les valeurs de base utilisées ici correspondent aux valeurs trouvées dans la littérature, puis deux autres paramétrisations obtenues en multipliant ou en divisant par deux ces valeurs sont testées, ce qui a pour effet d'augmenter ou de diminuer respectivement les différents retards (de pression et de séparation) du modèle. Ces trois cas sont également comparés à des simulations sans modèle de décrochage dynamique. Les valeurs des coefficients de portance révèlent qu'à environ 30% de la longueur totale de la pale, le modèle de décrochage dynamique a un impact significatif en doublant la valeur de la portance par rapport au cas sans modèle de décrochage dynamique. De plus, suivant les valeurs des constantes de temps, ce dépassement de la portance est accentué (constantes de temps doublées) ou diminué (constantes de temps divisées par deux). On constate également que la phase de la portance par rapport à la position azimutale est également impactée par les différentes paramétrisations. A l'échelle du rotor, on retrouve les mêmes effets sur les moments en haut de tour.

Les différentes observations précédentes sont réalisées pour un vent uniforme ce qui permet une analyse plus fine des différents modèles qu'avec un vent turbulent, mais qui n'est pas représentatif des

conditions réelles. Des simulations avec vent turbulent sont donc réalisées ensuite afin de vérifier que les conclusions sur l'impact du modèle de décrochage dynamique soient les mêmes qu'en vent uniforme. Tous les calculs avec la BEMT sont réalisés en utilisant le modèle de sillage déformé et sont présentés dans le tableau 4.13. Un profil vertical de vent est appliqué suivant une loi de puissance avec un coefficient de cisaillement de 0.13. Les simulations sont effectuées sur une durée de 10min avec un turbulence moyenne autour de 8% et issue de données réelles fournies par SGRE. Les séries de 10min de vent turbulents sont générées préalablement à l'aide du logiciel TurbSim. Plusieurs tirages aléatoires sont nécessaires, chacun générant une série temporelle de 10min différente. Les figures présentées tracent des données moyennées ainsi que les écarts-types par position azimutale et non des valeurs instantanées. Une étude sur les valeurs extrêmes est également réalisée en moyennant les valeurs extrêmes issues de 9 tirages aléatoires, ceci afin d'être le plus représentatif possible des conditions réelles. En effet, on remarque une forte variabilité des valeurs extrêmes d'un tirage à l'autre.
On remarque d'abord l'importance des écarts-types pour les moments en tête de tour : la turbulence a un fort impact sur ces valeurs, bien supérieure aux variations observées d'un modèle à l'autre. Cette observation révèle ainsi que la dynamique des modèles est certes importante, mais d'une influence minime par rapport à la dynamique du vent. Ainsi des comparaisons avec vent uniforme semblent indiquer des différences très importantes d'une méthode à l'autre, tandis qu'avec un vent turbulent ces différences sont moindres relativement à la turbulence. La même observation peut être faite sur les différentes paramétrisations du modèle de décrochage dynamique. On observe en effet des différences du même ordre de grandeur qu'en vent uniforme sur les valeurs moyennes, tandis que les valeurs extrêmes semblent beaucoup plus influencées par la turbulence.
Une analyse globale des charges est ensuite réalisée sur les extrêmes et sur les chargements en fatigue. Suivant les charges que l'on observe, les conclusions sont différentes. Ainsi sur certaines signaux les différentes paramétrisations de décrochage dynamique ou les différents modèles sont responsables de différences très importantes, tandis que sur d'autres ils n'ont qu'un impact minime. La conclusion principale de l'étude est donc que les différents modèles investigués sont en effet responsables de variations importantes de chargement, mais qu'afin d'être capable d'identifier la criticité de ces différences les modèles doivent être testés dans les conditions les plus proches possibles des calculs réalisés en ingénierie, et en analysant quelles forces sont critiques pour la turbine dans son ensemble. De plus, le modèle de décrochage dynamique est effectivement fortement sollicité dans les cas avec un désalignement important du rotor, ce qui justifie une investigation plus poussée.

Étude à l'échelle d'une section de pale

Si le chapitre précédent à permis d'identifier des cas de fonctionnement sur lesquels le modèle de décrochage dynamique est critique pour une juste détermination des charges, cette section vise à établir une méthodologie permettant d'approfondir l'étude du décrochage dynamique sur des profils éoliens. Le phénomène est compliqué à simuler pour plusieurs raisons : il implique de résoudre correctement l'écoulement en proche paroi, donc pour des Reynolds élevés nécessite un maillage très fin localement. De plus, les structures de l'écoulement ont des tailles de l'ordre de grandeur du profil, ce qui implique un domaine de calcul suffisamment grand en temps et en espace. Les publications disponibles sur le sujet révèlent que les méthodes RANS sont inadaptées pour ce genre d'étude car le spectre de la turbulence qui est résolu est trop limité pour permettre un développement correct des structures tourbillonnaires. La LES semble plus adaptée puisqu'elle résout un plus large spectre de turbulence. La problématique se

situe alors au niveau du temps de calcul puisque pour des hauts Reynolds une résolution de la couche limite devient rapidement prohibitif. La LES avec loi de paroi (Wall-Modeled LES, ou WMLES) répond à cette problématique : une résolution partielle de la couche limite et la possibilité de simuler correctement les grandes structures détachées. Si ce genre de simulation existe déjà dans la littérature pour des profils aérodynamiques classiques tels que le NACA0012, les profils éoliens beaucoup plus épais sont peu étudiés. Le comportement de ces profils à fort angle d'attaque ainsi que la présence ou non d'un tourbillon de bord d'attaque dans certains cas statiques et dynamiques sont des données relativement peu connues. Ce chapitre introduit d'abord la méthodologie développée afin d'étudier ce genre d'écoulement ainsi que les étapes de validation des calculs. Deux applications sont ensuite effectuées : une pour des écoulements totalement détachés avec un angle d'attaque jusqu'à 90°, et une pour des profils oscillants à haute fréquence réduite.
Les calculs réalisés dans ce chapitre sont effectués à l'aide du code YALES2 [138] développé au CORIA. Les principales caractéristiques du code tel qu'utilisé dans le cadre de cette thèse sont les suivantes :

- Méthode des volumes finis sur maillage non structuré avec schéma central d'ordre quatre.
- Solveur incompressible à densité constante
- Modèle de turbulence de WALE [143]
- Lois de paroi logarithmique et de Duprat [49].
- Méthode du repère tournant pour les cas oscillants, avec injection des termes sources appropriés dans les équations de Navier-Stokes.

L'étude est effectuée sur un profil extrudé dans la direction normale au profil, ce qui correspond à une géométrie dite *2.5D*. Le profil étudié est ici aussi le FFA-W3-241. L'envergure nécessaire à une résolution correcte de l'écoulement est investiguée de $0.25c$ à $4c$ en fonction du type d'écoulement. Le maillage est composé de tétraèdres dans la majorité du domaine et de plusieurs couches de prismes à la paroi. Les caractéristiques des maillages étudiés sont données dans le tableau 5.1. L'utilisation de prismes permet de diminuer la valeur du y^+ tout en conservant des x^+ et z^+ d'un ordre de grandeur plus élevé. Cela permet en effet de mieux résoudre les forts gradients de vitesse dans la direction normale à la paroi. Le maillage le plus résolu M5 a permis d'obtenir un y^+ inférieur à 1 sur toute la surface du profil : aucun loi de paroi n'a alors été utilisée dans ce cas tandis que pour les autres maillages la loi de Duprat est utilisée.

Les cas statiques décrits dans le tableau 5.2 permettent de simuler différentes valeurs d'angle d'attaque du profil, de 4° à 23.2°. Les résultats en terme de coefficients de force sont comparés à des données expérimentales ainsi qu'au code référence Rfoil [201]. Pour les plus faibles angles d'attaque, l'écoulement est attaché et une faible envergure de $0.25c$ a permis d'obtenir des résultats corrects même pour des maillages peu résolus. Les coefficients de pression et friction sont également correctement obtenus. Si la pression est correcte (et donc les coefficients de force) même pour les maillages les plus grossiers, on remarque que le coefficient de friction ne s'approche des résultats obtenus sur Rfoil qu'avec les maillages les plus fins : la prédiction de la transition laminaire/turbulent de la couche limite n'est pas gérée correctement par les lois de paroi et il faut résoudre au mieux la couche limite pour obtenir une transition à la bonne position.
L'obtention des mêmes résultats pour un écoulement détaché est cependant beaucoup plus compliquée.

Avec une envergure trop faible les structures tourbillonnaires propres au décrochage ne peuvent se développer correctement et l'écoulement reste attaché sur une trop grande partie du profil. De plus, il apparait qu'avec un maillage trop grossier le décrochage n'apparait pas correctement non plus. Enfin, l'écoulement étant plus instable, le temps simulé doit être beaucoup plus long qu'en attaché si l'on veut obtenir des valeurs moyennes correctes. Ces trois problématiques impliquent d'augmenter à la fois la taille du domaine, la résolution du maillage et le temps de calcul par rapport à une simulation en écoulement attaché. Il apparait ainsi qu'une envergure de $1c$ est nécessaire au minimum pour le développement de ces structures. Enfin les simulations avec un angle de 16.4° proche de la valeur du décrochage ne permettent d'obtenir un décrochage satisfaisant qu'avec le maillage M3, ce qui n'est pas le cas pour un angle plus grand de 23.2° pour lequel les maillages plus grossiers M1 et M2 donnent des résultats satisfaisants en terme de coefficients de forces. On voit ainsi que la limite de comportement attaché/détaché au niveau de l'angle de décrochage est la plus exigeante en terme de finesse de maillage puisqu'elle nécessite d'avoir la plus grande précision sur le développement de la couche limite turbulente et des échanges d'énergie cinétique permettant la séparation. Une fois ce palier dépassé et l'écoulement détaché, la raffinement du maillage est moins critique. Pour les cas avec maillage M1, il apparait clairement que la couche limite n'est pas résolue mais que l'ensemble de la méthodologie permet malgré tout d'obtenir des résultats satisfaisants en terme d'écoulement : coefficient de pression et position du point de séparation corrects par rapport à Rfoil. Les valeurs expérimentales donnent par contre un décrochage plus sévère et une portance moindre que ce qui est prédit par les deux méthodes numériques (Rfoil et LES). Les conditions de mesures peuvent être responsables de ces différences : turbulence de soufflerie élevée, géométrie du profil, etc...
Une fois les résultats obtenus sur des cas statiques, des cas dynamiques ont été effectués sur la base d'un mouvement oscillant périodiquement. Deux cas décrits dans le tableau 5.5 ont été étudiés pour valider la méthodologie. Ils correspondent à des cas expérimentaux pour lesquels les valeurs des coefficients dynamiques de portance, trainée et moment sont disponibles. Les résultats sur le cas attaché révèlent une prédiction correcte des boucles d'hystérésis en quelques cycles. L'écart type cycle à cycle est assez faible. Le cas détaché, effectué pour un angle moyen assez élevé de 24.6° afin d'avoir un écoulement correctement détaché, nécessite au contraire au minimum une vingtaine de cycles. Une forte variabilité est ainsi observée. Malgré le maillage relativement grossier utilisé et une résolution très partielle de la couche limite, une hystérésis semblable à l'expérimental est observée sur les différents coefficients de force. L'écoulement ne présente pas de tourbillon de bord d'attaque mais révèle une séparation par le bord de fuite typique des profils épais.

Ces simulations ont permis d'établir une méthodologie qui donne des forces aérodynamiques et une phénoménologie de l'écoulement correctes. Les cas étudiés par la suite visent à explorer des situations pour lesquelles des données expérimentales ne sont pas disponibles mais qui peuvent apparaitre sur des turbines réelles : des angles d'attaque jusqu'à 90° (turbine à l'arrêt et/ou avec fort désalignement) dans une première étude, puis des fortes variations d'angle d'attaque (turbulence, vibrations structurelles) dans la seconde. La connaissance de l'écoulement pour ces cas d'étude est enfin cruciale pour améliorer les modèles d'ingénierie tels que les modèles de décrochage dynamique. Il est en effet important de rappeler que certains modèles font l'hypothèse d'un tourbillon de bord d'attaque, tandis que d'autres estiment que ce dernier n'est pas présent pour les profils épais de l'éolien.
Dans une première simulation l'angle d'attaque est d'abord augmenté de 23.2° jusqu'à 40° avant de redescendre, avec une vitesse angulaire suffisamment faible pour que les effets dynamiques soient nég-

ligeables. En effet autour de 40° le décrochage profond est atteint pour lequel la totalité de l'extrado du profil est décroché. Cela implique théoriquement que passée cette limite, les fonctions de retard appliquées dans le modèle de décrochage dynamique ne sont plus valides. L'étude se propose donc de déterminer l'angle à partir duquel le décrochage profond est atteint ainsi que le comportement dynamique autour de cette valeur. Enfin, dans une deuxième simulation l'angle d'attaque est augmenté jusqu'à 90° afin d'étudier les détachements tourbillonnaires autour du profil.
On observe d'abord que plus l'on augmente l'angle d'attaque jusqu'à environ 30°, plus les signaux des forces aérodynamiques sont fluctuants. Les variations sont caractérisées par de hautes fréquences et faibles amplitudes autour de 23°, puis évoluent en un signal périodique de plus grande amplitude. Cela correspond à l'apparition de détachements tourbillonnaires dont l'intensité augmente avec l'angle d'attaque. On remarque également que la variation de la fréquence n'est pas continue : on observe ainsi des paliers pour lesquels une fréquence est identifiable. Plusieurs cas statiques sont alors simulés autour de ces paliers afin d'identifier clairement le comportement de l'écoulement. Cela permet de situer l'angle de décrochage profond entre 34° et 37°. La phase descendante et la phase montante de la simulation ne donnent pas exactement les mêmes valeurs pour les valeurs moyennes des coefficients de force ainsi que pour les fréquences d'oscillation. Il apparait donc que malgré la faible vitesse angulaire choisie une légère hystérésis causée par l'établissement de l'écoulement est observable. Lorsque l'angle d'attaque est augmenté jusqu'à 90°, la fréquence des tourbillons émis diminue ensuite de manière continue une fois que le décrochage profond est atteint. Ils sont émis successivement au bord d'attaque et au bord de fuite pour les angles supérieurs au décrochage profond, et uniquement au bord de fuite pour les angles inférieurs. Sur l'ensemble de la plage d'angle d'attaque étudiée, une bonne corrélation entre les forces aérodynamiques obtenues et des données expérimentales sur d'autres profils est obtenue. De même la fréquence des émissions tourbillonnaires est en accord avec la littérature. Le Strouhal basé sur la corde projetée reste effectivement constant et autour de 0.15 à partir de l'angle de décrochage profond et jusqu'à 90°.
Deux cas dynamiques sont ensuite réalisés proches de l'angle de décrochage profond : l'un autour de 30° (avant le décrochage profond) et l'autre autour de 40° (après le décrochage profond). Le premier cas révèle une hystérésis du même ordre de grandeur que celle du cas de validation proche du décrochage, tandis que le deuxième ne présente quasiment pas d'hystérésis. De plus on remarque que les émissions de tourbillons se synchronisent avec le mouvement oscillant du profil. Une analyse spectrale des signaux temporels sur les phases montantes et descendantes révèle que les fréquences sont plus hautes sur la phase montante que descendante. Il y a ainsi un retard à l'établissement des émissions tourbillonnaires. Ces observations peuvent aider à l'amélioration des modèles de décrochage dynamique : passé l'angle de décrochage profond, les forces ne présentent plus d'hystérésis mais évoluent vers un signal périodique dépendant des variations d'angle d'attaque et auto-entretenu. De plus, cette composante périodique a une fréquence qui dépend dynamiquement de l'angle d'attaque.
Trois cas dynamiques (voir tableau 5.8) avec de hautes vitesses angulaires sont ensuite présentés et comparés avec la théorie de Théodorsen et le code ARDEMA décrit au chapitre 4. L'amplitude du mouvement a été choisie suffisamment grande pour atteindre un angle maximal de 35°. Pour la fréquence réduite la plus faible, on voit apparaitre un tourbillon au niveau du point de séparation sur l'extrado qui est ensuite convecté : il est responsable d'un pic sur la trainée et sur le coefficient de moment qui n'est pas prédit par le modèle de décrochage dynamique implémenté dans ARDEMA. La boucle d'hystéresis sur la portance est très proche pour les deux codes, tandis que la théorie de Théodorsen donne une boucle beaucoup plus faible. En effet le phénomène de décrochage n'y est pas pris en compte. Pour la fréquence

réduite intermédiaire, la présence du tourbillon de point de séparation est moins marquée, tandis qu'elle disparait totalement pour la fréquence la plus haute : le profil ne décroche quasiment pas. Les boucles d'hystérésis sont alors très proches pour les trois méthodes, et les composantes circulatoires et impulsives de la théorie de Théodorsen prédisent correctement les efforts.

Conclusion

Le principal objectif de cette thèse était d'appliquer des modèles aérodynamiques avancés à l'étude d'une éolienne, en conservant la contrainte d'une utilisation industrielle. Dans ce cadre, deux modèles ont semblé pertinents :

- Une méthode des panneaux couplée à un code aéro-servo-élastique existant, permettant de réaliser des calculs de charges en un temps réaliste tout en intégrant plus de physique que les méthodes d'ingénierie comme la BEMT.
- Une méthodologie de Wall-Modeled LES permettant de simuler des écoulements attachés et détachés instationnaires autour de profils éoliens.

Le lien entre ces deux sujets est fondé sur la problématique principale de la simulation aérodynamique des éoliennes : la diversité des échelles spatiales et temporelles. En effet, à ce jour aucune méthode ne permet de simuler correctement un écoulement détaché autour d'une rotor complet en intégrant les contraintes industrielles, c'est à dire en considérant l'environnement turbulent du vent sur des durées suffisamment longues. L'idée est donc de trouver le meilleur compromis entre modèles d'ingénierie et équations de la physique. La limite est ici posée au niveau de la modélisation du décrochage dynamique : la méthode des panneaux ne pouvant résoudre le phénomène physique, on se propose d'explorer avec la WMLES le phénomène en question sachant que cette dernière est inapplicable pour des calculs de charge à l'échelle du rotor.
Les calculs réalisés avec la méthode des panneaux ont permis de comprendre l'importance de la prise en compte des conditions industrielles de simulation. En effet les comparaisons avec la BEMT donnent des conclusions très dépendantes de l'utilisation d'un contrôleur, de la présence de pales élastiques, ou d'un vent turbulent. Des cas spécifiques ont pu être identifiés pour lesquels les modèles semi analytiques de la BEMT sont mis à l'épreuve. La criticité du modèle de décrochage dynamique a ainsi été mise en évidence. Les perspectives d'utilisation du code couplé ont un intérêt à la fois académique et industriel : des comparaisons avec des données expérimentales permettraient de valider au mieux le code afin de l'utiliser pour des cas plus complexes. Ainsi on peut envisager de simuler plusieurs turbines et de comprendre l'impact du sillage sur les charges de la turbine en aval. Des profils complexes de vent pourraient également être inclus dans les simulations avec une meilleure prise en compte des phénomènes dynamiques qu'avec la BEMT.
Une fois établie l'importance du modèle de décrochage dynamique et ses hypothèses explicitées, la WMLES a permis de simuler des cas de décrochage dynamique sur des profils simples. Si la méthode ne permet pas de capturer correctement l'angle de décrochage, elle a permis cependant pour des cas fortement séparés d'étudier les forces statiques et dynamiques sur un profil éolien. Des résultats corrects ont été obtenus avec des maillages relativement grossiers, cependant l'implémentation de lois de paroi plus avancées permettrait sans doute d'améliorer la prédiction du décrochage. Plusieurs observations faites sur les signaux temporels des forces ainsi que le lien avec la phénoménologie de l'écoulement ont permis d'identifier les lacunes du modèle de décrochage dynamique utilisé dans cette thèse. Cela ouvre la porte

au développement de modèles adaptés à ces conditions.
La simulation de pales entières semble également réalisable ce qui permettrait d'étudier le comportement autour d'un objet 3-D et non pas d'une géométrie 2-D extrudée. De plus si le décrochage semble difficile à capturer les détachements tourbillonnaires typiques des très grands angles d'attaque sont obtenus relativement facilement. L'étude pour des pales entières en écoulement décroché serait alors intéressant. Industriellement l'intérêt serait grand aussi puisque ces tourbillons sont connus pour générer des vibrations sur les corps élancés tels que les pales ou les tours d'éoliennes.

Contents

Nomenclature

Dimensionless numbers

Symbol	Description
M	Mach number
Re	Reynolds number
St	Strouhal number $f_s U/c$

Roman letters

Symbol	Description	Unit
a	Axial induction factor	[-]
a'	Tangential induction factor	[-]
c	airfoil chord length	$[\mathrm{m}]$
C_d	Drag coefficient	[-]
C_f	Friction coefficient	[-]
C_l	Lift coefficient	[-]
$C_{l,max}$	Maximum lift coefficient	[-]
C_{l_α}	Lift coefficient linear slope	$[\mathrm{rad}^{-1}]$
C_m	Moment coefficient (at quarter-chord point)	[-]
C_n, C_N	Normal force coefficient	[-]
C_{N_α}	Normal coefficient linear slope	$[\mathrm{rad}^{-1}]$
C_P	Power coefficient	[-]
C_p	Pressure coefficient	[-]
C_S	Smagorinsky constant	[-]
C_t	Tangential force coefficient	[-]
C_T	Thrust coefficient	[-]
C_ω	Wale constant	[-]
D	Drag force	$[\mathrm{N}]$
f	Separation point position	[-]
f_s	Vortex shedding frequency	$[\mathrm{s}^{-1}]$

F	Sectional aerodynamic force	[N]
F_n	Sectional normal force	[N]
F_t	Sectional tangential force	[N]
k	Reduced frequency $\frac{\omega c}{2U}$	[-]
l_K	Kolmogorov length scale	[m]
l_t	Integral length scale	[m]
L	Lift force	[N]
M	Aerodynamic moment (at quarter chord point)	[N.m]
p	Pressure	[Pa]
p_0	Free stream pressure	[Pa]
P	Aerodynamic power	[W]
Q	Q-criterion	[s^{-2}]
r	Local radius	[m]
R	Rotor radius	[m]
s	Non-dimensional time scale $\frac{2Ut}{c}$	[-]
t	Time	[s]
T	Thrust force	[N]
U, u	local flow velocity	[$m.s^{-1}$]
u_τ	Friction velocity $\sqrt{\lvert\tau_w\rvert/\rho}$	[$m.s^{-1}$]
u_p	Pressure gradient velocity $\left\lvert\frac{\nu}{\rho}\frac{\partial p}{\partial x}\right\rvert^{1/3}$	[$m.s^{-1}$]
U_e	Boundary layer edge velocity	[$m.s^{-1}$]
V	Flow velocity	[$m.s^{-1}$]
U_0, V_0	Free stream wind or flow velocity	[$m.s^{-1}$]
u^+	Non-dimensional streamwise flow velocity u/u_τ	[-]
x	Streamwise distance	[m]
y	Normal distance to the wall	[m]
y^+	Non-dimensional distance to the wall $u_\tau y/\nu$	[-]
x^+, z^+	Non-dimensional distance in the streamwise and spanwise directions	[-]

Greek letters

Symbol	**Description**	**Unit**
α	Angle-of-attack	[°]
α_D	Duprat wall-law parameter $\left(\frac{u_\tau}{u_{\tau p}}\right)^2$ with $u_{\tau p} = \sqrt{u_\tau^2 + u_p^2}$	[-]
α_s	Stall angle	[°]
Δ	Filter size	[m]

δ	Boundary layer thickness	$[\mathrm{m}]$
δ_{ij}	Kronecker symbol	
Γ	Circulation	$[\mathrm{m}^2.\mathrm{s}^{-1}]$
λ	Tip Speed Ratio (TSR) $\frac{\Omega R}{V_0}$	[-]
μ	Dynamic viscosity	$[\mathrm{kg}.\mathrm{m}^{-1}.\mathrm{s}^{-1}]$
μ_b	Body dipole panel strength	$[\mathrm{m}.\mathrm{s}^{-1}]$
μ_w	Wake dipole panel strength	$[\mathrm{m}.\mathrm{s}^{-1}]$
ν	Kinematic viscosity	$[\mathrm{m}^2.\mathrm{s}^{-1}]$
ν_t	Turbulent kinematic viscosity	$[\mathrm{m}^2.\mathrm{s}^{-1}]$
ϕ	Inflow angle	$[^\circ]$
Φ	Flow potential	$[\mathrm{m}^2.\mathrm{s}^{-1}]$
σ_b	Body source panel strength	$[\mathrm{m}.\mathrm{s}^{-1}]$
ω	Pulsation	[rad] / $[\mathrm{s}^{-1}]$
$\overrightarrow{\omega}$	Vorticity vector	$[\mathrm{s}^{-1}]$
Ω	Rotor angular velocity	[rad] / $[\mathrm{s}^{-1}]$
τ	Viscous stress tensor	$[\mathrm{kg}.\mathrm{m}^{-1}.\mathrm{s}^{-2}]$
τ_w	Wall shear stress	$[\mathrm{kg}.\mathrm{m}^{-1}.\mathrm{s}^{-2}]$
ρ	Density	$[\mathrm{kg}.\mathrm{m}^{-3}]$

Mathematical operators

Symbol	**Description**
$\langle\phi\rangle$	Statistical averaging
$\overline{\phi}$	Spatial filtering operator
ϕ'	Deviation from the mean $\phi' = \phi - \langle\phi\rangle$
ϕ''	Fluctuations $\phi'' = \phi - \overline{\phi}$
∇	Gradient operator
$\nabla\cdot$	Divergence operator
$\nabla\times$	Curl operator
Δ	Laplacian operator
$\otimes$	Tensorial product

Abbreviations

Symbol	**Description**

AEP	Annual Energy Production
AoA	Angle-of-Attack
ARDEMA	Panel Method code developed by SGRE
BEMT	Blade Element Momentum Theory
B-L	Beddoes-Leishman
CFD	Computation-al Fluid Dynamics
CFL	Courant Friedrichs Lewy
CPU	Central Processing Unit
DES	Detached Eddy Simulation
DNS	Direct Numerical Simulation
DS	Dynamic Stall
FAST	BEMT code developed at NREL
HAWT	Horizontal Axis Wind Turbine
LCOE	Levelized Cost Of Energy
LES	Large Eddy Simulation
OWF	Offshore Wind Farm
OWT	Offshore Wind Turbine
PDE	Partial Differential Equation
PI	Proportional Integral
RANS	Reynolds-Averaged Navier-Stokes
RF	Reduction Factor
RNA	Rotor Nacelle Assembly
SGS	Sub-Grid Scale
SGRE	Siemens Gamesa Renewable Energy
TBL	Thin Boundary Layer
TI	Turbulence Intensity
TSR	Tip Speed Ratio λ
WMLES	Wall-modeled Large Eddy Simulation
WTG	Wind Turbine Generator
VAWT	Vertical Axis Wind Turbine
VIV	Vortex Induced Vibration
YALES2	Yet Another LES Solver: LES/DNS solver developed at CORIA laboratory

Chapter 1

General Introduction

Contents

1.1 Industrial context

1.1.1 Global energy transition

In 2019, the global warming due to human activity is only questioned by a few scientists. The reality and magnitude of the phenomenon has led to strong concerns by most of human organizations, but the effective actions to prevent it are still limited. The United Nations Framework Convention on Climate Change (UNFCCC), part of the United Nations Secretariat, is an international environmental organisation that leads some major political awareness achievements regarding climate changes. The main international treaties handled by UNFCCC are the Kyoto Protocol from 1997 that tackled the reduction of global greenhouse gases emissions, followed by the Paris Agreement from 2015 that targets an increase of global temperature of less than 2°C by 2100. For more information regarding these treaties, the UNFCCC website [4] contains the original texts, synthesis and explanations. The Intergovernmental Panel on Climate Change (IPCC) report from 2018 [168] is the latest international report proposing solutions to cap the temperature raise to 1.5°C showing the huge consequences of decreasing the temperature raise from 2°C (Paris Agreement) to 1.5°C, and promoting the use of renewable energies. Indeed, the production of electricity based on fossil fuels is one of the major source of greenhouse gases emissions, which itself is directly correlated to the average warming of the planet.

Figure 1.1 is extracted from [168] and shows the correlation between carbon dioxide emissions and the Earth surface temperature, based on observations and models for future trends. The trends based

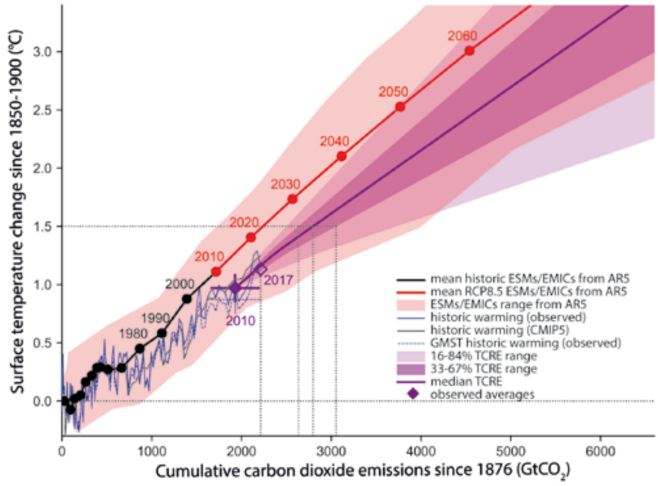

Figure 1.1: Correlation between the surface temperature and the cumulative carbon dioxide emissions since 1876 - [168]

on the previous IPCC reports from 2015 (AR5 reports) overestimates the temperature raise but underestimates the carbon emissions compared to latest models. However, both predict a global warming far above 2°C during 21st century. Even respecting the commitments of the Paris Agreement, temperature is expected to surpass 1.5°C. The 2018 IPCC reports suggests several scenarii implying different socio-economic pathways and technology choices, all showing a massive investment in solar and wind energies as illustrated in 1.2.

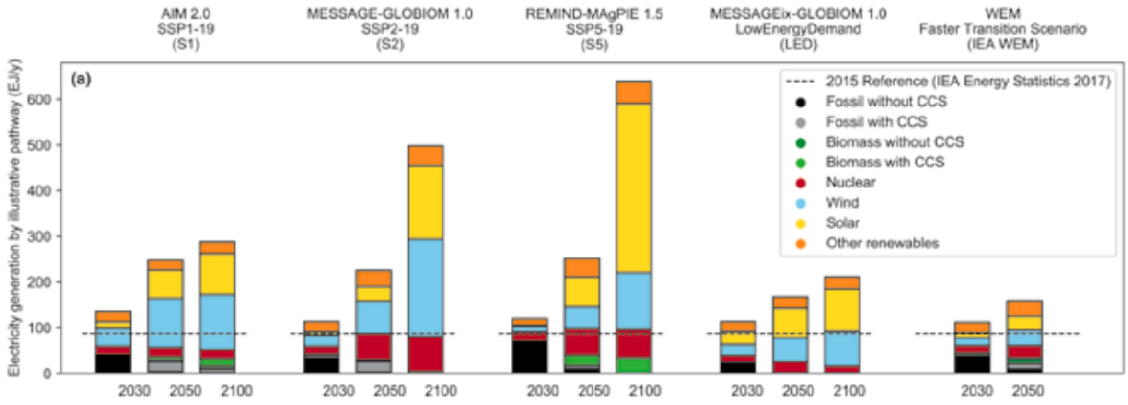

Figure 1.2: Energy production perspectives for global warm mitigation - [168]

This international code of practice has brought many countries to have new goals for energy production in order to cope with such dramatic perspectives. In that respect, European Union policies from 2007 [52] and then 2009 [53] propose to reach 20% of renewable energy sources in EU by 2020. All communications from EU regarding energy topics are avaible on European Commission website [2]. Each EU country then proposed an energy plan in order to achieve the target of an average of 20% over all EU. France targeted a 23% share of renewable energies while other countries had higher or lower targets (30% for Denmark, 18% for Germany or 15% for UK). In France, the Grenelle de l'Environnement in

2007 was a succession of decisions with environmental concerns. It was followed by the Programmation Pluriannuelle de l'Energie (PPE), or Multiannual Energy Plan from 2016 that describes the goals regarding energy production pursued by the French government. Some key numbers reveal the ecological ambitions for the next years: increase renewable energy sources by over 50% by 2023 while decreasing total energy consumption [132]. This document is renewed regularly in order to assess new environmental goals, and is considered as the French energy roadmap. The latest PPE from early 2019 targets to double the renewable energy installed power by 2028 compared to 2017.
Despite these political decisions and some progresses, the targets from 2009 do not seem to be achievable for all European countries in 2020: according to the International Energy Agency report on renewables energies from 2018 [91], in 2017, France had a 9.8% share of energy coming from renewable sources (35% for Denmark, 13.5% for Germany and 9.6% for UK). These numbers reveal the importance to have a faster energy transition from now on, with the development of promising technologies such as offshore wind energy.

1.1.2 Offshore wind energy in Europe

The trends in energy production for the next years reveal that renewable energies are considered as one of the energy demand solutions for the future by industrials such as DNV GL [45]. The investments from the past 20 years made in wind energy confirm this interest. More specifically, the growth of the offshore wind energy business in Europe with a total installed offshore wind capacity of 18499 MW in 2018 [5], with each year an increasing number of new turbines installed, is a clear indicator of these tendencies. However, Fig. 1.3 reveals that all European countries do not follow the same pattern regarding offshore wind energy.
Denmark was a pioneer in offshore wind energy, but in the recent years Germany and UK are the main

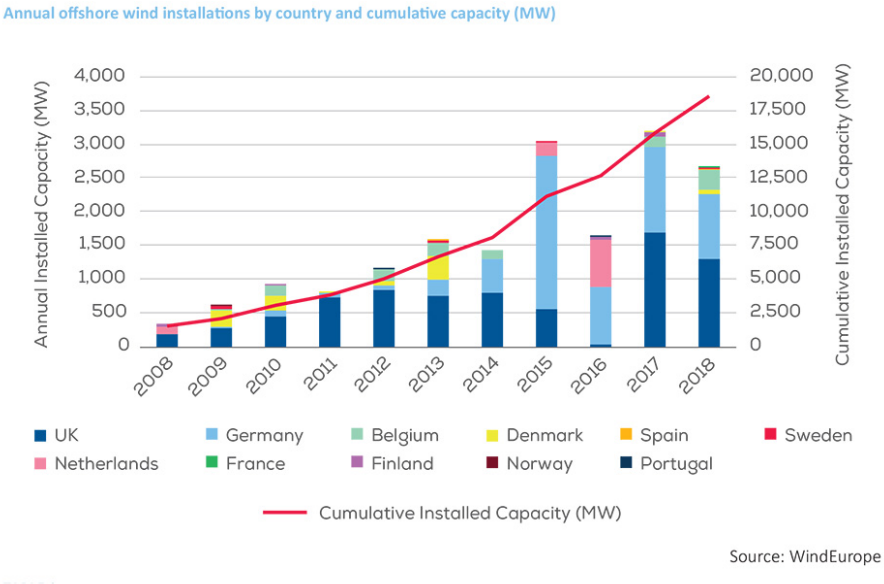

Figure 1.3: Offhsore wind in Europe - [5]

countries installing offshore wind farms. Rodrigues [167] or Präsller [155] investigate the main offshore

wind markets trends and notice that the attractiveness of offshore wind energy for a given country is dependent on many parameters: historical energy production but also the environmental conditions. For example, the average annual wind speed directly impacts the Annual Energy Production (AEP) and thus the profitability of a wind farm. The depth and type of soils also directly impact the cost of installation. The drop in the cost of energy (Levelized Cost Of Energy, or LCOE) for future wind farms is, aside from any environmental concerns also one of the main reason pushing investors toward offshore wind. Indeed, as illustrated in Fig. 1.4, the LCOE for the next installed wind farms is close to 50€/MWh, which is in the range of fossil energy cost.
France is very delayed mainly because historically power production comes from nuclear energy. Nuclear power is a carbon free provider but suffers from difficult cost evaluations, vulnerability to fuel providers and uncertainties regarding the treatment of nuclear wastes. Several calls for tenders for offshore wind farms have been launched by the French government in 2012 and 2014. Six wind farms of each 500MW are to be built in the next years. Several calls for tender have also been announced by the French government for the next years in the 2019 PPE. The offshore wind industry in France is suffering

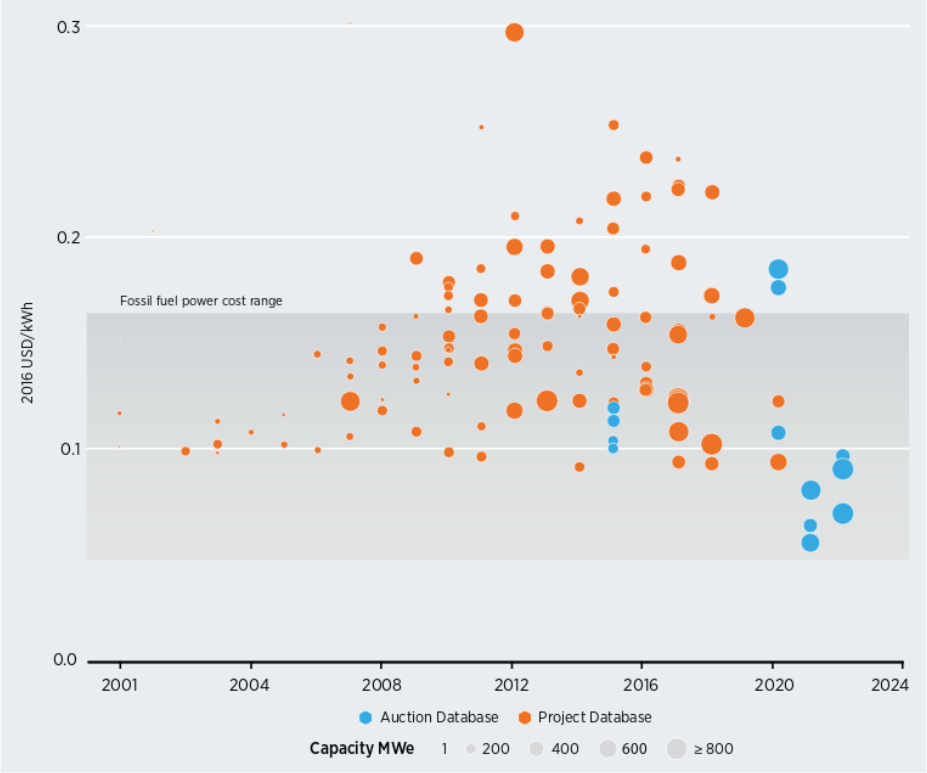

Figure 1.4: Cost of energy for Offshore wind farms in Europe- [93]

from this delayed involvement in offshore wind energy but thanks to these recent tenders several factories are being built in the country and engineering teams recruited by two main wind turbine manufacturers: Siemens Gamesa Renewable Energy (SGRE) and General Electric (GE).

1.1.3 Very large wind turbines: new challenges

There are several differences between offshore and onshore wind energy because of the marine environment:

- The cost of foundation for fixed Offshore Wind Farms (OWF) is much larger than onshore.
- The installation and maintenance imply to use costly vessels.
- The saline environment requires specific design to avoid corrosion.
- Less size constraints compared to onshore as the impact on population is lower.

The main consequence is that Offshore Wind Turbines (OWT) are growing in size as for a same installed capacity the number of turbines will be reduced, and thus also the costs for foundations, installation and maintenance. However building larger turbines is not straightforward. Indeed, Ashuri shows in several publications [7, 9] that increasing the size of the turbines without designing more optimized turbines is not improving costs. New concepts must then be investigated to take advantage of the increased rotor size.

The evolution of the wind turbine power and rotor size is illustrated in Fig. 1.5. The latest generation of

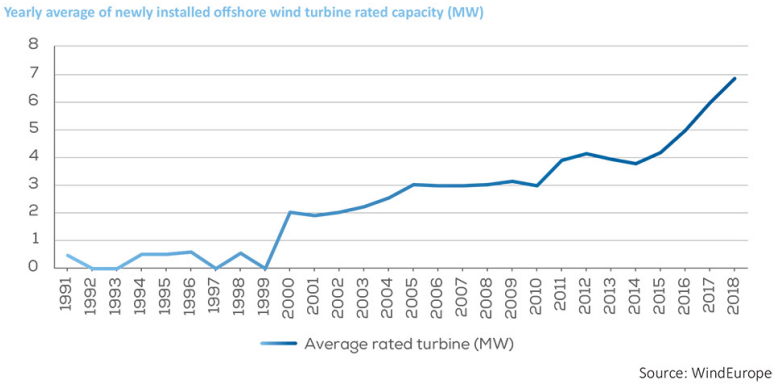

(a) Mean power of installed Offshore Wind Turbines (OWT) per year - [5]

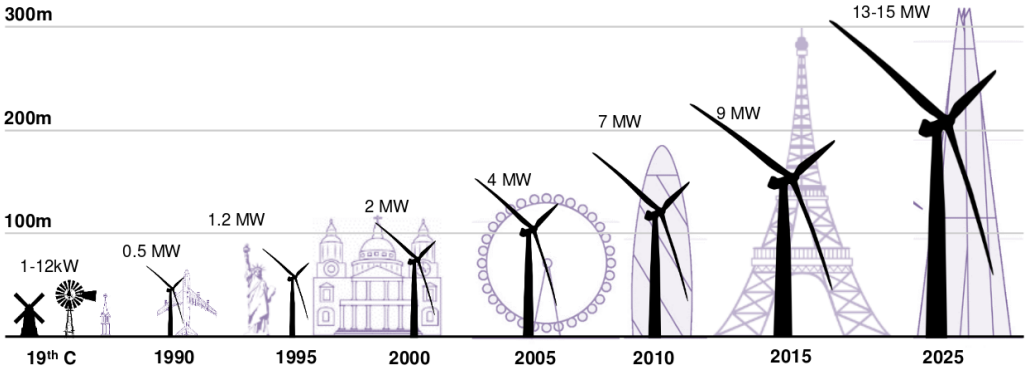

(b) Representation of largest wind turbine compared to famous man built structures along the years - [114]

Figure 1.5: Wind turbine size evolution

wind turbines have blades from 80m to 100m for a rated power of around 8MW to 10MW. Such blades are among the largest industrial composite structures.

1.2 Scientific context

1.2.1 Wind turbine optimization

The optimization of the cost of energy (LCOE) produced by wind turbines is a very active field of research [57][23] [208][36], with two main perspectives:

- Reducing the loads on the rotor in order to decrease the constraints in critical components of the turbine. The load reduction implies the possibility to reduce the mass of material used, and thus the price (considering equal manufacturing process) of each machine.
- Improve the Annual Energy Production (AEP) by improving the power curves (turbine level) and reducing wake effects (farm level)

The optimization process requires a multi-disciplinary approach: structural optimization requires adequate structural modeling while improvement of aerodynamic loads and AEP implies suitable aerodynamic models. Fig. 1.6 is extracted from Ashuri paper [8] and illustrates the design variables that must

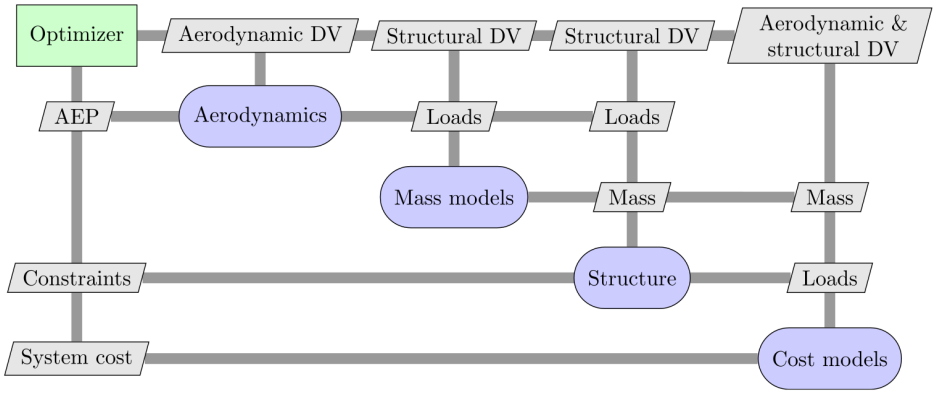

Figure 1.6: Optimization process of a wind turbine - [8]

be considered for optimization, the calculation modules and the flow charts between them. One must keep in mind that a wind turbine must be certified in order to be marketable, following specific standards regarding site conditions, lifetime, extreme loading, etc... The constraint of certification and the inclusion of such constraints in the optimization process is a challenge combining engineering processes and physics modeling.

1.2.2 Advanced models for improved performances

Aerodynamic modeling is necessary to predict the loads and the generated power, and thus is necessary for designing a wind turbine. State-of-the-art tools such as the Blade Element Momentum Theory (BEMT) have been used for certification despite the fact that they rely on many empirical models. Large safety factors are used to ensure that the effective loads will be lower or equal to the computed loads despite the uncertainties in these models. This process can result in an overestimation of the loads compared to reality and in a non-optimized turbine. On the other hand, the loads could in fact be underestimated in specific cases despite the safety factors, with a risk of failure of the turbine. Furthermore, new turbine

operating conditions, specific blade add-ons involving complex flow features, and challenging structural designs are more and more implemented on modern wind turbines to improve performances. The response of state-of-the-art tools to such conditions is not known, giving a priori inaccurate results. For example the yaw misalignment and standstill cases are both out of the validity range of state-of-the-art tools. For the yaw cases, the correct prediction of the induced velocity field requires to use empirical models such as yaw and dynamic stall models. Investigating such models is still an active field of research. Standstill cases also involve unsteady flows possibly responsible for Vortex Induced Vibrations (VIV). The prediction of the resulting unsteady forces in such configuration is also an active field of research for OWTs.
Large European Union research projects such as INNWIND.EU [3] and AVATAR [1] projects have been conducted lately in order to focus on the design of new large rotors and the benchmarking of aerodynamic tools for wind turbines. Computational fluid dynamics and vortex methods (see Chapter 3), which are not commonly used in industry, have been compared to state-of-the-art tools. However such tools are often not adapted to industry for the standard certification process which requires numerous calculations, because of the large CPU time needed by such methods. The challenge is thus to develop fast enough models and assess the specific conditions for which they can improve the aerodynamic calculations.

1.3 Thesis context

This thesis has been conducted in the framework of a partnership between Siemens Gamesa Renewable Energy (SGRE) and CORIA laboratory in Rouen, France. SGRE is a wind turbine manufacturer, world leader in offshore wind. Five 500MW french wind farms are planned to be built in the next years, supplied with SGRE 8MW wind turbines. To produce these turbines, two plants are under construction in Le Havre harbour. These projects generate activity linked to wind energy in the region. A SGRE R&D center is in development in Rouen, close to the future plants, in order to also develop connexions with labs and universities involved in wind energy. This center is focused on the development of new methods for loads calculation, and developed an industrial tool based on a panel method first developed at Delft University by Dixon [44]. The expertise of CORIA laboratory in Rouen in high performance computing and Computational Fluid Dynamics (CFD) raised interest to start a partnership between SGRE R&D center and CORIA in order to improve the performances of the panel method code and investigate other advanced tools. This PhD is one aspect of this collaboration.
The aim of the present thesis is to investigate advanced aerodynamic models compared to state-of-the-art tools in the framework of realistic industrial load calculations. Unsteady effects and more specifically dynamic stall are considered to be key phenomena to predict correctly the loads. The models investigated in this thesis should thus be able to improve the loads calculations involving dynamic stall and more generally unsteady flows. The main targets are the following:

- Integrate a dynamic stall model in a panel method code in order to obtain an advanced aerodynamic model capable of simulating wind turbines in challenging environmental conditions.
- Assess the impact of such model on the aero-elastic response of an offshore wind turbine in the framework of industrial load calculations.
- Investigate the possibility to improve dynamic stall predictions based on more advanced CFD tools by performing Large Eddy Simulations (LES) of dynamic stall cases. The LES code YALES2 developed at CORIA laboratory is used for this purpose.

1.4 Manuscript content

The manuscript is divided in the following chapters:

Chapter 1 General Introduction
The present chapter is a general introduction to wind energy main challenges. The relation between aerodynamic modeling and industrial challenges is addressed through the optimization of wind turbines.

Chapter 2 Aerodynamic principles of wind turbines
This chapter is an overview of main aerodynamic phenomena observed on wind turbines. The bases of aerodynamics are introduced with a focus on unsteady phenomena. A first characterization of flow unsteadiness is performed by analyzing the geometric inflow angle of a rotor for specific operating conditions.

Chapter 3 Aerodynamics modeling for wind turbines: state-of-the-art
In this chapter, several aerodynamic modeling theories are presented. The state-of-the-art Blade Element Momentum Theory is briefly explained and its main corrective models with a focus on dynamic stall models. Then vortex methods and potential theory are described through the lifting line theory and panel methods. Computational Fluid Dynamic and their main application for wind turbines are finally presented, in particular Large Eddy Simulation theory.

Chapter 4 From section to rotor: a panel method for viscous flows
Chapter 4 presents the panel method code ARDEMA and its coupling to FAST code. The dynamic stall model implemented in ARDEMA is validated against experimental measurements. ARDEMA is compared to the state-of-the-art aerodynamic code AeroDyn, in a standalone version and also with an aero-servo-elasto coupling. Comparisons of both methods are performed in yaw cases for several operating conditions. The impact of the dynamic stall model on the loads is then specifically investigated.

Chapter 5 Aerodynamic at section level: Large Eddy Simulation
This chapter focuses on the application of Wall-modeled Large Eddy Simulation to wind turbine airfoils. The flow around the thick FFA-W3-241 airfoil is first investigated in static cases and validated against experimental data and Xfoil code at a Reynolds number of $1.6 \cdot 10^6$. Attached and detached flows are simulated on coarse and refined grids. In the attached case, a wall resolved simulation is performed on a refined grid and compared against wall-modeled cases. Oscillating cases are then presented, for both attached and detached flows and compared to experimental data. Further investigation is then performed by investigating deep stall cases up to AoA of 90° and highly unsteady flow cases with high reduced frequencies.

Chapter 6 Conclusions and perspectives
The last chapter proposes a conclusion on the several models investigated in this thesis regarding their relevance for wind turbine aerodynamics. Ideas for future work are also presented.

Chapter 2

Aerodynamic principles of wind turbines

Contents

Wind turbine aerodynamics is at the heart of the wind energy industry as the price of generated electricity is correlated with the aerodynamic performance of the rotor. Most of the knowledge in this field comes from more than 50 years of development in aircraft industry adapted to wind turbines specificities in the 70s. The main challenge in wind turbine aerodynamics is the variability and unsteadiness of the wind [109] for which most steady models are not suited. In the present chapter, the main physical principles behind wind turbine aerodynamics are presented, and an in-depth focus is made on unsteady phenomena. The modeling of such phenomena will then be presented in Chapter 3.

The first section 2.1 of the present chapter introduces the 2-D aerodynamics, based on the study of the flow around an aerodynamic profile. Dynamic stall is specifically presented. However, a wind turbine blade is a 3-D shape designed as a succession of 2-D profiles, with some specific behavior caused by the 3-D nature of the flow around it. Some specific 3-D flow features are then presented in section 2.2. The main definitions of the flow around a 3-bladed rotor are then presented in section 2.3, focusing on the operating conditions creating unsteadiness with the possible apparition of dynamic stall.

2.1 2-D Aerodynamics

Planes, helicopters, propellers or wind turbines are all based on a fundamental technology and underlying physical principle: the aerodynamic profile, or lifting surface. A flow passing around a specific shape generates a lift force that is used efficiently to operate a given device. When extruding a 2-D shape in a way that the extruding length is much larger than the dimension of the shape, an incoming flow passing through the obtained volume perpendicularly to the extruding direction can be considered as a 2-D flow at mid-span as the flow velocity in the extruding direction is close to zero. Thus the flow passing through a wind turbine blade (a slender volume based on 2-D extruded aerodynamic profiles) mostly consists of a streamwise component and a much smaller spanwise component (radial flow), depending on the operating conditions of the turbine. For this reason, the study of 2-D flows is of interest when studying the aerodynamics of wind turbines.

2.1.1 Origin of lift

To get a simple understanding of the origin of lift, a few concepts can be introduced. A first explanation relates the lift force to the curvature of the streamlines around the airfoil [82]. Indeed the momentum equation for a perfect fluid (incompressible, uniform density, no viscosity) and in the case of a steady flow gives the following relation in the Frenet-Serret frame (natural coordinate system from Fig. 2.1) : $\rho\frac{V^2}{R} = \frac{\partial p}{\partial r}$. A strong curvature (small radius R) implies a strong pressure gradient linked to the lift force once integrated over the airfoil area.

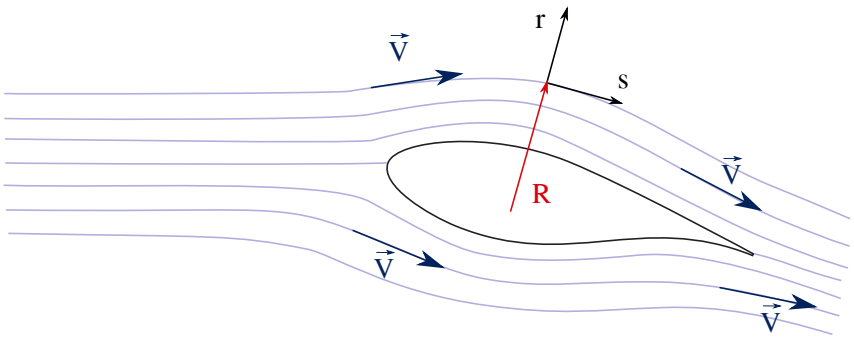

Figure 2.1: Streamlines around an airfoil and Frenet-Serret frame

Another explanation for the lift can be found with the Kutta condition illustrated in Fig. 2.2). Any streamlined body in a stream with a given angle of attack will have two stagnation points, the front and the rear stagnation points. For an airfoil with a sharp trailing edge, the Kutta condition implies that the rear stagnation point will move from a position on the suction side close to the trailing edge, to the exact position of trailing edge. The difference in velocity at the trailing edge between the pressure and the suction sides creates a vortex with a circulation Γ. The general definition for circulation around a closed curve is $\Gamma = \oint_C \overrightarrow{V} \cdot \overrightarrow{dl}$ with $\overrightarrow{V}$ the velocity at a small curve segment on the close curve and $\overrightarrow{dl}$ a vector representing the differential length of the small curve portion. To compensate for the circulation of the trailing edge vortex, an opposite circulation appears around the airfoil with the flow rotating in the opposite direction than the flow around the trailing edge vortex which is then convected downstream. The velocity on the suction side is then accelerated while the velocity on the pressure side is decreased. The

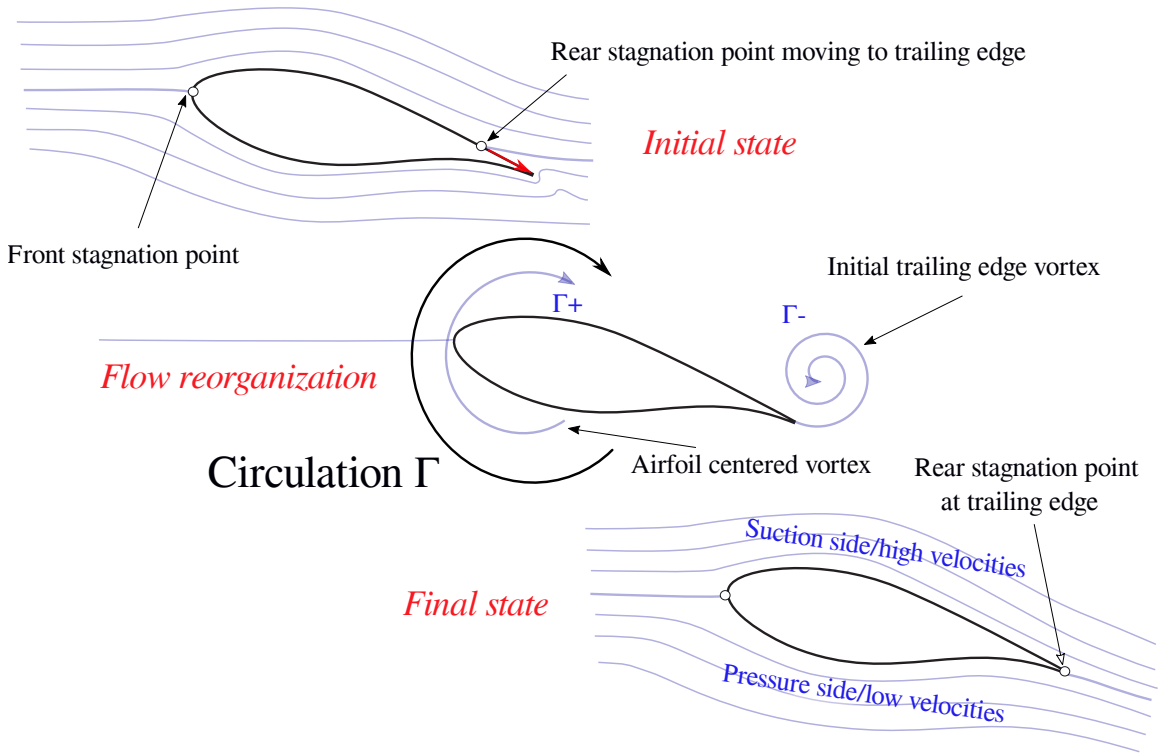

Figure 2.2: Circulation around a profile - Kutta condition

Bernoulli equation then implies that the pressure on the suction side will be lower than on the pressure side, creating lift. The Kutta-Joukowski theorem states that the lift L of an airfoil is proportional to the circulation around the profile with the following relation:

$$L = \rho V_0 \Gamma \tag{2.1}$$

2.1.2 Aerodynamic profiles and polars

A 2-D analysis is enough to understand the basic definitions of the forces applied on an aerodynamic profile (or airfoil). The main definitions are vizualised in Fig. 2.3.

- **Incoming velocity** V_0 is the unperturbed upstream flow velocity.
- **The leading and trailing edge** are respectively the fore and aft edges of a streamlined body.
- **Chord length** c is the length of the profile, from leading edge to trailing edge.
- **Angle of attack** α is the angle between the incoming flow and the chord direction.
- **Lift** L is the component of the total aerodynamic force F perpendicular to the incoming flow.
- **Drag** D is the component of F in the flow direction.
- **Moment** M is the moment generated by the aerodynamic forces, often given at the quarter chord point.

The lift C_l, drag C_d and moment C_m coefficients correspond to the non-dimensional aerodynamic forces and have the following definitions (considering aerodynamic linear forces per spanwise length):

$$C_l = \frac{L}{\frac{1}{2}\rho V_0^2 c}\,, \qquad C_d = \frac{D}{\frac{1}{2}\rho V_0^2 c} \tag{2.2}$$

and :

$$C_m = \frac{M}{\frac{1}{2}\rho V_0^2 c^2} \tag{2.3}$$

with ρ the fluid density. The aerodynamic forces can also be projected in the coordinates system of the airfoil defined by the chord and the perpendicular to the chord respectively called the tangential and normal forces, F_t and F_n. The corresponding non-dimensional coefficients are C_t and C_n.
A few other specific points are useful when defining airfoils. The *center of pressure* is defined as the point where the integrated surface forces (either only pressure forces, but most often pressure and viscous forces) acting on the profile have no moment. The position of the center of pressure is dependent on the angle of attack. The *aerodynamic center* of the airfoil is a point on the chord where the moment is not dependent on the angle of attack. It has been observed experimentally that this point is close to the quarter chord for many airfoils.

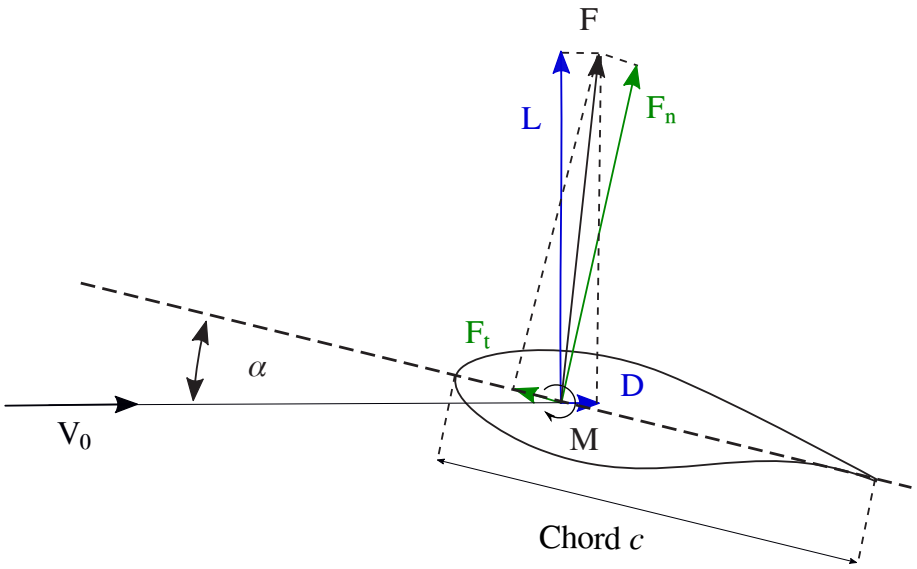

Figure 2.3: Definitions of lift and drag on an aerodynamic profile

The design of airfoils is of course driven by their aerodynamic performances, but constrained by structural limits. In the 1990s, many new airfoils have been designed specifically for wind turbines to replace the generic NACA airfoils designed for aeronautics. NREL (National Renewable Energy Laboratory) developped airfoils from the 1980s for relatively small blades (less than 25 meters) with the purpose to get airfoils with higher lift and less sensitive to blade degradation and dirt [190]. Risøe and Delft [194] universities also proposed airfoil designs with same purpose, with a synthesis from Risø [16] of the different airfoil families used or designed for wind turbines. All these airfoils are much thicker than the ones considered in aeronautic industry mainly for structural reasons. Large wind turbines blades are made of composite materials in order to have light blades with increased stiffness. Sections

close to the root are very thick to resist to the full blade loading and are thinner toward to the tip. For more information, Timmer and Bak delivered an interesting synthesis of wind turbine airfoils desired characteristics [195] :

- A high lift-to-drag C_l/C_d ratio to optimize aerodynamic performance;
- Smooth stall to reduce fatigue loads
- High relative thickness - ratio between thickness and chord length - to reduce blade weight
- High lift coefficient to reduce the chord and thus loading in standstill conditions.
- Low sensitivity to leading edge roughness caused by contamination or deterioration.

The FFA-W3-xxx airfoils series used on the DTU 10MW blade has been created by the Aeronautical Research Institute of Sweden in 1990 [18]. Four FFA-W3-xxx profiles from 21% to 36% of relative thickness are displayed in 2.4. It is worthwile to notice the presence of small flatbacks on these profiles, characterized by a flat vertical trailing edge that ensures good structural properties with limited aerodynamic losses.

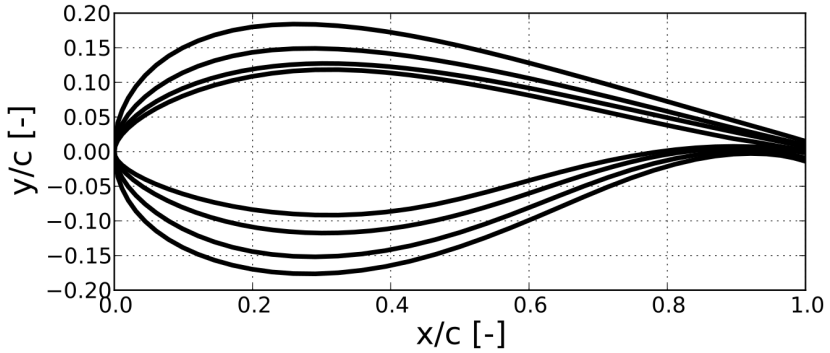

Figure 2.4: FFA-W3-xxx airfoils series of 21.1%, 24.1%,30.1% and 36% relative thickness [13].

More recently, Grasso proposed optimization methods taking into account structural and aerodynamic constraints to design new thick airfoils for sections close to the root of very large turbines [70]. Grasso also worked on specific airfoils with flatback in order to reduce the strong unsteadiness caused by the large sharp trailing edges of such airfoils [71]. Most recent concerns regarding airfoil design for new large rotors are addressed in the deliverable 2.12 from INNWIND.EU European research project [121].

The purpose of such research is to obtain specific aerodynamic behavior depending on the use of the airfoil. This behavior is mostly summarized by the *polar diagrams* of the airfoil which consists of the lift C_l, drag C_d and moment C_m coefficients given for a wide range of angle of attacks α. In Figure 2.5, polar data are presented for the FFA-W3-xxx series. For α approximately between $-10°$ and $+10°$, lift and moment coefficients are linear while drag is close to negligible. Then for higher absolute values of α, at the *stall angle* α_s, lift drops and drag increases: the phenomenon is called stall and is detailed in Section 2.1.3. These polars are mostly obtained with wind tunnel measurements, but more and more frequently

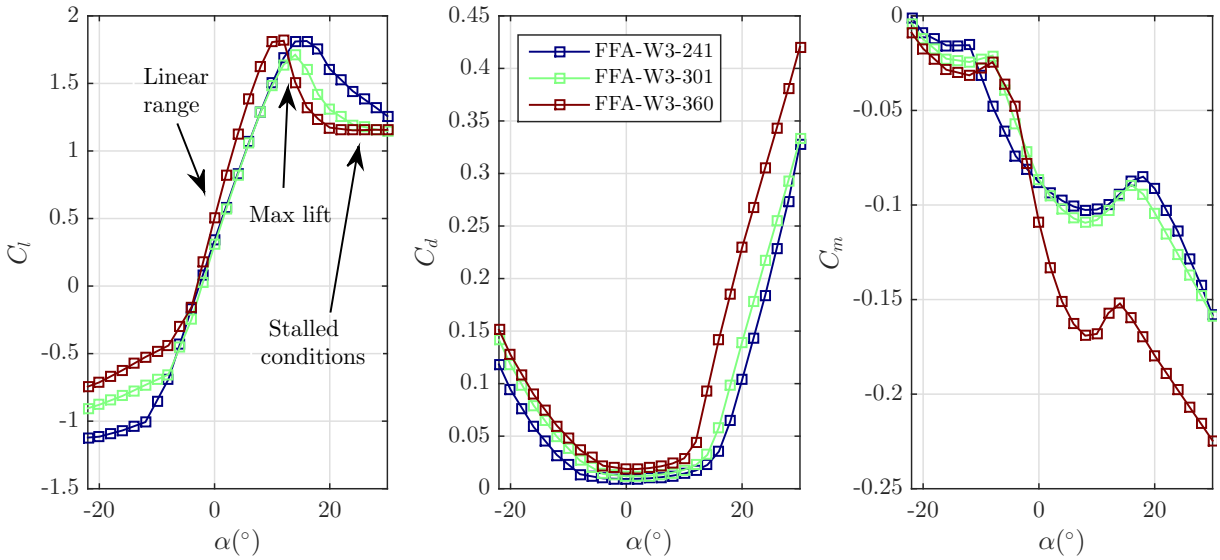

Figure 2.5: Lift, drag and moment coefficients of 3 airfoils from DTU 10MW turbine [13].

with CFD. The aerodynamic coefficients are dependent on the angle of attack α and the Reynolds Re and Mach M numbers defined by the following relations:

$$Re = \frac{\rho V_0 c}{\mu} \equiv \frac{\text{Inertial force}}{\text{Viscous force}} \tag{2.4}$$

and :

$$M = \frac{V_0}{V_{sound}} \tag{2.5}$$

with V_{sound} the speed of sound in the fluid. Re characterizes the balance between inertial and viscous forces in a fluid, while M is used to evaluate the level of compressibility of the flow.

For industrial wind turbines, Re range is approximately from 10^6 to 2.0×10^7 which is very high compared to a lot of domains, and the flow can be considered dominated by the inertial forces. With the increasing size of the blades, the blade section chords and thus Re are larger. Due to wind tunnel limitations, very few data are available at Reynolds numbers range above 10^7 which is common for recent turbines and new measurements have been performed recently to assess the impact of such high Re [152] [120]. In Figure 2.6, it appears that for the investigated airfoil the stall angle and the maximum lift coefficient $C_{l,max}$ increase with Re. However, wind tunnels are limited in size for obvious reasons and limited in flow velocity to avoid compressible effects, and few are able to reproduce such high Re. These limitations raise interest in new methods for obtaining polars, such as CFD (see chapter 3.3) or panel methods with boundary layer formulations (see chapter 3.2).

The Mach number M is of lesser importance as the values are always rather low for wind turbines, below the compressibility limit around 0.3. However, with the increasing size of turbines, the flow velocity at the tip sections get close to 0.3 and some compressible effects could appear. In order to avoid this issue that could result in some instabilities and additional loading, the large wind turbines have a low rotation speed compared to smaller ones. Some investigations are still conducted to develop airfoils with better handling of compressibility effects [121].

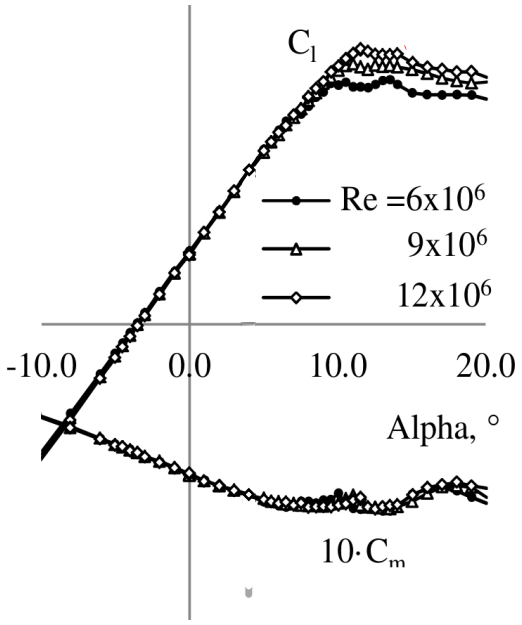

Figure 2.6: AWA18-1 lift and moment coefficients for three Re numbers [120].

2.1.3 Stall and viscous boundary layer

Stall is an important aspect of the airfoil aerodynamic behavior as it is responsible for fast changes in the loads applied on the airfoil, generating instabilities, increased fatigue and power loss at the turbine level. The shape of the airfoils directly impacts the stall, categorized in several typical behavior. Gault [64] suggests to classify the different types of stall depending on the upper surface ordinate at $0.0125c$. This value is related to the leading edge shape: the higher it is, the rounder the leading edge is. Sharp leading edges have *thin-airfoil stall* characterized by a smoother stall with a discontinuity in lift before stall. As the leading edge curvature radius increases, stall then goes from *leading edge stall* to *trailing edge stall*. The first is characterized by a very sharp stall, and the second by a smooth stall. Combinations of these stall types are called *combined stall* as it is shown in Fig. 2.7.

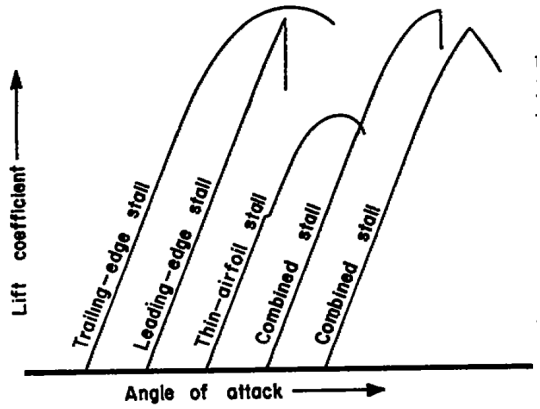

Figure 2.7: Classification of stalling characteristics by Gault [64]

The different stall types are caused by a very narrow flow zone attached to the airfoil surface called the boundary layer which detaches in different ways. It defines stalled conditions with an important shear in the so-called *separated flow* region. The shape of the airfoil in particular determines at which angle α_{stall} the boundary layer starts detaching.
At high Reynolds numbers, flow is dominated by inertial forces and can be considered as inviscid except in the boundary layer where viscous effects are predominant. The wall shear stress τ_w quantifies the friction between the flow and the airfoil surface:

$$\tau_w = \mu \left(\frac{\partial u}{\partial y} \right)_{y=0} \tag{2.6}$$

with μ the fluid dynamic viscosity.
Friction causes the flow velocity to be zero at the surface of the airfoil and then recovers up to the inviscid velocity far from the surface. The boundary layer thickness $\delta(x)$ is then often defined as the distance where velocity reaches 99% of the outer velocity [172], with x the distance from the front stagnation point to the considered point on the airfoil surface. The pressure gradient $\partial p/\partial x$ along the surface has a considerable importance in the development of the boundary layer. The pressure along x is the same inside and outside the boundary layer and is given by the inviscid flow. Indeed, the boundary layer is very small compared to the curvature of the streamlines, implying a negligible pressure gradient along the normal direction to the wall. Depending on the shape of the airfoil the outer flow accelerates or decelerates along x, respectively decreasing or increasing the pressure according to Bernoulli equation. Fig. 2.8 illustrates that for adverse pressure gradient ($\partial p/\partial x > 0$), the flow in the boundary layer with little kinetic energy cannot manage to get over the increasing pressure and decelerates until it is pushed backward. The boundary layer then thickens and detaches from the airfoil surface at the *separation point*, altering the whole downstream flow. The separation point is characterized by a wall shear stress τ_w equal to zero.

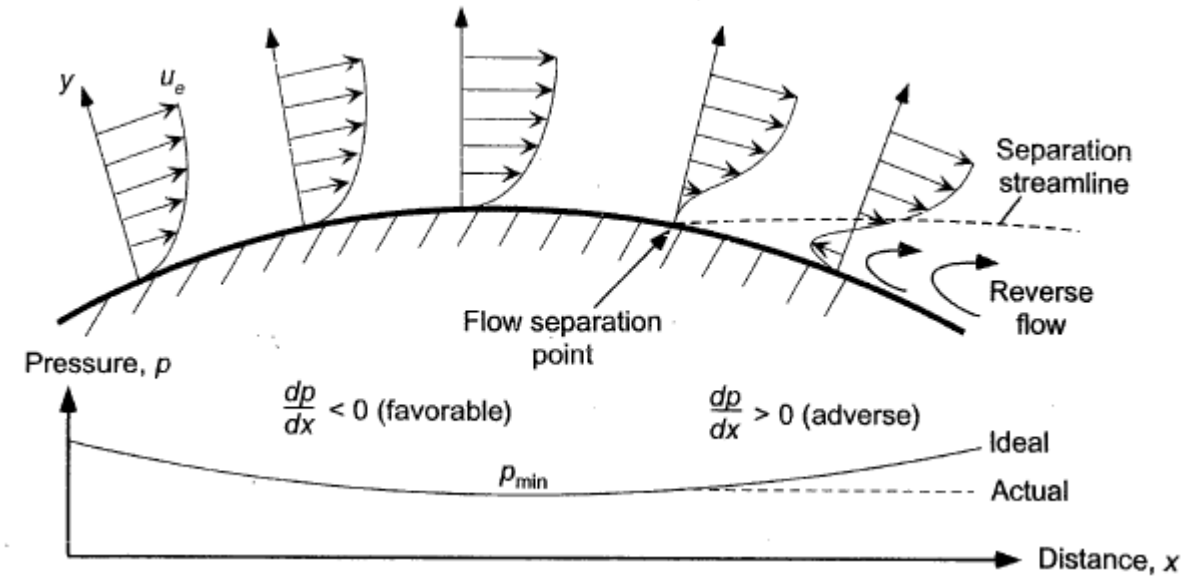

Figure 2.8: Development of boundary layer in an external pressure gradient [110]

The thin-airfoil stall is characterized by the flow separating from the trailing edge and reattaching

downstream at a given x value. As the angle of attack increases, the reattachment point moves to the trailing edge. The leading-edge stall is a massive flow separation at the trailing without reattachment on the chord, which explains the sharp lift loss. The trailing-edge stall starts with a separation point at the trailing edge that gradually moves upstream as the angle of attack increases. Finally, the combined stalls are a combination of these different flow behaviors resulting in different polar properties.

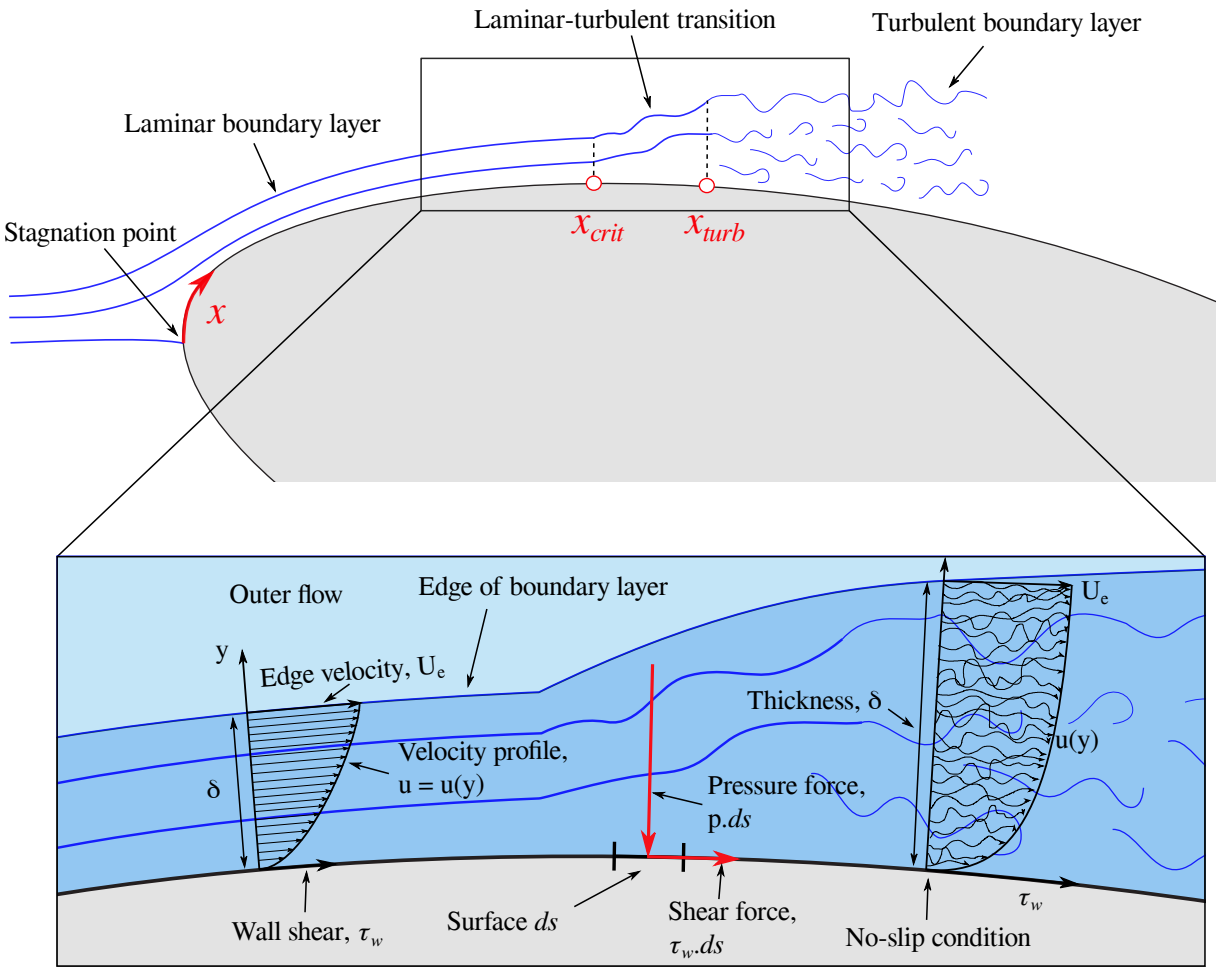

Figure 2.9: Laminar and turbulent boundary layer on a surface - Velocity profiles and forces acting on airfoil surface

Another important aspect is the difference between laminar and turbulent boundary layers as illustrated in Fig. 2.9. For small x values, the boundary layer is laminar : the streamlines are parallel to the surface without any perturbations. The flow then progressively evolves from laminar to turbulent at a critical position x_{crit} called the transition zone. The turbulent boundary layer is characterized by a strong mixing of the different layers that brings energy from outer to inner layers, hence stabilizing the flow and preventing the separation of the boundary layer. The outer velocity U_e is recovered faster with a larger velocity gradient at the wall, which means more friction due to a larger velocity gradient at the wall.
Some airfoils are designed in order to have large laminar zone that decreases the friction drag but suffer from massive separation with low stall angles. On the opposite, some devices such as vortex generators are installed on airfoils surface and force the transition to appear earlier in order to have a larger turbulent

boundary layer with delayed stalled.

The integration of the pressure forces projected on the flow direction is called *pressure drag*, while the integration of friction force is called *friction drag*. As the flow remains attached, the pressure drag is almost zero and the only drag is the friction drag. After stall angle, the flow around the airfoil is massively changed resulting in an increased pressure drag responsible for the high drag values observed in stalled conditions.

When increasing the angle of attack beyond stall, the *deep stall* regime is reached. For thick airfoils with trailing-edge stall, the separation point moves from trailing edge to leading edge. At a specific angle, the pressure gradient at the leading edge is strong enough to create a massive separation from the leading edge. The airfoil can then be considered as a bluff body, the flow becomes highly unsteady with a fully detached boundary layer on the suction side, generating shedding vortices at a given frequency (see Fig. 2.13). Timmer [195] proposes a linear correlation between the leading edge radius and the deep stall angle: a smoother leading edge with a higher curvature radius delays the apparition of deep stall. It is remarkable that no clear distinction is made between deep stall on thick airfoils and classic leading edge separation that appears on thin profiles. A distinction can however be made by considering in which order the events take place. This reveals the importance to consider that for most airfoils a combination of leading edge stall and trailing edge stall occurs in reality, at different angle of attacks depending on the previously mentioned parameters.

Both predictions of transition and separation are intensive fields of research responsible for many numerical models that will be overviewed in Chapter 3.

Lastly, one must keep in mind that in this section the flow has been considered as a 2-D flow. In reality, the flow over an airfoil is a 3-D flow with some impact on the polar data that is presented in section 2.2.

2.1.4 Unsteady flow

2.1.4.1 Phenomenology of dynamic stall

The previously defined polar curves are obtained in steady conditions: for each given steady flow conditions, a unique set of force coefficients are obtained. Forces on airfoils in unsteady flows with a time-varying angle of attack $\alpha(t)$ are not predicted by these static polar data and the history of the conditions applied on the airfoil are needed to determine the forces. The dynamic force coefficients are most of the time given for oscillating airfoils, showing hysteresis loops as can be seen in Fig. 2.10. Around the linear zone of the static curve corresponding to attached flows, thin loops appear, while for $\alpha(t)$ above the static stall angle, larger hysteresis loops are observed.

Theodorsen theory [192] is a reference in that matter and was the first to propose a solution for solving the loads on an oscillating airfoil in attached flow, studying the delay observed on dynamic forces in comparison to static ones. These cases are named *attached unsteady flows* in literature. The dynamic contribution to the aerodynamic forces are divided in a *circulatory* and a *non-circulatory* component. The first one is assimilated to a lag in the establishment of the steady circulation: when moving from an angle α_i to an angle α_{i+1}, the circulation around the profile changes from Γ_i to Γ_{i+1}. A vortex is created and emitted from the trailing edge to compensate for this change in circulation. Once emitted and far from the airfoil, new steady conditions are then reached at α_{i+1}. The creation and dynamics of the vortex are responsible for a delay before reaching these new steady conditions. The second *non-*

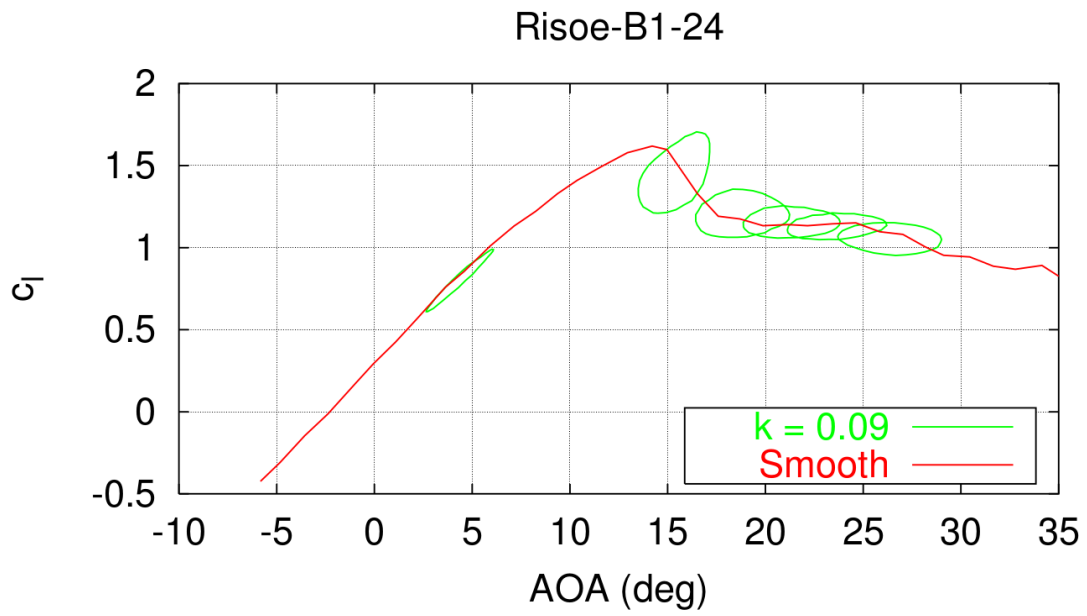

Figure 2.10: Risø-B1-24 static (red) and dynamic (green) lift coefficients [59]

circulatory component results from the acceleration of the flow mass around the airfoil and is also called *apparent mass* effect. Theodorsen proposes a set of hypothesis to represent these effects as detailed in Appendix B. The resulting hysteresis loop caused by the delay is represented by the loop around $5°$ in Fig. 2.10. It is rotating counter-clockwise, which means that when $\alpha(t)$ increases, the lift value is lower than the static value. The other loops for values of $\alpha(t)$ beyond the static stall angle α_s are rotating clockwise, and show maximum lift values above the maximum static lift $C_{l,max}$.
These loops are representative of a series of phenomena called *dynamic stall*. Carr [33] gives a detailed analysis of theses processes for three types of airfoil: a classical NACA0012, a cambered airfoil and a sharp leading-edge airfoil. These three airfoils are relatively thin compared to wind turbine airfoils, as in most of the experimental studies from the 70s and 80s that tackle helicopter issues. For these three airfoils oscillating around the static stall angle, the same phenomena can be observed with more or less intensity (see Fig. 2.11 for the equivalent flow visualization):

1. Before the static stall angle α_s, the main features of the flow remain the same as for steady conditions. The delay mentioned earlier is visible on force coefficients.

2. As the angle of attack exceed α_s, no modification of the flow appears: the flow remains attached, no flow reversal can be observed. The maximum static lift is exceeded, varying linearly.

3. Flow reversal spreads from trailing edge, boundary layer is thickened at the trailing edge and flow starts separating from trailing edge depending on the airfoil shape. For the sharp-leading edge airfoil, no separation appears nor flow reversal appears at the trailing edge, while it is quite important for the cambered airfoil and NACA 0012. The force coefficient still has a linear behaviour.

4. As α increases, flow reversal appears at the leading edge, creating a large leading edge vortex. For the NACA0012 the flow reversal at leading edge comes from the upwelling of the flow reversal from trailing edge, while it is not the case for the sharp leading-edge airfoil. The vortex grows and

then detaches from the leading edge, convected downstream. The vortex is diffuse and slower for the cambered airfoil, triggering a smoother separation. As it grows, it creates more suction and C_l slope increases. At the same time, the moment coefficient drops abruptly. When the vortex reaches a given point on the chord, maximum lift is reached ($4a$) followed by maximum negative moment($4b$) and maximum drag ($4c$). Lift and moment drop quickly afterwards. Full stall regime is reached.

5. Several other vortices with much lower intensity can be emitted from leading edge if α keeps increasing.

6. Flow reattaches slowly as α decreases, coming back to the initial state. Forces and moment are back on the linear curve.

An interesting observation that could explain the stall delay is the fact that separation point and flow reversal point are differentiated in unsteady flows while they are the same in steady conditions. This was first observed by Sears and Telonis [173] noticing that boundary layer equations (see Eq. 3.64) were still valid at the vanishing wall-shear point with $\tau_w = 0$, which is not the case when the boundary layer thickens and detaches from the wall. In a more generic approach, Schlichting [172] observes that the separation point for unsteady boundary layers is then defined as the point were a singularity occurs in the boundary layer solutions.

Aside the abrupt behavior of lift force, the pitching moment is also an important dynamic stall concern. During the convection of the leading edge vortex, the moment coefficient suffers strong variations, which can in some cases create instabilities depending on the shape of the hysteresis loops and its associated torsional aerodynamic damping [126]. Aerodynamic damping quantifies the capacity of the flow to absorb(positive damping) or give (negative damping) energy to an airfoil with a given motion. This notion is important in aeroelasticity, as negative damping can result in *stall flutter* which is an amplification of the initial motion caused by the aerodynamic forces with possible severe damages to the structure.

2.1.4.2 Influencing parameters

The succession of events defining dynamic stall is strongly affected by several parameters and it is not yet perfectly understood how they appear, which means that for a random set of parameters it is still difficult today to predict how a given shape will react to unsteady flows. From Carr [33] presented earlier but also McCroskey [128], it appears clearly that changing the shape of the airfoil modifies the separation process during dynamic stall events. Both of them list the different parameters that might impact the shape of dynamic stall in several publications [32] [126] [129]:

- Airfoil shape
- Mach number for $M > 0.2$
- Reynolds number
- Reduced frequency
- Mean angle and amplitude
- Type of motion

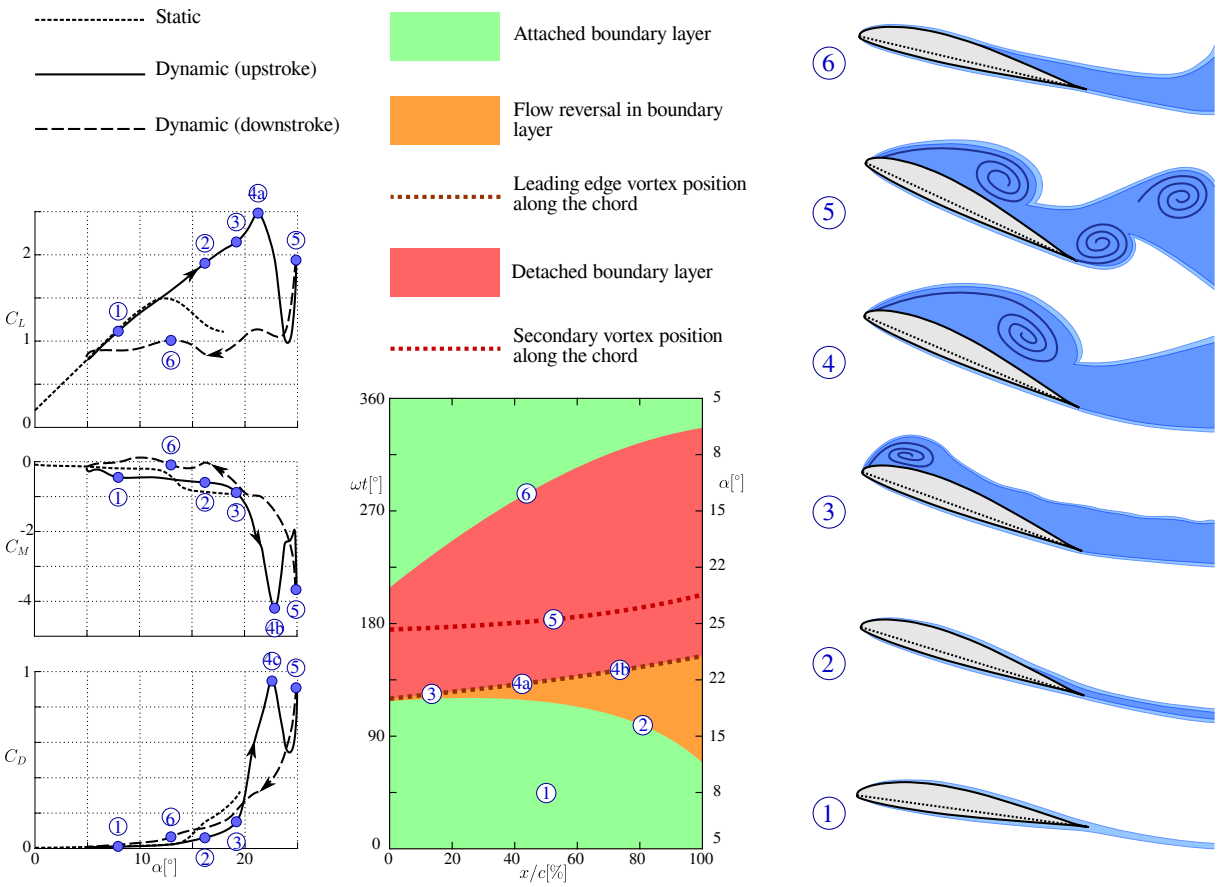

Figure 2.11: Dynamic stall, adapted from [15]

- 3-D effects

Dynamic stall of thin airfoils such as NACA0012 has been extensively investigated experimentally, but the behavior of other shapes of airfoils does not seem that obvious. Unfortunately, public experimental dynamic stall data for thick wind turbine airfoils are few and the phenomenology is not really investigated, focusing more and the values of force coefficients and the presence of devices on airfoils to improve their performances. It is however a common hypothesis to consider the absence of leading edge vortex for such thick airfoils with trailing edge separation. The measurements performed on s809 airfoil from [157] or [177] seems to reveal the presence of a small leading vortex on lift and moment coefficients hysteresis loops while Amandolese [6] does not notice such behavior on a NACA 63_4-421. The leading edge radius of the s809 airfoil is relatively small compared to the one from the FFA-W3 airfoil series or NACA 63_4-421, and it is difficult to conclude regarding the possible presence of leading edge vortex in some operating conditions. Regarding the measurements performed at Risø Velux wind tunnel [58] [60][59] [11] on several wind turbine dedicated airfoils, no specific peak characteristic of leading edge vortex can be observed on force coefficients. This could be caused either by the very round leading edge of the airfoils, the very small amplitude of the oscillations or the values of the mean angle of attack. Aside the absence of leading edge vortex for round and thick profiles, Müller-Vahl [141] observed on a relatively thick NACA0018 the formation of a vortex on the rear half of the airfoil prior to the creation of the leading edge vortex. This demonstrates the possible variations around the well-know dynamic stall

process described above.

Most studies are performed on pitching airfoil with sinusoidal variation of the angle of attack, with:

$$\alpha(t) = \alpha_0 + \alpha_1 * sin(\omega t) \tag{2.7}$$

In such case, the mean angle α_0, the amplitude α_1 and the angular velocity ω are the parameters of the motion. Angular velocity is mostly analyzed through the *reduced frequency* k definition:

$$k = \frac{\omega c}{2U_0} \tag{2.8}$$

The reduced frequency is used to characterize the level of unsteadiness of the flow for a given flow velocity and chord length. The physical scale $\frac{c}{2U_0}$ is the time needed for the flow to cover half the chord of the airfoil. Usual reduced frequency values experimentally investigated are in the order of magnitude of 0.1. For values lower than 0.01 the flow can be considered as quasi-steady [109]. In most previously mentioned studies on wind turbine dedicated airfoils, hysteresis loops are wider and maximum lift is higher when the reduced frequency increases. It appears clearly on s809 experiments from Ramsay [157] represented in Fig. 2.12. This is due to the increased delay in the flow reversal and trailing edge separation. For airfoils with leading edge vortex, Carr [33] shows that for low frequencies the vortex is convected downstream while $\alpha(t)$ is still increasing, while higher frequencies are characterized by a still increasing lift and forming vortex while $\alpha(t)$ is decreasing. However, McCroskey [126] notes that the reduced frequency dependency is affected by the type of separation: increasing k can change the stall regime from light to deep stall and inversely depending on stall type. Hence, on some profiles increasing k will increase the stall hysteresis loops while on others they will be decreased.

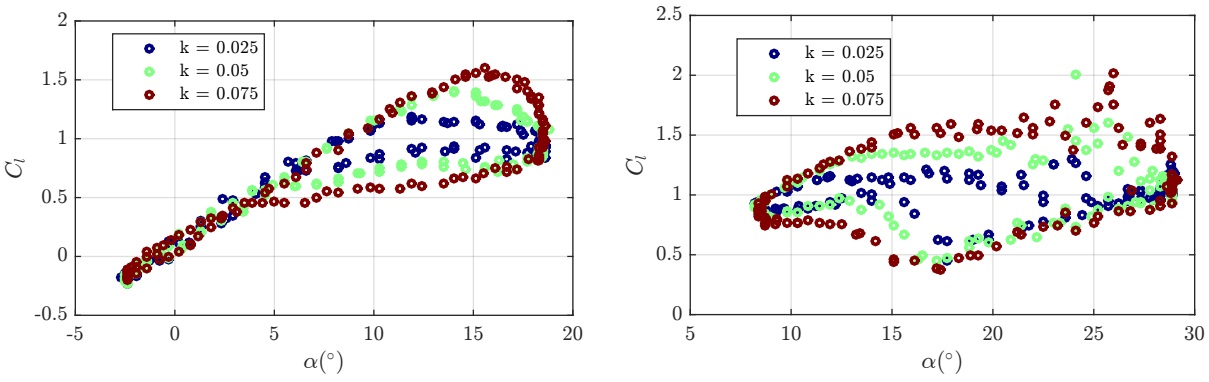

(a) Mean angle 8° (b) Mean angle 20°

Figure 2.12: Influence of reduced frequency k on dynamic stall - s809 profile - $Re = 1.0 \times 10^6$ - Data from [157]

The mean value α_0 strongly affects the hysteresis loops on force coefficients. McCroskey [127] makes a clear distinction between light dynamic stall and deep dynamic stall (see Fig. 2.13) following the same definition than the static light and deep stall, depending mainly on the values of the angle of attack. For the impact of amplitude α_1, Amandolese [6] shows that the flow regime changes from deep stalled to attached flow depending on the amplitude of the motion for a mean angle beyond α_s, resulting in very different force coefficients for the same angle of attack. McCroskey [126] and later Müller-Vahl

[142] develop the matched pitched rated concept. If $\alpha(t)$ matches for values above α_s (which means that the pitching rate is the same) for specific combinations of α_1,α_2 and k, then the force coefficient matches too.

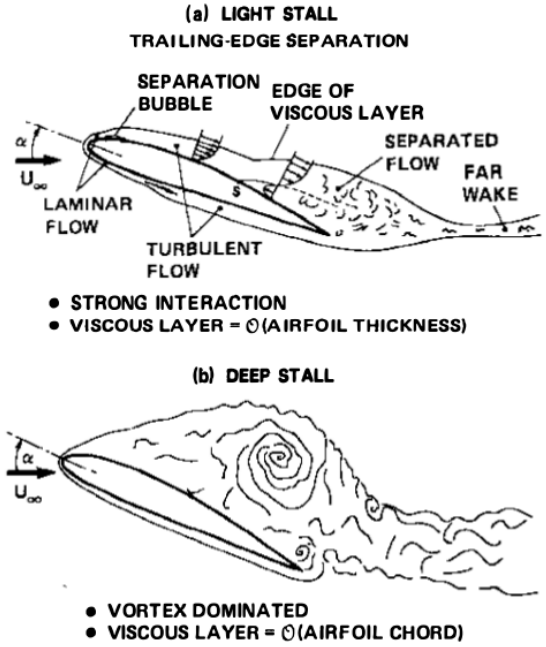

Figure 10 Sketches of flow fields during dynamic stall.

Figure 2.13: Light and deep stall - Flow fields during dynamic stall - [127]

Some other type of motion have also been investigated, as airfoils in real conditions does not necessarly oscillate in a perfectly sinusoidal motion. Most studies investigated plunging motions, oscillating freestream velocities, displacement of the rotation center which is usually at the quarter chord point or combinations of these motions. The main characteristics of dynamic stall are maintained in such cases, with variations regarding delay and separation type. Plunging airfoils have been compared to pitching airfoils by Carta [34] showing that the development of leading edge vortex could differ. The resulting torsional aerodynamic damping can then be positive or negative for the same angle of attack history, leading to stable or unstable aeroelastic conditions. Strangfeld [188] combines surge (freestream oscillations) and pitch motions on the relatively thick NACA0018. However, such studies have not been conducted experimentally yet on wind turbine profiles without leading edge vortex.
The Reynolds number is also considered as impacting dynamic stall despite few studies on the subject. It is mostly considered that for large Reynolds number the impact is not significant. However, Carr [33] noticed that for Reynolds number from 1.0×10^6 to 3.5×10^6, the flow reversal appears at higher angles of attack when Re increases. Gupta [77] also investigated two different Reynolds numbers of 0.5×10^6 and 1.0×10^6 on a NACA0012 airfoil and Ramsay [157] conducted experiments on s809 airfoils with Re from 0.75×10^6 to 1.4×10^6. Data from the latest are presented in Fig. 2.14 and show that increasing the Reynolds number decreases the unsteady behavior. However, the Reynolds numbers investigated are much lower than the ones typically encountered on large wind turbines which could impact such conclusions. Mach number can also have an impact on dynamic stall even for $M < 0.3$ because locally

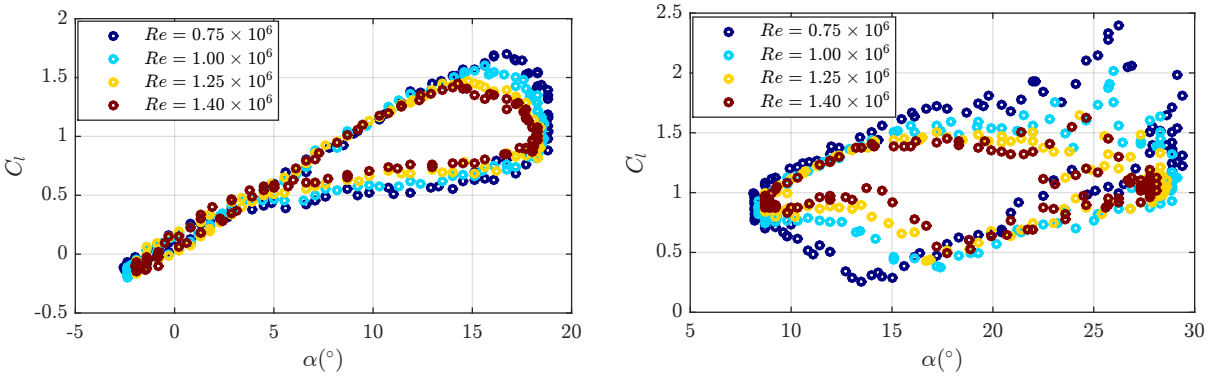

(a) Mean angle 8°

(b) Mean angle 20°

Figure 2.14: Influence of Reynolds number Re on dynamic stall - s809 profile - $k = 0.075$ - Data from [157]

the flow can reach higher velocities with compressible effects. Carr [32] shows that in some cases the separation type can be changed from trailing edge separation to combined separation when increasing M.It is relevant to notice that for wind tunnel experiment the effects of Mach number and Reynolds number are difficult to dissociate has there are both mainly obtained by increasing the flow velocity. This leads to some doubts about the first conclusions from Carr in 1977 [33] regarding the Reynolds number sensitivity study, as they seem to be the same than the ones he gives for Mach number in 1988 [32]. Furthermore, this sensitivity is not a major field of research for wind turbine airfoils, probably because the maximum flow velocity is reached at the blade tip where dynamic stall has the less probability to occur (see section 2.3).

At last, the 3-D effects are also a major problematic of dynamic stall. As said earlier, real flows always have a span-wise component that must be considered when analyzing wind turbine aerodynamics and the flow must then be considered as a 3-D flow. This will be considered in next section. For more information about unsteady 2-D flows around airfoil, the chapter 8 from Leishman's book "Principles of helicopter aerodynamics" [110] offers much insight into the subject. Research on Vertical Axis Wind Turbines (VAWTs) also produced a large number of publications around dynamic stall as it is a major concern for such turbines. However, VAWTs are mostly designed with thinner and more symmetric profiles than HAWTs and the leading edge vortex impact is the most tackled issue, which does not seem to be relevant for HAWTs.

2.2 3-D Aerodynamics

If 2-D aerodynamics are sufficient for understanding the basic forces acting on a wind turbine blade, the inclusion of 3-D effects are necessary to have a more realistic approach. The 3-D nature of the blade is responsible for the 3-D nature of the flow around it, implying that the angle of attack and thus the forces seen by a section are different than when considering that the flow is only 2-D even with the same inflow conditions.

2.2.1 3-D Wing

For a 2-D approach, a blade is considered of infinite span with a constant chord and airfoil shape, generating a constant lift distribution in the spanwise direction. A 3-D wind turbine blade consists of several airfoil shapes with different chord length, a twist angle that gives the relative position from one section to another, and most importantly a root and a tip end. The lift distribution is not uniform along the blade, and the flow suffers from discontinuities at the extremities. At the tip, a strong vortex is observed as the flow from the pressure side is accelerated around the tip toward the suction side. Spanwise velocities must thus be considered as well as the velocities generated by the tip vortex. The approach introduced earlier (see chapter 2.1.1) regarding circulation and lift around an airfoil can be generalized to the flow around a 3-D blade in order to describe this fundamental phenomenon. Branlard [25] and Hansen [82] books introduce the well-known Prandtl theory for the modeling of a blade considered as a succession of profiles. Each profile at a span position r is characterized by its circulation that generates lift, the *bound circulation* $\Gamma_b(r)$. As mentioned for 2-D unsteady attached flows, a change in the circulation generates a vortex at the trailing edge, whose strength is defined by the circulation along a contour surrounding it and equal to the difference of circulation around the profile. To simplify, the vortex strength is assumed to be contained in a *vortex line* emitted at the trailing edge and called the *shed vorticity* Γ_s:

$$\Gamma_s(r) = \frac{\partial \Gamma_b(r)}{\partial t} dt \tag{2.9}$$

The difference of circulation in the spanwise direction is called the *trailed vorticity* Γ_t:

$$\Gamma_t(r) = \frac{\partial \Gamma_b(r)}{\partial r} dr \tag{2.10}$$

Fig. 2.15 shows the continuous vortex sheets created by the discrete trail and shed vortex lines. The trail vorticity usually increases at the tip, creating the *tip vortex* and its characteristic roll-up of the flow. At the blade root, another vortex is created of lower magnitude.

Both trail and edge vorticities generate flow velocities called *induced velocities*, responsible for a change in the local flow perceived by a section. The local angle of attack is thus reduced (see Fig. 2.16) at the tips because of the tip vortex induced velocity, causing the so-called *tip losses* on lift coefficient and stall delay. The geometric angle of attack α_{geo} is defined as the angle between the unperturbed flow and the profile and corresponds to the angle of attack for a 2-D analysis. The induced and effective angles α_{ind} and α_{eff} are then defined to take into account the induced velocity V_{ind}. The force R generated by the effective flow velocity V_{eff} has a component parallel to the unperturbed flow velocity V_0 called *induced drag*, while the perpendicular component is the 3-D lift L, lower than a 2-D analysis lift. The definition of the angle of attack for 3-D flow is thus complex as it questions the necessity to consider either the local flow or the far upstream flow.

The tip vortex is responsible for a stall delay because of the downwash it induces. Fig. 2.17 and 2.18 are based on the work of Piziali [153] and Coton [39] on oscillating finite wings with NACA0015 profile. At the tips (high span in Fig. 2.17), the leading edge vortex creation is delayed and the static lift is lower than close to mid-span. The dynamic loops reveal that for the same angle of attack, a deep stall behavior appears at mid span while only light stall is observed at the tip because of the weaker dynamic stall vortex.

Aside the tip vortex impact on stall, three other aspects affecting static and dynamic stall seem important: stall cells, sweep angle effect and the stall delay for rotating blade. These three aspects have mostly been investigated independently but with the common observation that they have negligible impact on

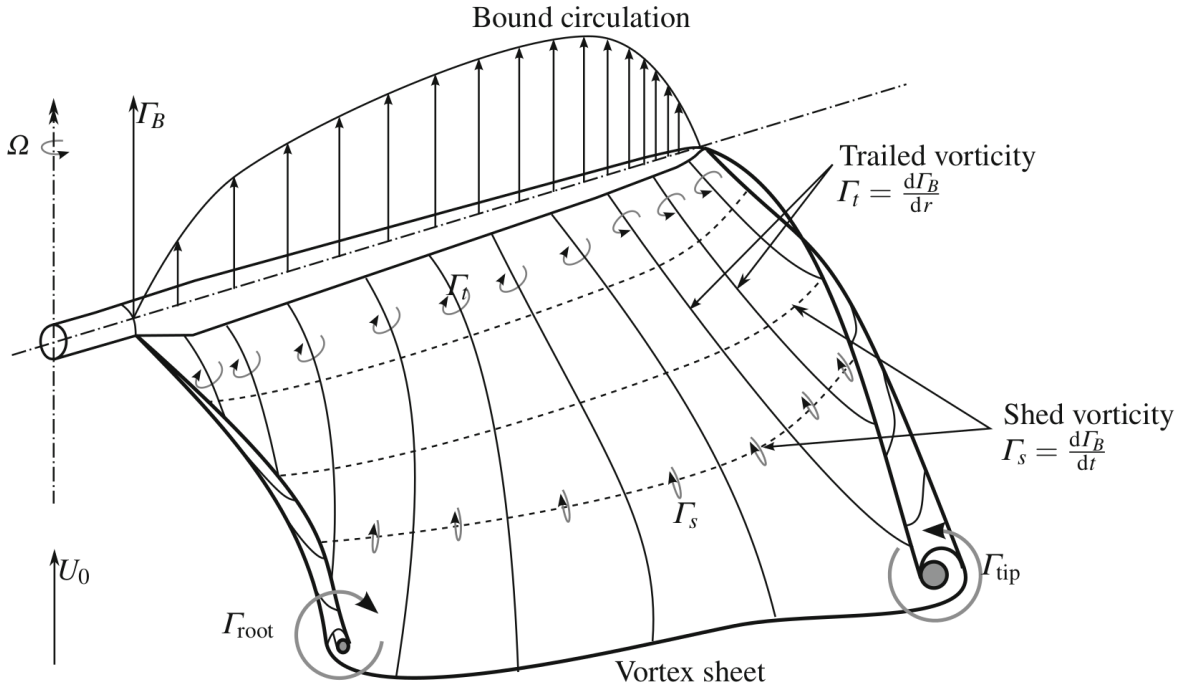

Figure 2.15: Circulation distribution on a wind turbine blade - [25]

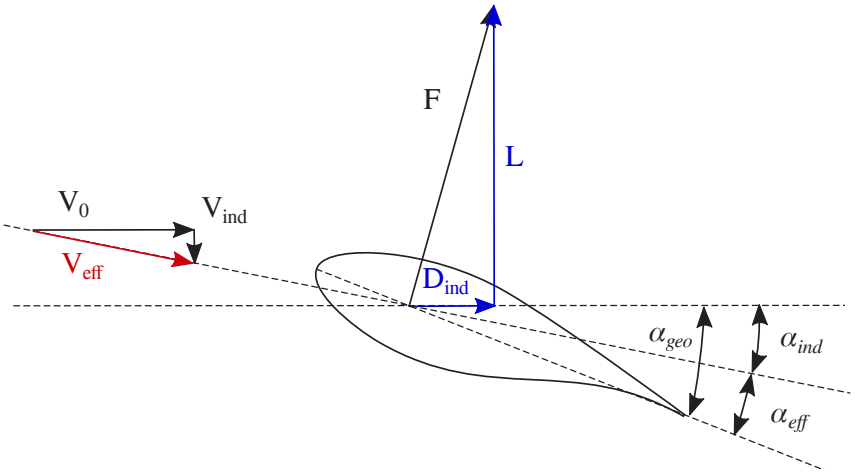

Figure 2.16: Induced velocity and drag - Adapted from [82]

attached flows, in contrast to tip losses and trail vorticity effects that affect both attached and separated flows.

2.2.2 Stall cells

For experiments, 2-D results are obtained on wings of a given spanwise length with specific treatments to remove either tip effects, wall effects and pressure increase due to the blockage of the flow, as infinite

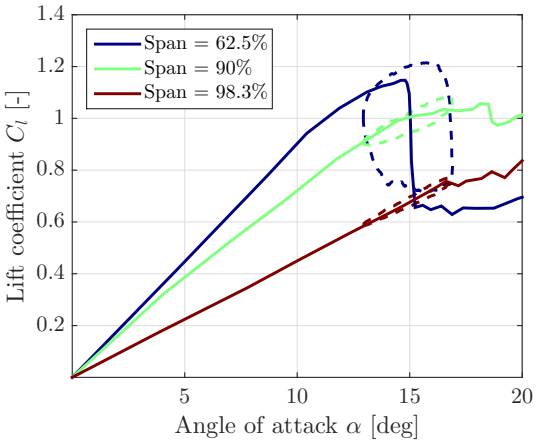

Figure 2.17: Static (solid line) and dynamic (dashed line) lift coefficients at three spanwise locations - Data from [153]

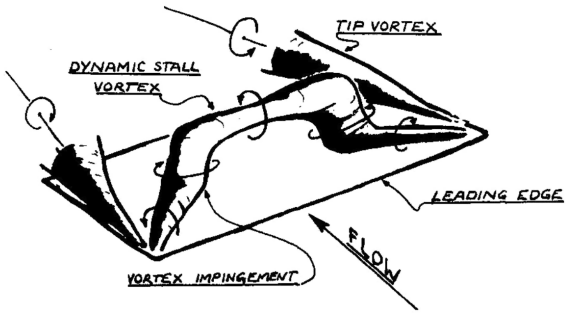

Figure 2.18: Influence of the tips on leading edge vortex - [39]

blades are not a possibility. In CFD, 2-D results can be obtained by removing all spanwise components from the equations governing the flow and studying a 2-D flow domain, or by studying a 3-D domain with a given spanwise length. However, either for experiments and CFD, 3-D flow structures appear on the airfoil in stalled conditions that can not be captured if the spanwise length is not large enough. Winkelmann [205] investigated these flow patterns and identified mushroom shaped *stall cells* in the separated flow, named after the observation of counter rotating vortices on the suction side of the airfoil. More recently, the phenomenon has been investigated with CFD and Manni [123] identifies such structures (see Fig. 2.19) on a NACA0015 airfoil with a large spanwise length.

Such investigations have been performed on thicker airfoils by Manolesos [124] and Ragni [158]. Both

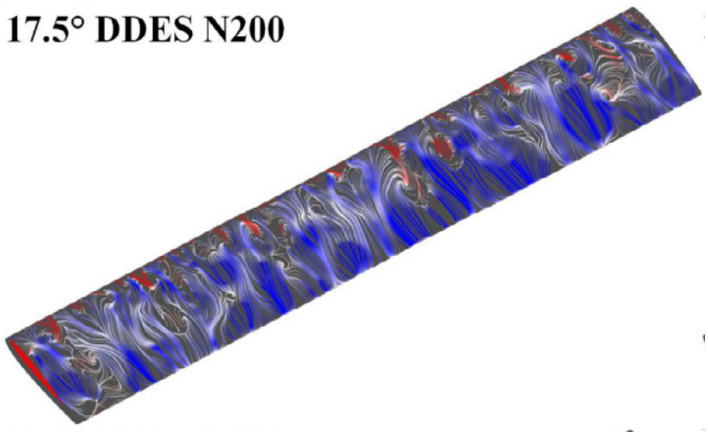

Figure 2.19: Visualization of stall cells on a NACA0012 wing obtained with CFD - [123].

notice that 2-D CFD is not able to capture correctly the force coefficients, overestimating the lift because of the impossibility to capture the 3-D nature of stall. Furthermore, the force coefficients are not the same along the spanwise direction depending on the position of the stall cells, with a time varying distribution depending on the dynamics of the stall cells. It also appears that the shape of the cells is independent

of the wing aspect-ratio, provided that the spanwise length is large enough to capture one cell whose characteristic size is around $0.2c$.

2.2.3 Sweep angle

Blades in real conditions are not perfectly orthogonal to the incoming wind direction, in particular in cases of yaw misalignment or with vertical wind shear. The angle between the spanwise direction and the flow is called the sweep angle Λ as defined in Fig. 2.20.

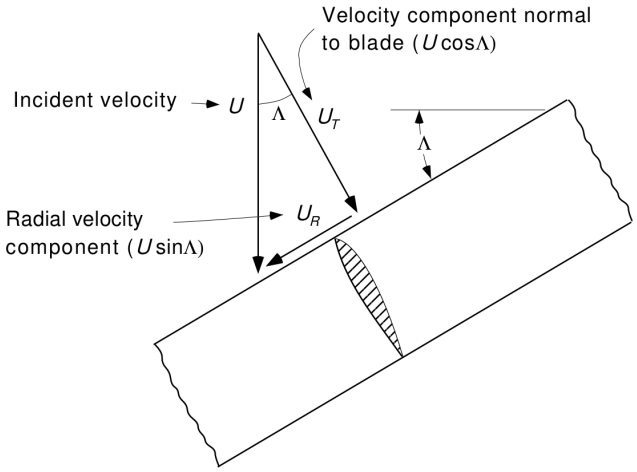

Figure 2.20: Definition of sweep angle for a blade section - [109].

The impact of the sweep angle on the flow over a blade has been investigated in static and dynamic conditions. Leishman [109, 110] proposes an overview of this effect. In static conditions, the force coefficients with and without sweep angles are the same in attached conditions, which is often called the *independence principle*. However, for stall cases, the cases with sweep show much higher maximum lifts with a significative stall delay. In dynamic conditions, the independence principle is still valid for attached flow but is a little bit more complex for dynamic stall. On a NACA0012 profile, it seems that the hysteresis loop is smaller for sweep cases, but still showing a larger stall delay than for cases without sweep. This is strongly dependent on the stall type and the interaction between leading edge vortex dynamics and the radial flow behavior, so such conclusion could be totally different for the thick wind turbine airfoils.

2.2.4 Stall delay for rotating blade

The stall delay effect, also named rotational augmentation or Himmelskamp effect from the name of the first observer of the phenomenon in 1947, appears mostly at the root of rotating blades. It is characterized by an increased lift and delayed stall compared to a non-rotating blade with same angle of attack. The phenomenon has been massively investigated experimentally and numerically ([35],[197],[75], [88]) since its discovery. Despite these insights, it is still an active field of research as the full understanding of the phenomenon that would help the development of the perfect engineering model is not yet reached. For the section close to the blade root where the angles of attack can be very high, stall regularly appear

on pitch regulated wind turbines. The state-of-the-art review from Lanzafame and Mauro [106, 125] estimates that most authors agree on the fact that in these separated flows, the axial velocity is strongly reduced and the rotational acceleration, Coriolis forces and radial pressure gradient create strong radial velocities close to the root, modifying stall behavior. The work of Guntur and Sørensen [75, 73, 76] is particularly interesting as it combines experimental results from the NREL UAE Phase VI and MEXICO measurements to CFD calculations. Static and dynamic stall on a rotating and non-rotating blade are investigated, with some results presented in Fig. 2.21 and 2.22. In Fig. 2.21, the radial velocities clearly appear before and after separation, and for different inflow conditions, with a stall delay observed when comparing 3-D rotational polars to 2-D polars.

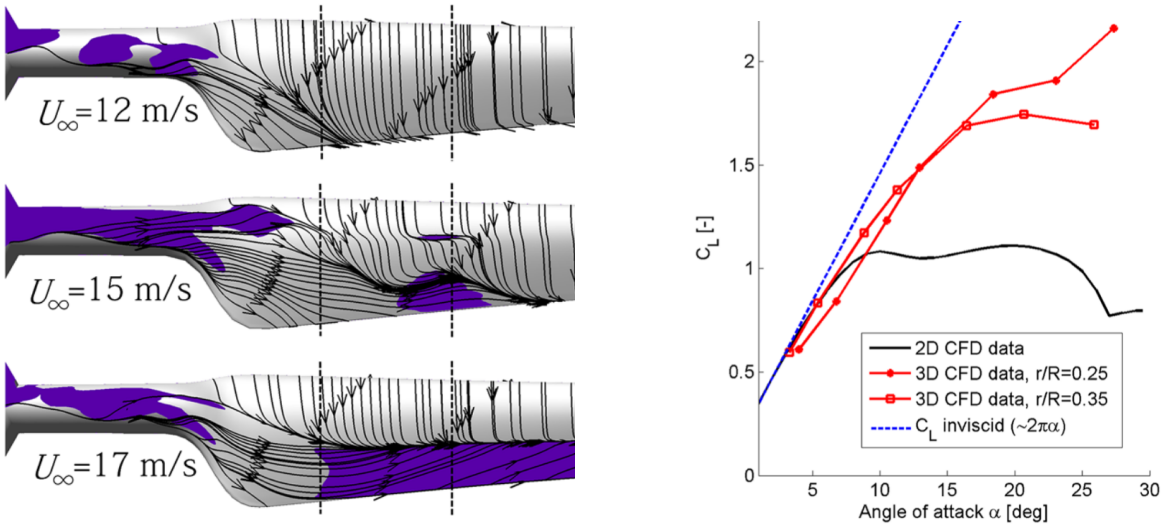

(a) Suction-side streamlines at the blade root for three inflow velocities - Shaded regions are separated flows.

(b) 2-D and rotating 3-D (two radial positions) lift polars for a DU91-W2-250 airfoil.

Figure 2.21: Rotational augmentation CFD study on MEXICO rotor from Guntur [73].

This has been extended to dynamic cases with a pitching wing in order to verify that the same behavior was observed for dynamic stall, as presented in Fig. 2.22. Four cases are compared by combining pitching and non-pitching blades, rotating and non-rotating turbine. It appears that the lift increase observed in non-pitching (static) rotating cases also appears in pitching (dynamic) rotating cases. Both dynamic and rotating effects are combined, but as the stall is delayed because of rotation, it appears that the hysteresis loop is smaller in the rotating case, corresponding to a lighter stall than the non-rotating case. The observation seems to be very close to what has been observed for cases with sweep angle, which could be explained by the presence of strong radial flows.

2.3 Horizontal Axis Wind Turbines

2.3.1 Definitions

The wind turbines investigated in the present work have an horizontal rotation axis and are often called Horizontal Axis Wind Turbines (HAWTs), in opposition to Vertical Axis Wind Turbines (VAWTs). The most common design, often referred as the *Danish design*, consists of three blades assembled on a hub. The blades and the hub form the rotor of the turbine and are connected to the generator through the

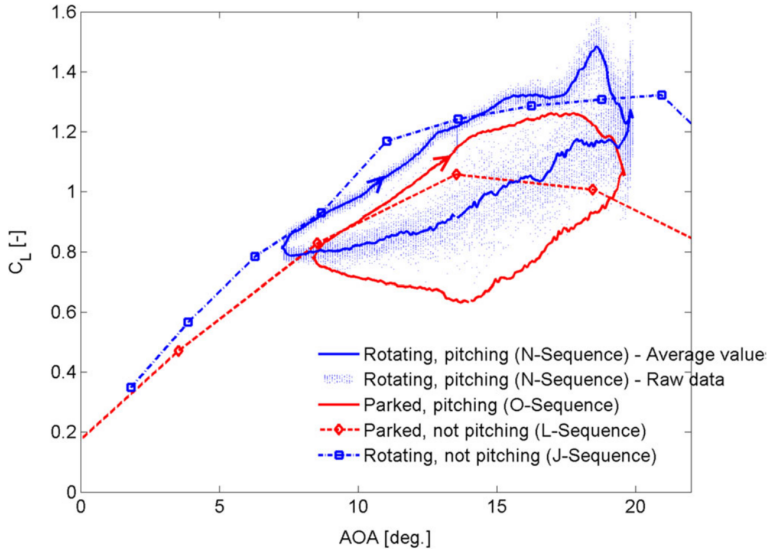

Figure 2.22: Experimental lift polars from UAE Phase VI rotor under several conditions - [76].

main shaft. The nacelle is the structure located at the top of the tower that contains the generator and the gearbox (for turbines with gearboxes) and rotates around the yaw axis in order to align the rotor axis with the wind direction. The blades can rotate around their spanwise direction, defining the pitch angle. The rotor rotation angle is the azimuth angle, and the yaw angle defines the angle between the rotor axis and the wind direction. These definitions are illustrated in Fig. 2.23. This figure is simplified and does not consider the tilt and cone angles. The first one is the angle between the rotor axis and the horizontal plane and the second one is the angle between the pitch axis and the rotor plane. Both of these angles are small (around 5° or less) and intend to keep the blades away from the tower.

Similarly to the 3-D wing, a vortex system is generated behind the blades forming an helicoidal shape called *wake* (see Fig. 2.24). This vortex system is responsible for induced velocities that modifies the angle of attack perceived by the blade. Fig. 2.25 describes the frames and the projected aerodynamic forces acting on a blade section. The axial direction is along the rotor axis, the radial direction is in the rotor plane along the pitch axis and the azimuthal direction is in the rotor plane and perpendicular to the radial direction. For a rotating blade, the incoming *geometric velocity* for a blade section has two components: the incoming wind V_0 and the flow velocity due the rotating blade motion $V_{rot} = \Omega r$ with r the radius at which the considered section is located on the blade. The axial induced velocity is defined by the axial induction factor a such that the total axial flow velocity is then $V_0(1-a)$ as the flow is slowed down by the rotor. The azimuthal (or tangential) induced velocity is on the opposite accelerating the azimuthal velocity and is defined by the tangential induction factor a' such that the total azimuthal velocity is $\Omega r(1+a')$. The sum of these two components that includes both geometric and induced velocities is named *relative velocity* V_{rel}. The angle between V_{rel} and the rotor plane is the angle of inflow φ. In order to have an optimal angle of attack on all blade sections, the blades are designed with a twist angle, which is a rotation of the section around the pitch axis. The total angle θ between the blade chord and the rotor plane is the sum of the pitch and twist angles. The angle of attack on a blade section is then $\alpha = \varphi - \theta$. The total aerodynamic force F is decomposed in the lift L and drag D forces which

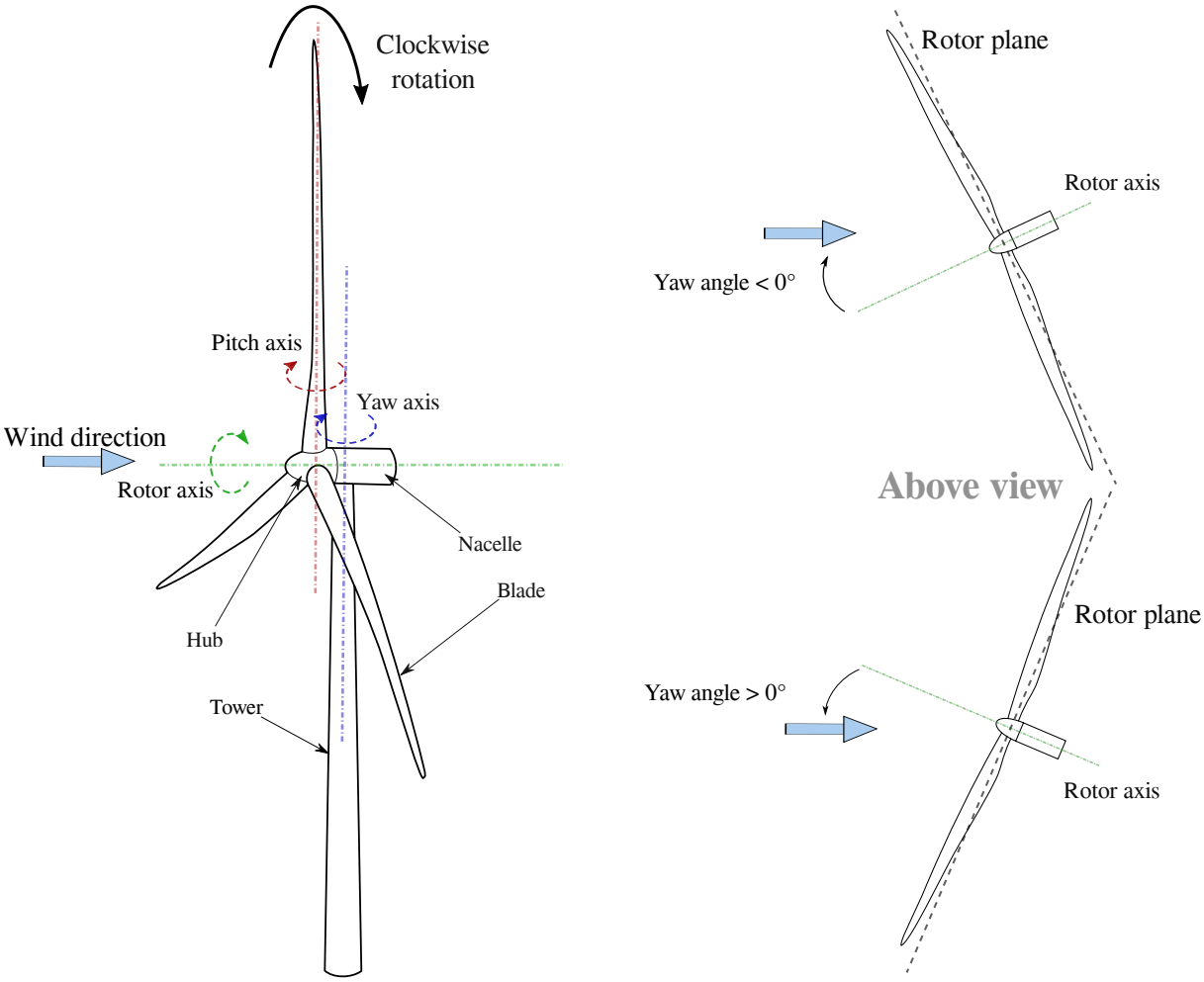

Figure 2.23: Main components and axis definitions for a HAWT

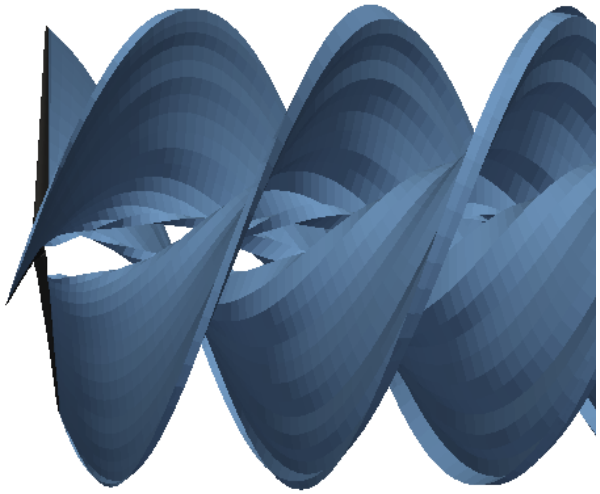

Figure 2.24: Helicoidal wake behind a wind turbine

are defined according to this angle of attack α. It is important to notice that such definition is affected by the estimation of the induced velocities, and the application of the 2-D definitions of lift and drag is not straightforward in such 3-D cases as the difference between the geometric and relative angles of attack is uneasy to determine. The projection of F in the rotor plane is the force F_{torque} generating torque on the rotor axis and is responsible for the rotation of the turbine, while the component along the rotor axis is the thrust force F_{thrust}. The thrust is related to the axial velocity deficit, while F_{torque} forces the wake to rotate in the opposite direction to the rotor rotation.

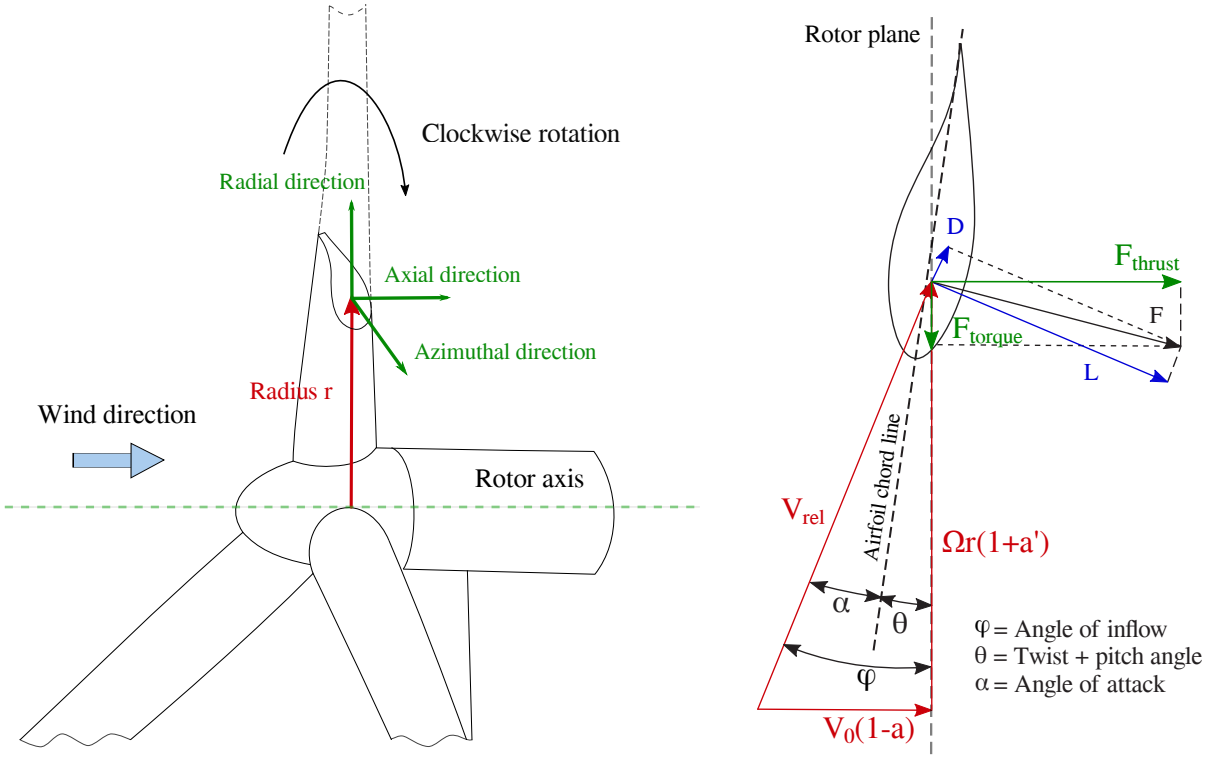

Figure 2.25: Forces, flow velocities and angles definitions for a wind turbine blade - Adapted from [195]

2.3.2 Ideal rotor

The momentum theory is the simplest way to compute the induced velocities for an ideal rotor. It will not be detailed here and more information can be found in reference books from Hansen [82] or Branlard [25], but the main assumptions and results are presented hereinafter. The rotor is then modeled as a disc (infinite number of blades) that applies an uniform pressure drop in the flow over the rotor area, the incoming wind velocity is constant and uniform with only an axial component. In the axial momentum theory, the velocity in the wake is also assumed as purely axial while in the streamtube theory (based on the work of Glauert from 1935 [50], also referred as *simplified momentum theory* by Branlard) the azimuthal component is also considered in order to take into account the wake rotation. In both theories the momentum conservation equation is applied in a domain surrounding the rotor, and by applying Bernoulli equation to the flow upstream, downstream and at the rotor, the power extracted from the flow is related to the axial velocity deficit. The power P extracted by the rotor from the flow is then defined

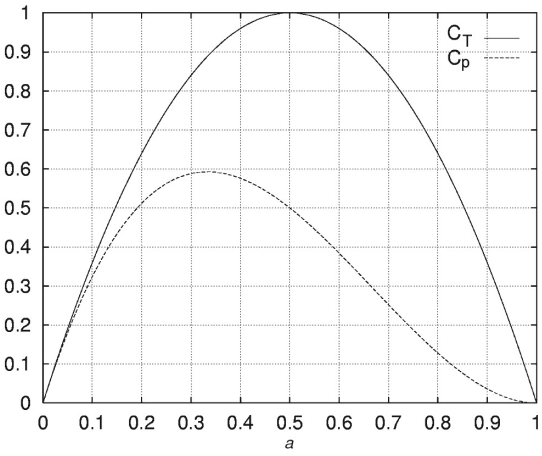

Figure 2.26: C_P and C_T curves for an ideal rotor - [82]

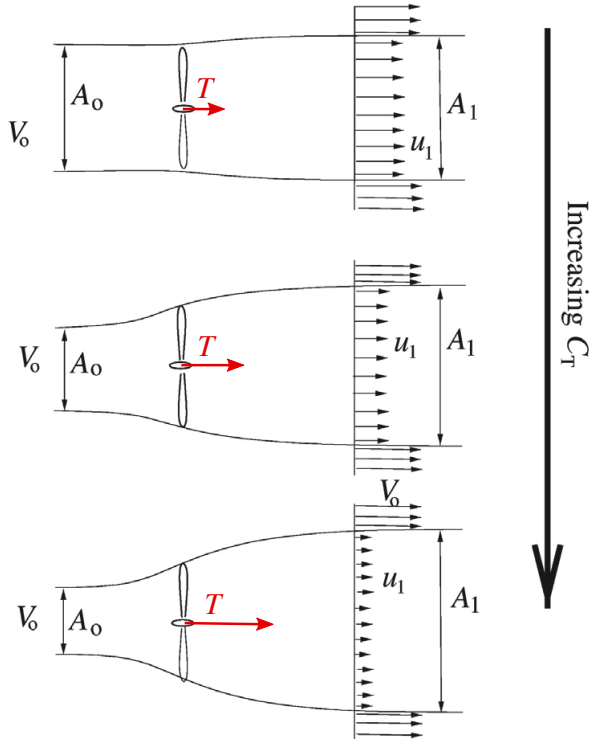

Figure 2.27: Downstream velocity and C_T - [82]

by:

$$P = \frac{1}{2}\rho A V_0^3 \left(4a(1-a)^2\right) \tag{2.11}$$

Knowing that the available power from the flow over the rotor area is $\frac{1}{2}\rho A V_0^3$, the non-dimensionalized power coefficient C_p is then related to a with the following relation:

$$C_P = \frac{P}{\frac{1}{2}\rho V_0^3 A} = 4a(1-a)^2 \tag{2.12}$$

The same process is conducted with the thrust force T which correspond to the axial pressures forces applied on the rotor disc:

$$T = \frac{1}{2}\rho A V_0^2 \left(4a(1-a)\right) \tag{2.13}$$

and:

$$C_T = \frac{T}{\frac{1}{2}\rho V_0^2 A} = 4a(1-a) \tag{2.14}$$

This formulation gives the C_P and C_T curves as a function of a, plotted in Fig. 2.26. The maximum theoretical C_P value that can be reached in the case of an ideal rotor is called the Betz limit with $C_{P,Betz} = 16/27$ and is reached for $a = 1/3$. It is shown that the ideal rotor concept is only valid for maximum values of a around $0.3 - 0.4$. In this range, Fig. 2.27 illustrates the action of the rotor on the flow: the more thrust is applied to the rotor, the more the flow is decreased and the induced velocities large. The rotor is then considered has heavily loaded or lightly loaded. For a given incident wind speed and turbine, the pitch angle and the rotation speed are the two parameters that will affect the geometric angle of attack seen by a blade section. By changing those two parameters, for the same wind conditions,

the rotor can be heavily loaded or lightly loaded. The parameter mostly used to define the load regime in which the turbine is running is the *Tip Speed Ratio* or TSR λ defined by:

$$TSR = \lambda = \frac{V_{rot}}{V_0} = \frac{\Omega R}{V_0} \tag{2.15}$$

R is the rotor radius, but the local radius r is used to define the local speed ratio λ_r based on the same definition than above but replacing R with r. The TSR can be interpreted as the angle between the rotor disc at the blade tip and the flow velocity without considering induced velocities. The speed ratio λ_r defines the same angle but at a radial position r. For low TSR, the angle is small and the rotor is lightly loaded while for high TSR the rotor is heavily loaded. Fig. 2.28 shows the optimal values of power ad thrust coefficients, axial and tangential inductions to optimize power obtained thanks to the streamtube theory (see 3.1.1). The usual TSR ranges are between 0 and 10.

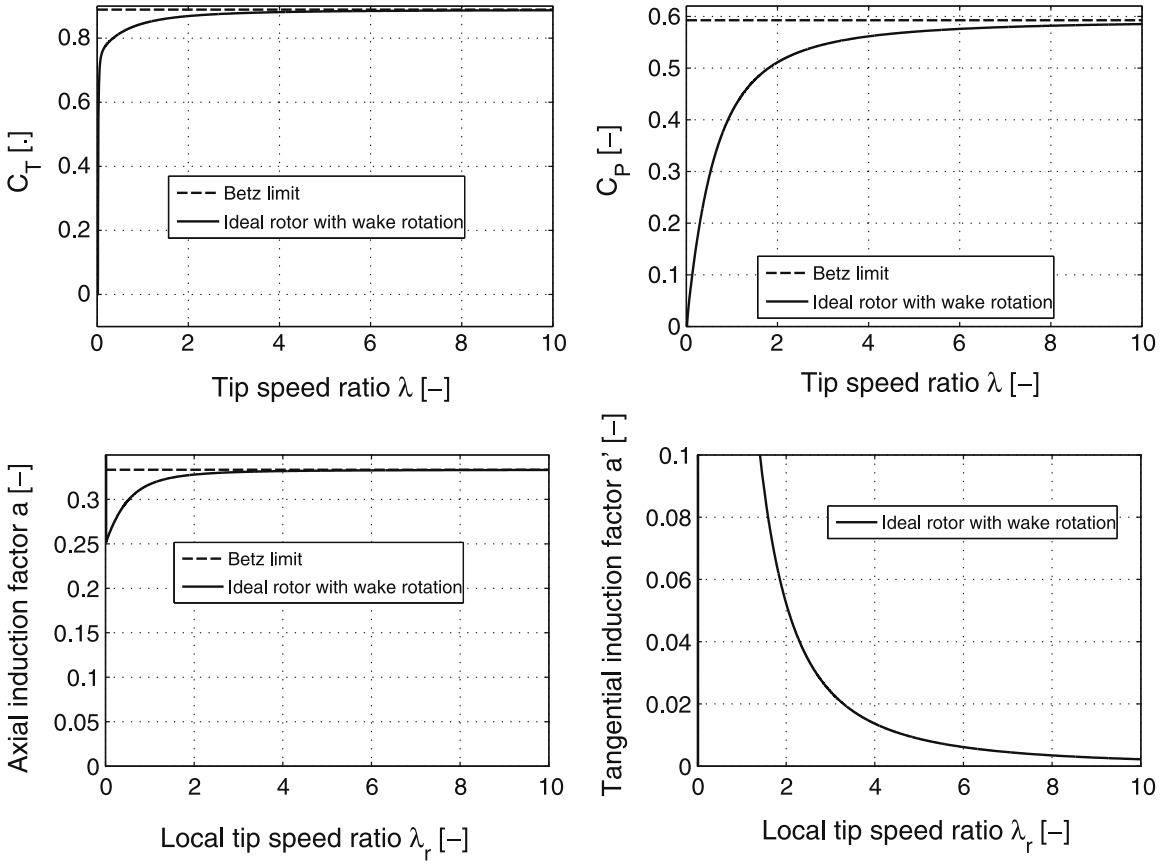

Figure 2.28: Optimal C_P, C_T, a and a' as function of the TSR based on the streamtube theory - [25]

The momentum theory is the basis to the Blade Element Momentum theory that will be introduced in Chapter 3.1, with many corrections and models needed to adapt the ideal rotor to a real rotor.

2.3.3 Sources of unsteadiness

For a rotor operating in a uniform and constant wind, without cone and tilt angle, the angle of attack on a blade section is constant and independent of the azimuthal position. However, real operating conditions

reveal strong variations of the angle of attack. The unsteady behavior modifies the extreme and fatigue loads (see Chapter 4.2.1) on the turbine and must be predicted correctly. Rezaeiha [165] investigates the impact of such variations on the fatigue loads of the DTU10MW. It appears clearly that the turbulence of the wind, the imbalance of blades, wind shear, tower impact or yaw misalignment are the main contributors to fatigue loading. Leishman [109] suggests to classify the unsteadiness in periodic and aperiodic phenomena as illustrated in Fig. 2.29. The periodic phenomena are dependent on the azimuthal position

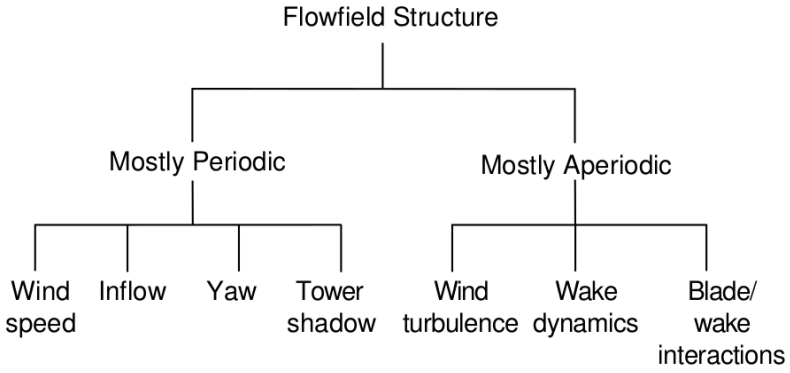

Figure 2.29: Sources of unsteadiness for a wind turbine - [110]

and their frequency is thus related to the rotation speed:

- The mean wind speed changes in time, causing fluctuations of the angle of attack.
- Yaw misalignment occurs when yaw angle is different from zero. The tracking of the wind direction is not perfect, and in real conditions is often not aligned with the rotor axis. This is responsible for angle of attack fluctuations that are investigated in the next section. In the same way, the presence of design tilt angle also modifies the inflow angle.
- The wind shear phenomenon correspond to a non-uniform wind speed distribution over the rotor area. A boundary layer effect must be considered when considering atmospheric flow that causes the flow to be slower at the ground level that at hub height level. The resultant velocity gradient referred as *vertical wind shear* is responsible for lower loads when the blade is closer to the ground, resulting in a periodic loading. The impact of wind shear on the angle of attack is investigated in the next section.
- The *veer* phenomenon correspond to a non-uniform wind direction distribution over the rotor area resulting in variation of the inflow angle.
- The presence of the tower modifies the flow around it, upstream and downstream. When the blade passes upstream the tower, the angle of attack is thus modified.

Except for the mean wind speed variations, the other fluctuations are dependent of the azimuthal position of the blade. For a three blades wind turbine, the phenomena occurs 3 times for each rotation, at a frequency referred as *3P* considering that the *1P* frequency is the rotation frequency. When designing a wind turbine, the 1P and 3P frequencies must be different from the natural frequencies of the structure in order to avoid resonance.
The aperiodic phenomena have a broad range of frequency:

- Turbulent wind represents a chaotic non-uniform flow that varies in time and will be characterized in section 2.3.3.2.
- The wind turbine wake is responsible for induced velocities. It responds dynamically to any change in the flow, and its strength depends on the emitted vorticity at the blades. In real conditions, the unsteady conditions are thus responsible for an unsteady wake with varying induced velocities.
- Neighbouring wind turbine wakes can cross the rotor swept area and modify the inflow conditions. In particular, half-wake situations correspond to a neighboring turbine wake crossing only a portion of the rotor and generating significant load imbalance.

In the following sections, the influence of yaw misalignment, wind shear and turbulent wind on the angle of attack is presented.

2.3.3.1 Periodic: inflow unsteadiness

This section aims at understanding the inflow angle variations without considering induced velocities, so a purely geometrical analysis of the flow velocity and blade motion vectors. The purpose is to understand in which cases the angle of attack will be unsteady, quantifying roughly the amplitude and frequency of the motion. More realistic simulations are performed in Chapt. 4 including all the present inflow variations, but with aero-elastic solvers. In such simulations, the induced velocities are also computed and the angle of inflow is then lower as the axial induction factor decreases the axial flow and the tangential induction factor increases the tangential flow (see Fig. 2.25).
Three effects are considered here: the tilt angle, the vertical wind shear and yaw misalignment. For several local speed ratio λ_r values, the variations of geometrical inflow angle are computed for a rotating blade with combination of these effects. The results are presented in Fig. 2.30 and 2.31. The 0° azimuthal position corresponds to a vertical blade above the nacelle, while the 180° azimuthal position corresponds to a vertical blade below the nacelle. The DTU10MW turbine geometrical data have been used to generate the following figures. The rotor radius, chord length distribution, tilt and cone angle have been extracted from the reference document [13]. The chosen operating conditions are the following:

- Wind speed of 11.4 m/s at 120 m and shear coefficient of 0.1
- Rotating speed of 9.6 RPM
- Yaw misalignment of $+20^\circ$

The yawed cases are investigated for positive and negative yaw misalignment (see Fig. 2.23) of 20°. The variations are much more important for low λ_r values as the wind velocity has more impact on the total flow velocity than for high λ_r values. It is important to notice that negative and positive yaw have the same shape but with a 180° phase shift. The 5° tilt angle is responsible for the same shape of variations than yaw angle, but with a 90° phase shift and much lower amplitude. Maximum angle of attack for positive yaw, negative yaw and tilt angle is reached for 180°, 0° and 270° azimuthal positions respectively (see Fig. 2.30a and 2.30b). Vertical wind shear influence is presented in Fig. 2.30c for a shear coefficient of 0.1 and based on the following formula:

$$V(h) = V_0 \left(\frac{h}{H}\right)^{\nu} \tag{2.16}$$

with $V(h)$ the wind speed at height h, V_0 the wind speed at hub height, H the hub height and ν the wind shear coefficient. The hub height chosen here is $H = 120m$. The wind speed is lower closer to the ground so when the azimuthal position is $180°$ the whole blade is undergoing a slower wind, in particular the tip sections. For this reason the angle of inflow is lower at this azimuthal position and the highest at $0°$, with the tip sections being the most affected. A combination of yaw, tilt and shear is then presented in Fig. 2.30d with the same previous values for each. As the $\pm 20°$ yaw misalignment is the strongest effect, it dominates the changes of inflow angle. However, it is interesting to notice that the combination of yaw and tilt creates a phase shift but does not change the amplitude of the inflow angle as the tilt angle is much smaller than the yaw angle. The maximum angles are not reached for $180°$ and $0°$, but respectively around $200°$ for positive yaw and $350°$ for negative yaw. The shape of variations is very close to sinusoidal functions for cases dominated by yaw, which justifies the unsteady pitching airfoils studies in 2-D presented earlier.

The amplitude of the variations are represented in Fig. 2.31. As mentioned previously, the amplitude

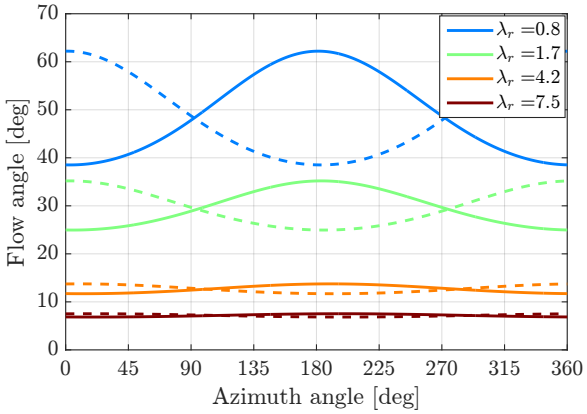

(a) Yawed rotor - Solid lines for $+20°$ yaw misalignment and dashed lines for $-20°$ yaw misalignment

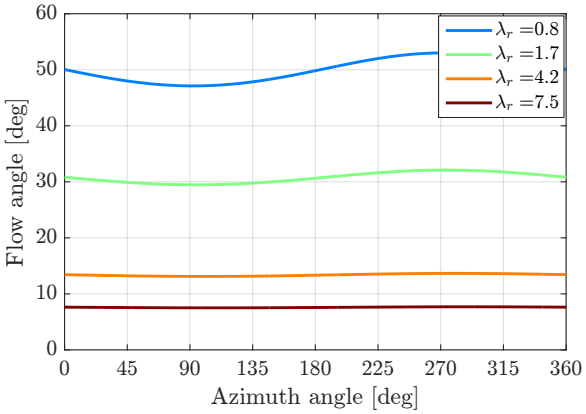

(b) Rotor with $5°$ tilt

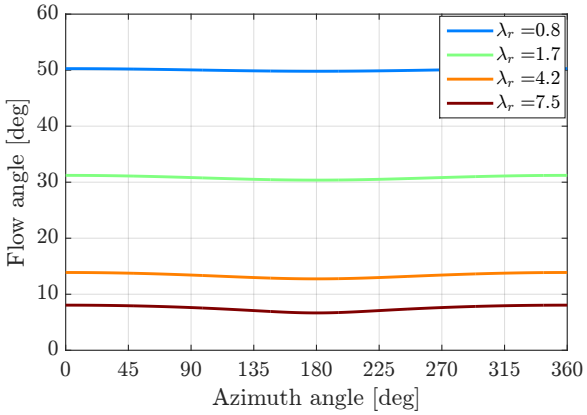

(c) Vertical wind shear - Shear coefficient of 0.1

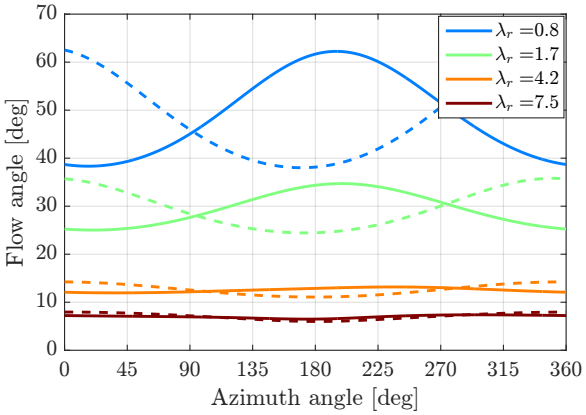

(d) Combination of shear, tilt and yaw misaligment - Solid lines for $+20°$ yaw misalignment and dashed lines for $-20°$ yaw misalignment

Figure 2.30: Geometrical inflow angle on a rotating blade for several local speed ratios λ_r

of inflow angle variations in yaw conditions without shear is directly linked to the yaw angle, and is the same for positive or negative yaw. For a same tilt or yaw angle, the amplitude is also the same (see

Fig. 2.31a). In the case of shear only (Fig. 2.31b), the amplitude is directly correlated to the wind shear coefficient. For the combination of shear, yaw and tilt (Fig. 2.31c) several observations seem relevant. It appears that combination of tilt and yaw does not change much the amplitude if yaw is much larger than tilt angle. However, the combination of yaw and shear reveals the impact of negative or positive yaw: for negative yaw, the amplitude is larger than for positive yaw angles. The unsteady effects in real conditions should then be more severe for negative yaw than positive yaw.

The variations of wind speed and reduced frequency are also investigated following the same methodol-

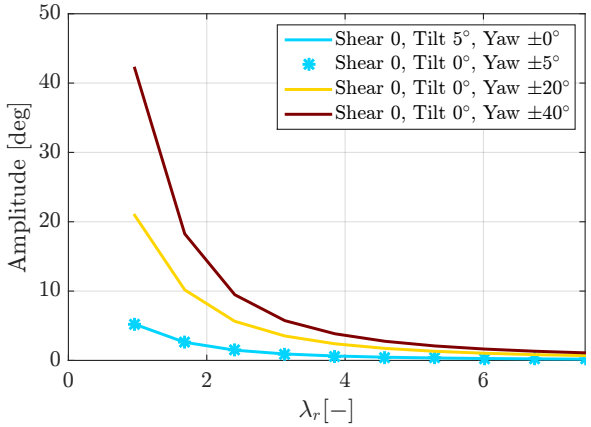

(a) Yaw and tilt cases

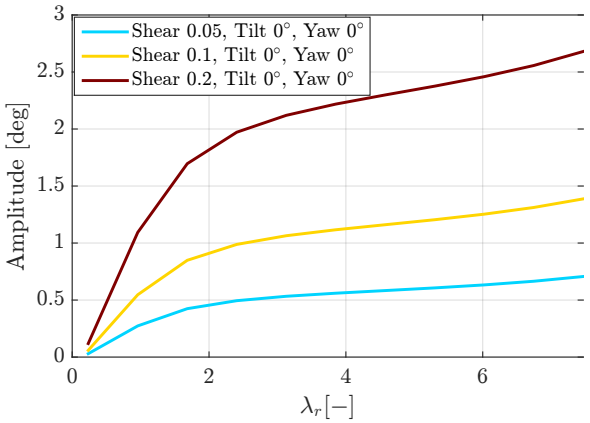

(b) Vertical wind shear cases

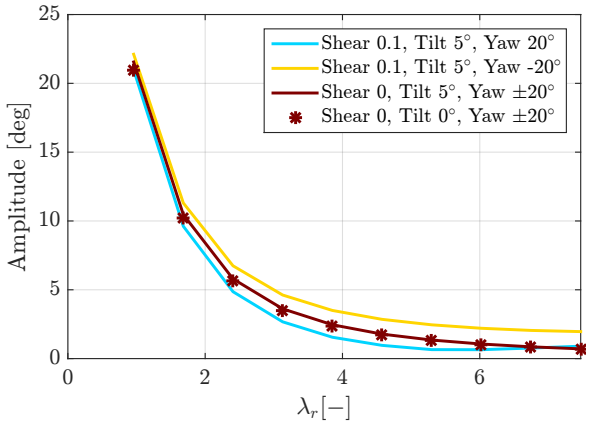

(c) Combined cases of vertical wind shear, tilt and yaw misalignment

Figure 2.31: Amplitude of geometrical inflow angle variations for several combinations of yaw, tilt and wind shear

ogy and combining a shear coefficient of 0.1, a yaw angle of $+20°$ and a tilt angle of $5°$. The fluctuations of the relative flow velocities for several spanwise positions are presented in Fig. 2.32a. The flow velocity is divided by the mean flow velocity over all azimuthal positions for each spanwise position (here as a function of λ_r) in order to have the relative fluctuations. It appears clearly that for low λ_r values close to the blade root, the fluctuations reach nearly 20% of the mean flow velocity, while it is less than 5% at the tip where the flow velocity is dominated by the blade rotation. In such conditions the unsteady flow is a combination of pitching and oscillating stream. Regarding the reduced frequency k presented in 2.32b computed with the formula $k = \pi f c/U$, the frequency f considered is the rotation frequency, c is the chord length and U is the geometrical relative flow velocity, both at a given radial position. The reduced

frequency is higher close to the root as U is lower and the chord length is larger. The solid and dashed line represent the reduced frequency calculated with the mean and the min/max envelope of flow velocity over one rotation respectively. As the velocity variations are high close to the root, the envelope is larger. The range of λ_r between 0 and 4 is characterized by reduced frequencies over 0.05 and amplitude of several degrees. The unsteady behavior can thus be considered as critical for sections close to the root.

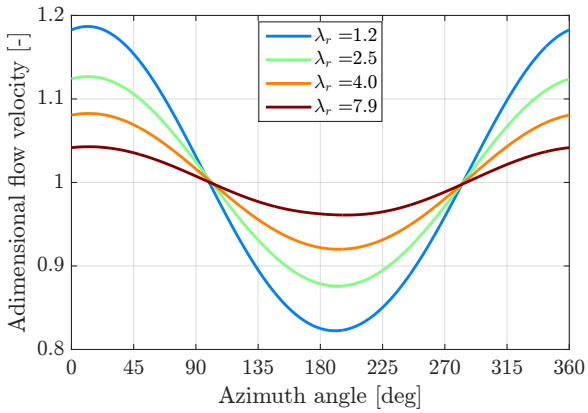

(a) Variations of geometric flow velocity for several radial positions

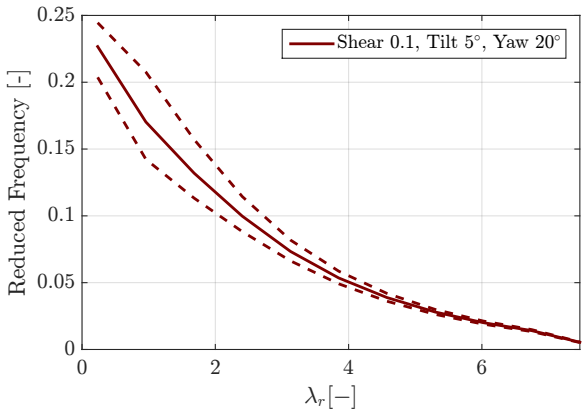

(b) Reduced frequency for mean (solid line), minimum and maximum (dashed lines) wind speed.

Figure 2.32: Geometrical flow velocity variations and reduced frequencies with combination of shear, yaw and tilt

2.3.3.2 Aperiodic: Turbulent wind

Appart from the effect of vertical wind shear, the inflow wind considered previously is uniform and constant over the rotor area. Real wind is a turbulent wind, changing in time and not spatially uniform, which implies that the angle of attack is different on all sections and time dependent. The present paragraph aims at characterizing the angle of attack variations caused by wind turbulence on the NREL 5MW academic wind turbine [101], once again from a purely geometrical point of view without any induction.

Several spectra are used in simulations to reproduce the spatial and temporal wind spectra. The turbulent wind field in the present results have been generated with the software TurbSim [98] from NREL that can simulate the Kaimal or Mann spectra used and described in engineering standards such as IEC 61400-1 [92]. The intensity of the turbulence is given by the turbulence intensity TI:

$$TI = \frac{\sigma_{V_0}}{V_{mean}} \tag{2.17}$$

with σ_{V_0} the standard deviation of wind speed V_0 and V_{mean} the mean wind speed over a given time period. In the present study, the wind field is generated with a 10% turbulence intensity, Kaimal spectrum and a vertical shear coefficient of 0.1. The NREL 5MW turbine has a $5°$ tilt angle, which in combination with the wind shear creates small angle of attack fluctuations as described in previous paragraph. In Fig. 2.33, the geometric (no induction is considered) flow velocity and angle of attack at different spanwise positions (given by the ratio of the local radius over rotor radius r/R) are represented for turbulent wind with and without yaw misalignment. As described previously, a large yaw misalignment creates large fluctuations depending on the azimuthal position of the blade, in particular at the sections close

to the root. The turbulent wind adds small random fluctuations to this periodic signal. These random fluctuations are also larger for sections close to the root as the flow velocity component due to the wind speed is relatively larger than for the sections close to the tip.

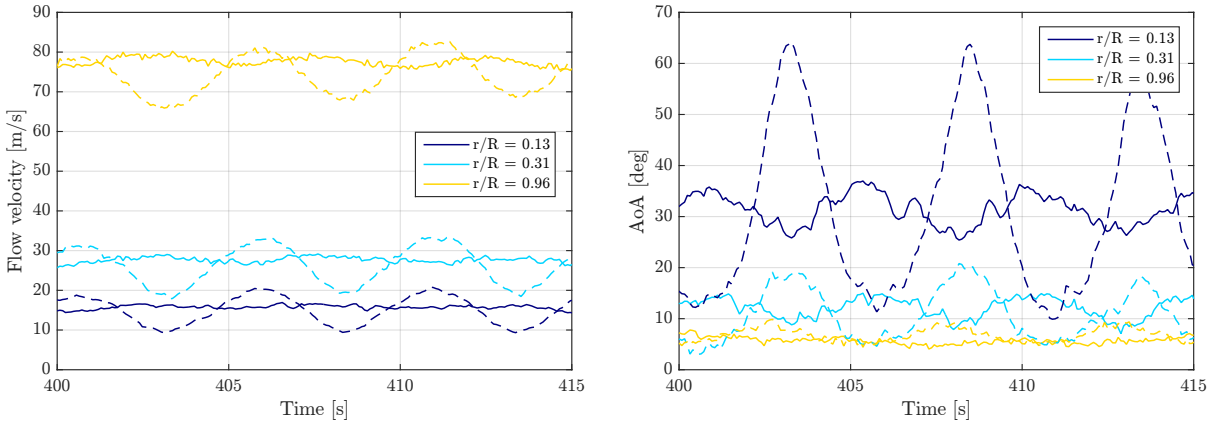

(a) Geometric velocity

(b) Geometric angle of attack

Figure 2.33: Geometric velocity and angle of attack for a turbulent wind distribution at different spanwise positions - Yaw misalignment of $0°$ (solid lines) and $-40°$ (dashed lines)

The angle of attack variations caused by turbulence are not periodic and the usual sinusoidal motion used to compute the reduced frequency can not be applied. Furthermore, the amplitude of variations is not constant neither. It is thus difficult to compare the unsteadiness caused by turbulence to the periodic variations due to yaw misalignment or wind shear. The geometric AoA reduced rate of change is computed and plotted in Fig. 2.34 in order to quantify differently the unsteadiness:

$$AoA_{rate,red} = \left|\frac{\partial \alpha}{\partial t}\right| \frac{c}{2V_{geo}} \tag{2.18}$$

with V_{geo} the local geometric flow velocity and c the airfoil chord. It appears clearly that turbulent cases have a much higher AoA rate than uniform cases, in particular for sections close to the tip. The values are very low for uniform flow as only tilt angle and wind shear are responsible for the variations. For cases with yaw misalignment, the same observation is made, and turbulence increases the existing AoA rate. These results are only an indication of the level of unsteadiness caused by turbulence. Firstly, the maximum observable frequency is proportional to both spatial and temporal discretisation of the continuous wind field. By changing the time steps, these results can change. It has been assumed here that the chosen time step of $0.02s$ used to describe the wind is much smaller than the characteristic time of the flow $\frac{c}{2V}$ with c the airfoil chord and V the flow velocity. Thus the turbulent structures generating unsteadiness of the same order of magnitude than the one caused by the periodic phenomena can be captured. Secondly, only the instantaneous angle of attack rate of change is investigated here. As said earlier, there is no full correlation possible between amplitude, frequency and AoA rate: on one side, a motion is considered with given characteristics, on the other, an instantaneous value with no history considerations. For an airfoil pitching with a sinusoidal motion $\alpha(t) = \alpha_0 + \alpha_1 sin(\omega t)$, the maximum reduced AoA rate or pitch rate is:

$$AoA_{rate,red}(max) = \alpha_1 \omega \frac{c}{2V_{geo}} = \frac{2\pi\alpha_1}{T} \frac{c}{2U_0} \tag{2.19}$$

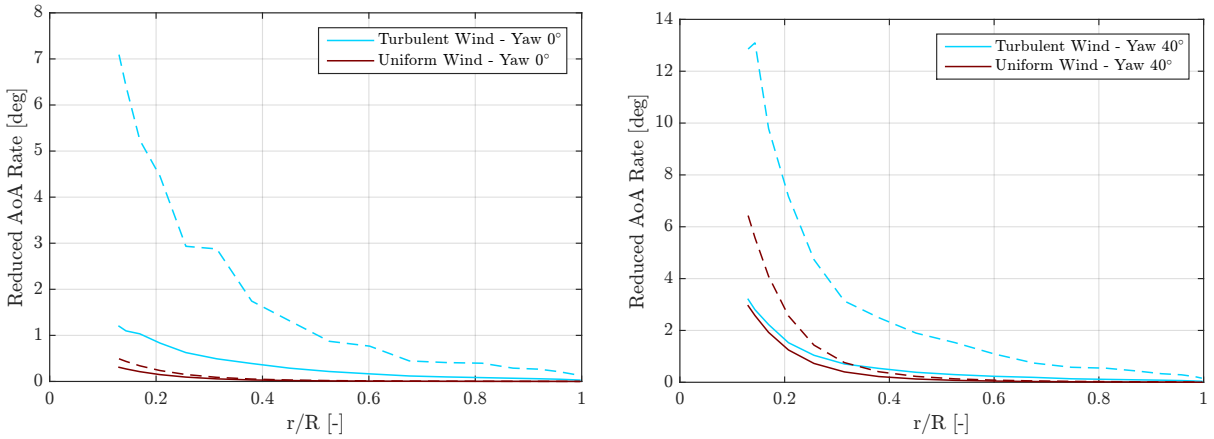

(a) No yaw misalignment

(b) $-40°$ yaw misalignment

Figure 2.34: Reduced geometric angle of attack rate of change as a function of spanwise position for turbulent and uniform winds - Mean (solid lines) and maximum (dashed lines) values

with T the period of the motion and U_0 the free stream velocity. In such case, the AoA rate is thus dependent of both amplitude and frequency, while reduced frequency definition does not consider the amplitude of the motion. The match pitch rate concept presented earlier shows that more importantly than reduced frequency or amplitude considered alone, the history of angle of attack is more suited to quantify the unsteady behavior. Thus to conclude, the fact that much higher values of AoA rate are observed in turbulent case implies that unsteady phenomena could have a larger impact than in uniform cases.

Furthermore, high frequency turbulence in reality correspond to small disturbances of the flow that might no impact the full airfoil, while lower frequency turbulence has a larger characteristic size . There is a limit to define for which large unsteady structures of the flow imply dynamic stall behavior, and small turbulence which impacts the boundary layer and will change the static polar characteristics. This kind of remark shows the limit of modeling the forces on an airfoil with static polar lookup tables: large scale turbulence would mean dynamic stall while small scale turbulence would mean modification of static polars.

Chapter 3

Aerodynamics modeling for wind turbines: state-of-the-art

Contents

One of the main difficulty for modeling the aerodynamics of wind turbines consists in the very different space and time scales involved in specific phenomena. For example, at the boundary layer scale the viscous and kinetic forces must be well predicted in order to be able to capture the laminar turbulent transition and the flow separation. The resulting stall process is described at the airfoil scale by specific flow observations such as leading edge vortex and corresponding aerodynamic forces. At the rotor scale, the change in the blade aerodynamic forces caused by stall is responsible of a variation of the induction field which modifies the full rotor performance. Then at the wind farm scale, the wind deficit behind one turbine evolves depending on the rotor performance and directly impacts the next row of turbines. This illustrates the influence of the smallest scales on the largest scales, and reveals the complexity of capturing all aerodynamic phenomena with one model. Indeed, the simulation with Computation Fluid Dynamics (CFD) of a full wind farm resolving the flow around the blade geometry including the boundary layer would require an unrealistically high number of CPU hours even considering the progress in computer power for the years to come. However the performances and loads of wind turbines have

been estimated in the past with very poor CPU capacities by using light models like the Blade Element Momentum Theory presented in the first section of the chapter. Such theory is still the standard tool in engineering where thousands of cases must be launched in order to assess the structural integrity of the wind turbines in many different environmental conditions. The very limiting assumptions behind this model implies that many empirical corrections must be included to handle realistic cases. To check and improve the predictions of these empirical models, other theories more complex but also more costly in terms of CPU hours have been developed such as singularity methods and CFD, both introduced in this chapter.

3.1 Blade Element Momentum theory

This section aims at introducing the Blade Element Momentum Theory (BEMT) and the main models used in state-of-the-art engineering solvers. Glauert [50] was one the first authors to introduce BEMT with two of its empirical models that are still widely used nowadays: the Glauert correction and the Prandtl tip-loss model. Most of the models presented in this section are based on several references. First Hansen [82] provides a very clear overview of modern state-of-the-art BEMT solvers, and inspired Branlard [25] book sections relative to the numerical implementation of a BEMT solver. The work of Sørensen [189], the PhD thesis of Sant [169] and Schepers [170] are references that offer much insight into the limits of BEMT solvers and ways to improve them. Finally, AeroDyn theory manual [137] is also a useful document that details the models used in AeroDyn BEMT code developed at NREL.

3.1.1 Steady and Unsteady BEM

The BEMT theory is a combination of the Blade Element Theory and the Momentum theory. The Momentum theory in the case of an ideal rotor is introduced in the previous chapter 2.3, where only the axial induction is considered. For most BEMT solvers, the momentum equation is also applied in the rotor plane to account for the wake rotation. Indeed, as the fluid creates torque on the rotor, the blade applies an opposite force on the fluid. The momentum theory that considers both axial and tangential inductions is referred as the *streamtube theory* by Branlard, and was introduced by Glauert [50].

The momentum theory is applied on an elementary annulus as illustrated in Fig. 3.1, for the conservation of both the angular momentum and the axial momentum of the control volume. The following equation can be derived from the conservation of angular momentum for the elementary power $dP(r)$ of the annulus:

$$dP(r) = 4\pi\rho\Omega^2 V_0 a(r)'\big(1-a(r)\big)r^3 dr \tag{3.1}$$

with ρ the fluid density, Ω the rotational speed, V_0 the incoming wind velocity, a' the tangential induction factor, a the axial induction factor and r the radius of the annulus.
Based on the axial momentum conservation, the elementary thrust force $dT(r)$ applied on the annulus is obtained:

$$dT(r) = 4\pi\rho V_0^2 a(r)\big(1-a(r)\big)r dr \tag{3.2}$$

On the rotor plane, the tangential flow velocity is $U_\theta = a'\Omega r$ and the axial velocity is $U_{ax} = V_0(1-a)$. The power and torque of the full rotor are then obtained by integrating the above formula over the rotor radius. Based on the velocities illustrated in Fig. 2.25, the inflow angle $\phi(r)$ can be expressed with the

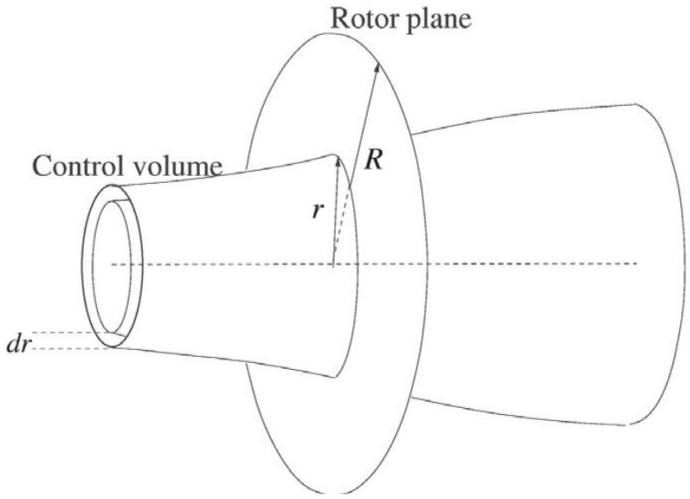

Figure 3.1: Streamtube control volume for momentum theory - [82]

following formula:

$$tan(\phi(r)) = \frac{\big(1 - a(r)\big)V_0}{\big(1 + a'(r)\big)\Omega r} \tag{3.3}$$

The Blade Element Theory (BET) considers that the blade can be discretized into several sections of a given spanwise length each defined by a unique airfoil. The aerodynamic forces on the blades are the sum of all section forces, and are obtained thanks to the polar data of each airfoil. The relative flow velocity V_{rel} seen by the airfoil and the AoA α are the only flow data needed to get the aerodynamic forces by using Eq. 2.2. By projecting the 2-D aerodynamic forces and the relative velocity V_{rel} in the normal (thrust force) and tangential (torque) directions as illustrated in Fig.2.25, the following relations are obtained for the elementary torque dM and thrust dT at a given radius:

$$dM = \frac{1}{2}\rho B \frac{V_0\big(1 - a\big)\Omega r\big(1 - a'\big)}{sin(\phi)cos(\phi)} cC_t r dr \tag{3.4}$$

and:

$$dT = \frac{1}{2}\rho B \frac{V_0^2\big(1 - a\big)^2}{sin(\phi)^2} cC_n dr \tag{3.5}$$

with B the number of blades, c the airfoil chord, C_n and C_t the normal and tangential force coefficients respectively. Torque and power are related through the relation $dP = \Omega dM$, and by equalizing equations 3.2 and 3.5 for thrust, then 3.1 and 3.4 for torque, the axial and tangential factors respectively can be expressed with the following equations:

$$a = \left[\frac{4sin(\phi)^2}{\sigma C_n} + 1\right]^{-1} \tag{3.6}$$

and:

$$a' = \left[\frac{4sin(\phi)cos(\phi)}{\sigma C_t} - 1\right]^{-1} \tag{3.7}$$

with $\sigma = cB/2\pi r$ the blade *solidity* which defines the fraction of the blade that covers the considered annulus area. This approach that simply equalizes the torque and thrust from both BET and Momentum theory has been proposed by Glauert and is used in most BEMT codes. However, other approaches have been developed, and are summarized by Sørensen [189]. The BEMT combines both momentum theory

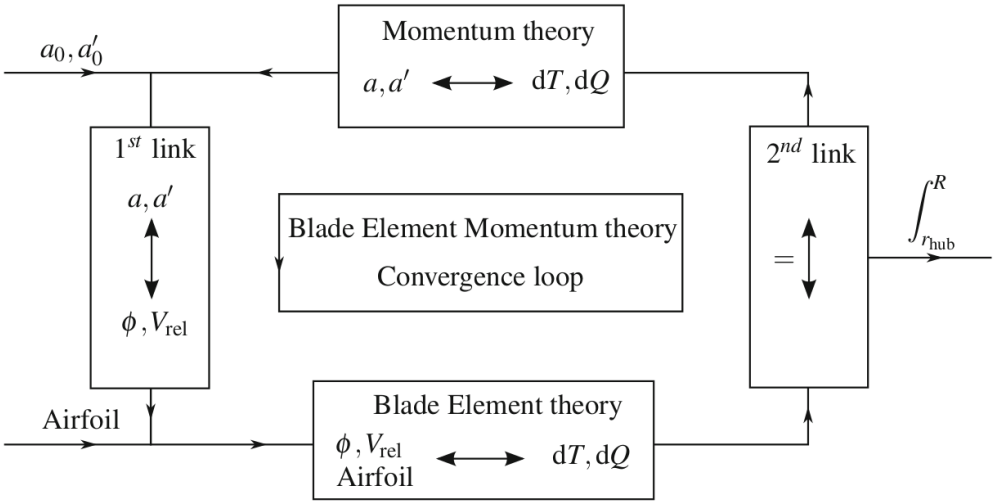

Figure 3.2: Blade Element Theory and Momentum Theory iterative process for a steady BEMT - [25]

and BET as illustrated in Fig. 3.2:

- The induction factors coming from momentum theory give the inflow information (inflow angle for AoA, and relative velocity) needed by BET to deduce the aerodynamic forces of each blade section defined by an airfoil.
- The aerodynamic forces from BET can be projected in order to deduce the torque and thrust created by each section. Thanks to momentum theory, Eq. 3.8 and 3.9 are used to obtain the induction factors.

In the *steady BEM* an iterative process is used to compute successively induction factors and aerodynamic forces, considering that at each time step an equilibrium state is reached. An assumption of steady conditions is thus made. In the *unsteady* BEM, several models can be used to take into account unsteady conditions. For example, the dynamic inflow models consider that a change in the aerodynamic forces has a time varying influence on the wake and thus induced velocities. The unsteady forces described in Section 2.1.4 are also representative of a dynamic system, and are considered by using dynamic stall models. When such models are used, the induction factors are obtained using temporal numerical schemes. The convergence of induction factors is then obtained by using time steps much smaller than the time constants from the different dynamic systems.
The BEMT theory relies on many assumptions, among which the most commonly considered are:

- Radial independency
- Blade force constant over the annulus, which is equivalent to consider an infinite number of blade.
- Inflow wind in the axial direction (no yaw angle)

- Lightly loaded rotors (axial induction factor $a < 0.4$)

Several models have been proposed to correct theses theoretical lacks of BEMT.

3.1.1.1 Tip-loss model

The tip loss model was developed originally to account for the finite number of blade (solidity lower than 1). An helicoidal wake is created by a blade, generating a specific induced velocity field which is not axisymmetric, including the tip losses. This behavior generates specific loads that are not taken into account by the streamtube theory. The Prandtl's tip loss model [50] modifies the equations for elementary forces from momentum theory by including a factor F in Eq. 3.1 and 3.2, which then modifies the equations for axial and tangential induction such as:

$$a = \left[\frac{4Fsin(\phi)^2}{\sigma C_n} + 1\right]^{-1} \tag{3.8}$$

and:

$$a' = \left[\frac{4Fsin(\phi)cos(\phi)}{\sigma C_t} - 1\right]^{-1} \tag{3.9}$$

The factor F is defined by the following relation:

$$F = \frac{2}{\pi} cos^{-1}(e^{-f}) \tag{3.10}$$

with:

$$f = \frac{B}{2}\frac{R-r}{rsin(\phi)} \tag{3.11}$$

where R is the rotor radius.
This model has been refined in numerous publications. The Master Thesis of Branlard [24] based on vortex methods gives an extensive overview of the possible improvements to Prandtl's tip loss model, mostly based on different estimations of f.

3.1.1.2 Correction for high induction

The comparison between experiments and momentum theory has shown that it is valid only for small values of the axial induction factor a as illustrated in Fig.3.3.
The thrust coefficient is thus modified in order to obtain realistic values when wind turbines operate in conditions with high induction, based on the relation for an ideal rotor $C_T = 4a(1-a)$:

$$\begin{cases} C_T = 4a(1-a)F & \text{for} \quad a \leq 1/3 \\ C_T = 4a(1-0.25(5-3a)a)F & \text{for} \quad a \geq 1/3 \end{cases} \tag{3.12}$$

with F the Prandtl's tip loss factor an a the axial induction factor. This formulation is the original Glauert correction [50]. In the case where $a \leq 1/3$, the two formulations for C_T from Eq. 3.5 in non-dimensional form and Eq. 3.12 give back Eq. 3.8 for axial induction. However, when $a \geq 1/3$, equalizing both equation does not give a direct value for a, and each much but solved independently in an iterative process. This process is costly and not robust, and other expressions are mostly used derived from Glauert empirical relation with the possibility to obtain a analytically based on those equations. Branlard [25] summarizes these models. The AeroDyn theory manual proposes the same kind of modification to

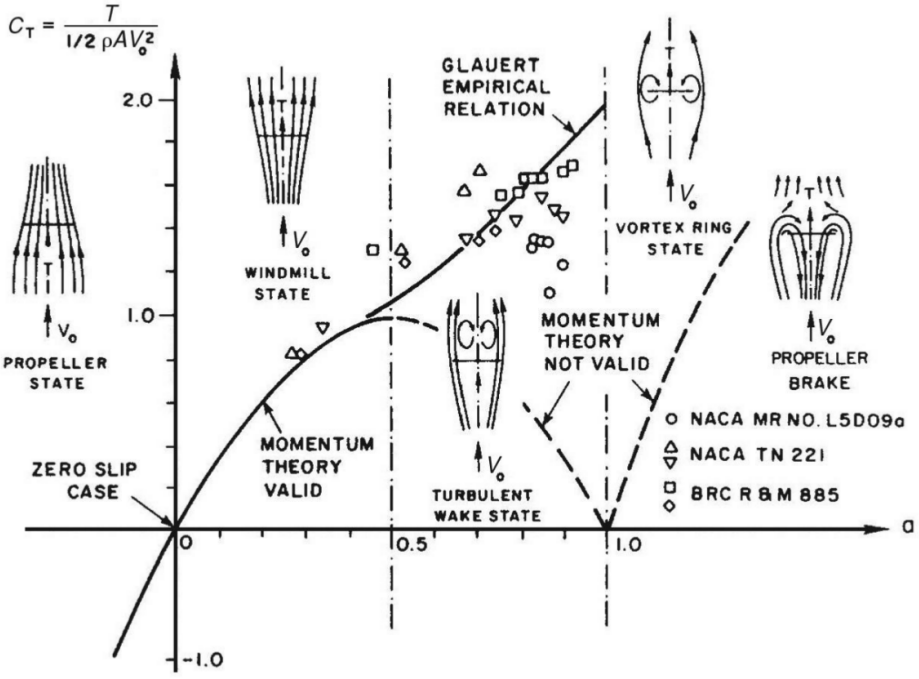

Figure 3.3: Comparison between thrust coefficients C_T according to BEMT, Glauert correction and experimental results - [82]

Glauert correction but with a different formulation of the $C_T(a)$ relation. In practical, wind turbines are not often operating in such conditions as the maximum TSR is most often the optimum TSR, with $a = 1/3$.

3.1.1.3 Skewed wake

The skewed wake models handles the variations in induction caused by the misalignment between the wind direction and the rotor axis. As the yaw misalignment creates periodic variations of AoA perceived by a section, the local forces and thus induction are also modified. The corrected axial induction factor a_{skew} proposed first by Glauert assumes that the wake is cylindrical:

$$a_{skew} = a\Big(1 + Kf(r/R)cos(\theta - \theta_0)\Big) \tag{3.13}$$

with a the axial induction factor computed without correction, $K = tan(\chi/2)$, χ the wake angle with the wind direction named *wake skew angle*, $f(r/R) = r/R$ with r the radius of the considered section and R the rotor radius, θ the blade azimuthal position and θ_0 the blade azimuthal position the most downstream in the flow (either 90° or 270° depending on the yaw angle sign).
This formula thus proposes an azimuthal varying induction factor. The axial induction is thus reduced when the blade is upstream and increased when downstream.
A possible interpretation that justifies such behavior is given by Branlard in Fig.3.4. By considering the wake as a succession of vortex rings, it appears that depending on the wake skew angle the contribution of the vortex rings on the induction factor can either be positive or negative upstream and only positive downstream. Many models for yaw have been proposed along the years, most based on the model of

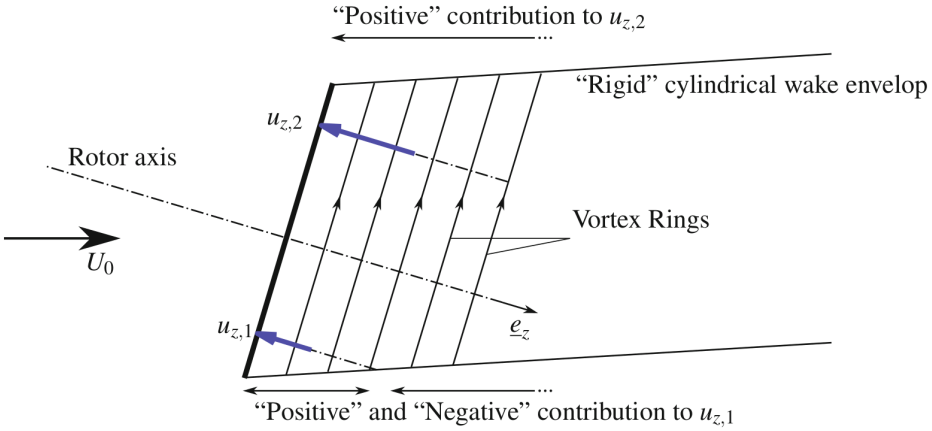

Figure 3.4: Vortex rings induction for a yawed rotor - [25]

Glauert and proposing modifications for the $f(r/R)$ function. Different formulations for K also exists, mainly based on different formulations for the computation of the wake skew angle which is different from the yaw angle. The model implemented in the NREL BEMT code AeroDyn [145] is another example of a Glauert type model with specific formulations for $f(r/R)$ ad K.
Schepers [170] proposes and exhaustive comprehension of the yaw effect on axial induction and loads. He also developed a different skewed wake model [171] based on the observation that not only the tip effect should be taken into account, but also the root effect.

3.1.1.4 Dynamic wake

The skewed make models implies that the axial induction factor changes with the azimuthal position, and thus changes in time. Many different reasons can lead to a change in time of induction, such as pitch motion, turbulent wind or starting/stopping of the turbine. According to the steady BEMT, any change in the rotor loading is instantaneously equilibrated by a proportional change in the induction, which means that the wake volume is fully accelerated or decelerated instantaneously. In reality, a delay is needed to reach a new equilibrium state. The dynamic wake models (also called dynamic inflow models) take into account this delay and replace the instantaneous induction factor by a delayed induction factor. Snel and Schepers [183] propose an exhaustive study of dynamic wake models, among which the Øye model, based on a set of two first-order differential equations, is commonly presented in literature [82] [25]. The ECN model proposed by Snel and Schepers is even simplier and based on the following equation:

$$\tau \frac{da}{dt} + 4a(1-a) = C_T \tag{3.14}$$

where τ is a constant that depends on the radial position, a is the axial induction and C_T is the thrust coefficient. This formula can be applied for each annular element, in which case induction and thrust are local coefficients. It appears clearly that for stationnary conditions, the formulation for C_T from Eq.2.14 is obtained, while a decaying term is added in unsteady conditions.

3.1.2 Dynamic stall models

Among all the models used in BEMT codes, the dynamic stall models aim at predicting the unsteady aerodynamic forces on each section of the discretized blade. These models mostly try to reproduce the dynamic stall phenomenon presented in 2.1.4, based on some physical considerations and relying on the static polar data to extrapolate the dynamic data through filtering. For this reason, theses models are called *semi-empirical models*. Three main categories are often defined (see [107]):

1. Dynamic AoA models, for which the static angle of attack is modified by introducing lags or other filters.

2. Models that do not consider any specific flow physics but are based on the observation of the experimental dynamic polar curves that are reproduced with appropriate functions.

3. Models based on the decomposition of the dynamic stall phenomenon in several physical sub-phenomena, each modeled individually.

This classification helps understanding the main trends in models, but it should be clear that many of the existing models are in fact combinations of these three categories. A list of several models is presented in table 3.1 with the reference publications. Some other listof existing dynamic stall models can be found in litterature [110] [107] [15] and [134]. The recent work from major universities specialized in wind energy show that the dynamic stall modeling in engineering codes is still an open field. Indeed several comparisons are made between the most frequently used models by the Energy research Centre of Netherlands (ECN) in [90], TU Delft in [104] or DTU Risø in [54].

Model	**Year**	**Type**	**Publications**
Beddoes-Leishman	1986, 1989	3	[111] [112]
Øye	1991	3	[147]
	2006	3	[83]
Larsen	2007	3	[107]
Onera EDLIN	1980, 1989	2	[196] [150]
Onera BH	1993	2-3	[198]
Gormont (Boeing-Vertol)	1972	1	[191] [69]
Snel	1997	2-3	[182]
Goman-Khrabrov	1994	3	[67]

Table 3.1: Listing of dynamic stall models

3.1.2.1 Øye model

The Øye model [147] is a very simple model that deals with only one aspect of the dynamic stall phenomenon presented in Chapter 2.1.4: the difference in the position of the separation point between static and dynamic cases.
The model is based on the definition of a fully-attached lift polar and a fully-separated polar (see Fig. 3.5) that will respectively match the static polar in the linear region and in deep-stall regime. The fully-attached polar $C_{l_{fa}}$ is considered as a linear function of the angle of attack, with a slope of 2π in the

original publications based on the thin airfoil theory. The slope C_{l_α} of the real static polar at the zero-lift angle α_0 is used in most applications of the model, such as $C_{l_{fa}} = C_{l_\alpha}(\alpha - \alpha_0)$. The fully-separated polar $C_{l_{fs}}$ is not properly defined in the publication but the slope around α_0 should be half the one of the static lift, and the lift should coincide with the static lift at 30° angle of attack. Some polynomial functions can be used to describe this fully-separated lift curve matching these conditions. The static lift is then defined as a linear interpolation between both polars through a separation point function f_{st}:

$$C_{l_{st}} = C_{l_\alpha}(\alpha - \alpha_0) f_{st} + C_{l_{fs}}(1 - f_{st}) \tag{3.15}$$

f_{st} can be considered as the position of the separation point in static conditions for a given angle of attack. A first-order differential equation is then used to introduce a lag in the position of the separation point, as this lag has been observed in experiments (see Chapter 2.1.4). In the original Øye model, this lag is discretized through a first-order scheme very easy to implement:

$$\frac{df}{dt} = \frac{f_{st}(\alpha) - f}{\tau} \quad \text{discretized in} \quad f_i = f_{i-1} + (f_{st}(\alpha) - f_{i-1})\frac{\Delta t}{\tau} \tag{3.16}$$

with τ a time constant that should be fit experimentally. The resulting dynamic separation point f is then used to compute a dynamic lift C_l by replacing f_{st} with f in equation 3.15. No corrections are proposed on drag and moment coefficients.

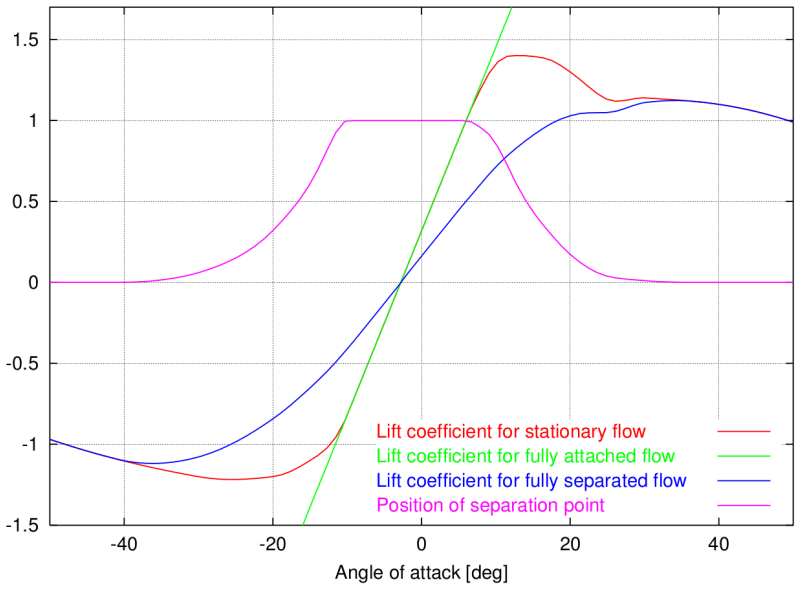

Figure 3.5: Example of fully-attached and fully-separated polars - [83]

This model is considered as relatively efficient for wind turbine applications, and very robust. However one of its main limitation is the lack of modeling for the attached unsteady flow behavior.

3.1.2.2 Beddoes-Leishman original model

The widely popular Beddoes-Leishman (B-L) model is fully described in the 1986 and 1989 publications from Beddoes and Leishman [111] [112], and is based on the work from Beddoes in the 70s joined by Leishman in the 80s. The main idea of the model is to differentiate several aspects of the dynamic stall

phenomenon and to propose simple models to solve each of these elementary blocks. As the model was dedicated to helicopter aerodynamics, some aspects are not really suited to wind turbines aerodynamics: handling of compressibility effects and of the leading edge vortex that does not seem relevant for thick wind turbine airfoils. Some other models based on the B-L model but dedicated to wind turbines have been proposed along the years and will be presented briefly in the next section.
Four specific modules can be identified in the original B-L model:

- The attached flow module, including circulatory and impulsive terms based on Theodorsen theory.
- The leading edge pressure lag module that introduces a delay on the triggering of the leading edge separation.
- The trailing edge separation module which accounts for the dynamics of the separation point.
- The leading edge vortex module, modeling the effect of the large vortex dynamics created by the leading edge separation.

For these four modules, the same modeling idea is used: lags are applied on several variables through first-order ordinary differential equations (ODE). This state-space formulation of the model based on first-order differential equations is described in Ref. [113]. These equations are solved numerically by a specific scheme presented in Fig. 3.6 based on a deficiency function $\mathcal{D}$ and applied on all the variables in red in the figure. A specific dynamic flow behavior is represented by each of these deficiency functions, with specific constants A_i and T_i. The non-dimensional time scale s is used instead of time t:

$$s = \frac{2}{c}\int_0^t U dt \tag{3.17}$$

which describes the distance traveled by the flow in semi-chord unit.
The attached flow module, based on the theories of Theodorsen and Wagner, considers the dynamic lift response to a succession of indicial variations of flow conditions. The normal force coefficient is used instead of the lift coefficient, both are very close for small angles of attack. The response to an impulse variation of AoA $\Delta\alpha$ is:

$$\Delta C_n(s) = \left(\frac{4}{M}\Phi_\alpha^I(s) + C_{N_\alpha}\Phi_\alpha^C(s)\right)\Delta\alpha \tag{3.18}$$

with Φ_α^I and Φ_α^C indicial functions. The first term is called the non-circulatory term, or *impulsive* term while the second is the *circulatory* term. In the case of a compressible flow, the impulsive lift is an initial loading decaying quickly corresponding to a pressure wave on the airfoil surface. For a pitching motion it is modeled through an exponential decaying function such as:

$$\Phi_\alpha^I(s) = \exp\left(-\frac{s}{T'}\right) \tag{3.19}$$

with T' a Mach number dependent time constant. The circulatory term aims at modeling the transitional variation of circulation around the airfoil due to the shed vorticity in the wake. Plunge (with a rate of plunging q) and pitching (pure variations of α) motions can both be considered, with the same type of formula based on Wagner function. For a pitching motion, Φ_α^C is thus defined by:

$$\Phi_\alpha^C(s) = 1.0 - A_1\exp(-b_1\beta^2 s) - A_2\exp(-b_2\beta^2 s) \tag{3.20}$$

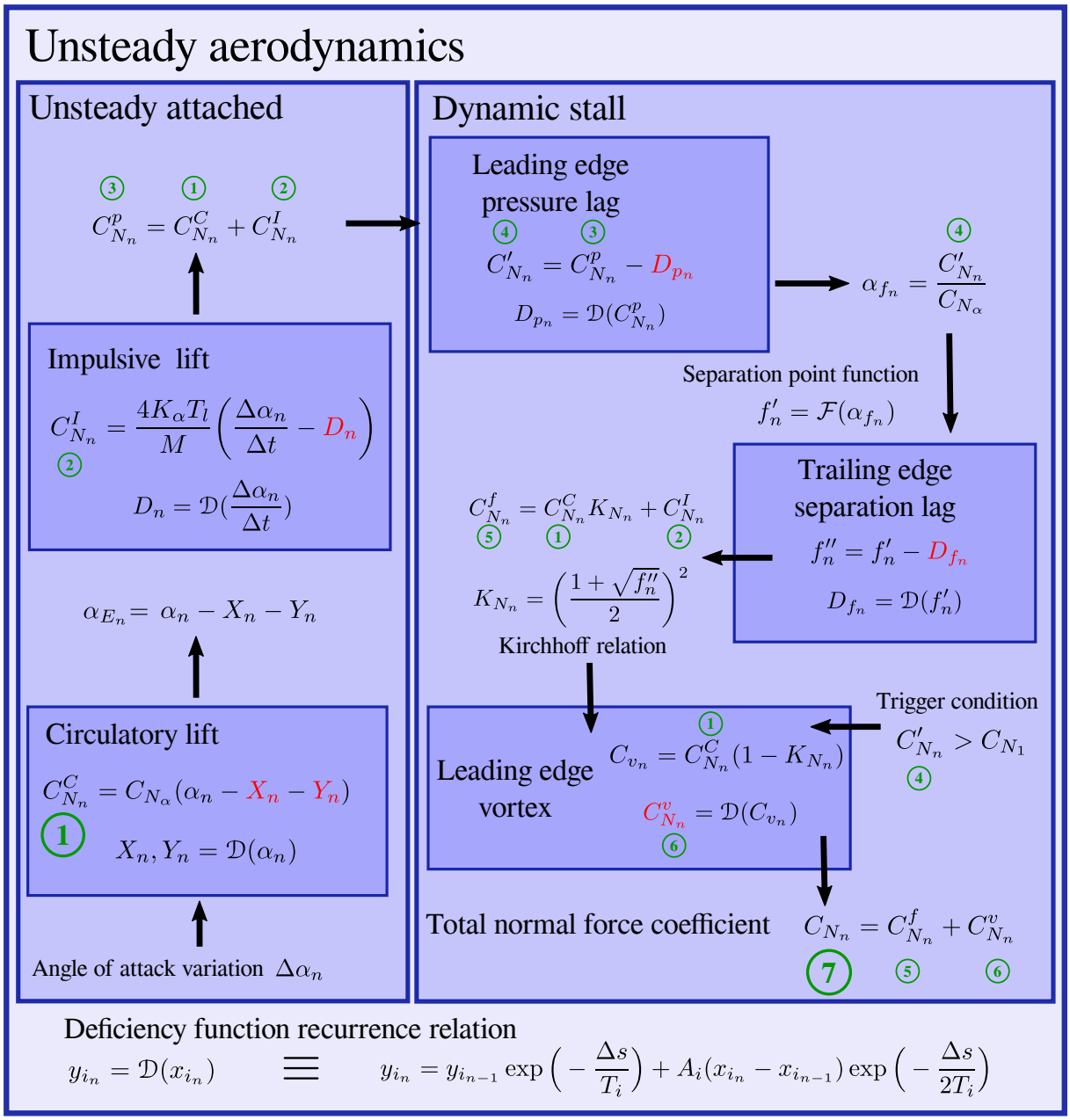

Figure 3.6: Beddoes-Leishman dynamic stall model representation

with A_1, b_1, A_2 and b_2 specific constants depending on the considered motion. The constant $\beta = \sqrt{1-M^2}$, with M the Mach number, is used to take into account compressibility effects. The normal coefficient for both impulsive and circulatory lift is then obtained thanks to the superposition principle and Duhamel integral. For the circulatory normal coefficient the equation is:

$$C^C_n(s) = C_{N_\alpha}\left(\alpha(0)\Phi^C_\alpha(s) + \int_0^s \frac{d\alpha(\sigma)}{dt}\Phi^C_\alpha(s-\sigma)d\sigma\right) = C_{N_\alpha}\alpha_E \tag{3.21}$$

with α_E the effective AoA that contains the influence of the shed vorticity in the wake. The numerical solution to the Duhamel integral proposed by Beddoes and Leishman is given through the scheme contained in the deficiency function presented in Fig. 3.6. In this figure, the discrete form at a time step n is

given for all variables. For more details about the discrete solution to the Duhamel integral, see Chapter 8 from Ref. [110].

The leading edge pressure module has been developed based on the observation that the triggering of the leading edge vortex is delayed in experimental cases compared to the static cases. An accumulation of pressure suction at the leading edge is considered as a condition to trigger separation, the corresponding dynamic behavior is thus to consider a delay for reaching this critical condition. The idea is then to link the pressure at the leading edge to the normal force coefficient and to introduce a criterion for the triggering of the leading edge vortex. The delay is thus applied on the normal coefficient by introducing a delayed normal coefficient C'_N, and the critical value C_{N_1} is the triggering limit, with $C'_N > C_{N_1}$ the condition for leading edge vortex triggering.

The Øye model deals with trailing edge separation: the trailing edge separation module from the B-L model has an equivalent behavior, applying a lag on the separation point. However, the calculation of the normal coefficient is based on the Kirchhoff relation for flat plates that relates the position of separation point to the normal coefficient:

$$C_N = C_{N_\alpha}\left(\frac{1+\sqrt{f}}{2}\right)^2 \alpha \tag{3.22}$$

The separation point function $f = \mathcal{F}(\alpha)$ is built empirically and based on exponential functions. In the trailing edge separation module, the input AoA is a delayed AoA α_f obtained by reversing the attached flow relation between normal coefficient and AoA as shown in Figure 3.6:

$$\alpha_f = \frac{C'_N}{C_{N_\alpha}} \tag{3.23}$$

In a similar way to the Øye model, a lag is applied on the separation point f' but using the specific numerical scheme used in the B-L model. The delayed separation point f'' is then used to compute the normal coefficient C_N^f thanks to Kirchhoff relation. A specific formula is given by Kirchhoff for the computation of tangential coefficient based on separation point.

The leading edge vortex module is handled through a complex set of logical conditions, as it models the vortex apparition, its decaying and convection over the section. A specific variable τ_v is used to track the position of the vortex along the chord, and modifying its influence depending on its position. Furthermore, once the shedding process is started by the leading edge vortex, several secondary vortices may appear. This behavior is handled by resetting τ_v after a given time constant based on the shedding frequency. The Strouhal number $St = f_s U/c$ is used as input to obtain the shedding frequency f_s. More details can be obtained in the original publications [111] [112], however the complete set of logical conditions is not fully detailed and is subject to interpretation. The strength of the vortex is modeled as the difference between the attached flow and the separated flow circulations. Fig. 3.6 shows the relation between the vortex contribution C_v and the attached and separated normal coefficients. The vortex dynamics is then modeled through an accumulative term and a diffusive term computed thanks to the deficiency function $\mathcal{D}$ applied to C_v. The impact of the vortex on force coefficients is taken into account by summing the vortex contribution on the normal force coefficient in order to obtain the total normal force coefficient C_N.

The four modules are described above based on their impact on the normal coefficient, but the dynamic tangential and moment coefficients are also handled by the B-L model, based on the same principles than for the normal coefficient.

The B-L model has been intensively used, validated and modified by several authors, including Leishman himself. The validation performed by Gupta and Leishman [78] for the s809 airfoil is dedicated to the

application of the model to wind turbines by adapting the static separation function $f = \mathcal{F}(\alpha)$ to the s809 airfoil. Pereira [149] proposes a 3-D validation by comparison with MEXICO experiments, which shows good agreements with measurements. Gonzales [68] also performed a 3-D validation on the NREL phase VI experiment, showing some discrepancies on two main aspects that are considered as the most challenging of dynamic stall modeling: the reattachment process and the vortex shedding.

3.1.2.3 Beddoes-Leishman inspired models

The original B-L model has been continuously modified along the years by many authors in order to improve and adapt it. The main contributors will be presented in the present section, focusing on the contributions dedicated to wind turbines. The master thesis from Pierce from 1996 [151] proposes some simple modifications of the angle of attack definition in order to handle large angle of attacks. Pierce also suggests to compute separation point f in a different way for the tangential force coefficient C_T, observing that it is poorly estimated when using the Kirchhoff formula based on normal coefficient. Furthermore, both separation points for C_N and for C_T are obtained by reversing Kirchhoff relation instead of using the formula from the original B-L model based on exponential functions. This strategy has also been used by Beaudet [15]. Pierce also defines his own interpretation on the setting of the logical conditions for the leading edge vortex initialization and resetting.
Niven and Galbraith [146] noticed that the delay applied on C_N was not enough to predict accurately the leading edge vortex apparition. They suggested a second pressure lag to improve the prediction on some airfoils. This methodology has been investigated by Sheng [175] and Beaudet [15] as they also noticed that the triggering of the leading edge vortex was predicted too early with the original B-L model. Sheng proposed several modifications of the B-L model summarized in Ref. [176]. A comparison with several airfoils from NREL such as the s809 airfoil reveals great improvements in the prediction of leading edge vortex and reattachment process (see Fig. 3.7). In particular, Sheng developed a new criterion for the onset of the leading edge vortex based on a delayed angle of attack instead of a delayed normal coefficient. The impact of the vortex is also taken into account differently: a second lag is applied on separation point and the strength of the vortex is modulated by a specific function depending on the position of the vortex along the chord.
Minnema [133] suggested some modifications on the pitching moment calculations by using a specific delayed angle of attack for the moment coefficient lag. This theory has been used and described in FAST code [42].
Two well-known models dedicated to wind energy have been developed based on the B-L model: the Risø model [83] and the Larsen model [107]. In Risø models, the attached flow part is modified in order to consider an incompressible flow as the Mach number is considered below 0.3. For incompressible flows, the impulsive lift is then based on the added mass principle, corresponding to the acceleration or deceleration of the flow by the airfoil surface. Only a first-order term proportional to the AoA time derivative is included. The impact of freestream velocity variations is also included in the attached flow regime, which modifies the circulatory lift equation by including the time derivative of velocity in the differential equation for the effective angle of attack. The leading edge pressure lag is the same as the one from the original B-L model. However, no leading edge vortex module is included in Risø model as it is considered by the authors that it does not appear on such thick airfoils. The pressure lag is then only used for modifying the effective angle of attack used to compute the separation point, and not as a trigger criterion for the leading edge vortex. The trailing edge separation module is a mix between the Øye model and the one from the B-L model: the separation point f is obtained by inversion of the

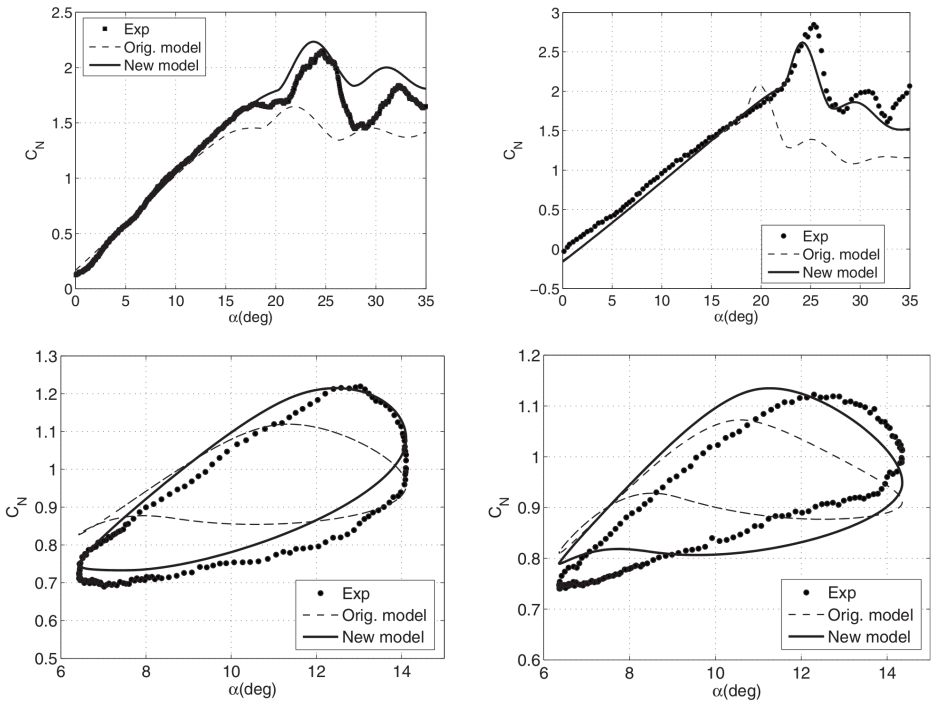

Figure 3.7: Comparison between Sheng model and original B-L model - Ramp-up test on NACA0012 and s809 profile (top left and right respectively) - Oscillatory test on s809 profile with $k = 0.05$ (bottom left)and $k = 0.10$ (bottom right) - [176]

Kirchoff formula, a lag is then applied on f, and the lift is reconstructed thanks to a linear combination of a fully attached and a fully separated polar.
The dynamic stall model from Larsen [107] is based on the same hypothesis than the Risø model for attached flows: no compressibility effects and impulsive term reduced to first-order terms. However, freestream variations are not included in the model. The separation function is based on Kircchoff formula but mapping the variable f on an unit circle with a parameter θ in order to avoid singularities. The delay in separation is then applied on θ. Furthermore, the leading edge separation is modeled by considering the leading edge vortex influence like in the original B-L model, but without adding the lag that accounts for the dynamics of the leading edge pressure. The condition to trigger the leading edge vortex is a critical AoA α_v and the dynamics of the vortex is handled by the dimensionless variable τ that gives the position of the vortex on the airfoil.
More recently, Elgammi and Sant [51] suggested to improve the prediction of the separation point by mean of statistical tools. However, their methodology is based on the analysis of temporal dynamic stall data for the s809 airfoil and few experimental measurements can be found with such data. The applicability of their model to other airfoils is thus uncertain.

3.1.2.4 Onera models

Two models have been developed at ONERA: the ONERA EDLIN model in the 80s and the ONERA BH model in the 90s. The EDLIN model is based on the work from Tran and Petot [196] [150] while the BH model was proposed by Truong [198]. The EDLIN model is based on a set of linear second-order

differential equations. The lift is considered as the sum of two components:

$$C_l = C_{l_1} + C_{l_2} \tag{3.24}$$

with C_{l_1} governed by the following ODE:

$$\frac{dC_{l_1}}{dt} + \lambda C_{l_1} = \lambda C_{l_{fa}}^{static} + (\lambda s + \sigma)\frac{d\alpha}{dt} + s\frac{d^2\alpha}{dt^2} \tag{3.25}$$

and C_{l_2}:

$$\frac{d^2C_{l_2}}{dt^2} + a\frac{dC_{l_2}}{dt} + rC_{l_2} = -r\Delta C_l^{static} - E\frac{d\alpha}{dt} \tag{3.26}$$

C_{l_1} gives the unsteady attached flow behavior while C_{l_2} is the component that must be added to C_{l_1} in order to take into account the dynamic stall behavior. $C_{l_{fa}}^{static}$ is the linear fully attached static lift and ΔC_l^{static} is the difference between $C_{l_{fa}}^{static}$ and the real static lift C_l^{static}. λ, s are constants that must be determined experimentally, dependent on the Mach number, and σ, a, r and E are functions of ΔC_l^{static}. The observed delay to reach stalled conditions in dynamic conditions is modeled through the leading edge pressure lag in the B-L model. In the EDLIN model, it is considered by introducing a lag τ in the calculations of ΔC_l^{static} such that the static angle used is $\alpha_{lag} = \alpha(t - \tau)$. The same type of modeling is used for drag and moment coefficient, and for other types of motions such as plunging and surging.
Very few experimental data provide temporal signal of lift during dynamic stall cycles as most of them only give averaged data over many cycles. The consequence of this is that the shedding variations are only considered as a standard deviation around a mean value. In reality, the shedding process at high Reynolds number is highly chaotic and each cycle of dynamic stall is different from another. The main idea behind the BH model is to consider the triggering of the leading edge vortex as a Hopf bifurcation. This principle based on dynamic systems considers that when a parameter reaches a certain value, the system switches from an equilibrium state to another equilibrium state. In the present case, the system switches from a time invariant flow to a periodically shedding flow. The total lift is the sum of two components like in the EDLIN model:

$$C_l = C_{l_s} + C_{l_u} \tag{3.27}$$

C_{l_s} is called the steady component and C_{l_u} the unsteady component. The steady component C_{l_s} contains the EDLIN model but modeled slightly differently:

- The unsteady attached flow modeling is based on Eq. 3.25.
- The separated flow behavior is based on the B-L model, by using the Kircchoff law, separation function and a lag on f in order to obtained a delayed separated lift coefficient C_l^{dyn}.

The pressure lag is obtained with the lag on α, used to compute the separation point. C_l^{dyn} is then used in Eq. 3.25 in replacement of $C_{l_{fa}}^{static}$. When the angle of attack reaches a critical stall angle value, then the second term C_{l_u} is activated and based on a non-linear differential Van-der-Pol Duffing equation:

$$\frac{d^2C_{l_u}}{dt^2} - \omega_s(\beta - \gamma C_{l_u}^2)\frac{dC_{l_u}}{dt} + \omega_s^2(C_{l_u} - \eta C_{l_u}^3 - a_2 C_{l_u}^2) = -E\omega_s\frac{d\alpha}{dt} - D\omega_s\frac{d^2\alpha}{dt^2} \tag{3.28}$$

The set of used constants is different depending on the sign of $\frac{d\alpha}{dt}$, changing the solution from a growing to a decaying oscillator. The constant ω_s is the Strouhal frequency of the airfoil. With this modeling, Truong is the first to introduce the shedding phenomenon as self-sustained and not only as a transitory

phase. The model is then supposed to have the capacity to predict the periodic forces due to the shedding vortices observed at very high angles of attack, in static and dynamic cases. The non-repeatability of each loop is also handled by the model, as a consequence of using a Van-der-Pol Duffing equation. Truong also proposed the inclusion of 3-D effects in the model in Ref. [199], which was later tested by Rapin [164] with some success. However, few authors have implemented and tested the BH model, and the EDLIN model is in most cases referred to as the "ONERA" model, for example in Ref. [204], [90],[54] or [104]. One of the reasons for this might be due to the linearity of the EDLIN model which makes it very well suited for stability analysis. Cafarelli [29] compares both models, showing the advantages of BH model over the EDLIN model as can be seen in Fig. 3.8: the shedding process clearly appears on the lift coefficient when using the BH model.

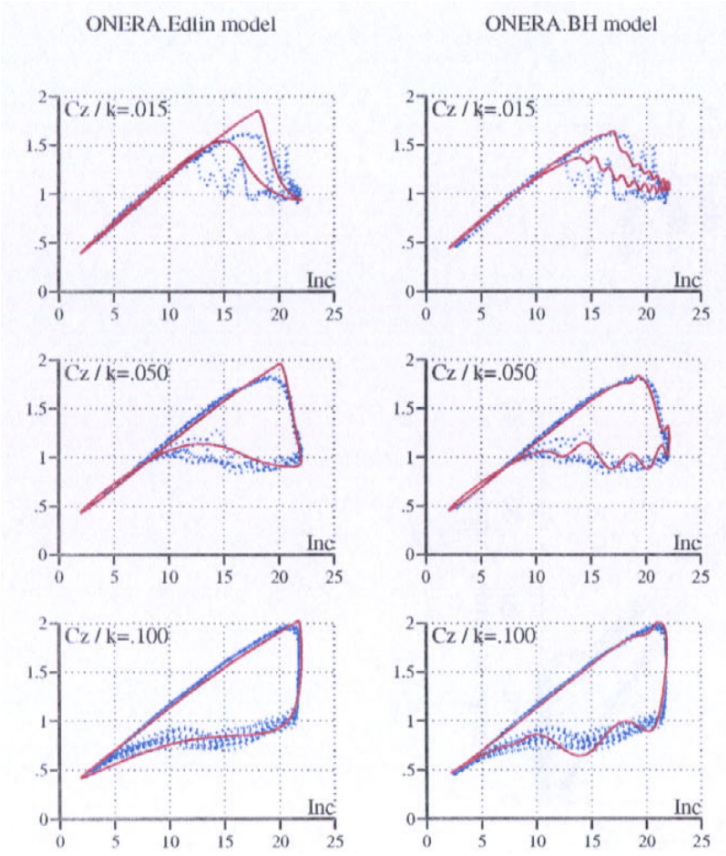

Figure 3.8: Lift coefficient for OA213 airfoil oscillating loops - Comparison between ONERA EDLIN (left), BH (right) models and experiments (blue curves) for 3 different reduced frequencies - [29]

The Snel model [182] is inspired by ONERA BH model regarding the inclusion of a self-sustained periodic lift component to model the vortex shedding. The total lift is given by the following formula:

$$C_l = C_l^{static} + \Delta C_{l_1} + \Delta C_{l_2} \tag{3.29}$$

The first corrective term ΔC_{l_1} is based on SIMPLE model [135] and corresponds to the steady component of the BH model. It introduces a lag through a first-order ODE with variable coefficients: the coefficients are dependent on the difference ΔC_l^{static} between attached flow and real flow. The second corrective term ΔC_{l_2} is the oscillating part modeling the vortex shedding, and is obtained with the same

type of non-linear second-order equation than for the BH model. However, the model needs much less parameters than the ONERA models and for this reason is much easier to use.

3.1.3 Aerodynamic polars corrections

Airfoil polar data are the base of the forces obtained in the BEMT. These data are dependent on many parameters such as Reynolds number, turbulence, blade surface among others. Different operating conditions, such as the use of clean or dirty blades or highly turbulent flow could lead to very different loads results when comparing experimental data to simulations because of polar data not adapted to these conditions.

3.1.3.1 3D correction

As presented in 2.2.4, stall is delayed on a rotating blade. In order to account for such behavior, the 2-D polars are modified based on empirical models derived from boundary layer equations that include rotational terms. The Rfoil code [201] is a panel method with a boundary layer formulation that includes such effects. Full CFD rotor computations have also been conducted in order to assess such effects [35] and to improve the empirical models. The most common base model is based on the work from Snel [181]:

$$C_{l,3D} = C_{l,2D} + f(C_{l,att} - C_{l,2D}) \tag{3.30}$$

with $C_{l,3D}$ the lift coefficient accounting for stall delay, $C_{l,2D}$ the lift coefficient without stall delay, f a function dependent on the blade geometry and $C_{l,att}$ the attached flow lift coefficient. Many different formulations for f have been proposed along the years, several of them presented in the papers from Bak [10] and Breton [26]. The NREL pre-processor AirfoilPrepPy [144] proposes a 3-D correction based on this formulation with the relation of Du and Selig [47] for f.
In a BEMT code, dynamic stall is applied to force coefficients that already contain the rotationnal effects.

3.1.3.2 Polar extension from -180° to +180°

Most available and reliable 2-D polar data are based on experimental data. Polars based on CFD computations are however progressively replacing experimental data. In both cases, the force coefficients for AoAs beyond stall angle are difficult to obtain because of the highly unsteady flow behavior for such AoAs. Several empirical methods have been proposed to extend existing 2-D polars to the full range of AoAs, from -180° to +180°. The work of Viterna [203] is a reference for the extrapolation of polar data and is used by NREL pre-processor AirfoilPrepPy [144]. The work of Montgomerie [136] and Spera [185] should also be considered.

3.2 Singularity methods

Singularity methods (also called *vortex methods*) are based on the assumption of an incompressible inviscid fluid, where the effects caused by viscosity are concentrated in specific locations called singularities. This hypothesis of inviscid fluid gives the possibility to simplify the fluid equations in a way that exact solutions can be found, reducing a lot the CPU cost compared to viscous flows for which the non-linear equations require to use costly numerical methods. The Katz and Plotkin book [102] is considered as a reference for such models. In this section, the main methods used for wind turbine applications are

introduced, in particular the free-wake and panel methods. The references used for this section are the Master Thesis of Dixon [44] who developed a 3-D panel method with free-wake at Delft University and the book of Branlard [25] which focuses on all vortex methods applied to wind turbines. Both of these references along with the Katz and Plotkin book provide much information on how to implement singularity methods practically, while this chapter focuses on the main principles of such methods.

3.2.1 Introduction

The general flow equations based on the conservation of the fluid extensive quantities are called the Navier-Stokes equations. The conservation of mass for a small fluid volume in differential form is:

$$\frac{\partial \rho}{\partial t} + \nabla \cdot (\rho \overrightarrow{u}) = 0 \tag{3.31}$$

For the conservation of momentum, the equation is:

$$\frac{\partial (\rho \overrightarrow{u})}{\partial t} + \nabla \cdot (\rho \overrightarrow{u} \otimes \overrightarrow{u}) = -\nabla p + \nabla \cdot \bar{\bar{\tau}} + \rho \overrightarrow{g} \tag{3.32}$$

where ρ is the fluid density, $\overrightarrow{u}$ the fluid velocity vector, ∇ the nabla operator, p the pressure, $\bar{\bar{\tau}}$ is the part of the stress tensor due to viscous effects and $\overrightarrow{g}$ the gravity force.

The formulation of Navier-Stokes equations using indicial notation is given in Section 3.3. With the hypothesis of inviscid and incompressible flow, the above equations are transformed in the Euler equations:

$$\nabla . \overrightarrow{u} = 0 \tag{3.33}$$

$$\frac{\partial \overrightarrow{u}}{\partial t} + \overrightarrow{u} \cdot \nabla (\overrightarrow{u}) = -\frac{\nabla p}{\rho} + \overrightarrow{g} \tag{3.34}$$

By using Kelvin theorem that states that the circulation around a close curve does not change in time, the fluid is then also irrotational and the velocity can be expressed as the gradient of a potential Φ:

$$\overrightarrow{u} = \nabla \Phi \tag{3.35}$$

The mass conservation equation can then be written as a Laplace equation:

$$\nabla^2 \Phi = \Delta \Phi = 0 \tag{3.36}$$

From the momentum conservation equation, the Bernoulli equation for potential flow becomes:

$$\frac{\partial \Phi}{\partial t} + \frac{\| \overrightarrow{u} \|^2}{2} + \frac{p}{\rho} = f(t) \tag{3.37}$$

with $f(t)$ and arbitrary function of time. Both equations 3.36 and 3.37 are the basis of potential method. In order to model boundaries, singularities are introduced in the flow in singular locations all solutions of Laplace equation. Several types of singularities exist such a source, sink, doublet and vortex, each with a specific formulation. They can be expressed in singular points, lines, surfaces or volumes. For each of these singularities, a specific solution for the Laplace equation exists, and each individual solution for Φ can be summed as Laplace equation is linear. The velocity induced by each singularity can be obtained in any point of the flow domain thanks to the Biot-Savart law. The velocity direction for doublet and vortex constant surface distributions are represented in Fig. 3.9. The flow solution is computed in the entire domain excepted the singularities by summing all their individual contributions to the velocity field. The

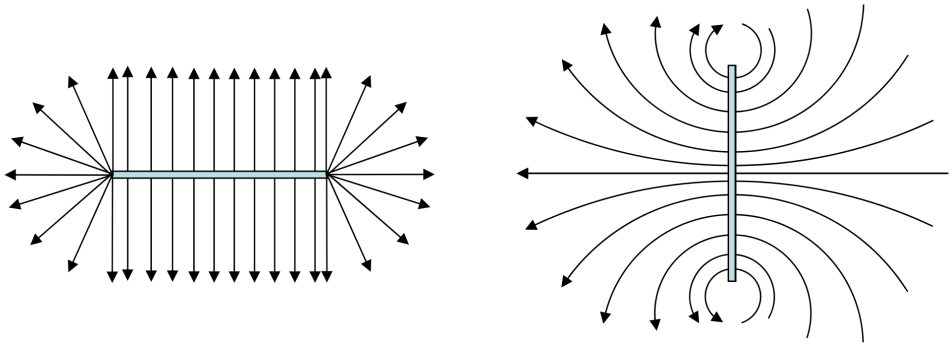

Figure 3.9: 2-D constant source (left) and doublet (right) panels with velocity directions - [44]

singularities are then treated as boundary conditions.
The vorticity $\overrightarrow{\omega} = \nabla \times \overrightarrow{u}$ is commonly used instead of the velocity in potential method, and the conservation equation for vorticity (or transport equation) considering only conservative exterior forces is obtained by applying the curl operator to Eq.3.32 with the hypothesis of incompressible flow:

$$\underbrace{\frac{\partial \overrightarrow{\omega}}{\partial t}}_{\text{Time dependency}} + \underbrace{(\overrightarrow{u}.\nabla)\overrightarrow{\omega}}_{\text{Advection}} = \underbrace{(\overrightarrow{\omega}.\nabla)\overrightarrow{u}}_{\text{Stretching}} + \underbrace{\frac{\nabla \times \nabla.\bar{\bar{\tau}}}{\rho}}_{\text{Diffusion}} \tag{3.38}$$

The pressure and gravity forces are based on the gradient of a potential distribution and disappear when applying the curl operator. This is one of the advantage of the transport equation of vorticity: the pressure is not needed to solve the equation. The vortex sheets are a common way to represent the shear layer of a viscous flow, and by assuming that the vorticity is contained in reduced dimension singularities, the viscous effects of the flow are thus represented by these singularities.

Fig. 3.10 shows the different types of vorticity representation in space. For example, the vortex sheet is based on a volumic distribution of vorticity integrated in one direction to have a surface distribution. This representation is well suited to airfoils for which the trailing edge creates vorticity as explained in Section 2.1.1. However it appears that some representation such as vortex line implies a jump in the velocity when crossing the singularity. In reality, the velocity jump is decreased because of viscous diffusion. This shows the limits of the singularities representation. In order to obtain a more physical representation of the vortex that takes into account the different terms of Eq. 3.38, several empirical models can be used:

- Core velocity models for desingularization of the vortex, by applying specific velocity profile near the vortex.
- Core deformation models to account for the stretching terms.
- Core growth models for the diffusion term.

The vortex methods presented below, the lifting line and the panel methods, are thus based on this flow representation. When applied to wind turbine (and more generally to aerodynamics), the main assumptions for potential flows can be considered as a good approximation of a real flow:

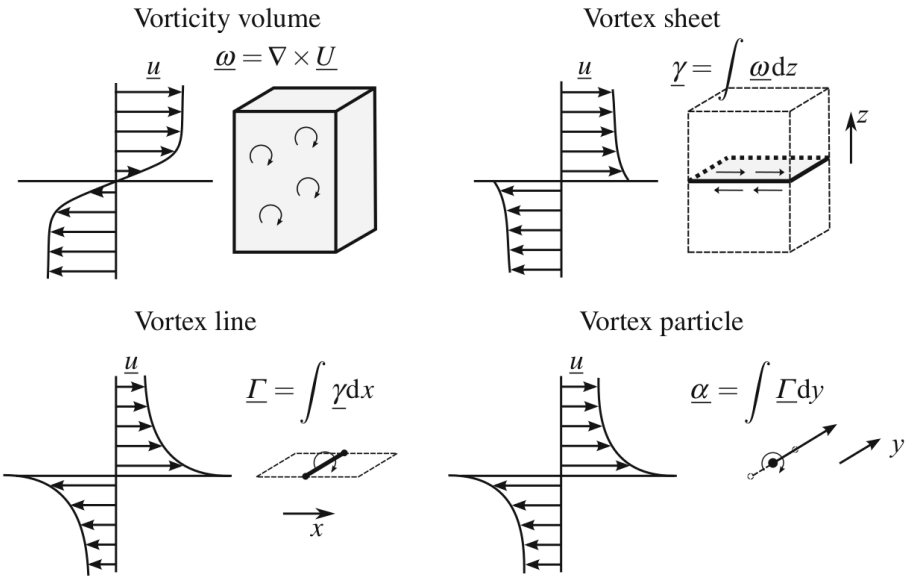

Figure 3.10: Vorticity representations in several reduced dimensions and velocity field - [25]

- In the fluid domain, the flow is *incompressible*. This assumption is justified by the low Mach number encountered in the operating conditions of a wind turbine.
- In the fluid domain, the flow is *irrotational*. The vorticity is only concentrated at the boundaries of the fluid domain. This assumption can be justified by the fact that away from solid boundaries (boundary layer) and from the wakes, the effect of viscous forces tends to be negligible with regards to the effects of inertial forces. Therefore, the solid bodies boundary layers and the wakes are considered as infinitely thin.
- The fluid is *inviscid* in the fluid domain. This is to be related with the two previous assumptions.

The main difference between lifting line and panel methods considered here is the modeling of the blade and wake with vortex line (lineic distribution of singularities) or in panels (surfacic distribution of singularities) respectively as illustrated in Fig. 3.11.

3.2.2 Lifting lines and wake modeling

The lifting line model (see the work of Garrel [63] or Sebastian [174] for lifting line code examples) assume that the vorticity generated by the blade is concentrated in a vortex line positioned at the aerodynamic center of the airfoil, most often considered to be the quarter-chord point. At the trailing edge, vorticity is emitted creating a wake that is modeled as a *vortex sheet* as represented in Fig.2.15. The Stokes' theorem relates the circulation to vorticity:

$$\Gamma = \oint_C \vec{u}.\vec{dl} = \int_S \nabla \times \vec{u}.\vec{n}\, dS = \int_S \vec{\omega}.\vec{n}\, dS \tag{3.39}$$

By considering a closed path surrounding a plane orthogonal to the vortex line of surface S, the equation is in fact similar to the definition of the strength of the vortex line obtained by integration of a volumic

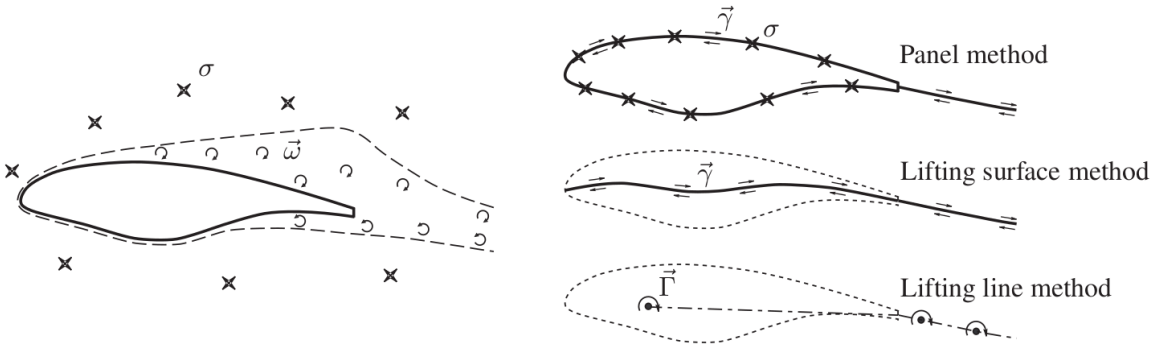

Figure 3.11: Blade modeling for several vortex methods - [63]

distribution of vorticity (see Fig. 3.10). This implies that through the Kutta-Joukowski theorem 2.1, the strength of the lifting line is given by the lift force.

Vortex sheet

The vortex sheet is a surface in 3D that represents an infinitesimal thin shear layer in the flow. This is a simplified view, as in reality this sheet rolls up and can have complex connections. In numerics, it is difficult and costly to represent a continuous vortex sheet. In the case of lifting lines the sheet is discretised into finite wake elements formed by vortex lines as illustrated in Fig. 3.12. The blade is splitted in several segments like in the BEMT, each assigned with a given airfoil an associated polars. The vortex filaments are closed in order to create vortex rings an obey to Helmholtz theorems:

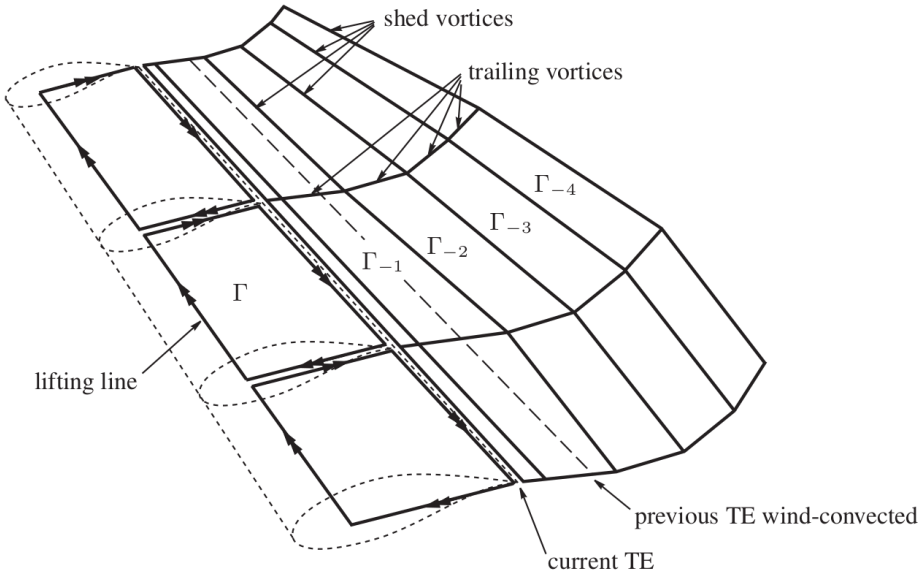

Figure 3.12: Wake discretization in vortex rings - [63]

- The circulation strength of a vortex line is constant along its length

- A vortex line must extend to the boundaries of the fluid domain or form a close path.
- An irrotational fluid element remains irrotational in the absence of rotational external forces.

Furthermore, the Kelvin theorem also states that the vortex filaments strength remains constant in time. The principle of the wake model is then to create a new vortex ring at each time step attached to the trailing edge and then convected with the flow. The strength of each vortex ring created at a time step t is the strength of the airfoil vortex ring obtained thanks to Kutta-Joukowski relation at the time step t. This vortex ring attached to the trailing edge has a length which common practice takes at from 20% to 30% of the length of a fully convected vortex line during one time step.
The AoA and flow velocities are needed for the calculation of the lift based on the viscous polars. The induced velocities are obtained based on Biot-Savart law applied to a vortex ring:

$$\overrightarrow{u_{ind}(\overrightarrow{r})} = -\frac{\Gamma}{4\pi}\oint \frac{\overrightarrow{r} \times \overrightarrow{dl}}{r^3} \tag{3.40}$$

with $\overrightarrow{r}$ a location on the vortex line and the *control point* where the velocity is calculated, Γ the strength of the vortex line. It is then possible to define the shed and trail vorticity from Fig. 2.15 with:

$$\Gamma_{shed}(n,t) = \Gamma(n,t+\Delta t) - \Gamma(n,t) \tag{3.41}$$

$$\Gamma_{trail}(n,t) = \Gamma(n,t) - \Gamma(n-1,t) \tag{3.42}$$

where n is the index of the considered segment in the spanwise direction of the blade, t the time and Δt the time step. The shed and trail vorticities can be considered as the strength of one vortex line resulting from the summing of the two vortex lines belonging to two adjacent vortex rings, of opposite signs because of the orientation of the vortex rings. The total flow velocity is at a given location the sum of the freestream velocity, the blade motion and the induced velocities from all vortex lines.

Free wake

In the case of a free wake, the vortex lines are considered as Lagrangian marker, which means that they move with the fluid, with the following equation:

$$\frac{\mathrm{d}\overrightarrow{x}}{\mathrm{d}t} = \overrightarrow{u}(x) \tag{3.43}$$

where $\overrightarrow{x}$ is the position vector of the considered and $\overrightarrow{u}(x)$ is the flow velocity for this position, that takes into account the induced velocities from all other wakes. This equation can be solved with several types of time-marching schemes. The works of both Sebastian [174] and Garrel [63] is based on free wake methods.

Prescribed wake

For prescribed wake, the positions of the vortex lines are prescribed thanks to arbitrary formulas. Currin [41] for example developed such model. The main advantage compared to free wake models is the gain in CPU time. Indeed, the most CPU time consuming part of the lifting line method is the calculation of induced velocities in specific control point thanks to the Biot-Savart equation. In the case of the prescribed wake, the only control points are the blade control points commonly located at the three-quarter chord of the airfoil. In the case of the free wake method, each wake vortex rings has a control point at the center of the ring, implying that each time step the number of control points increases with the number

of emitted vortex rings.

Free wake lifting line models have been used widely for wind turbine applications. The main advantage compared to BEMT is that a number of flow features are captured by the wake induced velocities instead of applying corrections to a steady theory such a BEMT. The dynamic of the induction is captured inherently by the strength and positions of the vortex lines, and BEMT models such as tip loss, corrections for high inductions, skewed wake or dynamic inflow are not needed any more. However the viscous 2-D polars are still needed, and viscous effects such as rotational stall delay or dynamic stall are not accounted for, thus still need modeling. The impulsive term of the unsteady attached flow behavior are not capture either as the blade boundary surface is not modeled. Gaertner [62] included a dynamic stall model in a lifting line code.
The common application cases are the situations for which the BEMT is known to rely on its empirical models such as skewed wake or dynamic inflow models. Assymetric pitch default events [86], large yaw misalignment [156][95] , extreme wind shear [22], half wake situations [85] or floating wind turbines [174] are typical application of lifting lines codes.

3.2.3 Vortex panel method

This section mainly describes the code from Dixon [44], and thus the panel code ARDEMA presented in next chapter. In panel methods, the blade surface is modeled with surface distribution of singularities called panels. The wake here is also considered and modeled with panels. However steady panels code exists such as Xfoil [46], in which case the wake is not modeled.
The Laplace equation implies that the flow is linear. Thereafter, the flow equations can be set in an integral form. The idea behind singularity method (or *Boundary Element Method*, BEM) is that finding boundary values into the integral equation is enough to calculate numerically the solution directly at any desired point in the interior of the fluid domain. As the fluid model satisfies a linear equation, the boundary values can be constructed as a linear combination of elementary solutions of the flow equations. In the panel method the flow can be calculated using the linear combination of the induced perturbations of each panels. The same idea lies in the lifting line model, however no specific treatment of boundary conditions needs to be applied as the strength of each element is known directly thanks to the Kutta-Joukovski relation.

The Laplace equation is defined at a domain $\mathbf{R}$ that typically is unbounded (exterior problem). It is however bounded to the inside by the blade surface $\partial\mathbf{R}$ (boundary of $\mathbf{R}$).

Boundary conditions

By applying the Dirichlet boundary condition to the solution of a Laplace equation for a point inside the blade, the following equation is obtained (see [44] for more details):

$$\Phi_i(x) = \frac{1}{4\pi}\int\limits_{S_B}\left[\sigma_b\frac{1}{r} - \mu_b\frac{\partial}{\partial n}\left(\frac{1}{r}\right)\right]dS + \frac{1}{4\pi}\int\limits_{S_W}\left[\mu_w\frac{\partial}{\partial n}\left(\frac{1}{r}\right)\right]dS = 0 \tag{3.44}$$

where Φ_i is the interior potential, S_B is the blade surface, S_W the wake surface, r the distance from the elementary surface dS to the considered point x and n the surface normal direction. In this case, the potential distribution chosen to represent this solution is based on a source and doublet surface distribution to model a wall, and a doublet surface distribution for the wake as illustrated in Fig.3.13. The

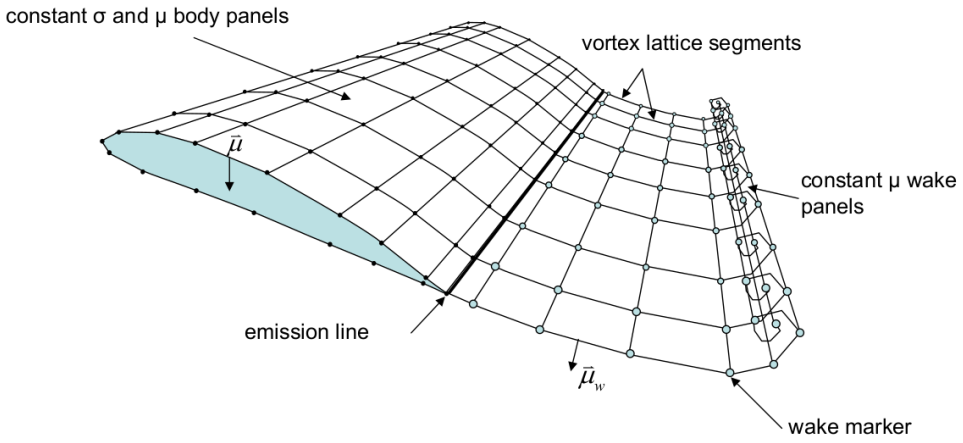

Figure 3.13: Panneling of the blade and wake - [44]

source distribution of strength σ_b ensures the non-penetration of the flow in the blade while the doublet distribution of vorticity μ_b is needed for the creation of circulation around the body, and thus lift. The wake panels strength is μ_w. This type of distribution is chosen by Dixon [44] to model the blade wall and the wake. This equation is obtained with the assumption the constant potential interior to the blade is equal to the potential very far from the blade Φ_∞ and set to zero in a fixed inertial frame. This boundary

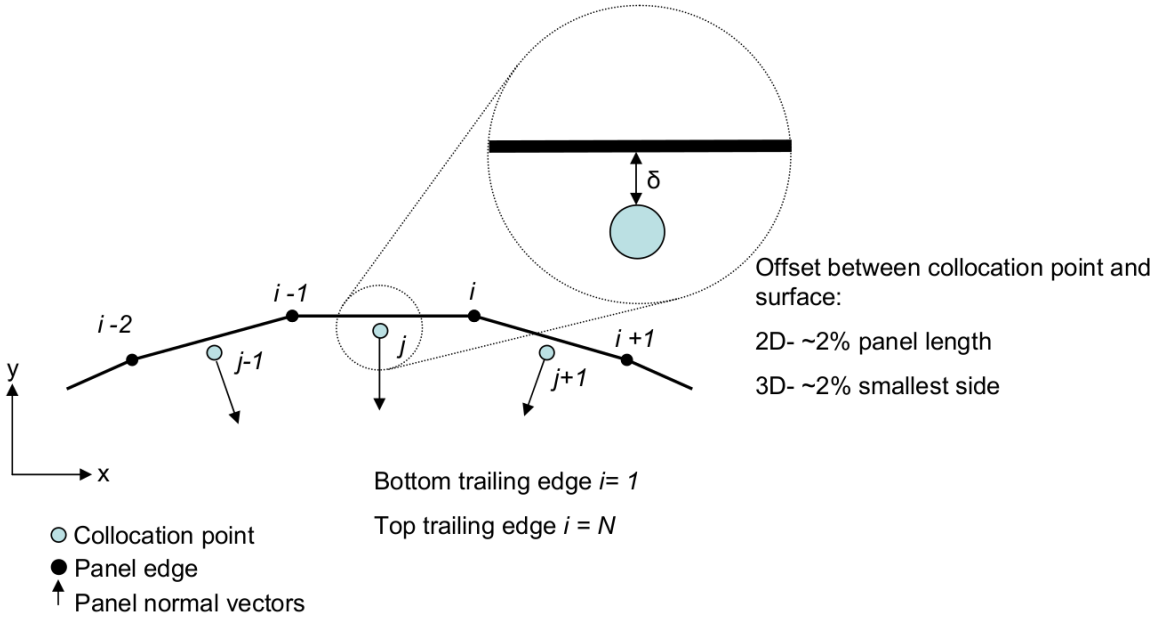

Figure 3.14: Collocation point - [44]

condition is applied at the *collocation point* very close to the panel surface as illustrated in Fig 3.14. The Neumann boundary condition of the Laplace equation is:

$$\frac{\partial \Phi}{\partial n} + u_n = \overrightarrow{n} \cdot (\nabla \Phi + \overrightarrow{u}_{motion}) = 0 \tag{3.45}$$

where u_n is the projection of the velocity $\overrightarrow{u}_{motion}$ in the normal direction. The velocity $\overrightarrow{u}_{motion}$ contains the wind velocity, the panel motion and the induced velocities of the wake (without near wake pannel). The Neumann boundary conditions ensures the no-penetration of the fluid in the blade.
By definition the source strength σ (see Katz and Plotkin [102] for more details) is defined in the case of a constant interior potential by:

$$-\sigma = \frac{\partial \Phi}{\partial n} \tag{3.46}$$

By combining Eq. 3.45 and 3.46, the strength of the source doublet panels is known. Two mains assumptions are hidden by such results:

- The doublet and source terms from Eq. 3.44 can be decoupled
- Each source panel has no influence on the others

At an infinite distance from the singularities, the boundary condition is:

$$\nabla \Phi_\infty - \overrightarrow{V}_0 = \overrightarrow{0} \tag{3.47}$$

where $\overrightarrow{V}_0$ is the freestream velocity.

AIC matrices

At this stage, the strength of source panels is known. The position and strength of the wake panels (apart from the first wake pannel called *near wake panel*) is also known from the previous time steps. The strength of the blade doublet panels is then obtained with the Dirichlet boundary condition. In discretized form and with Einstein notation, the Dirichlet boundary condition becomes for each collocation point i:

$$A_{ij}\mu_{b,j} + B_{ij}\sigma_{b,j} + C_{ik}\mu_{w,k} = 0 \tag{3.48}$$

where i and j indices are looping over the number of blade panels and k is looping over the number of wake panels. This simplification of Eq. 3.44 is possible assuming constant strenght of source and doublet- panels. Higher order panels complexify the integration of the different terms from Eq. refeq:dirichlet. The A_{ij}, B_{ij} and C_{ik} coefficients represent the *Aerodynamic Influence Coefficients* (AIC) of the blade doublet, blade source and wake doublet panels respectively. They are only dependent of the geometry and positions of all panels respectively to each other. They are the coefficients of the so-called *AIC matrices*. The near wake panels strength are creating more unknows than the number of equations, and another hypothesis is required to solve the system.

Kutta condition

The Kutta condition states that the velocity at the trailing edge should be finite. A simple way to ensure such condition is to set the vorticity at the trailing edge to zero. As the trailing edge the vorticity is the sum of the strenght of the near wake panel, bottom and top trailing edge pannels, the following relation is thus obtained:

$$\mu_{top} - \mu_{bottom} = \mu_{wake} \tag{3.49}$$

The direction and length of the near wake panel are subject to multiple possibilities. In the ARDEMA code, the bisector of the top and bottom trailing edge panels is chosen for the direction and the near wake length is set to 25% of the convected length during one time step.
The wake is then considered the same way as in the lifting line theory with free wake presented above. The doublet/vortex ring equivalence is useful to switch from one model to another: a surfacic doublet distribution is equivalent to a vortex panel which strength is the derivative of the doublet distribution plus a vortex ring of strength equal to the doublet strength. In the case of constant doublet panel, only the vortex ring is to consider as the doublet strength gradient is zero. Depending on the calculations needed, doublet panels or vortex rings can be used.

3.2.4 Handling viscous flows in panel methods

The assumptions of panel methods imply that viscous effects are not directly taken into account but modeled through vorticity. However, specific flow features can not be modeled with the models presented above:

- Panel method does not require polar data but the forces obtained are inviscid forces. This implies that the stall is not captured for example. For lifting line however the forces on the blade are based on 2-D viscous polars and the emitted wake strength is thus based on viscous forces.
- Flow separation is not considered, and the Kutta condition is always applied at the trailing edge. In reality, after stall a second vorticity emission should be considered on the blade surface due to the shear layer starting at the separation point.
- Dynamic stall phenomenon, that involves the separation point prediction.

Some models to model such flows are introduced below.

3.2.4.1 Viscous boundary layer coupling

The Navier-Stokes equations including viscosity can be simplified near the wall to compute the boundary layer flow. By coupling these equations to a panel method, the viscous forces can be obtained. The steady code Xfoil [46] is a well know example of panel method with viscous boundary layer coupling. This method offers reliable results in attached conditions and is able to give good estimation of the stall angle and maximum lift. However after stall the code is not reliable as the flow is separated and the boundary layer simplified equations hypothesis does not hold in such cases. The Rfoil code [201] is a modified version of Xfoil more suitable to wind turbine aerodynamics. 3-D rotationnal effects are obtained by modifying the original Xfoil boundary layer equations, and other modifications improve the results for thick airfoils and around stall compared to Xfoil. Some recent modifications to Rfoil have been propose by Ramanujam [160] in order to improve stall prediction for thick airfoils.
The work of Ramos-Garcia is also remarkable as it combines a 3-D free wake panel method with a quasi 3-D viscous boundary layer formulation [162] [163]. Full unsteady rotor simulations are then achievable without using viscous 2-D polar data.

3.2.4.2 Double wake

A main limitation of the standard panel method appears in stalled flows. In such cases, the flow separates in two points: at the trailing edge and at the separation point on the suction side of the airfoil. Both

separation points generate vorticity, and the Kutta condition is not giving enough information to predict the emitted vorticity at both points. In double wake models, the vorticity is emitted both at the trailing edge and at the separation point, generating two distinct wake sheets. This implies that the separation point must be correctly predicted, either by empirical laws or by using a boundary layer coupling. The strength of both emitted vorticities requires specific handling. Several implementations of such solutions in 2-D have been found in litterature [209] [161][200] with a boundary layer coupling. Riziotis also includes a dynamic stall model [166]. No 3-D implementation has been found in literature.

3.2.4.3 With viscous polar data

Another solution consists in using polar data to correct the inviscid forces computed by the panel method. The correction can be applied on the blade forces and also on the wake based on the calculation of reduction factors. This model has been used in ARDEMA, and will be detailled in Chapter 4.

3.3 CFD: Computational Fluid Dynamics

3.3.1 Introduction and general equations

In the singularities methods presented above, the Laplace equations is a particular form of the mass conservation equation which can be solved easily in a way that the knowledge of the potential only at the boundaries is enough to obtain the flow in the wall domain analytically. This kind of method is also called a *grid free method* as it does not require to divide the flow domain into many sub-domains. On the opposite, The Computational Fluid Dynamic methods involve the solving of the Navier-Stokes equation in a discretized form of the whole flow domain. The advantage of such method is to include all the intrinsic physics of turbulent flows such as non-linear and viscous effects. The flow is no longer irrotational, the Laplace equation is not valid anymore and the non-linear momentum equation has no direct solution for a general flow. The idea is then to solve the equations numerically by discretizing the flow domain into a grid called *mesh*, and to integrate the conservation equations onto each elementary volume (or cell). Such methods are then called Finite Volume Methods. The integration of conservative transport equations leads to the computation of fluxes on the volume boundaries which imply relations between the variables of one cells and the adjacent cells. Then, by using specific boundary conditions to the flow domain, the flow can be solved in the whole domain through iterative processes (to handle non-linearity) and large matrix inversion. Comparatively to grid free methods, the CPU time needed is much larger as the flow in the whole domain is solved instead of being solved in specific chosen points. The Navier-Stokes equations are given below using Einstein convention for indices. The mass conservation gives:

$$\frac{\partial \rho}{\partial t} + \frac{\partial \rho u_i}{\partial x_i} = 0 \tag{3.50}$$

And the momentum equation:

$$\frac{\partial \rho u_j}{\partial t} + \frac{\partial \rho u_i u_j}{\partial x_i} = -\frac{\partial p}{\partial x_j} + \frac{\partial \tau_{ij}}{\partial x_i} \tag{3.51}$$

For a Newtonian fluid, the viscous stress tensor τ_{ij} can be expressed with the following relation:

$$\tau_{ij} = \mu\left(\frac{\partial u_i}{\partial x_j} + \frac{\partial u_j}{\partial x_i}\right) - \frac{2}{3}\mu\frac{\partial u_k}{\partial x_k}\delta_{ij} \tag{3.52}$$

where μ is the dynamic viscosity of the fluid δ_{ij} is the Kronecker symbol. This section is a brief introduction to CFD and in particular to some models implemented in the LES code YALES2 [138] developed at CORIA laboratory and used in Chapt. 5. More information about numerical methods for CFD can be found in the book of Ferziger and Perić [55], while the book of Pope [154] is a reference regarding the different approaches for modeling turbulence in CFD.

3.3.2 Different methods for handling turbulence

A flow is considered as turbulent when it is dominated by fluctuations of the fluid velocity of different length and time scales. On the opposite a laminar flow has an uniform distribution of velocity. When applied to a boundary layer flow, these definitions correspond to the turbulent and laminar boundary layers described in Chapter 2.1.3. The Reynolds number defined in Eq. 2.4 quantifies the balance between the kinetic forces and the viscous forces. For small values of Re, the flow is laminar and dominated by viscous effects. The flow perturbations are damped by the molecular viscosity and the trajectory of fluid particles follow a mean trajectory. For high Re number like the ones considered for wind turbine applications, the flow is turbulent. The kinematic forces are then stronger than the viscous forces and the molecular viscosity does not damp small velocity perturbations which thus destabilize the flow. The flow is chaotic and characterized by a large range of spatial and temporal 3D structures. The transfer of kinetic energy among these structures has been theorized by Richardson and Kolmogorov in the first half of the 20th century. Several range of structures are identified based on their kinetic energy and their characteristic length as illustrated in Fig.3.15. The turbulent energetic spectrum is plotted against the wave number which is inversely proportional to the characteristic length of the vortices. The kinetic energy is produced at the *integral scale* l_t. These large structures tend to break into several smaller vortices, transferring their kinetic energy to smaller scales in the *inertial range*. This process is repeated up to the so-called *Kolmogorov scale* l_K where the kinetic energy is dissipated into heat because of the molecular viscosity. From a modeling point of view, the different approaches for handling turbulence are also represented in Fig.3.15 and are further detailed in the next sections.

3.3.2.1 DNS

In Direct Numerical Simulation (DNS), all the turbulent scales of the flow are resolved. The Navier-Stokes equations in the discretized form 3.50 and 3.51 are then solved under the assumption that the cells are small enough to capture correctly the continuous flow behavior. No modeling (excepted the intrinsic modeling introduced by the Navier-Stokes equation themselves) is required, and the only errors are caused by the representation of the domain in a discretized form. The main issue of this type of approach is the very high CPU time needed to solve real problems. For example in aerodynamics, the high Reynolds number and the wall bounded flow imply that many scales of turbulence are significant in the flow. Solving all these scales is impossible even with the modern supercomputers and for this reason DNS is mainly used for academic test cases at lower Reynolds number.

3.3.2.2 RANS and URANS methods

The Reynolds-Averaged Navier-Stokes (RANS) equations are obtained by decomposing the flow variables into two components, a statistical averaged value and a fluctuating value. For the velocity:

$$u_i = \langle u_i \rangle + u_i' \tag{3.53}$$

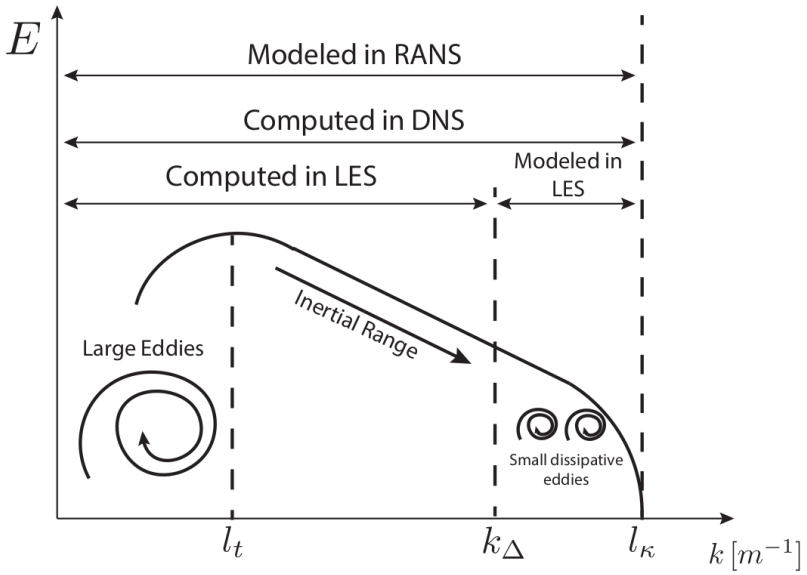

Figure 3.15: Turbulent energy spectra resolution with DNS, LES and RANS - [94]

with $\langle u_i \rangle$ the averaged velocity and u_i' the fluctuating velocity. By introducing this formulation for all variables (with constant fluid properties such as density ρ) in both Eq. 3.50 and 3.51 and by applying the averaging operator, the RANS equations are obtained:

$$\frac{\partial \rho \langle u_i \rangle}{\partial x_i} = 0 \tag{3.54}$$

$$\frac{\partial \rho \langle u_j \rangle}{\partial t} + \frac{\partial \rho \langle u_i \rangle \langle u_j \rangle}{\partial x_i} = -\frac{\partial \langle p \rangle}{\partial x_j} + \frac{\partial \langle \tau_{ij} \rangle}{\partial x_i} - \frac{\partial (\rho \langle u_i' u_j' \rangle)}{\partial x_i} \tag{3.55}$$

These equations are solved instead of Eq. 3.50 and 3.51. The additional term $-\rho \langle u_i' u_j' \rangle)$ is the Reynolds stress tensor. The turbulence modeling in RANS consists in formulating the Reynolds tensor in a way that the equations above can be solved numerically.
By substituting Eq. 3.55 to the fully developed Navier-Stokes equations with Reynolds decomposition, the same form of equations can be obtained for the fluctuating variables, with some additional terms. This later form is then useful for obtaining the turbulent kinetic energy equation which is not detailed here. By essence, RANS can only compute steady flows and the turbulence is thus entirely modeled.

3.3.2.3 LES and its derivatives

In Large-Eddy Simulation (LES), part of the turbulent spectrum is solved (the "large" eddies) while the smallest vortices are modeled: LES acts like a low-pass filter for turbulence. This is achieved by applying a spatial filtering to the Navier-Stokes equations different from the RANS filtering which is based on statistical averaging. A variable ϕ can be decomposed into:

$$\phi(t,x) = \overline{\phi}(t,x) + \phi''(t,x) \tag{3.56}$$

The filter variable $\overline{\phi}(x,t)$ and $\phi''(t,x)$ thus do not have the same meaning than for RANS averaging. $\overline{\phi}(x,t)$ is representative of the turbulence scales larger than the filter size Δ, and $\phi(t,x)''$ of the smaller

scales. For a fluid with uniform density and incompressible, the continuity equations for mass and momentum including the above decomposition can be simplified by applying the spatial filtering and neglecting specific terms:

$$\frac{\partial \overline{u}_i}{\partial x_i} = 0 \tag{3.57}$$

$$\frac{\partial \overline{u}_j}{\partial t} + \frac{\partial \overline{u}_i \overline{u}_j}{\partial x_i} = -\frac{1}{\rho}\frac{\partial \overline{p}}{\partial x_j} + \frac{1}{\rho}\frac{\partial \overline{\tau}_{ij}}{\partial x_i} - \frac{\partial}{\partial x_i}[\overline{u_i u_j} - \overline{u}_i \overline{u}_j] \tag{3.58}$$

In a similar way as for the RANS equations, a sub-grid stress tensor can be identified as $\tau''_{ij} = -\rho(\overline{u_i u_j} - \overline{u}_i \overline{u}_j)$, and the turbulence modeling in LES consists in proposing formulations for the sub-grid stress tensor based on the filtered variables of the above equations. The main advantage of LES over RANS method is its intrinsic capacity to capture many turbulent features, however at a higher CPU cost than RANS. Furthermore the sub-grid-scale (SGS) turbulent structures are more suited for modelling because of their universal behavior whereas larger scale structures are more dependant on the geometry and boundary conditions. Approaches combining RANS and LES such as Detached Eddy Simulation [184] (DES) have been formulated in order to take benefit from both models which is particularly useful for high Reynolds flows. Most often, these formulations use RANS equations near the wall where the turbulent structures are very small and would require a huge number of cells to be properly resolved, and LES equations far from the wall.

3.3.3 LES sub-grid scale modeling

Most of the sub-grid stress models are based on the Boussinesq hypothesis which suggests that the sub-grid stress tensor can be formulated like the viscous stress tensor by using an additional viscosity term called *turbulent viscosity* $\nu_t = \mu_t/\rho$ such as:

$$\tau''_{ij} = \mu_t\left(\frac{\partial \overline{u}_i}{\partial x_j} + \frac{\partial \overline{u}_j}{\partial x_i}\right) - \frac{2}{3}\mu_t \frac{\partial \overline{u}_k}{\partial \overline{x}_k}\delta_{ij} \tag{3.59}$$

The sub-grid scale turbulence models in LES are formulations for ν_t. In the next sections, models implemented in the LES code YALES2 used in Chapter 5 are presented.

3.3.3.1 Smagorinksy model

The classical Smagorinsky model [180] considers an equilibrium between the creation and the dissipation of kinetic energy at the filter scale Δ, with the following formulation for ν_t:

$$\nu_t = (C_S \Delta)^2 \sqrt{2\overline{S}_{ij}\overline{S}_{ij}} \tag{3.60}$$

with C_S the Smagorinsky constant, Δ the filter size proportional to the grid size and $\overline{S}_{ij}$ the filtered deformation tensor:

$$\overline{S}_{ij} = \frac{1}{2}\left(\frac{\partial \overline{u}_i}{\partial x_j} + \frac{\partial \overline{u}_j}{\partial x_i}\right) \tag{3.61}$$

The usual values used for the constant C_S are in the range $[0.1 - 0.2]$. The main known limitations of the Smagorinsky model are a too dissipative behavior and a poor handling of the turbulence near walls.
The dynamic Smagorinksy model from Germano [65] and Lilly [115] suggests to modify the constant C_S locally and in time. The constant is then determined by applying a second spatial filter at the scale of

the smallest resolved structures, which is larger than Δ, and by using the two differently filtered velocity fields. The model is more costly to use, but gives better results for a wide range of applications.

3.3.3.2 WALE model

The WALE (*Wall-Adapting Local Eddy-Viscosity*) model from Nicoud and Ducros [143] proposes a better handling of the turbulence near walls. Indeed, the Smagorinsky model is based on the assumption of isotropic turbulence which is not valid in sheared flows such as wall flows. This implies a poor prediction of the laminar turbulent transition for example. The formulation for the turbulent viscosity is:

$$\nu_t = (C_w \Delta)^2 \frac{(s_{ij}^d s_{ij}^d)^{3/2}}{(\overline{S}_{ij}\overline{S}_{ij})^{5/2} + (s_{ij}^d s_{ij}^d)^{5/4}} \tag{3.62}$$

where C_w is a constant with a recommended value of 0.5 and s_{ij}^d is defined by:

$$s_{ij}^d = \frac{1}{2}(\overline{h}_{ij} + \overline{h}_{ji}) - \frac{1}{3}\overline{h}_{kk}\delta_{ij} \tag{3.63}$$

with $\overline{h}_{ij} = \overline{g}_{ik}\overline{g}_{kj}$ and $\overline{g}_{ij} = \frac{\partial \overline{u}_i}{\partial x_j}$. By using the tensor s_{ij}^d instead of $\overline{S}_{ij}$ in its formulation, this model can consider rotation and strain rates thus all turbulent structures are considered for dissipation. Furthermore it can be shown that the turbulent viscosity μ_t tends to zero in sheared flows with this formulation which is the expected behavior for the near-wall zones. This behavior is also favorable for a good prediction of the laminar turbulent transition.
For both the Smagorinsky and the WALE models, the filtered velocity field is then directly used for computing the turbulent viscosity.

3.3.4 Wall models for LES

Resolving the near-wall flow can be quite a challenge at high Reynolds numbers. Indeed, the turbulent boundary layer (see Chapt. 2.1.3 for the laminar and turbulent boundary layer definitions) is very thin compared to the flow domain dimensions which requires to have a large number of cells to solve it correctly. For wind turbine typical Reynolds number of several millions, solving the boundary layer with LES would require a huge number of CPU hours. Choi and Moin [38] estimated the minimum grid size for resolving the full flow around an airfoil at a given Reynolds number, with a number of cells proportional to $Re^{13/7}$. In order to perform simulations with a realistic grid size, a specific modeling of the flow near the boundary layer can be performed involving a wall law. Such simulations are called wall-modeled LES (WMLES), and the estimated grid requirement for such cases is a grid size proportional to Re. A state-of-the-art of the different wall models developed for LES along the years has been proposed by Larsson [108]. Larsson identifies three different flow zones affected by the wall as illustrated in Fig. 3.16: the inner layer, the outer layer and the detached shear layer much further from the wall. The closest zone to the wall is the inner layer in which the viscous forces dominate the flow. Larsson differentiates in three groups the several modeling techniques used to reduce the CPU time needed for computing wall flows. The first group includes the original DES from Spalart [184] and is not considered by Larsson as a WMLES because it does not solve the outer boundary layer. The two other groups are considered as WMLES because they solve the outer layer. In wall-resolved LES, all three layers are solved. The first WMLES group considers all techniques involving an hybrid RANS/LES approach where RANS is used up to a certain distance of the wall while LES is used in the outer region and further. The second

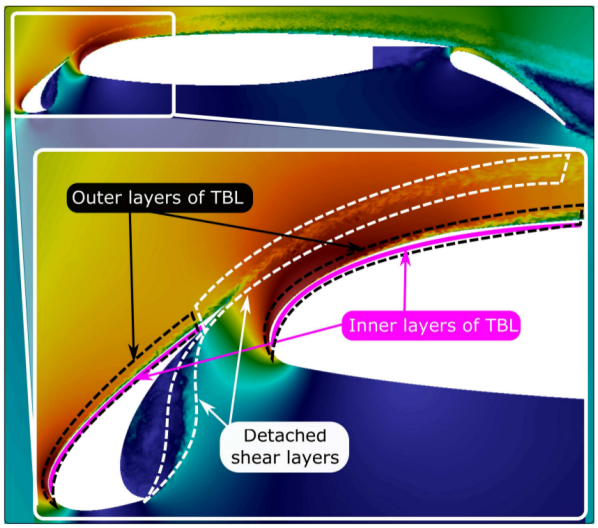

Figure 3.16: Instantaneous flow field around an airfoil and identification of the different boundary layer zones - [108]

WMLES group defines wall-stress models for which RANS equations are also considered near the wall but only to feed the LES model through the wall shear stress.
The different near wall regions of a turbulent boundary layer are also illustrated in Fig. 3.17. On the left part, the velocity profile is represented along with the different regions. The wall shear stress τ_w is used to define the friction velocity $u_\tau = \sqrt{|\tau_w|/\rho}$ and the non-dimensional wall distance $y^+ = u_\tau y/\nu$. The non-dimensional velocity profile $u^+ = u/u_\tau$ is then represented in the right part as a function of y^+. In the viscous sublayer, the viscous forces are much larger than the kinetic forces, and it can be demonstrated that u^+ evolves linearly with y^+. In the buffer zone, the viscous and kinetic forces have the same order of magnitude. Then in the log zone, kinetic forces are more important and it has been observed that u^+ evolves linearly with $log(y^+)$.

The Thin Boundary Layer (or TBL) equations are mostly used to explain such velocity profile. The incompressible Navier-Stokes equations under the assumption that the horizontal length scales are much greater than the wall-normal scales become:

$$\frac{\partial u_j}{\partial t} + \frac{\partial u_i u_j}{\partial x_i} = -\frac{1}{\rho}\frac{\partial p}{\partial x_j} + \frac{\partial}{\partial y}\left[(\nu + \nu_t)\frac{\partial u_j}{\partial y}\right] \tag{3.64}$$

The equation stands for the LES filtered velocity, and is assumed to be equivalent to the Reynolds averaged velocities close to the wall. The turbulent viscosity ν_t is a RANS turbulence model for closing the Reynolds stress tensor. This model has little impact in the viscous sublayer as the Reynolds stress tensor is negligible compared to viscous forces (see Fig. 3.17), but is significant in the log-law region. The full TBL equations can be solved numerically but this requires to either have a refined grid at the wall or to create a second dedicated grid in addition to the LES grid [14][20]. In order to avoid such procedure, the TBL equations can be simplified and solved algebraically. The simpliest way consists in assuming an equilibrium between the convection term and the pressure gradient term. Such models are called *equilibrium* models. If other terms are retained, the model is then called a *non-equilibrium* model. The two next sections focus on the classical equilibrium log-law model as proposed by Cabot [27] and on the Duprat non-equilibrium wall model [49]. Those two models are implemented in YALES2 code.

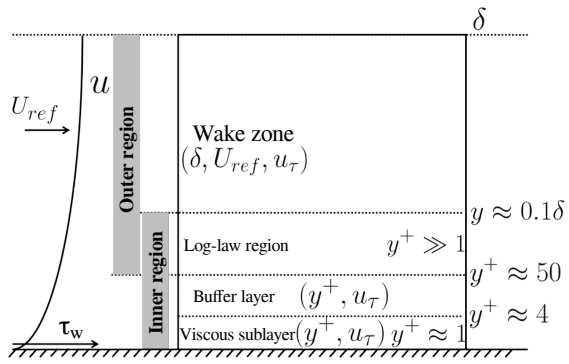

(a) Boundary layer regions

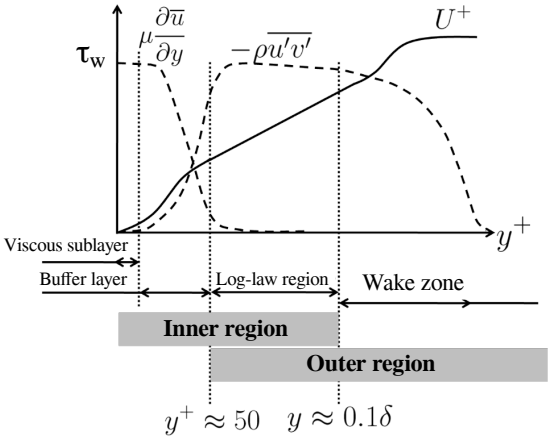

(b) Scheme of mean velocity profile - Viscous and turbulent contributions to shear force

Figure 3.17: Wall flow regions - Adapted from [19]

3.3.4.1 Log-law model

The equilibrium model implemented in YALES2 code is based on the simple LW0 model from Cabot [27][28]. The time derivative, convective and pressure gradients terms are neglected in Eq. 3.64. By integrating this simplified equation in the wall-normal direction and using the previously introduced non-dimensional variables, the following relation can be derived:

$$\frac{\partial u^+}{\partial y^+} = \frac{\text{sign}(\tau_w)}{1 + \nu_t/\nu} \tag{3.65}$$

with τ_w the wall shear stress $\tau_w = \rho\nu \left(\frac{\partial u}{\partial y}\right)_{y=0}$. The formulation for ν_t introduces the distance to the wall:

$$\nu_t = \kappa y^+ \nu \left[1 - \exp(-y^+/A^+)\right]^2 \tag{3.66}$$

With $\kappa \approx 0.40$ the Von Kármán constant and $A^+ = 17$ a damping constant. This set of equations can be solved with a Newton-Raphson algorithm in order to determine τ_w. This wall law is able to handle the viscous sublayer and the log-law behaviors.
In YALES2 implementation, the velocity and distance considered are the ones of the first fluid near-wall nodes and the constants have slightly different values than in the original publications: $\kappa = 0.42$ and $A^+ = 18$.

3.3.4.2 Duprat model

The Duprat [49] model includes the streamwise pressure gradient term which implies to introduce new non-dimensional variables for the wall distance y and the flow velocity u:

$$y^\star = \frac{y u_{\tau p}}{\nu}, \qquad u^\star = \frac{u}{u_{\tau p}} \qquad \text{where} \qquad u_{\tau p} = \sqrt{u_\tau^2 + u_p^2} \quad \text{and} \quad u_p = \left|\frac{\nu}{\rho}\frac{\partial p}{\partial x}\right|^{1/3} \tag{3.67}$$

This wall law is thus better suited for airfoils as the streamwise pressure gradient is not negligible on curved walls. The parameter α_D is used to quantify the magnitude of shear stress relatively to streamwise

pressure gradient:

$$\alpha_D = \left(\frac{u_\tau}{u_{\tau p}}\right)^2 \in [0,1] \tag{3.68}$$

The integrated TBL equation then becomes:

$$\frac{\partial u^\star}{\partial y^\star} = \frac{\mathrm{sign}(\frac{\partial p}{\partial x})(1-\alpha_D)^{3/2} y^\star) + \mathrm{sign}(\tau_w)\alpha_D}{1+\nu_t/\nu} \tag{3.69}$$

The associated turbulence model is defined by:

$$\nu_t = \kappa y^\star \nu \Big[\alpha_D + y^\star (1-\alpha_D)^{3/2}\Big]^\beta \Big[1 - \exp\big(-y^\star/(1+A\alpha_D^3)\big)\Big]^2 \tag{3.70}$$

with β a constant equal to 0.78 and $A = 17$. It is interesting to notice than in the case of a negligible pressure gradient, $\alpha_D = 1$ and the equations 3.69 and 3.70 are similar to the equilibrium log-law model presented earlier.

The YALES2 implementation uses a bisection method to determine α_D which requires a non negligible CPU time. In order to reduce the CPU time needed, a tabulated version [122] of the Duprat wall law is also implemented in YALES2 code.

Chapter 4

From section to rotor: a panel method for viscous flows

Contents

4.1 ARDEMA: a panel method code

This chapter focuses on the comparison of an in-house panel method to a state-of-the-art BEMT solver. The main features of this in-house code *ARDEMA* are first presented. The work of this PhD relative to ARDEMA mainly consists in the integration of a dynamic stall model, its validation and the assessment of its influence on realistic engineering cases. Thus, the coupled aero-servo-elastic code is also briefly presented. After a validation of the calculation chain from dynamic stall to fully coupled code, challenging cases of yawed turbines are investigated in order to determine the influence of both BEMT and panel method on specific loads.

4.1.1 General equations and numerical setup

ARDEMA is a panel method based on Dixon master thesis [44]. A free panel wake is emitted at each time step from the blade body. The blade are modeled base on a source/doublet distribution and the wake with vortex rings. The blade consists of both source panels and vortex rings. Two core models are implemented for desingularization of the vortex rings, the Rankine and Lamb-Oseen models (see Dixon's master thesis [44] for more information). The Lamb-Oseen model is used in the presented calculations. The near wake length is set to 0.25 based on Katz and Plotkin recommendations [102]. No core growth nor stretching models are implemented in the code. The time marching scheme for the position of the wake panels is a first order Euler scheme.
The paneling of the blade is based on the definitions of blade sections. Each section has a local coordinate system, and the meshing of the surface is done accordingly to this reference frame and connectivity between two sections. For most of the study, 60 panels are used to describe one airfoil, with a cosine distribution in order to increase the number of panels at the leading edge where the pressure gradients are the largest. The panel strength is piece-wise constant for both the blade and wake (no high-order elements).
The code is developed in a Matlab environnment. In order to gain speed, the calculation of induced velocities is performed on GPU via CUDA functions. The AIC matrices (see Chapt. 3.2.3) inversion uses OpenMP parallelization. A typical 10-min HAWT simulation is done in around 12 hours on dedicated GPU cluster.

4.1.2 From 3D to 2D: Angle of Attack (AoA) and velocities estimations

The angle of attack (AoA) is a concept mainly created to investigate the effect of the pitch orientation of an infinitely long wing on its aerodynamic characteristics. It is particularly meaningful for a static thin airfoil tested in wind tunnels. The usual definition of the AoA is the angle between the chord line and the relative flow direction. But since the flow is altered by the presence of an airfoil, the general idea is to choose the relative local flow direction without the influence of the airfoil. In other terms, the flow direction is then represented by the motion velocity (in case of a moving wing in static fluid) or the free stream velocity (in case of a static wing in moving fluid). Although very useful, this concept is more ambiguous in configurations that differ from wind tunnel ones, where the definition of the free stream velocity is unclear. For example, when the flow is curved or in three-dimensional cases. Different techniques exist to extend the concept of AoA in more complex cases. For wind turbines, this issue is still an active field of research [159] [72] [89]. The following paragraphs detail the methods integrated in ARDEMA to get the AoA for the elements. The first method is based on the calculation of the velocity vector. The two other methods are based on the use of tabulated inviscid lift coefficients.

4.1.2.1 AoA from velocity vector

The first method consists in applying the definition strictly by getting the angle between the chord line and the relative velocity vector at the airfoil's location as if there was no airfoil. There are many questions arising from this, in particular:

- What components the velocity is composed of.
- How to get a flow direction without considering the airfoil influence.

- How to select the point where the velocity is computed.

Regarding the first point, the process to go from a 2D notion of AoA to a 3D one also gives rise to the question of the treatment of the spanwise flow. In ARDEMA, the relative flow velocity vector is projected onto the element/section plane. It is worthwhile to recall that the projection is done onto the element/section plane, and not on a plane orthogonal to the spanwise direction. The two planes can differ in case of a swept wing. The way a wing or a blade is sliced into several sections has a significant influence on the projection of the velocity. This choice has consequences on the aerodynamic properties since the AoA can be affected, as well as the velocity magnitude used to calculate the coefficients.

Regarding the airfoil influence, it is important to recall that in a vortex flow method the flow equation system is linear and the superposition principle applies. The local flow velocity (see Fig. 2.25) is computed as the sum of the flow velocity (i.e. motion of the airfoil + wind velocity) and some perturbation velocities (i.e. induced velocities by the wake and by the bodies). The problematic part is the induced velocity. The airfoil is responsible of two induced velocities: the one created by its emitted wake and the flow perturbation caused by the airfoil itself. Removing both of these induced velocities would lead to serious inaccuracy in the calculation of the AoA. A compromise has to be found regarding which influence should be kept. In the version implemented in ARDEMA, the induced velocity includes the full wake induced velocity (all the wake panels are considered). The body induced velocity is not supposed to be considered as we aim to be in a case "as if there was no airfoil", but some of its contribution is necessary anyway: the wake is attached to the trailing edge and the edge the wake sheet shares with the airfoil comprises a vortex that is fully compensated by the circulation around the airfoil through the Kutta condition. If the airfoil is removed, a strong vortex would exist at the edge of the wake sheet. The solution used in ARDEMA is to replace the wing/blade elements by incomplete lifting lines (see 3.2.2). A 3D lifting line is generally composed of a bound vortex at quarter chord point, two side vortex segments and a vortex segment at the trailing edge, such that the lifting line forms a closed path to satisfy the Helmholtz's second theorem. The vortex system used in ARDEMA is incomplete in the sense that only the bound vortex is removed, leaving the lifting line as an open contour violating the Helmholtz's second theorem. This methodology has shown to give concrete results. To summarize, the AoA is computed as:

$$\alpha = \arctan\left(\frac{\overrightarrow{U}_{\perp} \cdot \overrightarrow{e_n}}{\overrightarrow{U}_{\perp} \cdot \overrightarrow{e_t}}\right) \tag{4.1}$$

Where:

- $\overrightarrow{e_t}$ is the unit vector tangent to the element's chord line,
- $\overrightarrow{e_n}$ is the unit vector normal to the element's chord line and to the span,
- $\overrightarrow{U}_{\perp}$ is the relative flow velocity projected onto the section/element's plane, defined as $\overrightarrow{U}_{\perp} = \left(\overrightarrow{U} \cdot \overrightarrow{e_n}\right)\overrightarrow{e_n} + \left(\overrightarrow{U} \cdot \overrightarrow{e_t}\right)\overrightarrow{e_t}$ with $\overrightarrow{U} = \overrightarrow{U}_{\infty} - \overrightarrow{U}_{motion} + \overrightarrow{U}_{ind,wake} + \overrightarrow{U}_{ind,LLT}$ where $\overrightarrow{U}_{\infty}$ is the wind velocity, $\overrightarrow{U}_{motion}$ the motion velocity, $\overrightarrow{U}_{ind,wake}$ the velocity induced by the wake and $\overrightarrow{U}_{ind,LLT}$ the velocity induced by the lifting line model without the bound vortex.

The velocity vector is computed at a reference point specified by the user to be representative of the airfoil as a whole. Indeed, the notion of free stream velocity is not trivial either, in the sense that in case of rotating motions or in turbulent inflow wind, the flow perceived by an airfoil is curvy. The orientation

is thus dependent on the selected point of reference. The idea is to select a point which is representative of the airfoil as a whole, since the AoA is meant to be "at the airfoil's location". Several points are relevant:

- *The quarter chord point*: For a thin airfoil, the forward quarter chord point is an important reference point. It is both the location of the aerodynamic center and the location of the vortex line system when the airfoil is replaced by a lifting line.
- *The three-quarter chord point*: For a thin airfoil, analytical models show that the lift coefficient is directly proportional to the AoA at three-quarter chord point in case of vertical-translation oscillations. This means that taking the AoA at the three-quarter chord point is representative of the aerodynamic behavior of the airfoil in a specific curved flow and often called the rear aerodynamic center.
- *The attachment point*: The attachment point is the mounting point, along which the twist is usually applied. This is a worthy point of interest.
- *The centroid*: The centroid is the average position of all the points in the shape of the airfoil. From a geometric point of view, this can be representative of the airfoil as a whole.

In all next sections, the quarter chord point has be chosen as reference point.
The geometric AoA can also be computed in the same way by keeping only the wind velocity and the airfoil motion, thus removing all effects of the bodies and wake.

4.1.2.2 AoA from bound circulation

A lifting airfoil generates a circulation around it, and this bound circulation is related with the lift acting on the airfoil thanks to the Kutta-Joukowski theorem. The Kutta-Joukowski theorem states that for an unseparated flow (so inviscid) over a lifting body:

$$\Gamma = \frac{1}{2} c U C_l \tag{4.2}$$

Where:

- Γ is the bound circulation,
- c is the chord length,
- U is the relative flow velocity magnitude: this value can be obtained from the velocity vector at a point provided by the user,
- C_l is the lift coefficient.

So for lifting elements, reciprocally, it is possible to relate lift coefficient with bound circulation, and by assuming that AoA can be related to the lift coefficient, one can deduce the AoA from the bound circulation. The relation between AoA and the inviscid lift coefficient is obtained through a tabulated static inviscid lift polar curve. The assumption relies on the idea that an unsteady AoA can be obtained from the unsteady lift coefficient by looking up the equivalent static angle generating the same amount of lift based on a static polar curve.

To summarize, the AoA is computed as:

$$\alpha = f^{-1}(C_l) \tag{4.3}$$

Where:

- f^{-1} is the reciprocal of the tabulated steady inviscid lift polar curve $C_l = f(\alpha)$,
- $C_l = \frac{2\Gamma}{cU}$ is lift coefficient deduced from the bound circulation.

One benefit of this method compared to the method from velocity vector is the ability of bound circulation to represent the airfoil as a whole because it does not depend on a unique point. This method is thus less sensitive to the proximity with singularities (like wake elements). The only dependence on a reference point is to get the velocity magnitude, but choosing one point or another does not condition much the order of magnitude.

4.1.2.3 AoA From pressure integration using polar tables

Just like the method from bound circulation, the method to obtain the AoA from pressure distribution relies on the idea that from a known lift coefficient, one can deduce an AoA based on a tabulated static inviscid lift polar curve. This method can be related to the one used by Bak [12] to determine the AoA along the span of an operating real scale wind turbine by estimating, in an optimization process, where pressure distributions measured at the rotor are compared to pressure distributions measured in a wind tunnel (by minimizing the standard deviation of the pressure differences). The differences are: (1) in a curved flow, this method would fail (like when operated in a VAWT), so comparing the lift coefficients is preferred here, and (2) the comparison is not based on wind tunnel test data but to the results that the code would give in a static 2D configuration (a wind tunnel-like configuration).
The integration of pressure distribution over an element is done by assuming a constant pressure over a panel, resulting in a sum of panels forces in place of an integral. As the pressure comes from an inviscid solver, the integrated force includes only the effects of lift and induced drag (because of the finite span). To extract lift from the integrated force, a projection is performed based on a preliminary estimation of the AoA. The user can decide to use either the AoA obtained from the velocity vector $\mathrm{AoA}_{\mathrm{Press}}$ or from the bound circulation $\mathrm{AoA}_{\mathrm{PressGamma}}$. This preliminary AoA is used to determine a flow direction, used afterwards to define the lift direction as the cross product of the flow direction and the span unit vector of an element.

Once the lift is obtained, it is normalized to get the lift coefficient and from it, the AoA is finally deduced using the tabulated static inviscid lift polar curve.

To summarize, the AoA is computed as:

$$\alpha = f^{-1}(C_l) \tag{4.4}$$

Where:

- f^{-1} is the reciprocal of the tabulated steady inviscid lift polar curve $C_l = f(\alpha)$,
- C_l is the lift coefficient deduced from the projection and the normalization of the integrated force. C_l is defined as $C_l = \frac{\overrightarrow{F}.\overrightarrow{e_L}}{\frac{1}{2}\rho c U^2}$ with ρ being the fluid density, c the chord length, U the relative flow velocity magnitude, $\overrightarrow{F}$ the integrated force obtained from the inviscid pressure distribution and $\overrightarrow{e_L}$

the unit vector defining the direction of lift based on the AoA provided by the user.
The integrated force is approximated by the sum of the panels forces oriented by the panels normals: $\overrightarrow{F} = \oint_a^b p(s)\overrightarrow{\mathrm{d}s} \approx \sum_{i=1}^{N} p_i \mathrm{d}s_i \overrightarrow{e_{\nu,i}}$ where:

- p_i is the pressure on the i^{th} panel,
- $\mathrm{d}s_i$ is the area of the i^{th} panel,
- $\overrightarrow{e_{\nu,i}}$ is the normal vector to the i^{th} panel.

This method has the same benefit than the one using bound circulation, but is more adapted to unsteady flows. The bound circulation indeed considers the influence of the wake only through circulation while the present method also account for the impulsive part of the unsteady lift through the unsteady Bernoulli formulation used to compute the pressure on panels.

4.1.2.4 Lift coefficient

The issues encountered to compute the angles of attack are also encountered with the lift coefficient since the definition of the lift is dependent on the oncoming flow direction. Lift is expected to be the component of the aerodynamic force that is perpendicular to the relative flow direction. The methods implemented in ARDEMA are related to the methods previously detailed for the AoA.

From velocity vector using polar tables This method uses the AoA based on the velocity vector. The lift coefficient is finally evaluated using an interpolated value of the tabulated steady inviscid lift polar curve at the given AoA. If a viscous polar curve is used, the lift component will be the viscous one. The moment and drag coefficients can also be computed if the corresponding tabulated data are provided.

From bound circulation This method directly uses the Kutta-Joukwski theorem to compute the lift. A drawback of this method is that only the inviscid lift coefficient can be calculated.

From pressure integration Pressure is integrated on each element to get a force vector which is then normalized like described in the section related to the calculation of the AoA based on pressure integration. The force coefficients obtained are inviscid, to obtain viscous force coefficients a correction step described in next sections must be applied.

4.1.3 Viscous corrections to an inviscid solver

4.1.3.1 Force corrections

Summary of the process Viscous polars provide the values of the aerodynamic coefficients for a given AoA. The idea of the viscous correction in ARDEMA is to reduce the magnitude of the inviscid force vector computed with the inviscid solver based on viscous coefficients at the estimated AoA. The issue with polars is that they only provide magnitude and not vectors. The assumption is made that the direction of the inviscid force also applies for the viscous forces.

The viscous coefficients that are used to determine the reduction factors can either come from quasi-static viscous polars or from the output of a dynamic stall model to account for the dynamic effects.

It should be pointed out that as the simulations are done in 3D, the inviscid force vector contains both the lift and the induced drag. Applying the reduction factor to the force vector implies that both the lift

and the induced drag are reduced. The viscous drag should be added afterwards. It is done by adding a drag force vector whose magnitude is the viscous drag and direction is the flow direction.

For the moment, a specific methodology is applied to obtain the viscous moment.

Detailed process for the force In ARDEMA, the process is different for lifting and non lifting elements. The non-lifting elements are the two tip elements composed of the closing panels at the tip, and the cylindrical elements very close to the blade root assimilated to a cylinder.

For lifting elements, the viscous force is calculated with:

$$\overrightarrow{F_{visc}} = RF.\overrightarrow{F_{inv}} + \frac{1}{2}\rho SU^2 Cd_{visc}.\overrightarrow{flowdir} \tag{4.5}$$

Where:

- RF is the viscous reduction factor, calculated as the ratio $RF = \frac{Cl_{visc}}{Cl_{inv}}$ (or a filtered version of the ratio if Cl_{visc} is the output of a dynamic stall model)
- $\overrightarrow{F_{inv}}$ is the inviscid force coming from the integration of pressure around the blade
- $\frac{1}{2}\rho SU^2 Cd_{visc}$ is the viscous drag force, with U being the local flow velocity magnitude.
- $\overrightarrow{flowdir} = \cos(\alpha)\overrightarrow{x} - \sin(\alpha)\overrightarrow{y}$ is the direction of the flow relative to a given element, with α being the AoA specified by the user.

For non-lifting elements, the viscous force is calculated with:

$$\overrightarrow{F_{visc}} = RF.\overrightarrow{F_{inv}} + \frac{1}{2}\rho SU^2 Cl_{visc}.\overrightarrow{flowdir} \times \overrightarrow{z} + \frac{1}{2}\rho SU^2 Cd_{visc}.\overrightarrow{flowdir} \tag{4.6}$$

Where:

- RF is the viscous reduction factor, calculated as the ratio $RF = \frac{Cl_{visc}}{Cl_{inv}}$
- $\overrightarrow{F_{inv}}$ is the inviscid force coming from the integration of pressure around the blade, which is almost zero for non-lifting elements item $\frac{1}{2}\rho SU^2 Cl_{visc}$ is the viscous lift force, with U being the velocity magnitude specified by the user. This should in principle be 0 but can be set to other values to account for lift on elements from which no wake is emitted.
- $\frac{1}{2}\rho SU^2 Cd_{visc}$ is the viscous drag force, with U being the velocity magnitude specified by the user.
- $\overrightarrow{flowdir} = \cos(\alpha)\overrightarrow{x} - \sin(\alpha)\overrightarrow{y}$ is the direction of the flow relative to a given element, with α being the AoA specified by the user.
- $\overrightarrow{z}$ is the direction of the spanwise vector relative to the element ($\overrightarrow{z}$ axis in the element's base).

The benefit of this method is to keep the direction of the inviscid force for the lift. The viscous corrected force is then modified by the drag applied onto a direction that can potentially be not correlated to the inviscid force direction.

All viscous corrected force components and coefficients are then just projections of the viscous force onto different bases vectors.

Detailed process for the moment In ARDEMA, the viscous moment is obtained with the following correction to the inviscid one, including the unsteady effects. All moments are computed at quarter chord points.

$$\overrightarrow{M_{visc}} = \overrightarrow{M_{inv}} - \overrightarrow{M_{pitch,inv}} + \left[M_{pitch,inv} - M_{pitch,polar,inv}\left(\alpha\right) + M_{pitch,polar,visc}\left(\alpha\right)\right].\overrightarrow{z} \tag{4.7}$$

Where:

- $\overrightarrow{M_{inv}}$ is the inviscid moment coming from the integration of pressure around the blade.
- $\overrightarrow{M_{pitch,inv}} = \left(\overrightarrow{M_{inv}}.\overrightarrow{z}\right).\overrightarrow{z}$ is the inviscid moment vector coming from the integration of pressure around the blade.
- $M_{pitch,inv}$ is the signed magnitude of the inviscid moment vector coming from the integration of pressure around the blade.
- $M_{pitch,polar,inv}\left(\alpha\right)$ is the inviscid moment coming from the tabulated polar. This is a quasi-static result.
- $M_{pitch,polar,visc}\left(\alpha\right)$ is the viscous moment coming from the tabulated polar. This is a quasi-static result.
- $\overrightarrow{z}$ is the direction of the spanwise vector relative to the element ($\overrightarrow{z}$ axis in the element's base).

The idea is to isolate the pitching moment from the other moments (the others should in principle be very close to 0 anyway and are left unchanged) and to correct this pitching moment. The correction consists in applying the offset between the unsteady and the quasi-static inviscid pitching moment with respect to the quasi-static viscous moment from the polar at the estimated AoA.

4.1.3.2 Wake corrections

Using the fact that the wake potential is directly proportional to the resulting force, the reduction factor can be defined straight-forwardly as:

$$\mathrm{RF} = \frac{\text{viscous forces}}{\text{inviscid forces}} = \frac{C_{l,\mathrm{visc}}}{C_{l,\mathrm{inv}}} \tag{4.8}$$

and the potential strength assigned to the wake becomes:

$$\mu_{\mathrm{wake,visc}} = \mathrm{RF}.\mu_{\mathrm{wake,inv}} = \frac{C_{l,\mathrm{visc}}}{C_{l,\mathrm{inv}}}\mu_{\mathrm{wake,inv}}. \tag{4.9}$$

For smoothing purposes when the dynamic lift and drag coefficients are used, the reduction factor is filtered. The viscous vorticity at the panel edges is then calculated as defined by taking the difference between the panels sharing an edge:

$$\overrightarrow{\omega}_{\mathrm{edge}} = \Delta\mu_{\mathrm{visc}}.\overrightarrow{t}_{\mathrm{edge}} \tag{4.10}$$

This approach directly fulfills the Helmholtz theorem for incompressible flows, that the sum of the vorticity is zero at each wake vertex. This can be seen directly, taking a closed line integral:

$$\oint_{\partial A} \omega\overrightarrow{n} \times \overrightarrow{\mathrm{d}s} = \oint_{\partial A} \Delta\mu \mathrm{d}s = 0 \tag{4.11}$$

This integral in the wake sheet around a wake vertex is zero, as the start and end points are at the same value of the panel, no matter whether the contour integral is inside one panel only or over the panel edge or corner.

4.1.4 Polar corrections

4.1.4.1 A Beddoes-Leishman type model

Dynamic stall (DS) is another viscous effect that is not handled by the panel method, and a dynamic stall model must be included in order to consider its effects on the loads. In ARDEMA, the model proposed by Beaudet [15] has been implemented. The detailed model is presented in Appendix A. The model contains two pressure lags as proposed by Niven [146] and a lag on separation point. The leading edge vortex module has not been included, considering like the Risoe model [83] that for thick wind turbine airfoils, the effect of leading edge vortex is negligible. The attached flow behavior is handled by computing an effective AoA that already contains the hysteresis from the circulatory behavior through the wake. The airfoils DS characteristics such as the 0-lift AoA and the lift slope are computed thanks to the static polars at the beginning of a simulation. This implies that no specific DS data need to be introduced aside from the 3 time constants T_p, T_f and T_b. The calculation of the separation point is obtained by using Kirchoff law as explained in Appendix A. Despite that it has no physical meaning, the separation point can reach values higher than 1 (fully attached boundary layer) in the case where the viscous polar is higher in absolute value than the attached viscous polar. This behavior can be observed in Fig. 4.1, but it ensures that the reconstructed polar will match perfectly the original viscous polar. No lag is applied to the moment coefficient except the one based on the effective AoA calculation.

The Beddoes-Leishman model outputs are used for the wake and force reductions. It must be noted

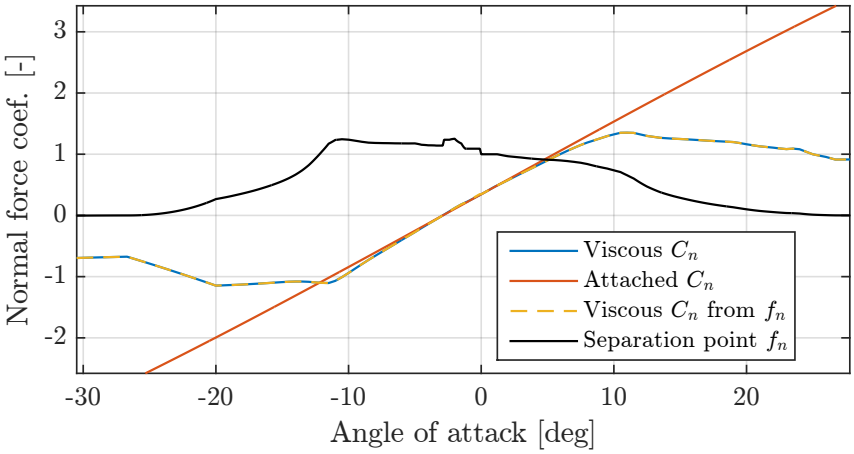

Figure 4.1: Separat+ion point and C_n calculation in ARDEMA based on Kirchoff law

that the AoAs used during calculation of the DS data are not exactly the same than the one used in post processing. For the first ones, the AoA used for DS data does not contain the viscous correction on the last emitted panels as the inviscid flow solver solution is needed before calculation of the AoA. On the opposite, the AoA used for post-processed forces calculations already contains the reduction on all wake panels. Including or not the DS data in the wake reduction can be related to the question of including DS data in the computation of induction factor in BEMT. A significant difference must be noted however:

BEMT always considers an equilibrium state without dynamic effects (considering no dynamic inflow model is used) while it is not the case with a free wake method. By considering the total induction as the sum of a mean stationary induction and of an unsteady induction, it can be considered that ARDEMA intrinsically computes the total induction while a BEMT solver only computes the stationary induction. The circulatory part of the attached flow module from the B-L model is then based on the modeling of the influence of this unsteady induction on the force coefficients. It is however not possible in ARDEMA to dissociate the stationnary induction from the unsteady induction, and the viscous correction thus always contains the unsteady induction influence while it is not the case in the BEMT induction.
Several solutions have been proposed in literature to tackle this issue and include a DS model in a vortex code. Coton and Wang[40] included a full B-L model in a prescribed wake model, attached and separated flow modules. In order not to include twice the unsteady induction with the attached flow module and the prescribed wake, the wake from the considered blade is not used in the calculation of the induction. Only the wake from the other blades is then used for computing induction on this blade. Dumitrescu [48] included a full B-L model in a lifting line code, without any specific treatment regarding the unsteady induction taken twice into account.

4.1.4.2 Correction for radial flows

In order to account for the stall delay induced by radial flows, Snel [181] stall delay model is implemented in ARDEMA and modifies the input polars during initialization. The following formula is used to obtain the lift coefficient including stall delay:

$$C_{l,3D} = C_{l,2D} + 3\left(\frac{c}{r}\right)^2 (C_{l,att} - C_{l,2D}) \tag{4.12}$$

with $C_{l,3D}$ the lift coefficient accounting for stall delay, $C_{l,2D}$ the lift coefficient without stall delay, c the chord length, r the distance from the section to the rotor axis and $C_{l,att}$ the attached flow lift coefficient. Like in the DS model, $C_{l,att} = C_{l,slope}(\alpha - \alpha_0)$.

4.2 Aero-elasto-servo coupled code

In reality, the aerodynamic forces acting on the wind turbine have an incidence on the geometry of the turbine: the blades and the tower deforms. Furthermore, the operational condition of the turbine is controlled in order to rotate the turbine at an optimum velocity and pitch the blades in order to reduce the aerodynamic forces at high wind speeds. Both structure and control must be modeled to have a realistic estimation of the forces. More information regarding state-of-the-art on aeroelastic modeling for wind turbines is presented in Hansen reference study [84]. The present section introduces the principles of aero-elasto-servo simulations in wind turbine engineering. Specifically, the FAST code is briefly introduced has it is coupled to ARDEMA aerodynamics solver. The main principles of wind turbine control are also presented along with the controller used in the present work.

4.2.1 Standards and DLCs

Wind turbines must be certified by independent companies (DNV-GL, Bureau Veritas, etc...) following a process specified in industry standards, with numerous loads calculations with simulation codes that

include control, structure and aerodynamics. Offshore wind turbines must also include wave and currents impact on the structure, adding an hydrodynamic solver. The reference standard regarding loads is the IEC 61400-1 [92]. This standard specifices the environmental conditions to take into account and calculations to perform in order to assess the structural integrity of a wind turbine on a given site for its lifetime design. The specific simulations to perform are called Design Load Cases (DLCs). Some recent studies have been conducted in order to optimize the turbines with engineering models on specific DLCs [8] [23]. This reveals how important it is to keep in mind design standards when developing models that are to be applied in industry. From a scientific point of view, improving the models used for the requested simulations is a challenge as it combines at least knowledge in aerodynamics, structure and control. In the present study, only the aerodynamic part is modified by using a panel method instead of a BEMT code. The purpose of using ARDEMA in a coupled code instead of a purely aerodynamics standalone version is to assess the differences between the two aerodynamics solvers in realistic engineering cases. The classical BEMT code have been developed in order to comply with the most frequent operating conditions of a turbine. The deviation between reality and BEMT in more challenging cases is then handled by applying safety factors on the simulated loads. However, by reducing these safety factors thanks to a better confidence in the simulated loads, the design of the turbine can be optimized.
Two main types of load calculations are defined in standards: ultimate loads and fatigue loads. Ultimate loads investigate the material strength, structural stability and tip deflections in all types of conditions. Fatigue loads aim at verifying the fatigue strength in the most frequent operating conditions. For both, some DLCs investigate specific failures. The controller must be able to handle all DLCs types, such as start-up and shutdown of the turbine, emergency stop, or parked conditions. Typical failures are loss of electrical network, default in pitch or yaw angles. Depending on these DLCs, specific aeroelastic phenomena can appear. Standstill conditions have proven to be responsible for vortex induced vibrations, startup and shutdown implies quick changes in induction, and high yaw error generates oscillating inflow conditions with possible dynamic stall. BEMT solver is not able of capturing such specific flows accurately, leading to high safety factors that does not reflect the real loads.

4.2.2 FAST code

4.2.2.1 Presentation

FAST [100] [97] is a multi-physics code developed by NREL. The used version of FAST considered is the v8.15, which was the latest version of FAST available at the time of the beginning of this study. FAST is a coupled code including aerodynamics and structural modeling, with possibilities to include control and hydrodynamic loads. The coupling is a two-way coupling: the computed aerodynamic forces modify the structure, which in return modifies the aerodynamic forces. The code structure is presented in Fig. 4.2. The structural solver used in the study is ElastoDyn, which is based on a modal analysis of pre-computed mode shapes. Three modes are computed for the blade: the first and second flapwise modes and the first edgewise mode. Torsion of the blade is not computed in ElastoDyn. The code handles multi-body problems, which is necessary to compute the dynamic of several bodies in motion. The aerodynamics module, AeroDyn, is a BEMT solver with several of the typical corrections applied to BEMT, such as Prandtl tip loss mode and Glauert correction (see Section 3.1). A skewed wake model[145] based on the so called Pitt and Peters model and presented in the state-of-the-art from Snel [183] is also implemented. The unsteady module is a Beddoes-Leishman model [43]. No variable induction model is available in

the version of AeroDyn used in this study. FAST has been broadly used in many scientific publications and recently validated against SGRE in-house aeroelastic code BHawC [74].

4.2.2.2 Coupling with ARDEMA

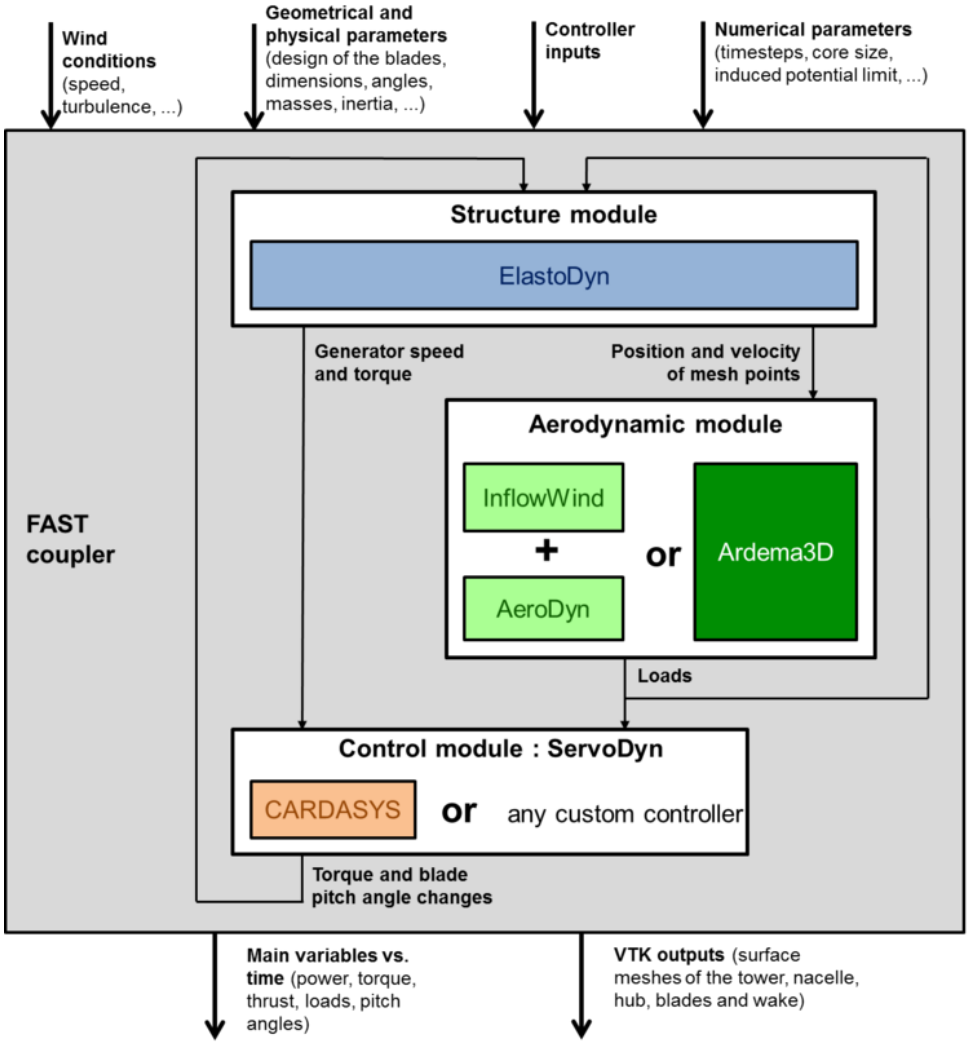

Figure 4.2: Structure of FAST and coupling with ARDEMA

The highly modular development of FAST makes it very suitable for coupling purposes. ARDEMA was thus coupled to FAST in the framework of SGRE R&D activities. The coupling is performed by including a compiled version of ARDEMA in the source code of FAST as an external library. The aerodynamic forces are computed at each ARDEMA section and sent to ElastoDyn in replacement of AeroDyn forces. The positions and velocities of sections are then computed by ElastoDyn and sent to ARDEMA. The mesh generation in ARDEMA is done during initialization, and the connectivity of blade panels is fixed during a simulation. The position of each panel however is modified thanks to the information on the sections position: each section is considered as rigid, but the position of each section relatively to the other is modified during a simulation. This implies that AIC matrix must be recomputed

at each time step. In order to decrease the computational time, the time step in ARDEMA is reduced compared to ElastoDyn time step, and the last computed aerodynamic forces are applied on the structure between two ARDEMA time steps.

4.2.3 Controller

Before nominal wind speed, the rotor speed must be adapted in order to operate at a maximum aerodynamic efficiency. After nominal wind speed, the aerodynamic efficiency must decrease in order to keep a constant power. Two types of power limitation historically exist: the stall and the pitch regulated turbines. The stall regulated turbines handle high wind speed thanks to the stall process. By controlling the speed rotation, the AoA is increased and the airfoils reach stall regime characterized by a loss of lift and thus power. This type of power control is not used anymore on modern industrial wind turbines. The pitch regulated wind turbines control the power extraction by pitching the blades around their axis in order to decrease the AoA when the wind is increasing, thus decreasing lift. The main advantage is that the flow remains attached in normal conditions on most of the blade, which is much easier to predict and less chaotic than the stall process.
To handle rotor speed and pitch angle, a controller operates the wind turbine by applying a given torque on the main shaft through the generator and by controlling the pitch angle. A wind turbine controller is

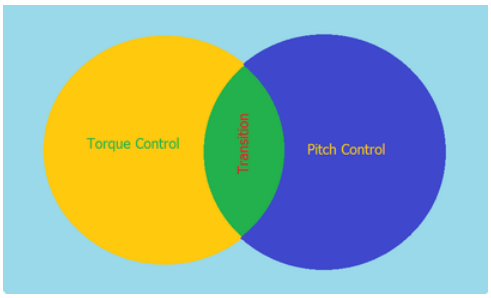

Figure 4.3: WTG Control operating area

mainly composed of two main control loops: the torque and the pitch loop. The two loops have a very similar target, which is interchangeable depending on which loop is in operation. For example, the target of the torque loop, is to maintain the generator speed within the optimum and constant speed area. This target is handed over to the pitch loop, when the pitch loop is in operation. As a result, the torque loop either maintains the torque or the power at a constant level. This basically defines the *constant torque* or *constant power* control design. There is a small area where the two control loops are overlapping for wind speeds close to the rated power as illustrated in Fig. 4.3. A smooth transition from one loop to another is required extracting as much power as possible.
The controller used in the present study is a constant power controller with two main loops for torque and pitch represented in Fig. 4.4.

Torque loop The basic torque loop has different tasks depending mainly on the generator speed. At very low wind speeds, the generator torque is kept at a very low level allowing the rotor to accelerate from the wind. If the wind is strong enough and the minimum rotational speed is reached, then a PI controller regulates the generator speed maintaining it at the minimum speed. If the wind continues to

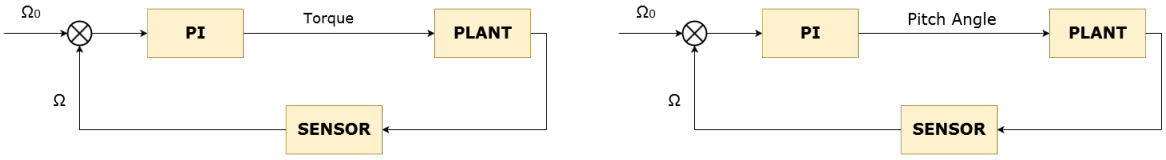

(a) Torque control loop (b) Pitch control loop

Figure 4.4: Control loops for torque and pitch

increase, then the torque is a function of the generator speed squared as this is the optimal torque, hence the maximum power output. In the case where the maximum generator speed is reached, then another PI controller operates in order to maintain the generator speed at a constant level, with an error of 5 - 10%. The converter's limits need to be available to the controller, because once the torque limits are reached, then it is time for the pitch loop to take over the control of the generator speed. The torque loop either maintains the torque or the power at a constant level depending on the design. In general, *constant torque controllers* are proved to perform better in terms of loads, but there is a compromise on the power output, whereas the *constant power controllers* perform better in terms of the power output. The operating area for a constant power controller is illustrated in 4.5. This description refers to the

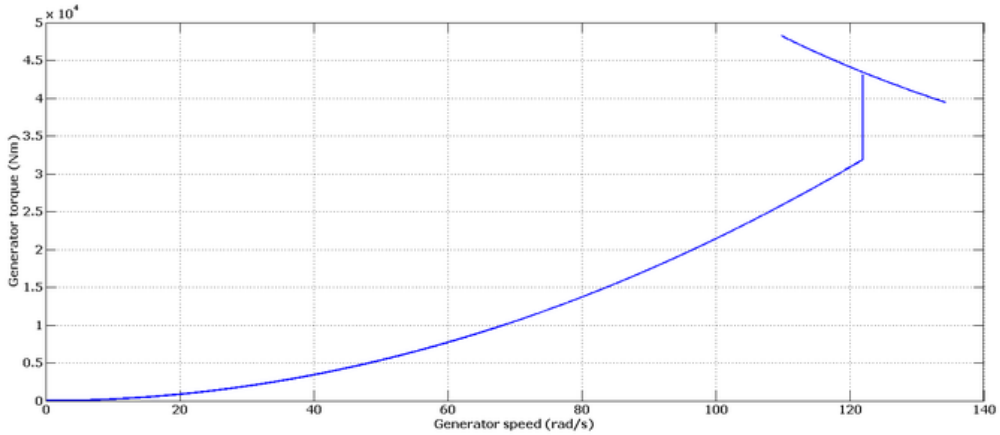

Figure 4.5: Constant power control type

basic torque control design. Advanced features are essential as they are able to alleviate loads from the turbine's main components. These features add an additional torque filtering unwanted frequencies that potentially reduce the life-time of the components.

Pitch loop The basic operation of the pitch loop is to regulate the generator's speed aerodynamically. once the limits of the torque loop have been reached, the generator speed is controlled by the pitch loop, whilst the torque loop contributes to different objectives such as power output and loads reduction. By pitching the blades collectively a significant aerodynamic effect is achieved allowing sufficient control of the turbine. In general, the PI controller is tuned in such way that a certain level of variation around the generator's rated speed is allowed. It is noteworthy, the fact that the pitch sensitivity is almost in linear relation with the blade pitch angle. This variation justifies the necessity of a well designed gain schedule able to alternate the Kp and the Ki values of the controller.

Apart from the regulation of the generator's speed, the pitch and torque loop contribute to the reduction of the fatigue and extreme loads from the turbine's main components. Advanced functions such as tower damping are indeed implemented in the controller in order to alleviate the loads caused by the tower motion. A 3-P frequency filtering is also applied on the rotation speed used as input for both torque and pitch control loops. In the present calculations, no tower damping is activated but the 3-P filtering is used in order to prevent 3-P variations of the torque response.

4.3 AeroDynamic validation of the unsteady viscous flow methodology

As ARDEMA code is based on the panel method from Dixon [44], the validation of the inviscid flow solver is not considered here. Validation of the panel method from Dixon against Theodorsen function is available in his Master Thesis. In the present section, the viscous corrections results are compared with experimental data and state-of-the-art theories such as BEMT. The 2-D validation mainly focuses on the dynamic stall module by comparing it with experimental data from Piziali [153] on the NACA0015 airfoil and Fulgsang [58] on the FFA-W3-241 airfoil. The finite wing experiments from Piziali are also used for 3-D validation of dynamic stall. The modeling of a full wind turbine is then performed using the NREL 5MW generic wind turbine [101] data and comparing it with results from a BEMT solver. Originally, the purpose was to compare ARDEMA with a BEMT solver using the DTU 10MW generic wind turbine as a test case. As the NREL 5WM is a FAST test case, it then seemed faster and more reliable to use the NREL 5MW instead. Furthermore, simulations conducted on SGRE blades, more flexible like the DTU 10MW blade than then NREL 5MW blade, have shown no significant differences in the code to code comparisons.

4.3.1 2-D Validation

For the 2-D validation, two types of flows are investigated, the attached and separated flows. In the case of attached flows, the dynamic behavior in ARDEMA is obtained through the calculation of the induced velocities from the wake (circulatory lift) and the unsteady pressure distribution on the panels (impulsive lift). For separated flow, the dynamic stall module presented earlier is responsible for the stall delay and hysteresis. The symmetric NACA0015 profile has a mixed stall type, with smooth trailing edge separation and massive leading edge separation behavior. The asymmetric FFA-W3-241 is a wind turbine thick airfoil with smooth trailing edge separation. The static polars used for the viscous correction are the experimental static polars given by Piziali and Fulgsang in their study reports.
ARDEMA is a 3-D code and 2-D analysis is not possible. In order to compare ARDEMA results with airfoil data, 3-D effects must be removed. In the present cases, the considered geometry is a blade with an aspect ratio of 1000 discretized in 10 sections. The sections at mid-span are then used to compute aerodynamic coefficients, and it is assumed that tip effects are negligible in such conditions. This has been verified by comparing inviscid polars obtained with such geometry with inviscid polars obtained in the 2-D panel code Xfoil, both giving similar results.
Both wake and force corrections are enabled in ARDEMA. A comparison is also made for some cases between a wake correction based on DS forces coefficients or based on unsteady force coefficients without DS. The AoA used as input for the DS module is $\mathrm{AoA}_{\mathrm{PressGamma}}$ defined earlier, computed at the quarter chord point.

4.3.1.1 Comparison of attached unsteady cases

Three cases are presented in this section, described in Table 4.2. Two cases are performed on a NACA0015 in the attached region of the polar curve with same mean AoA and amplitude, with two distinct reduced frequency in order to assess the capacity of the methodology to capture correctly the sensitivity to reduced frequency. Another case based on the FFA-W3-241 airfoil is then investigated in order to check the validity of the model for a wind turbine dedicated airfoil, cambered and thicker than the NACA 0015.

Table 4.1: Unsteady attached cases description

Airfoil	α_{mean}	α_{amp}	k
NACA0015	4.0°	4.0°	0.040
NACA0015	4.0°	4.0°	0.100
FFA-W3-241	3.8°	1.4°	0.093

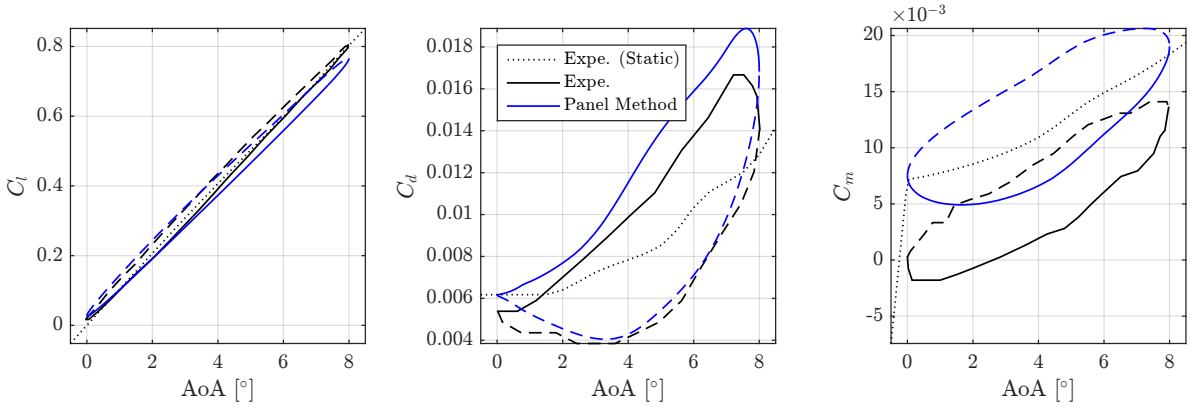

(a) $\alpha_{\text{mean}} = 4.0°$ - $\alpha_{\text{amp}} = 4.0°$ - $k = 0.04$

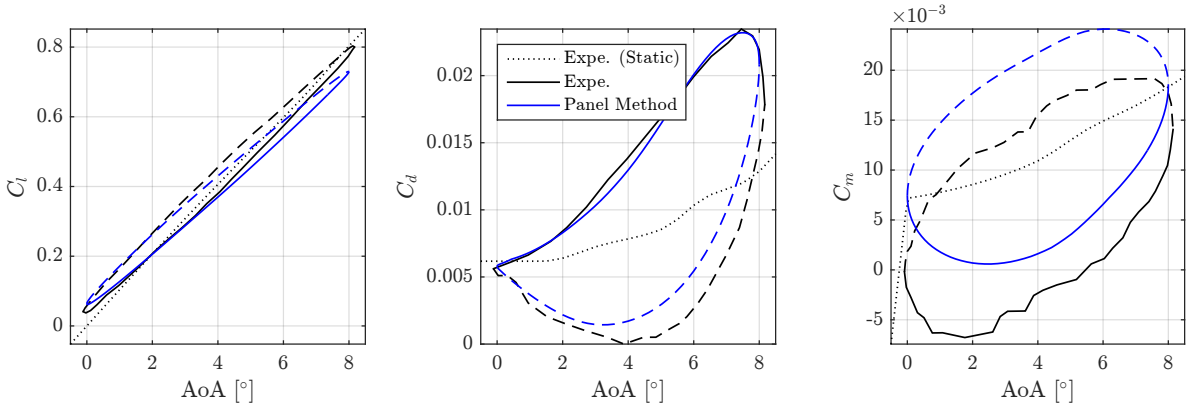

(b) $\alpha_{\text{mean}} = 4.0°$ - $\alpha_{\text{amp}} = 4.0°$ - $k = 0.10$

Figure 4.6: Force coefficients in 2-D attached cases - NACA 0015 - AoA up in solid lines, AoA down in dashed line

Fig. 4.6 and 4.7 present the unsteady force coefficients for the investigated cases, plotted against the geometrical AoA. ARDEMA code results are compared with experimental steady and unsteady experimental results. For the NACA0015 cases, the hysteresis loops are predicted correctly for the three force

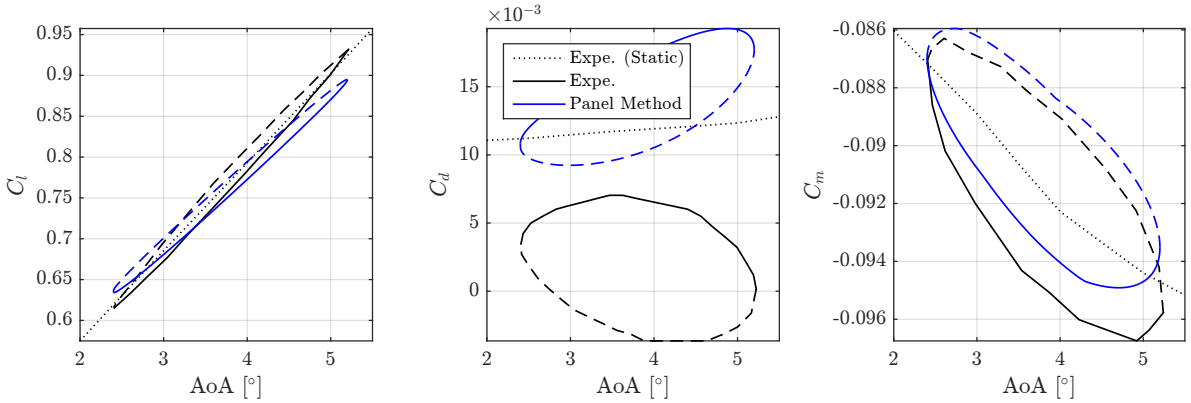

Figure 4.7: Force coefficients in 2-D attached cases - FFA-W3-241 - $\alpha_{\text{mean}} = 3.8°$ - $\alpha_{\text{amp}} = 1.4°$ - $k = 0.093$ - AoA up in solid lines, AoA down in dashed line

coefficients, in both cases. The loops for the highest frequency are wider than for the lower frequency, despite the fact that the difference between both is slightly underpredicted compared to the experimental cases. All ARDEMA loops are centered on the static force coefficients as they have been used as input to the viscous corrections, while experimental dynamic loops can be shifted compared to static polars probably because of measurement uncertainties. The slope of the ARDEMA lift loops also appears to be lower than for the experimental cases, with a lower amplitude of the lift coefficient. The case with the FFA airfoil has the same behavior, which is also observed with the attached module from the BL model implemented in a BEMT code presented later on in section 4.2.2.

4.3.1.2 Comparisons of separated unsteady cases

Four cases are presented here and described in Table 4.2 for assessing the validity of the DS model implemented in ARDEMA, with the same profiles than in the attached cases. The output unsteady forces from the DS model are included in the wake reduction. This methodology is compared to a version using the unsteady forces without DS for the wake reduction in two cases.

Table 4.2: Unsteady separated cases description

Airfoil	α_{mean}	α_{amp}	k	Comparison DS in wake
NACA0015	15.0°	4.0°	0.040	-
NACA0015	15.0°	4.0°	0.100	Yes
FFA-W3-241	13.5°	1.7°	0.093	Yes
FFA-W3-241	24.6°	1.9°	0.093	-

For the NACA0015 cases presented in Fig.4.8, the effect of the leading edge vortex appears clearly on the experimental force coefficients, with a higher lift coefficient and delayed stall, and the presence of peaks on drag and moment coefficients. This behavior is not predicted by the DS module from ARDEMA, which does not contain leading edge vortex modeling. The reattachment process seems however correctly obtained. For the FFA-W3-241 profile force coefficients presented in Fig. 4.17, the experimental hysteresis loops do no reveal the presence of a strong leading edge vortex. The lift however

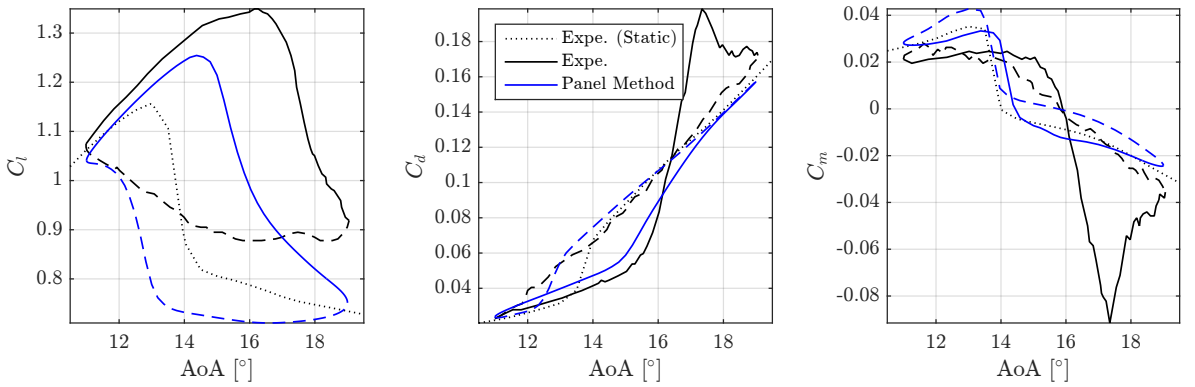

(a) $\alpha_{\text{mean}} = 15.0°$ - $\alpha_{\text{amp}} = 4.0°$ - $k = 0.04$

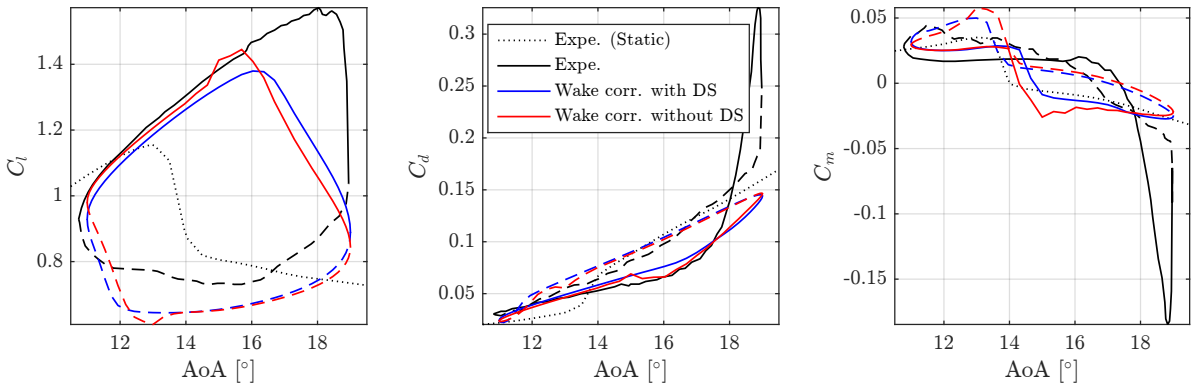

(b) $\alpha_{\text{mean}} = 15.0°$ - $\alpha_{\text{amp}} = 4.0°$- $k = 0.10$

Figure 4.8: Force coefficients in 2-D separated cases - NACA 0015 - AoA up in solid lines, AoA down in dashed lines

is slightly underpredicted with ARDEMA in the case centered around $13.5°$, and the moment coefficient reveals a curved loop that is not predicted by ARDEMA. The cause of such behavior is not clear based on such observations, and further insight in the flow structures is necessary to understand it. For the case centered on $24.6°$, the loop in ARDEMA is not as wide as the experimental loop, with a slope equal to the static polar slope which is not the case for the experimental case.

The red curves in the previous figures are a comparison of the unsteady forces when the DS output are not included in the wake reduction. The difference is negligible with the cases including DS outputs in wake reduction. However some peaks are observed on the force coefficients: the DS acts like a filter that smooths the lift curve. When the airfoil reaches stall, the difference in the reduction factors applied in the wake before and after stall can be great when DS is not applied, creating instabilities in the wake. Including the dynamic stall smooths the reduction factor variations. These observations tend to justify the inclusion of DS in wake reduction. Furthermore, from a physical point of view, it seems more realistic to include DS as the emitted wake strength should depend on the real forces, thus the dynamic forces.

4.3.1.3 Modifications of the dynamic stall module from FAST code

A Beddoes-Leishman DS model is implemented in FAST, with several modifications to the original model presented in Damiani [43] work. Three variations of the B-L model are implemented, though the third model (UAMod = 3 in AeroDyn input file) is recommended to be used. The main difference

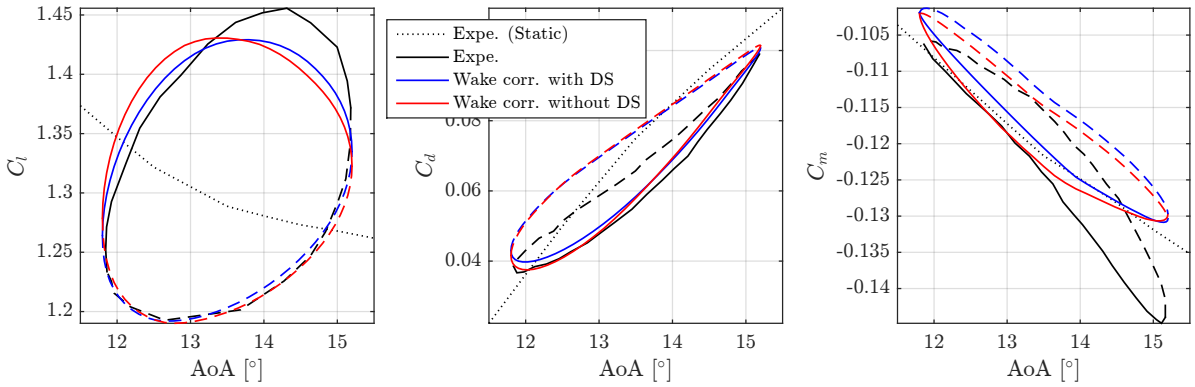

(a) $\alpha_{\text{mean}} = 13.5°$ - $\alpha_{\text{amp}} = 1.7°$ - $k = 0.093$

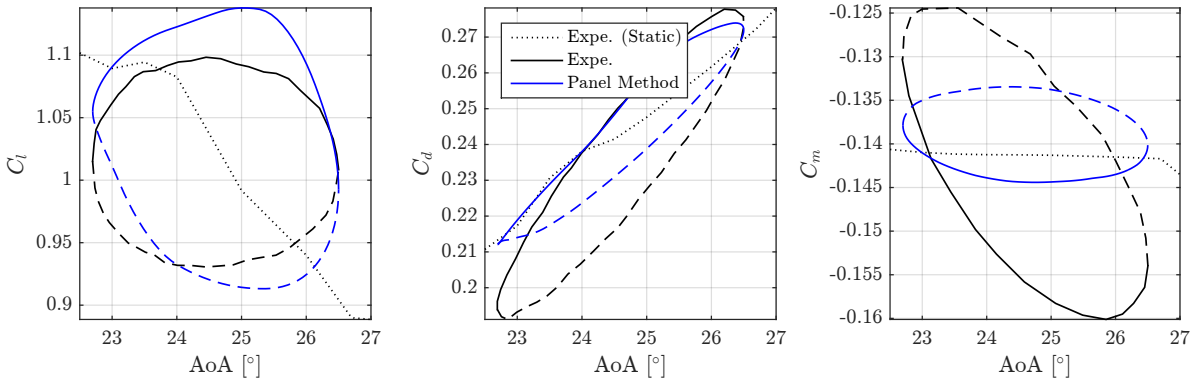

(b) $\alpha_{\text{mean}} = 24.6°$ - $\alpha_{\text{amp}} = 1.9°$ - $k = 0.093$

Figure 4.9: Force coefficients in 2-D separated cases - FFA-W3-241 - AoA up in solid lines, AoA down in dashed line

with original B-L model lies in the calculation of separation point which is based on the static polars and Kirchoff's equations instead of using exponential curves. This process is close to what is done in ARDEMA. All inputs of the DS model such as normal coefficient slope, stall angle and time constants are given in the input polar data file of AeroDyn. While in ARDEMA these data are computed based on the static polars, and external tool provided by NREL must be used for FAST: Airfoil Preppy. This Python tool has been used in this study to generate the DS inputs for the NACA0015 and the FFA-W3-241 airfoil, using as input their respective experimental static polars. In order to compare FAST and ARDEMA dynamic stall modules, the source code from FAST containing the DS functions have been extracted and recompiled in a standalone version that computes the unsteady forces of a single airfoil in oscillating conditions. Three cases are investigated based on the cases from Table 4.2, one attached case on NACA0015 airfoil and two separated cases for FFA-W3-241 and NACA0015 airfoils.

First, it appears from Fig. 4.10 that in the attached region both ARDEMA et AeroDyn unsteady lift and drag forces match well. The loop of the unsteady moment coefficients however is not giving satisfactory results in AeroDyn as it rotates in the opposite direction than ARDEMA and experimental results. This poor prediction of the unsteady moment has however little impact in the present calculations as the torsion in not taken into account in ElastoDyn.

The force coefficients in Fig. 4.11 and 4.12 are plotted with and without leading edge vortex in FAST. In order to remove the leading edge vortex influence, the critical value C_{N_1} (limit value of C_N that triggers the vortex shedding, see section 3.1.2) is set to 100 in the input polar file of AeroDyn. A modified

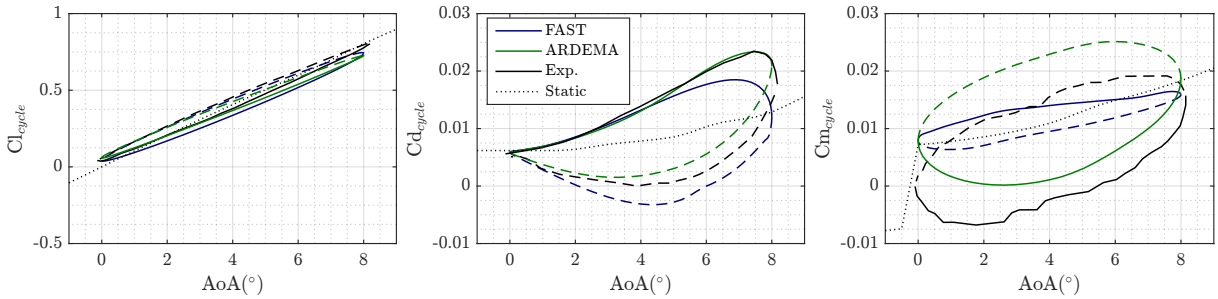

Figure 4.10: Comparison between ARDEMA and AeroDyn unsteady models - NACA0015 - Attached case: $\alpha_{\text{mean}} = 4.0°$ - $\alpha_{\text{amp}} = 4.0°$- $k = 0.10$

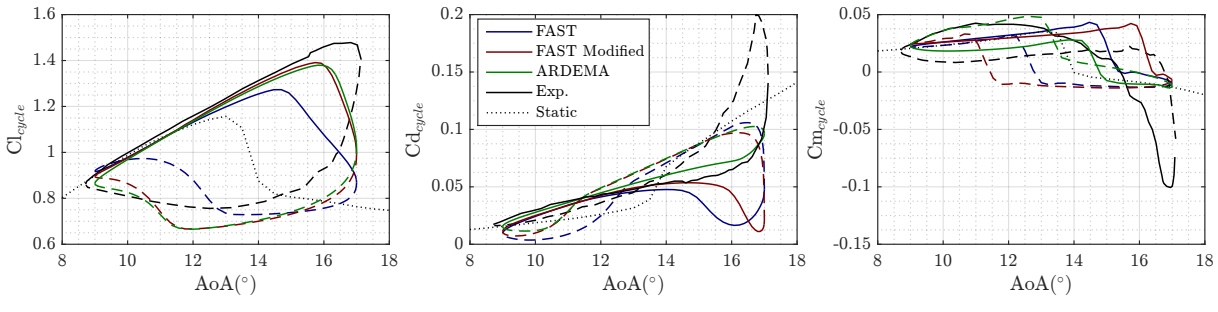

(a) Without LE Vortex

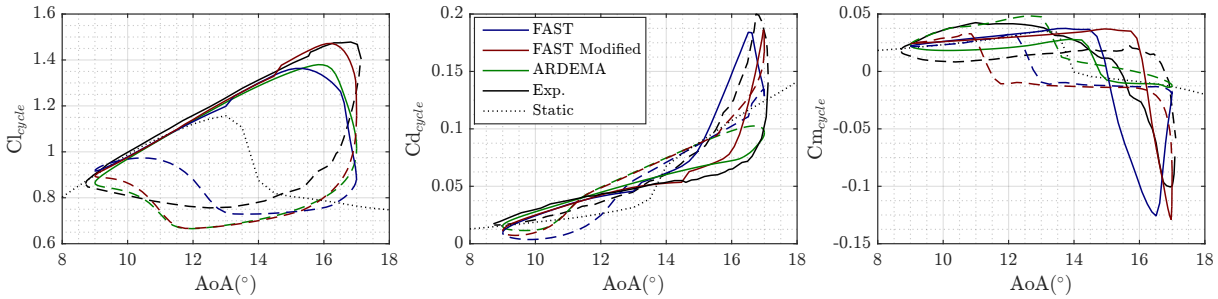

(b) With Vortex

Figure 4.11: Comparison of unsteady models - NACA 0015 - Separated case: $\alpha_{\text{mean}} = 15.0°$ - $\alpha_{\text{amp}} = 4.0°$- $k = 0.10$

version of FAST DS module is also included in the comparison. In this modified version, a second pressure lag identical to ARDEMA has been added in FAST source code. On the NACA0015 airfoil, Fig. 4.11 reveals that the leading edge vortex is necessary to have a good correlation with experimental data. The overshoot in the lift coefficient and the peaks observed on drag and moment characterize the presence of a LE vortex and are only captured when it is enabled. The second pressure lags seems to improve the prediction of the LE vortex triggering. For the NACA0015 airfoil, the configuration with the modified FAST DS and LE vortex gives the best results. ARDEMA results are very close to the results obtained with the modified DS without LE vortex, which is in line with the fact that the underneath theory is the same for both codes in separated flows. In Fig. 4.12, the same comparison is performed for the thick FFA-W3-241 airfoil. In this case, the LE vortex module does not produce satisfying results, creating unrealistic peaks in all force coefficients. Several parametrizations have been investigated by

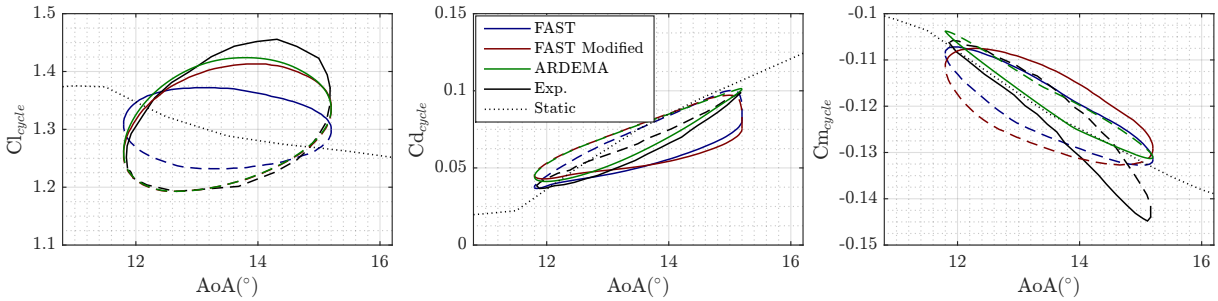

(a) Without LE Vortex

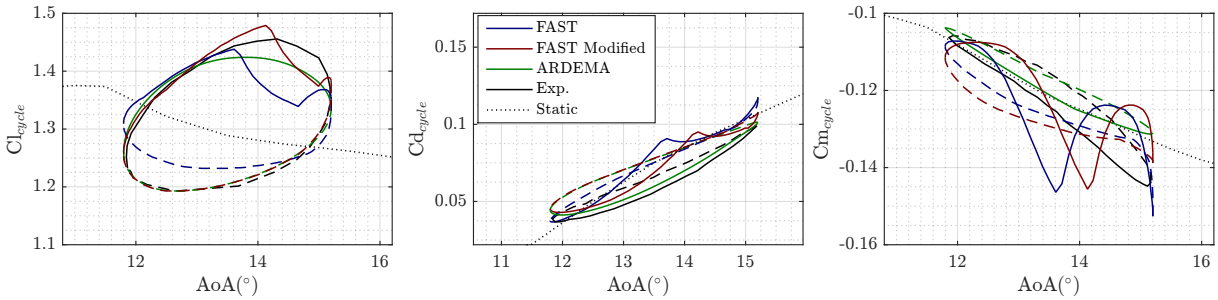

(b) With LE Vortex

Figure 4.12: Comparison of unsteady models - FFA-W3-241 - Separated case: $\alpha_{\text{mean}} = 13.5°$ - $\alpha_{\text{amp}} = 1.7°$ - $k = 0.093$

changing time constants or triggering values, none producing satisfying results. The original FAST model without DS underestimates the lift overshoot. Like in the attached case, the moment loop is not oriented in the correct direction in FAST. For such thick airfoil, the modified FAST DS without LE vortex gives the best results, very close to ARDEMA results. As dynamic stall occurs much frequently close to the root on HAWTs where the airfoil section are even thicker than the FFA-W3-241, this configuration seems to be the more suited for simulations of HAWTs.

Another modification has been included in FAST DS module: in FAST v8.15, the DS is deactivated

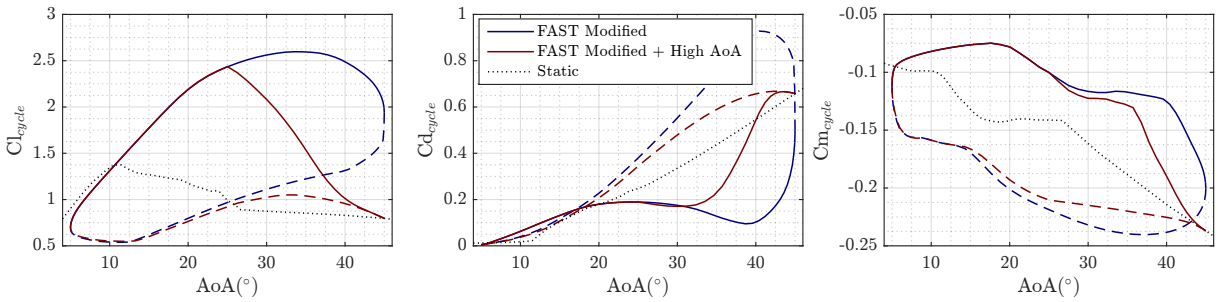

Figure 4.13: Modification of FAST dynamic stall model - Handling of high AoA - FFA-W3-241

when the AoA reaches values higher than 45°. Once it has been deactivated for a certain time step, it is not reactivated for the rest of the simulation. Furthermore, when increasing the limit AoA further than 45°, some unrealistic results have been observed. In order to be able to simulate situations where the AoA faces large amplitudes, a fading of the unsteady coefficients has been implemented the same way in ARDEMA and FAST. When the AoA is between 25° and 45°, a weighting function is applied to the

DS time constants. The usual values are used when the AoA is below 25°, and they fade to 0 at 45° and beyond. This removes progressively all the applied lags. In FAST the weighting is also applied between the unsteady coefficient and the steady coefficient in order to use only the steady coefficient for AoA above 45°. The DS data are however still computed and no re-initialization is needed if the AoA switches from high values to values below 45° . The results for such model can be observed in Fig. 4.13.

4.3.2 3-D Validation

The 3-D validation focuses on two main cases: a straight blade, and a HAWT. The straight blade case assesses the tip effects in a static case, and the validity of the DS model in an unsteady case with tip effects. The HAWT validation is performed against a BEMT solver on cases where the validity of BEMT is assessed with a high level of confidence.

4.3.2.1 3-D Wing

The experimental investigations from Piziali are performed on a semi-finite wing with aspect ratio of 5 and constant chord. In ARDEMA a full wing is modeled with an aspect ratio of 10, and the location of the experimental pressure taps defines the discretization of the blade in several sections. The investigated case are presented in Table 4.3. The steady case is performed in ARDEMA by pitching up and down the wing at a very low reduced frequency of 10^{-4} between 0° and 20°, and then averaging up and down phases. Two unsteady cases are presented, one in attached conditions and the other one in separated conditions. Force coefficients are compared at several spanwise positions.

Table 4.3: 3-D finite wing validation cases - NACA 0015 - Aspect ratio of 10

Case	α_{mean}	α_{amp}	k	Spanwise positions
Steady	0°- 20°	-	-	62.5%, 73.8%, 90%, 98.3%
Unsteady att.	3.9°	2.2°	0.20	73.8%, 98.3%
Unsteady sep.	14.9°	2.0°	0.04	73.8%, 98.3%

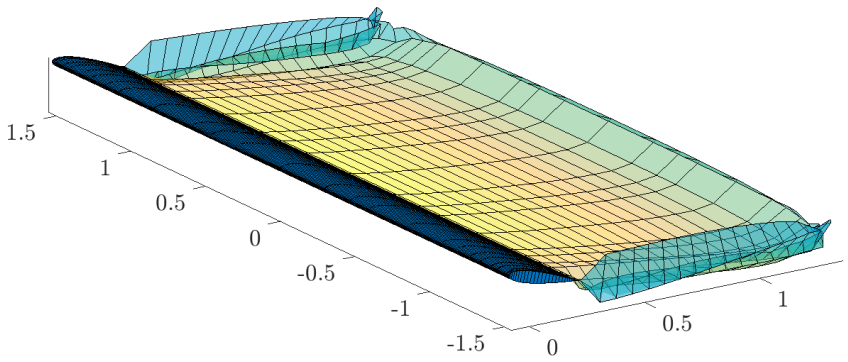

Figure 4.14: Finite wing in ARDEMA and panel wake for a constant AoA of 14°

Fig. 4.14 illustrates the discretization of the blade and wake in panels. The wake panels are coloured by the doublet strength. At the tip, the wake is stretched and rolled up as a consequence of the change in

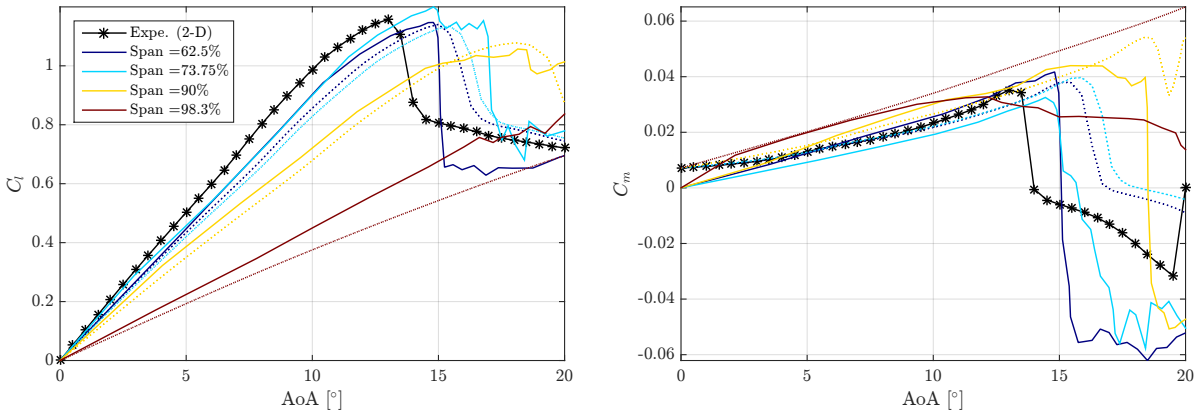

Figure 4.15: Force coefficients on a finite wing at different spanwise positions - Comparison between Piziali experiments (full line) and ARDEMA (dotted line)

the spanwise distribution of trailed vorticity, creating the tip vortex. The induced velocities from this tip vortex then creates a downwash that bends the wake down and reduces the local AoA. The starting vortex is also visible in this figure, and must be convected further downstream by increasing the simulation time in order to have as little impact as possible on the flow around the blade.

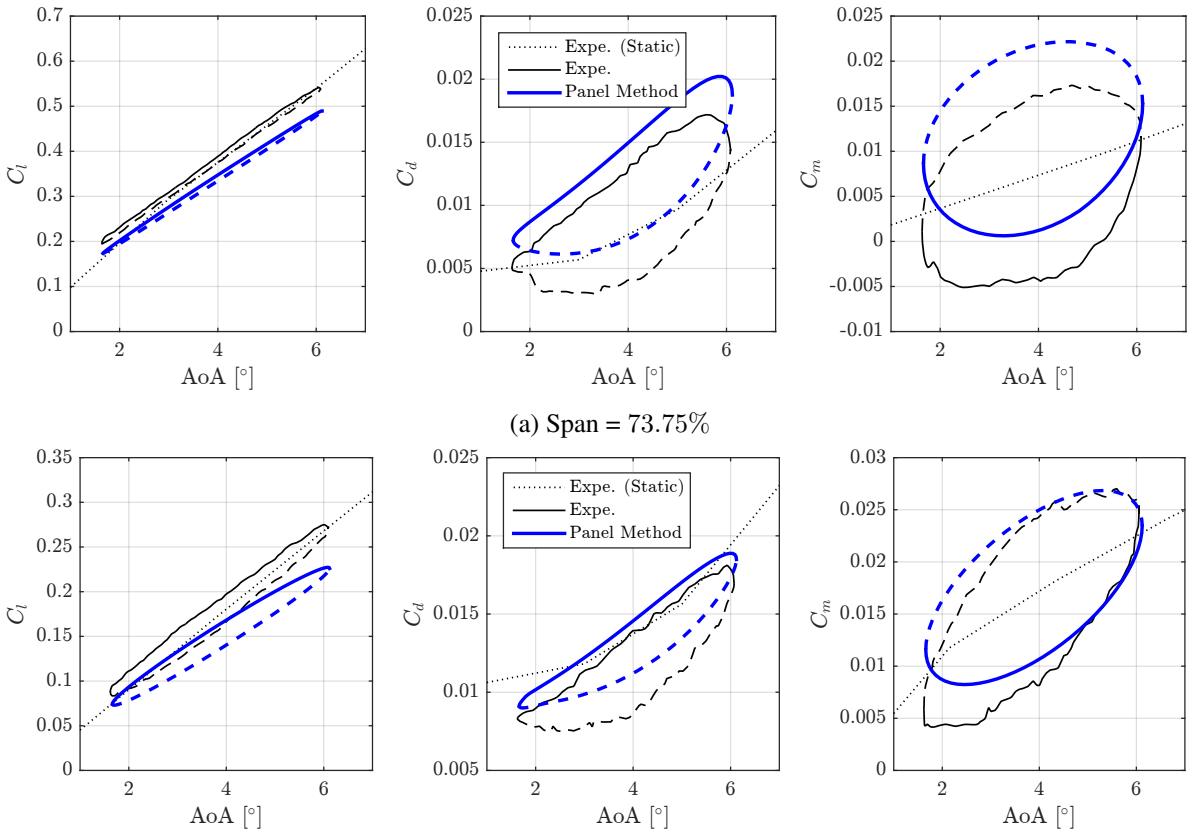

(a) Span = 73.75%

(b) Span = 98.30%

Figure 4.16: Force coefficients in 3-D unsteady attached case - AoA up in solid lines, AoA down in dashed line

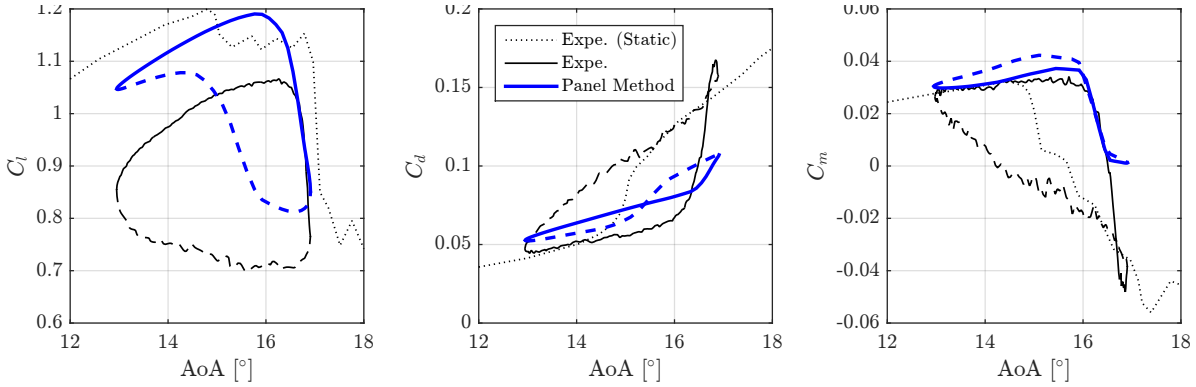

(a) Span = 73.75%

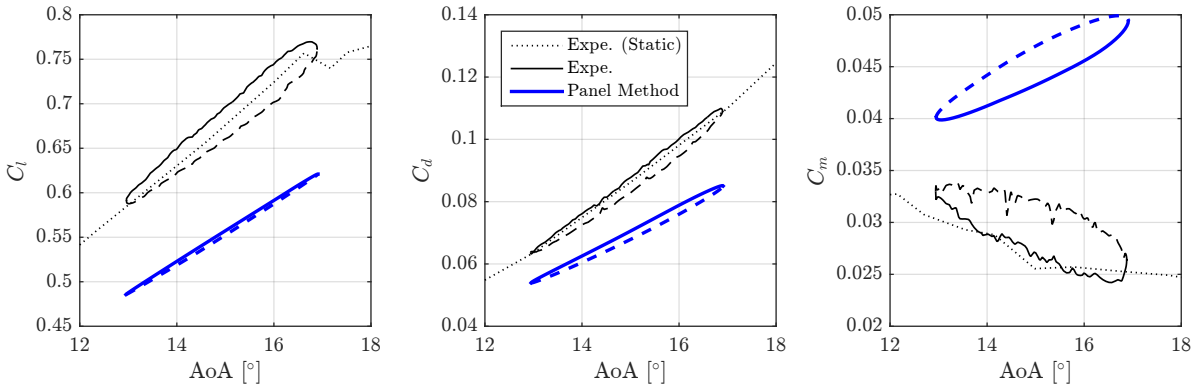

(b) Span = 98.30%

Figure 4.17: Force coefficients in 3-D unsteady separated case - AoA up in solid lines, AoA down in dashed line

The resulting lift and moment coefficients are presented in Fig. 4.15 and compared to the experimental results from Piziali. The measurements for the sections near the center of the blade (spanwise positions of 62.5% and 73.8%) are close to the 2-D experimental results as 3-D effects have less influence far from the tip. The change in slope for the attached region and the delayed stall angle are correctly predicted by ARDEMA. The slopes for experimental lift are steeper than the simulated ones, and the 3-D stall appears to be more pronounced. As a consequence the stall for both lift and moment coefficients is delayed and lighter in ARDEMA compared to experimental data. This could be explained by the fact than the 3-D stall behavior can not be captured in a panel method, in particular the spanwise distribution of the separation point.

The unsteady attached case results presented in Fig. 4.17 reveal a good correlation of all force coefficients with experimental data, with the same shift observed in static conditions. It is interesting to notice that the loops are the AoA up phase as an higher lift than the AoA down phase, which is the opposite of what is observed in the 2-D unsteady cases presented in 4.3.1. This is caused by the high reduced frequency of 0.20 of this case. The unsteady separated cases from Fig. 4.17 are in line with the observations on the static case regarding 3-D stall. The dynamic stall behavior creates large loops in experimental results, which is not the case for ARDEMA. The typical structure for such flow, the omega vortex described by Coton [39], can not be captured by the present methodology revealing its limits in 3-D modeling of stall.

4.3.2.2 NREL 5MW

The NREL 5MW generic wind turbine [101] is used for validation and compared with results from an opensource BEMT code, AeroDyn v15.02.03 [99] developed at NREL. The blade is 61.5m and is defined by 6 profiles distributed along the blade span. The original distribution of sections provided by NREL has been modified in order to have a better discretization of the blade at the root and at the tip. The blade is thus defined in 22 sections in both ARDEMA and AeroDyn. The blade geometry and discretization in panels is presented in Fig. 4.18.

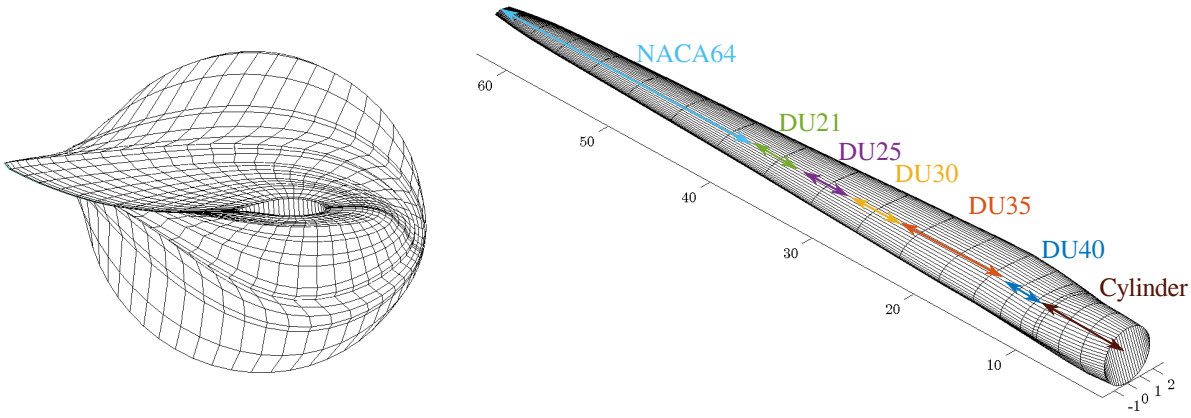

Figure 4.18: NREL 5MW generic wind turbine blade discretized in panel for ARDEMA and airfoils distribution

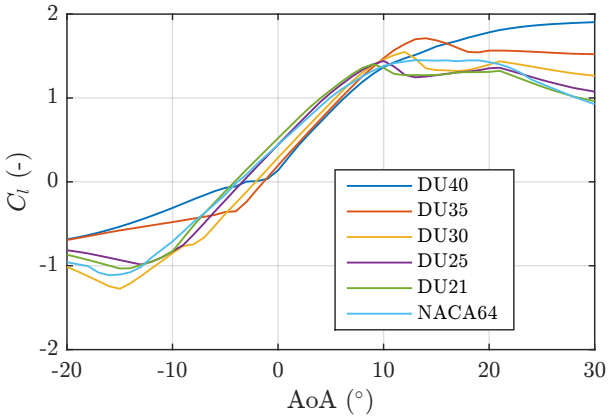

Figure 4.19: Lift coefficient polar for NREL 5MW airfoils

The lift polars of the different airfoils used in BEMT and the viscous correction for ARDEMA are presented in Fig. 4.19. These polars are the ones provided by NREL and corrected for rotationnal effects, thus in all calculations performed on NREL 5MW with ARDEMA, the Snel correction for radial flows is not applied. The thick DU40 profile, located close to the root has a high maximum lift, probably because of the applied stall delay corrections. The maximum lift is then decreasing for all sections from root to tip, with a stall AoA decreasing from around 14° to 9° for DU35 and DU21 airfoils respectively. The DS data used in AeroDyn are provided with the airfoil polars: the original data provided by NREL

have been modified in order to be the same as the ones computed in ARDEMA, in particular the normal coefficient slope. In ARDEMA, the wake of the first nearly circular sections close to the root is removed as these sections are not generating lift and create instabilities if not removed. These sections are defined as *non-emitting* sections.

Table 4.4: Cases for validation on the NREL 5MW wind turbine - Uniform wind with no shear

Wind vel.	TSR	Pitch angle	Yaw angle
11.4 m/s	7.0	0°	0°
15 m/s	5.3	10.5°	0°
25 m/s	3.2	23.5°	0°

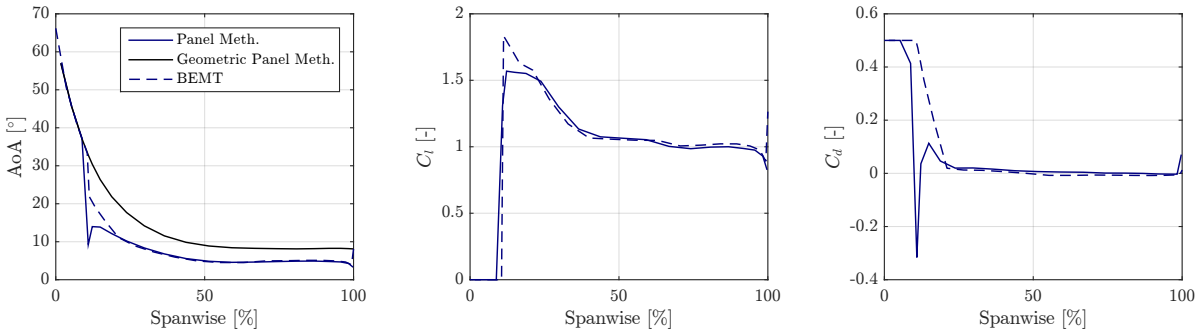

(a) AoA, lift and drag coefficients along the blade span

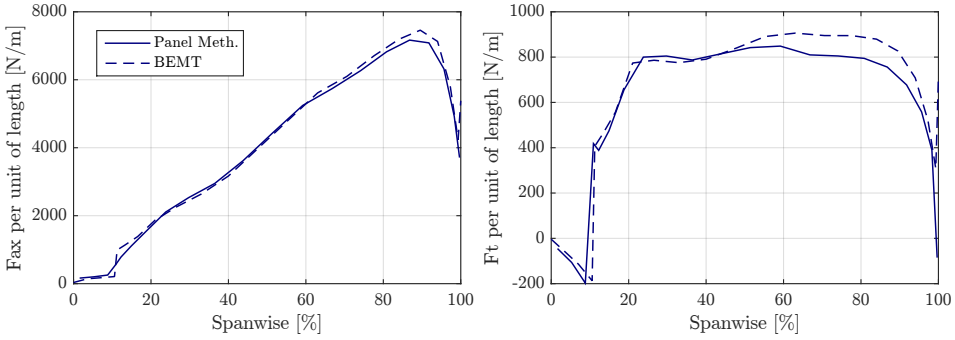

(b) Axial and tangential forces along the blade span

Figure 4.20: NREL 5MW case comparison between ARDEMA and AeroDyn - Validation for TSR = 7.0 - $V = 11.4m/s$

The NREL turbine is designed for an optimal TSR of 7.5. The nominal regime is reached for a wind speed V=11.4m/s, rotation speed of 12.1 RPM and TSR of 7. The rotor has a 5° tilt angle and a precone angle of 2.5°. The cases investigated in the present section are described in Table 4.4. Three different wind speeds corresponding to different operational conditions of the turbine are presented. The chosen pitch angles are based on the reference values given in NREL 5MW report [101], with an expected power output of around 5.3 MW. In these three cases, a uniform wind is applied with no shear nor turbulence. The impact of tower on the aerodynamic loading is not considered in ARDEMA, so it is disabled in AeroDyn simulations. The time step in ARDEMA is 0.08s and 0.02s in FAST, with around 60 times

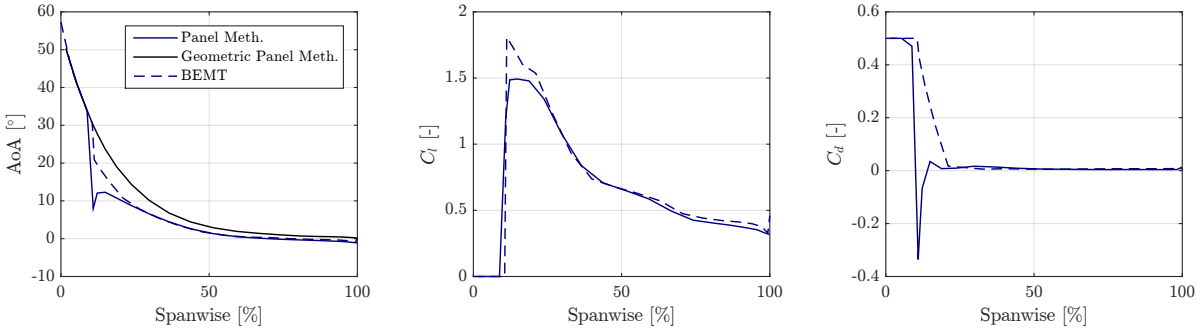

(a) AoA, lift and drag coefficients along the blade span

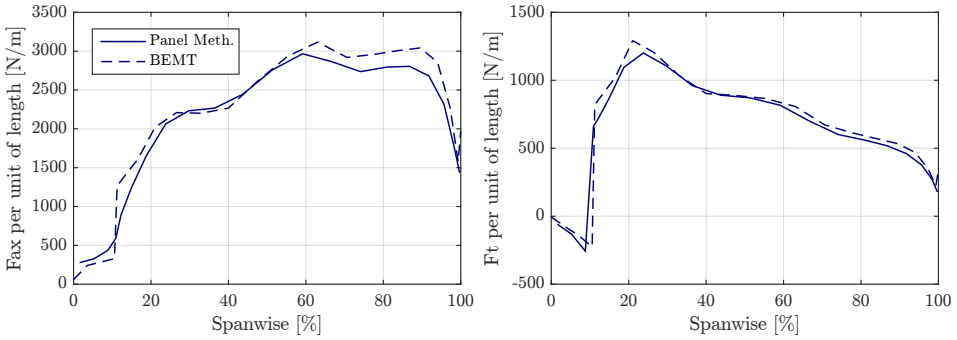

(b) Axial and tangential forces along the blade span

Figure 4.21: NREL 5MW case comparison between ARDEMA and AeroDyn - Validation for TSR = 5.3 - $V = 15m/s$

steps per rotation for ARDEMA. Sensitivity studies have shown that decreasing ARDEMA time step does not significantly change the results, but increases a lot the computational time. The simulated time needed for proper convergence of the wake in ARDEMA is around 100s, i.e. 20 rotations.
The present cases are in line with the validity domain of the BEMT: steady conditions, very lightly skewed wake caused by the tilt angle and realistic TSR values. Fig. 4.20 to 4.22 present the main aerodynamics results obtained with both BEMT (AeroDyn) and panel method (ARDEMA). The mean AoA, lift and drag coefficients, axial and tangential forces along the blade span are plotted. For the three cases, the same trends can be observed. In ARDEMA, a peak can be observed close to the root in the AoA, causing large difference in lift and drag coefficients compared to AeroDyn. This is caused by the separation between emitting and non-emitting sections: a tip effect is created at the end of the wake close to the root because of the spanwise gradient of vorticity, with a downwash that reduces the effective AoA. This issue has little impact on the whole forces as they are small for these sections. A good agreement is found for the three cases, despite some differences depending on the cases. For the highest TSR case at $V = 11.4m/s$ where the rotor is the most loaded for $V = 11.4m/s$, a significant discrepancy is found on the tangential force after midspan, with a higher value for AeroDyn. This is also observed on axial force and lift coefficient, but with a much lower intensity. The difference between geometrical and effective AoA is the largest in this case and induction is thus the strongest in such case. The largest differences are thus expected for this high TSR value, as it is the most challenging case regarding calculation of induction. At the lower wind TSR of 5.3, and wind speed of $V = 15m/s$, the load distribution on the blade changes. The AoA at the tip is much lower because of the pitch angle, and the axial and tangential forces are reduced. The tangential force, responsible for the torque and thus the power generated by the

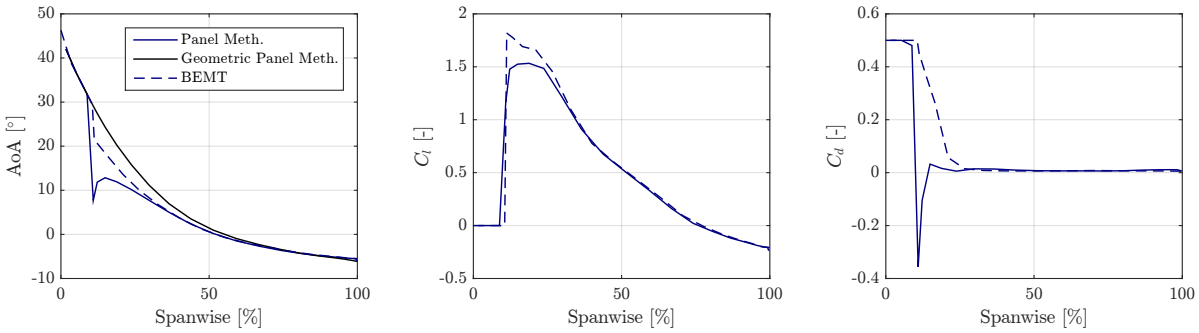

(a) AoA, lift and drag coefficients along the blade span

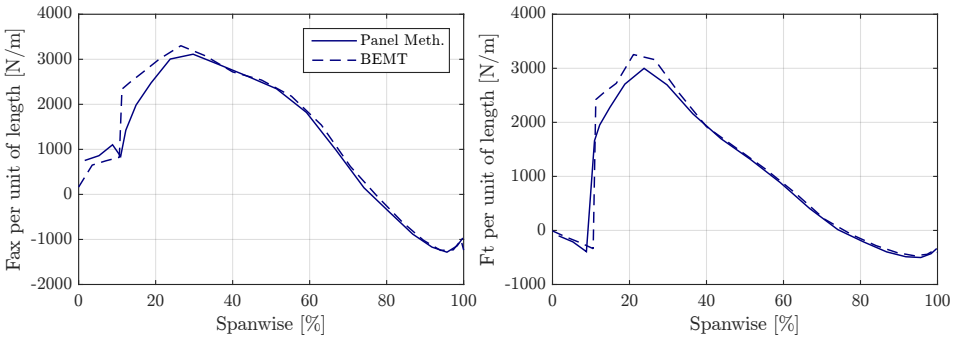

(b) Axial and tangential forces along the blade span

Figure 4.22: NREL 5MW case comparison between ARDEMA and AeroDyn - Validation for TSR = 3.2 - $V = 25m/s$

turbine is larger in the first half of the blade. At $V = 15m/s$, this behavior is even more pronounced as the AoA are negative on a large span of the blade. The torque is then mostly generated in the first half of the blade, while at the tip, the axial and tangential force are negative. Table 4.5 compares the mean

Table 4.5: Comparison between panel method and BEMT - Torque and thrust - No Yaw, Uniform wind, rigid case

Code	Panel Method		BEMT		Relative diff.	
Wind vel. [m/s]	P_{aero} [kW]	T_{aero} [kN]	P_{aero} [kW]	T_{aero} [kN]	P_{aero} [%]	T_{aero} [%]
11.4	5520	740	5960	745	+8.0	+0.7
15	5091	406	5294	422	+4.0	+3.8
25	4388	237	4789	251	+9.1	+5.6

aerodynamic power and thrust between ARDEMA and AeroDyn. For all cases, it appears that power and thrust are overpredicted in AeroDyn compared to ARDEMA, which is in line with the observations made on the tangential forces in the previous figures. At the nominal wind speed of $11.4m/s$, the aerodynamic power is higher than expected. At $25m/s$, the power predicted is lower than the expected 5.3MW, which can be explained by a too high pitch angle for this configuration. These differences observed in both ARDEMA and FAST with the expected power are caused by the difference in the DS data, in particular the normal coefficient slope computed by ARDEMA.

4.3.3 Validation of coupling between FAST and ARDEMA

In the present sections, the impact of controller and elasticity is considered. For all computations presented in this work on NREL 5MW turbine, a time step of 0.02s has been used for ElastoDyn, while a time step of 0.08s is used in ARDEMA. This ensures to have at least 60 time steps per rotation. The aerodynamic forces are kept constant during the time steps were ARDEMA is not called. The time step in AeroDyn is the same as ElastoDyn. The cases investigated are presented in Table 4.6. The three

Table 4.6: Cases for validation of the coupling FAST/ARDEMA - Uniform wind with no shear

Wind vel.	TSR	Pitch angle	Yaw angle	Controller	Elasticity
11.4/15/25 m/s	7.0/5.3/3.2	0°/10.5°/23.5°	0°	No	Elastic
11.4/15/25 m/s	Controlled	Controlled	0°	Yes	Elastic

cases presented in the purely aerodynamics validation are simulated including elasticity of the blades and tower with and without controller. If elasticity is enabled and no initial deflections are provided, strong oscillations appear at the beginning of the simulation and fades slowly thanks to damping. A case without controller but with elasticity thus requires around 200s of simulated time, so around 40 rotations in nominal regime. Only the 20 last rotations can be used for analysis in order to have a convergence of both structure and wake (in the case of ARDEMA). When the controller is enabled, the rotational speed and pitch angles are handled by the controller instead of being fixed at a constant value. A case with controller requires 400s of simulated time as the controller needs around 200s to go from startup to nominal regime.

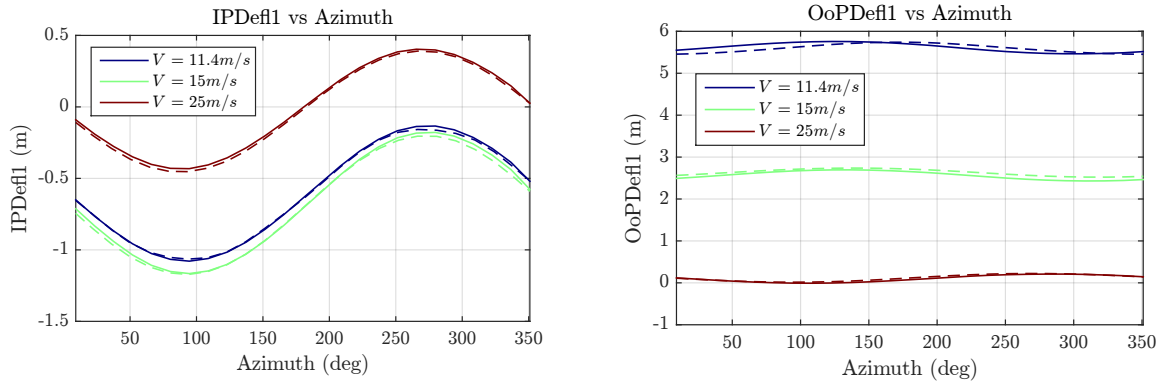

(a) In the rotor plane

(b) Out of the rotor plane

Figure 4.23: Comparison between ARDEMA (full) and AeroDyn (dashed) - In-plane (left) and Out-of-plane (right) deflections of blade 1 per azimuthal position - Yaw 0° - Elastic case without controller

The in and out of rotor plane deflections are presented in Fig. 4.23 for the cases without controller. The deflections are very similar for both ARDEMA and AeroDyn. The maximum deflections are observed for $V = 11.4m/s$ while at $V = 25m/s$ nearly no deflection is noticed. The spanwise distribution of the axial and tangential forces can explain this behavior, with forces concentrated at the tip for $V = 11.4m/s$ while the first half of the blade is more loaded at $V = 25m/s$.

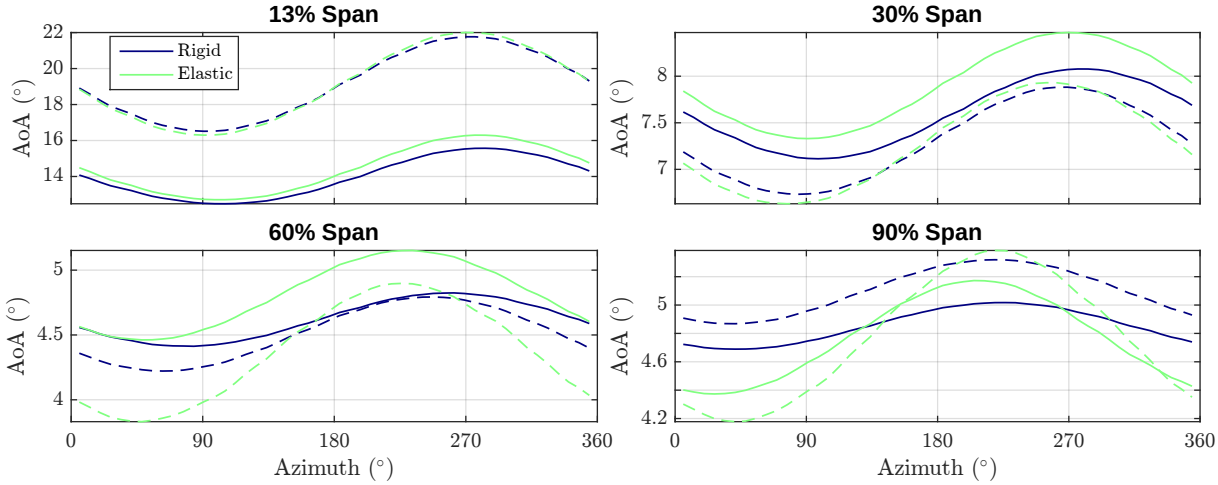

Figure 4.24: Comparison of AoAs for several spanwise positions - ARDEMA (full line) and FAST (dashed line) - $V = 11.4m/s$

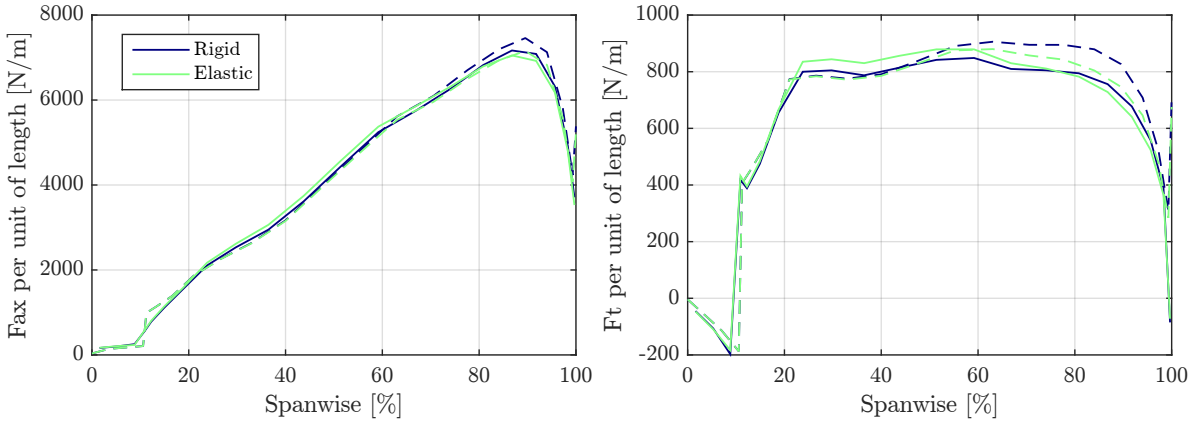

Figure 4.25: Comparison between axial and tangential forces - ARDEMA (full line) and FAST (dashed line) - $V = 11.4m/s$

Remarks on aerodynamics post-processing in ARDEMA and FAST: The results comparing variables at specific spanwise positions must be considered keeping in mind some important aspects regarding the discretization of the blade in ARDEMA and AeroDyn. The same discretization of the input sections is used in both codes. However, in AeroDyn v15, the sections are used for calculations of all aerodynamics variables, while in ARDEMA values are computed between two sections, defined as elements. These elements correspond to the panels between two sections, and the pressure can be integrated over these panels to obtain the inviscid force on the corresponding element which is then corrected to account for viscous effects. An interpolation is performed in ARDEMA between the polars of the two closest sections to define the polars at elements. The output variables in ARDEMA are then defined at these elements spanwise positions. In order to compare aerodynamics values at the same spanwise positions during post-processing, the closest section from a given spanwise position is chosen in FAST while in ARDEMA, the values of the two adjacent elements are averaged. This methodology gives accurate results in case of linear variations from all variables from one element to another. Close to the

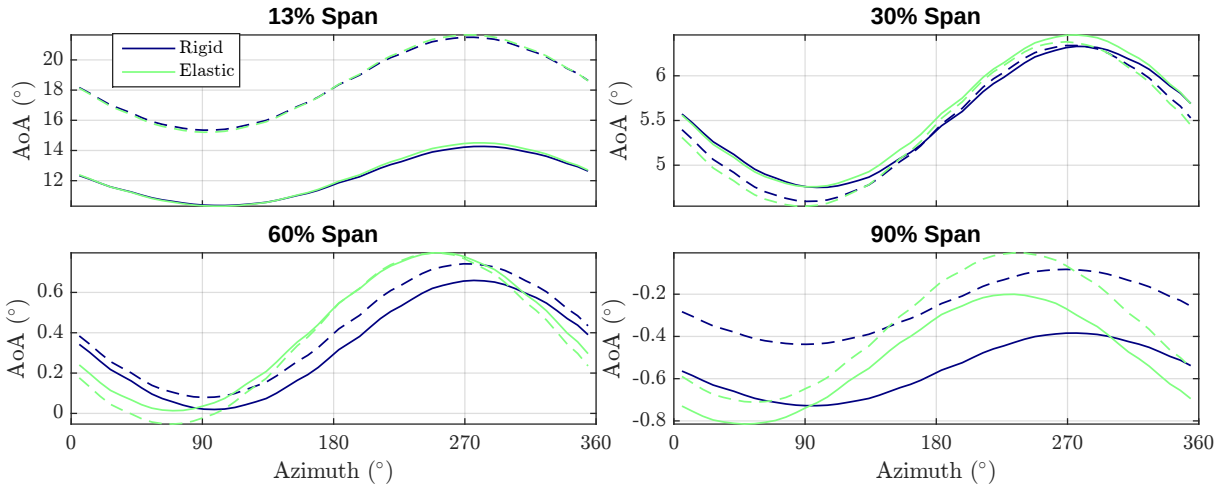

Figure 4.26: Comparison of AoAs for several spanwise positions - ARDEMA (full line) and FAST (dashed line) - $V = 15m/s$

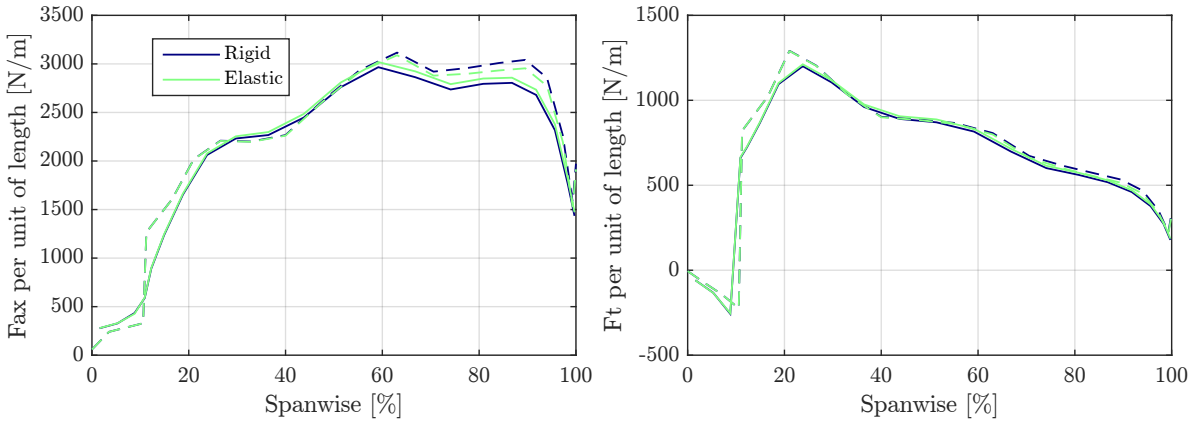

Figure 4.27: Comparison between axial and tangential forces - ARDEMA (full line) and FAST (dashed line) - $V = 15m/s$

root, the strong variations of sectional geometry can induce some differences. More specifically, the stall angle and force coefficients around stall can be very different from one section to another for a given AoA, and thus the force coefficients plotted for FAST and ARDEMA can show significant differences. The same process is conducted to obtain the sectional forces passed to the structural solver which are then interpolated on the structural grid. In most of the next figures comparing AoA, force coefficients or other aerodynamics variables, four spanwise locations have been chosen: 13%, 30%, 60% and 90% of the rotor radius. For the spanwise location of 30%, the section geometry evolves quickly, and thus the differences observed between ARDEMA and AeroDyn on force coefficients must be considered keeping these limitations in mind. However, the plotting of this variables as functions of spanwise position is not suffering from this issue as the spanwise location plotted are the section positions for AeroDyn and the element positions for ARDEMA.

Fig. 4.24 to 4.29 present the effective AoA at several spanwise positions, and the axial and tangen-

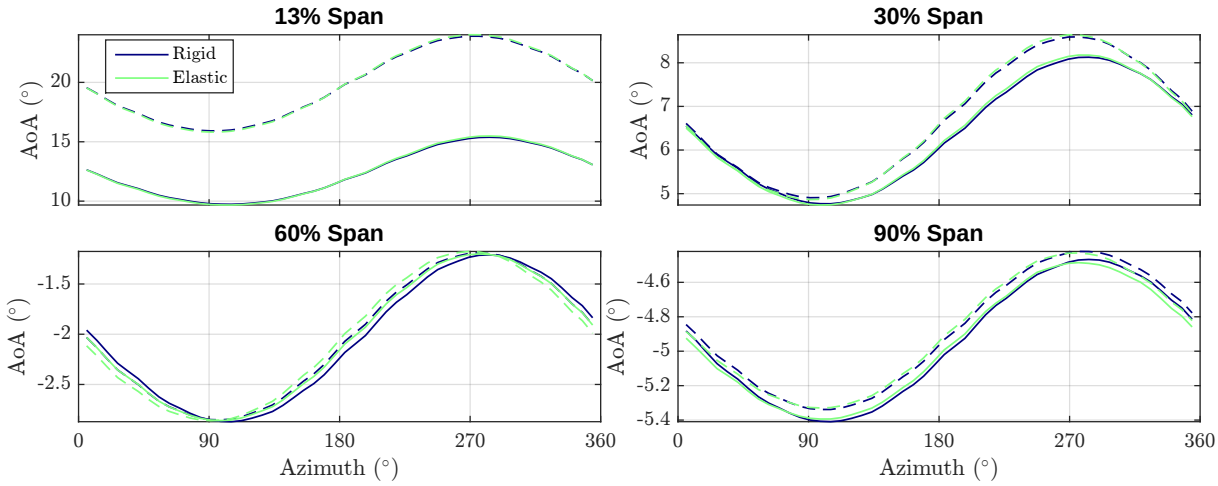

Figure 4.28: Comparison of AoAs for several spanwise positions - ARDEMA (full line) and FAST (dashed line) - $V = 25m/s$

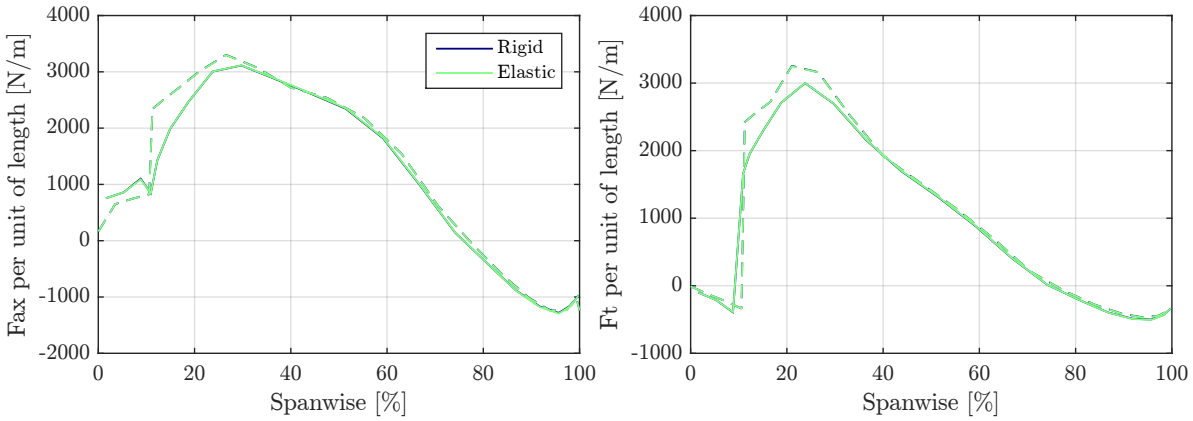

Figure 4.29: Comparison between axial and tangential forces - ARDEMA (full line) and FAST (dashed line) - $V = 25m/s$

tial spanwise force distributions. They are plotted against the azimuthal position θ of the blade, with a value of 0° when the blade is in top vertical position. The rigid cases presented in the previous section are compared to the elastic cases without controller. For the cases with $V = 11.4m/s$ and $V = 15m/s$, the AoAs are not the same when comparing elastic and rigid cases. In the case of the panel method, elasticity increases the AoA for sections around midspan, increasing the forces. The behavior is the opposite for the tip, with a smaller AoA. For AeroDyn, the AoA decreases over the full span for elastic cases. When looking at the tangential force along the span, it appears that the tangential force at the tip decreases a lot in AeroDyn when elasticity is enabled, while it increases in ARDEMA at the root. This is clearly in line with the observations on the AoA. It can also be noticed that when enabling elasticity the amplitude and phase of the AoA variations caused by the tilt angle change. At $V = 25m/s$, the deflection out of the rotor plane is very small as the main axial forces are located closer to the root. The consequence is that for this case the AoAs and forces along the blade are very similar between rigid and elastic cases.
Such observation can be explained by the way induction is treated in both methods. As elasticity modi-

fies the shape of the blade, the aerodynamic influence of each section on the other and thus the induced velocity fields are not the same. In the case of the panel method, the trailed vorticity is taken into account and the induction is changed even on sections close to the root not affected by the geometry deformation. In the case of BEMT the differences are mostly caused by the different position of the sections themselves compared to rigid case. The consequence is that the AoA is modified mostly on the tip parts where the change in geometry is the largest for the BEMT, while the AoA can be modified everywhere on the blade for panel method.

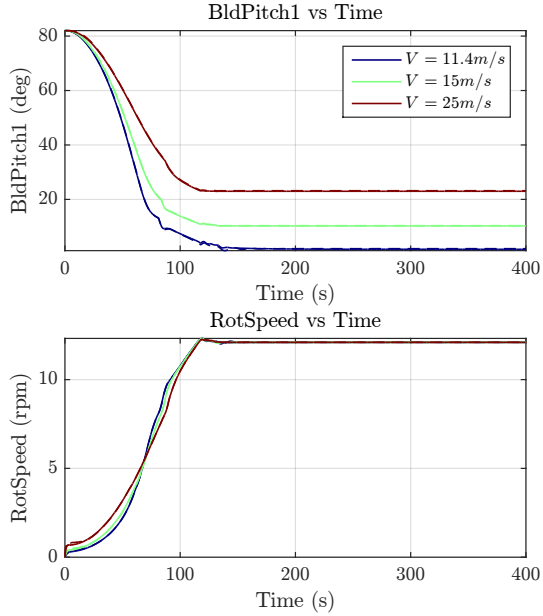

(a) Blade pitch (top) and rotational speed (bottom)

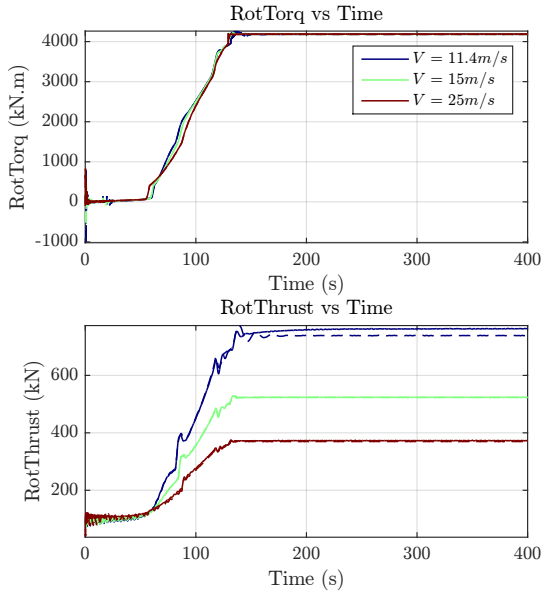

(b) Rotor torque (top) and thrust (bottom)

Figure 4.30: Comparison between ARDEMA (full) and AeroDyn (dashed) - Yaw 0° - Elastic case with controller

In Fig.4.30, pitch angle, rotational speed, torque and thrust are plotted against simulated time for the cases with controller and elasticity enabled. With the enabled controller, the pitch angle is modified in order to reach the correct rotation speed, keeping constant nominal torque and thus power. The beginning of the simulation corresponds to the start-up of the turbine, with blades in standstill position (pitch angle of 82°) and no rotational speed. The thrust is the highest for the case with highest TSR and induction, at $V = 11.4m/s$. In next tables 4.7 and 4.8, the power and thrust are not directly the ones obtained through the summing of the aerodynamic forces on the blade sections, but are the mechanical forces transmitted to the generator shaft. The impact of gravity and acceleration forces of the full mechanical chain is accounted for.

For the cases without control, the power in the rigid case (see Table 4.5) is much higher for AeroDyn at $V = 11.4m/s$ while it is very similar between both methods in the elastic case, as a consequence of the observations on the tangential forces from Fig. 4.25. At $V = 25m/s$ the difference between both methods remains the same as the blade deformation is very small. Including the controller modifies these observations: the power output is kept constant for all cases, around 5.3MW, by adapting the pitch values. It appears that very small variations in the pitch angle change a lot the power output: at $V = 25m/s$, the nearly 10% difference observed in power for the case without controller is erased by the 0.9% difference in pitch angle. The thrust is then also the same for ARDEMA and AeroDyn, except for the case at

Table 4.7: Comparison between panel method and BEMT - Torque and thrust - No Yaw, Uniform wind, elastic case, no control

Code	Panel Method		BEMT		Relative diff.	
Wind vel. [m/s]	P_{rotor} [kW]	Thrust [kN]	P_{rotor} [kW]	Thrust [kN]	P_{rotor} [%]	Thrust [%]
11.4	5659	848	5713	829	+0.9	-2.3
15	5148	511	5211	517	+1.2	+1.1
25	4367	334	4781	347	+9.5	+4.1

Table 4.8: Comparison between panel method and BEMT - Torque and thrust - No Yaw, Uniform wind, rigid case, controller

Code	Panel Method			BEMT			Relative diff.		
Wind vel. [m/s]	P_{rotor} [kW]	Thrust [kN]	Pitch [°]	P_{rotor} [kW]	Thrust [kN]	Pitch [°]	P_{rotor} [%]	Thrust [%]	Pitch [%]
11.4	5308	762	1.7	5297	738	1.9	-0.2	-3.1	+13.7
15	5301	524	10.3	5297	524	10.4	-0.1	0.0	+0.8
25	5305	373	23.0	5297	370	23.2	-0.1	-0.8	+0.9

$V = 11.4m/s$ where ARDEMA thrust is higher than in AeroDyn. The high induction for this case can indeed reveal some differences in the spanwise force distributions caused by differences in induction between both codes. Fig. 4.25 illustrates this phenomenon, with a small difference in power output of less than 1%, but with a very different spanwise distribution of the tangential forces. This clearly reveals that by including elasticity and control, the differences observed between two aerodynamics solvers can be totally different than in a rigid case.

4.4 Application to yaw misalignment

Historically, wind turbines operating in yaw conditions have suffered increased damages not predicted by standard BEM. Hansen [80] and Snel [183] conducted extensive studies on the topic in the 90s in order to understand the yaw loads and propose suitable models for engineering. Some specific DLCs recommend to investigate yaw control failure at extreme loads conditions, justifying the need to estimate correctly the loads in such conditions. Wake steering is another topic that raises interest in better predicting fatigue loads of turbines operating in yaw conditions. Indeed in large wind farms with several rows of wind turbines, each turbine often operates in the wake of other turbines. The wind received by a downstream turbine is lower than upstream, with a loss of power that can reach 40%. In order to reduce this loss, the principle of wake steering is to yaw the upstream turbine in order to change the wake orientation so it has a reduced impact on downstream turbines. The work of Jimenez [96] with LES or Fleming [56] with experimental measurements provides much insights in the topic. The purpose of the section is to compare a panel method and a BEMT solver in yaw conditions, analyzing the impact of DS and skewed wake model on the resulting loads. Some differences are known to be expected from a purely aerodynamics point-of-view, and the idea here is to assess whether realistic simulations including control,

turbulent wind and elasticity change the conclusions compared to only aerodynamics simulations. Simulations are conducted on the NREL5MW wind turbine in yawed conditions in uniform and turbulent winds. Maximum investigated yaw angle is $+/-40°$. For higher yaw, difficulties appeared on ARDEMA because of the large AoA in turbulent wind. Such conditions create strong rollups with penetrations of panels into others. The core models handle such issues, but at certain levels, singularities appear in the wake with unrealistic panel strength. The wake is then destabilized because of high induced velocities on some panels, and the flow solver ends up crashing. It is considered here that investigating higher yaw angles is also too challenging for the DS models that do not handle correctly very high AoAs.

4.4.1 Uniform Wind

4.4.1.1 Comparison between aerodynamics solvers

Uniform wind conditions are first investigated, with cases presented in Table 4.9. In this section, ARDEMA is compared to AeroDyn with and without skewed wake model in yawed conditions to test the accuracy of the skewed make model against a panel method. The purpose here is to assess the differences between the several models with wind conditions that do not interfere with the load analysis. To compare

Table 4.9: Yaw misalignment cases - Uniform wind with no shear

Wind vel.	TSR	Pitch angle	Yaw angle	Controller	Elasticity
11.4 m/s	7.0	0°	-40°,-20°,0°,20°,40°	No	Rigid
25 m/s	3.2	15.95°	-40°	No	Rigid
5-25 m/s	Controlled	Controlled	-40°,-20°,0°,20°,40°	Yes	Elastic

aerodynamics solvers for the same operating conditions of the wind turbine, rigid cases without controller are performed. At the nominal wind speed of $11.4m/s$, a constant rotational velocity of 12.1 RPM has been chosen for all yaw angles despite the fact that for high yaw angles the controller would operate the turbine at a lower speed, as the torque (and power) would be lower than without yaw. At $25m/s$, the pitch angle chosen is the one obtained with the controller for the rigid case without yaw misalignment. Then wind speeds from $5m/s$ to $25m/s$ with wind speed bins of $2m/s$ are investigated including controller and elasticity, for five yaw angles. In most of the next figures, the cases named "BEMT" correspond to AeroDyn with skewed wake model while the "BEMT No Skew" cases correspond to AeroDyn without skewed wake model.

The results for the cases at $11.4m/s$ are presented in Table 4.10. At such high TSR, with the same pitch angle and constant rotational speed, BEMT predicts much lower power and thrust than panel method as the yaw angle increases. The skewed wake model has little influence on both power and thrust, except at +/-40° yaw misalignment where the skewed wake model increases the power. Small differences can be noticed at 0° yaw misalignment between the two AeroDyn configurations caused by the tilt angle. It is also interesting to notice that positive and negative yaw angles give very close power and thrust.

Fig. 4.31 to 4.35 plot the AoA, axial and tangential forces for the rigid case without control at $V = 11.4m/s$. When comparing ARDEMA, AeroDyn with and without skewed wake model, the phasing and amplitude of AoA is different depending on the model. Positive and negative yaw angle give the same mean AoA and forces over one rotation, but with a phasing of 180°. When the skewed wake

Table 4.10: Comparison between panel method and BEMT - Torque and thrust - With Yaw, $V = 11.4m/s$, rigid case, no controller

Code	Panel Method		BEMT		BEMT No Skew		Relative diff. vs Panel Meth.			
Yaw angle [°]	P_{aero} [kW]	T_{aero} [kN]	P_{aero} [kW]	T_{aero} [kN]	P_{aero} [kW]	T_{aero} [kN]	P_{aero} %		T_{aero} %	
-40	3387	582	2670	389	2540	387	-21.2	-25.0	-33.2	-33.5
-20	4962	702	4962	642	4934	640	0.0	-0.6	-8.5	-8.8
0	5520	740	5960	745	5923	742	8.0	7.3	0.7	0.2
20	4970	702	4962	642	4934	640	-0.2	-0.7	-8.5	-8.9
40	3388	582	2670	389	2540	387	-21.2	-25.0	-33.2	-33.5

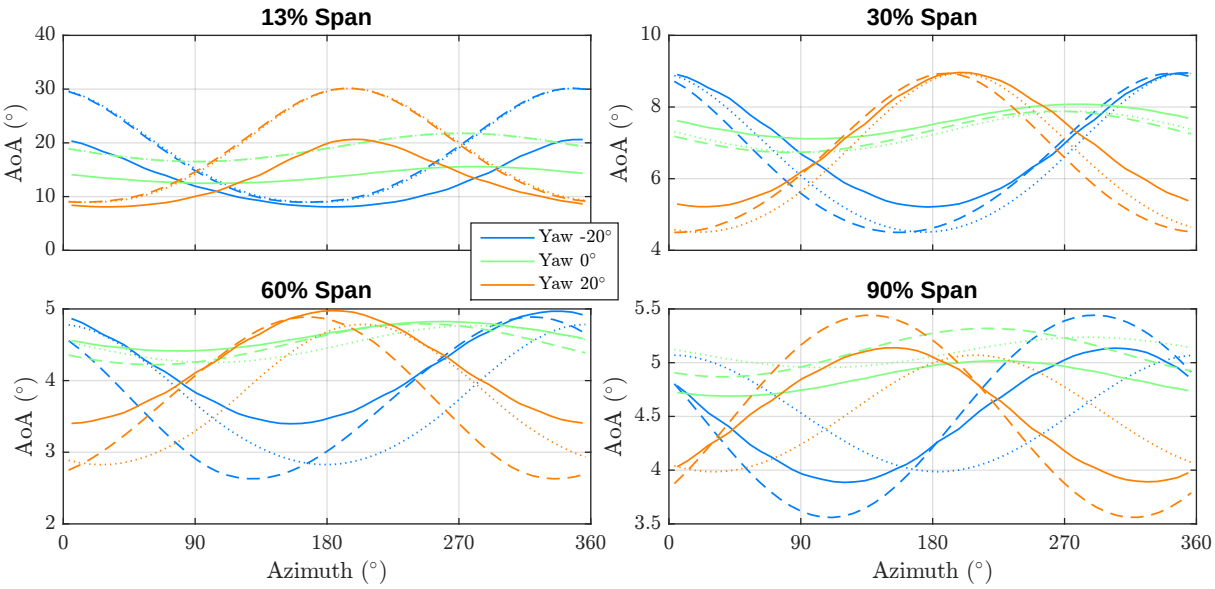

Figure 4.31: AoA comparison between ARDEMA (full line), AeroDyn with (dashed) and without (dotted) skewed wake model - Rigid case without control - Yaw +/-20° - $V = 11.4m/s$

model is deactivated, it appears that the phasing is closer to the geometrical variations of AoAs, which can be understood by the fact that no specific azimuthal handling of induction is done. The 0° yaw misalignment case reveal a 90° difference in phasing because of the tilt angle. AoA phases without skewed wake model are thus the same as the ones identified in Chapter 2.3.3. However, the skewed wake model implemented in FAST introduces a different phasing than the geometrical one in the calculation of induction, thus modifies the phase of the AoA. Compared to ARDEMA, it appears that the difference in phase and amplitude is overestimated by the skewed wake model from AeroDyn. For a yaw misalignment of +/-20°, the mean axial and tangential forces over one period are very close for both solvers as illustrated in Fig. 4.32, and the same for positive and negative yaw. This however does not reflect the variations over one rotation, and when plotting the standard deviation in Fig. 4.33 it can be observed that at the tip a much higher standard deviation is observed for AeroDyn with skewed wake model. This implies that different fatigue loading can results from this different models despite very close mean values. With a yaw misalignment of +/-40°, the same differences in the phasing of AoA is noticed. The mean AoA

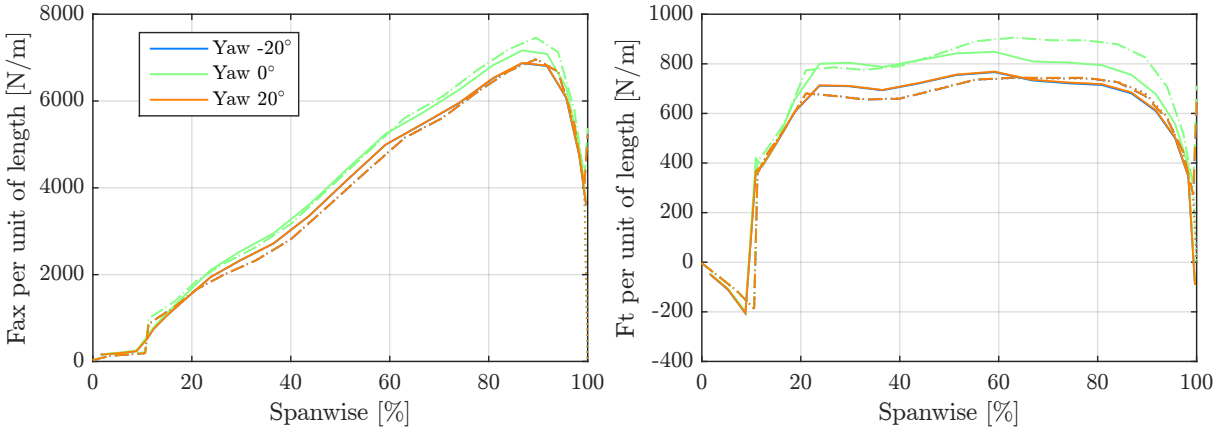

Figure 4.32: Mean axial and tangential forces comparison between ARDEMA (full line), AeroDyn with (dashed) and without (dotted) skewed wake model - Rigid case without control - Yaw +/-20° - $V = 11.4m/s$

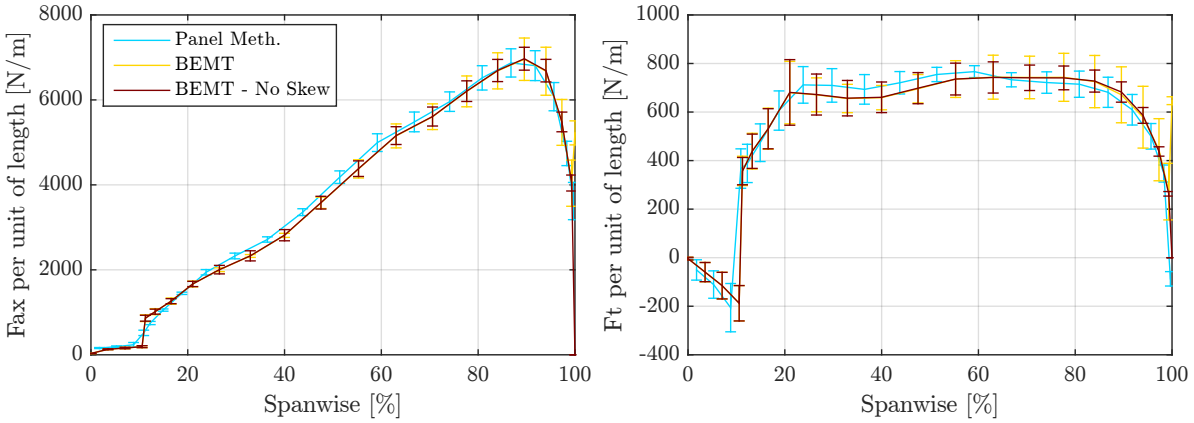

Figure 4.33: Mean value and standard deviation of axial and tangential forces comparison - Rigid case without control - Yaw -20° - $V = 11.4m/s$

appears to be higher in ARDEMA on the whole blade span, with higher axial and tangential forces, explaining the higher power and thrust from Table 4.10.

The main axis definitions and corresponding moments in FAST are illustrated in Fig. 4.36. The different names of the output channels of AeroDyn used in this study are also defined. The fore/aft RNA (Rotor Nacelle Assembly) moment is named *YawBrMyn* and is positive when the hub is pushed up (nose-up moment). The side/side RNA moment *YawBrMxn* is related to the torque applied by the rotor on the shaft, and is thus always positive. The yaw RNA moment *YawBrMzp* is negligible when no shear, tilt or yaw is applied. For the blade, the flapwise moment *RootMyb1* is also mainly positive when the blade is loaded while the edgewise moment *RootMxb1* is strongly affected by the azimuthal position because of the impact of gravity.

In Fig. 4.37, the side/side, fore/aft and yaw RNA moments are plotted against the azimuthal position of blade 1. At 0° blade 1 is in top vertical position. For the three moments, the variations during one rotation have a 3-p period as the RNA moments result from the forces on the 3 blades. It can also be noticed that

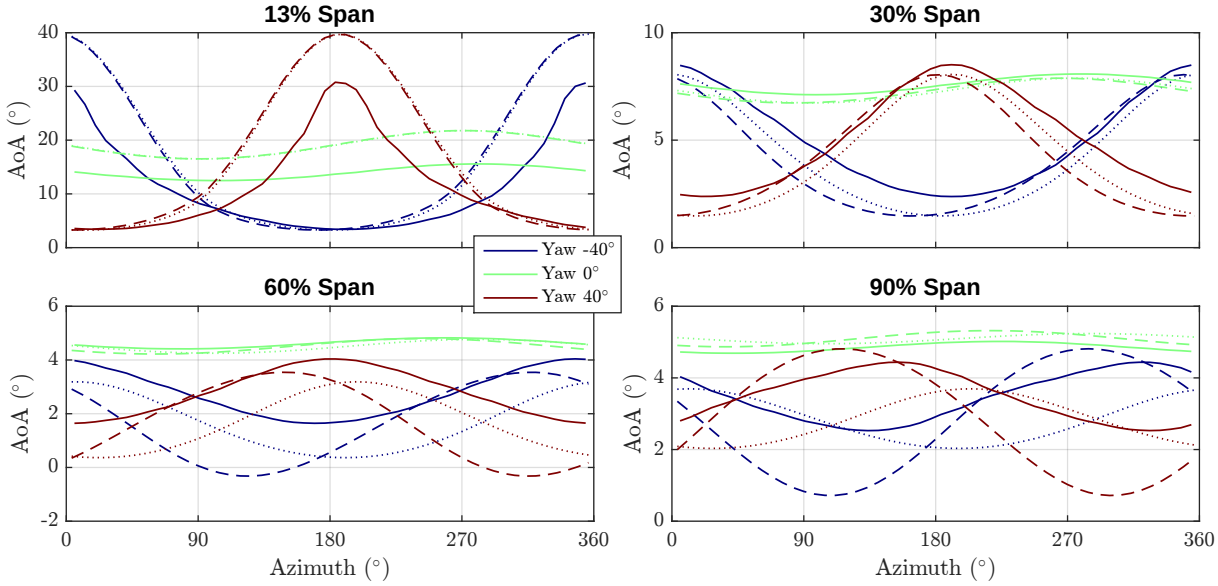

Figure 4.34: AoA comparison between ARDEMA (full line), AeroDyn with (dashed) and without (dotted) skewed wake model - Rigid case without control - Yaw +/-40° - $V = 11.4m/s$

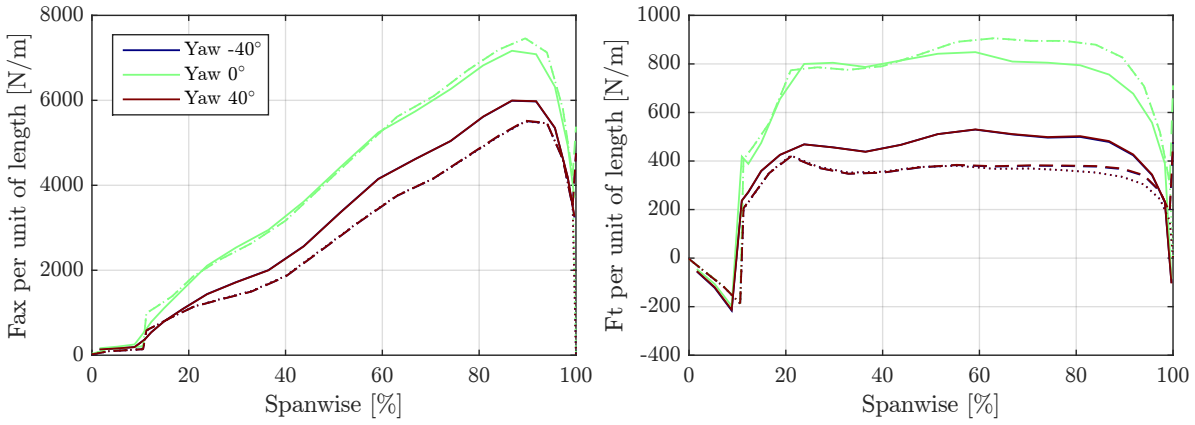

Figure 4.35: Mean axial and tangential forces comparison between ARDEMA (full line), AeroDyn with (dashed) and without (dotted) skewed wake model - Rigid case without control - Yaw +/-40° - $V = 11.4m/s$

the sign of yaw misalignment has a huge impact on the fore/aft and yaw moment, while the side/side moment behavior is following the tendency of torque: higher torque and power in AeroDyn implies higher side/side moment compared to ARDEMA. However, despite same power output at +/-20°, the two AeroDyn configurations reveal some differences in the side/side moment, with a higher amplitude when the skew wake model is enabled. The yaw moment is very poorly predicted when using no skewed wake model, with opposite sign values compared to panel method and BEMT with skewed wake. Considering that the skewed wake models have been developed in order to improve the prediction of yaw moment, this result makes sense, but compared to ARDEMA the values obtained with skewed wake model seem very conservative. Furthermore the fore/aft RNA moment with the skewed wake model is not closer to

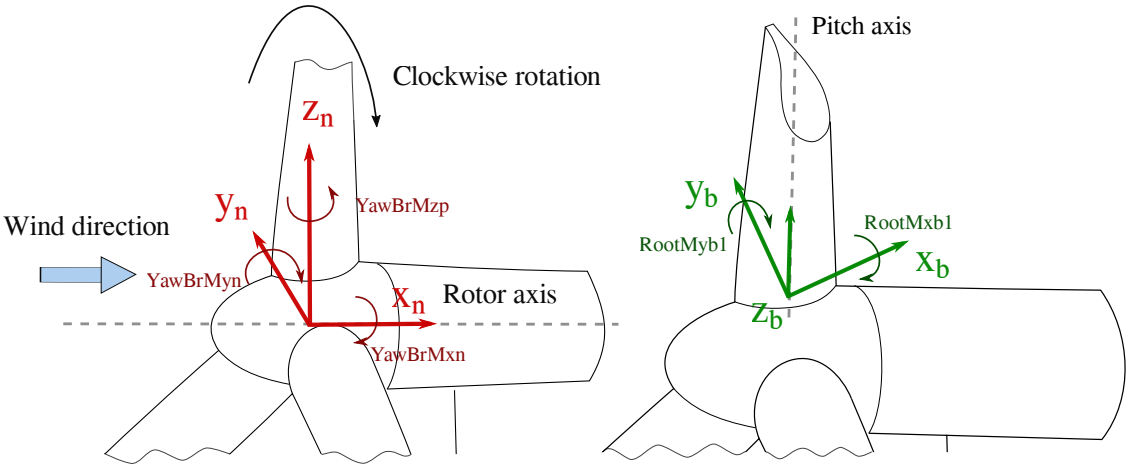

Figure 4.36: Definition of nacelle (left) and blade (right) reference frames in FAST

ARDEMA, in particular with a yaw misalignment of +40°.

In the next figures, the controller and elasticity are enabled and calculations are performed with wind speed varying from $5m/s$ to $25m/s$. The mean power, rotational speed and pitch angle are plotted against wind speed in Fig. 4.38. The nominal wind speed increases with yaw angle, as yaw misalignment reduces the efficiency of the turbine. Rotational speeds are then very different below nominal speed if the power output between two solvers is different. Once nominal wind speed is reached, a small difference in the pitch compensates the power difference between two solvers. It is important to keep in mind, when comparing two aerodynamics solvers in cases with a controller, that before nominal speed the output power and thus torque is not conserved, while after nominal wind speed it is.

The impact of elasticity and controller in a case with yaw misalignment is illustrated in Fig. 4.39. With the controller, the rotationnal speed and blade pitch variations are varying at a frequency different than 1-p or 3-p frequencies: the tower first natural frequency which is slightly excited by the periodic forces caused by yaw misalignment. The 3-p frequency also has some impact on rotational speed. The torque variations are smoothed by controller and elasticity compared to the rigid case. As a consequence, the amplitude of variations of the RNA moments is decreased.

The mean side/side, fore/aft and yaw moments are plotted against wind speed in Fig. 4.40. The maximum side/side moment appears for the highest torque, reached at nominal power. These values are not reached at the same time depending on the yaw angle, as the extracted power is lowered with yaw misalignment. Positive and negative yaw angles have a small impact. When using the skewed wake model, the difference in side/side moment before nominal wind speed is larger than without. The prediction of fore/aft moment in AeroDyn is closer without skewed wake model, especially around nominal wind speed where the induction is the highest. The yaw moment appears to be overestimated compared to ARDEMA when skewed wake model is used, and underestimated when not used respectively. At high wind speed where the induction is low and thus potential differences between ARDEMA and AeroDyn are reduced, all moments are in good agreement. The small difference with and without skewed wake model at yaw 0° is caused by the tilt angle. It is also responsible for the negative slope of the yaw moment at yaw 0°, as the impact of tilt on yaw moment is from a purely geometrical point of view equivalent to

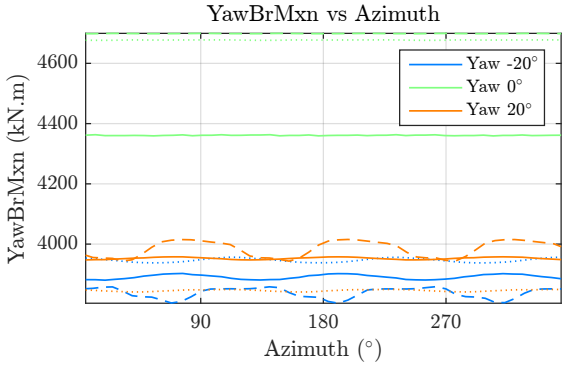

(a) Side/side moment - Yaw -20°, 0°, 20°

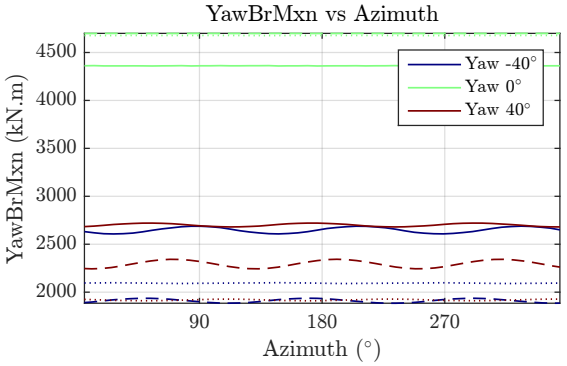

(b) Side/side moment - Yaw -40°, 0°, 40°

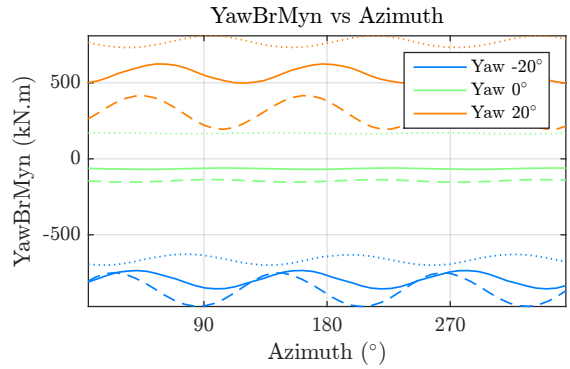

(c) Fore/aft moment - Yaw -20°, 0°, 20°

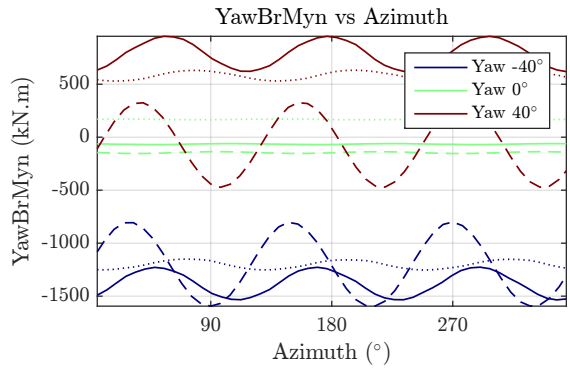

(d) Fore/aft moment - Yaw -40°, 0°, 40°

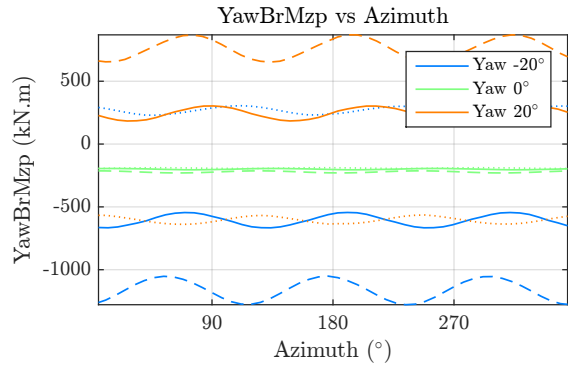

(e) Yaw moment - Yaw -20°, 0°, 20°

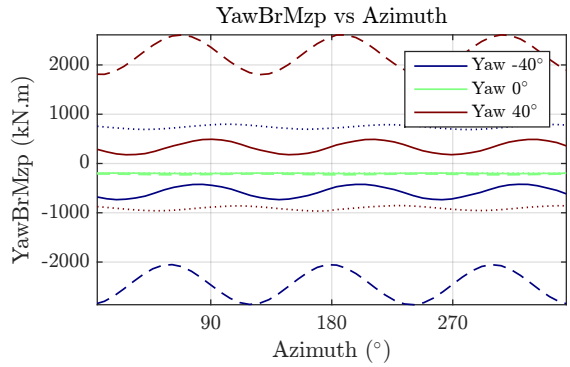

(f) Yaw moment - Yaw -40°, 0°, 40°

Figure 4.37: RNA Moment for several yaw misalignments - ARDEMA (full line), BEMT (dashed line) and BEMT without skewed wake model (dotted line) - Rigid cases without control - $V = 11.4m/s$

the impact of yaw misalignment on fore/aft moment.

Fig. 4.41 plots the AoA, the relative velocity and the axial force per unit length as function of the azimuthal position of the blade, for a section at a spanwise position of 90%. Two wind speeds are investigated: before nominal speed at $V = 13m/s$ with high induction and after nominal wind speed at $V = 25m/s$ with low induction. Both controller and elasticity are enabled. These figures help understanding the evolution of RNA moments with the wind speed represented in Fig. 4.40. The fore/aft RNA moment can be represented as the difference in axial force between the top and bottom half rotor disks, while the yaw tower top moment is induced by the difference in axial force between the left and right half rotor disks. For the fore/aft moment, the top half disk corresponds to the azimuthal positions

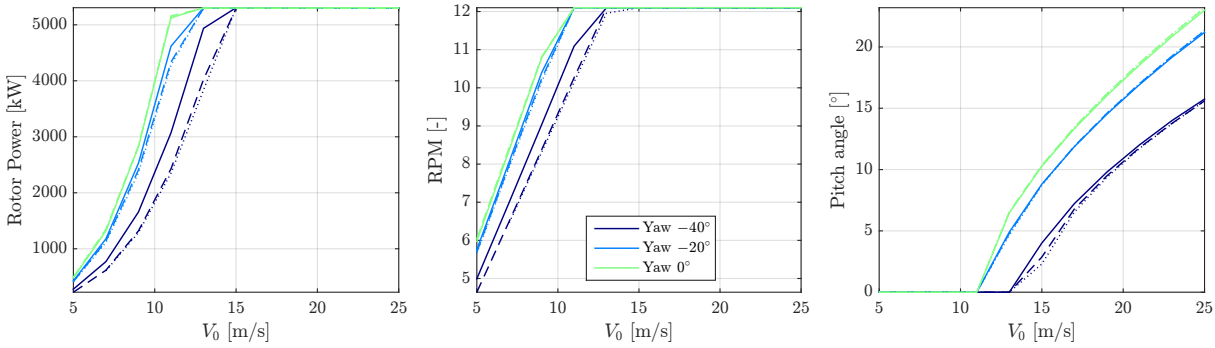

Figure 4.38: Rotor Power, rotationnal speed and blade pitch in yawed conditions - Comparison between ARDEMA (full line), AeroDyn with (dashed) and without (dotted) skewed wake model - Controller and elasticity enabled

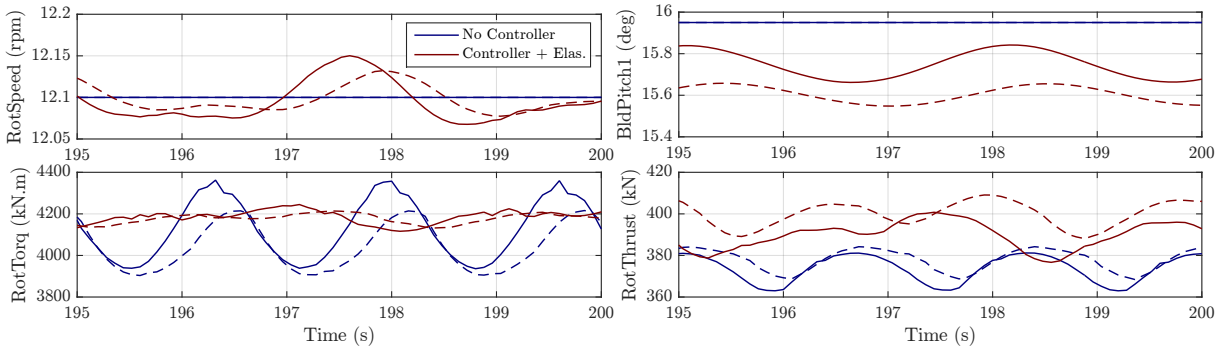

(a) Rotationnal speed (top left), blade pitch (top right), rotor torque (bottom left) and thrust (bottom right)

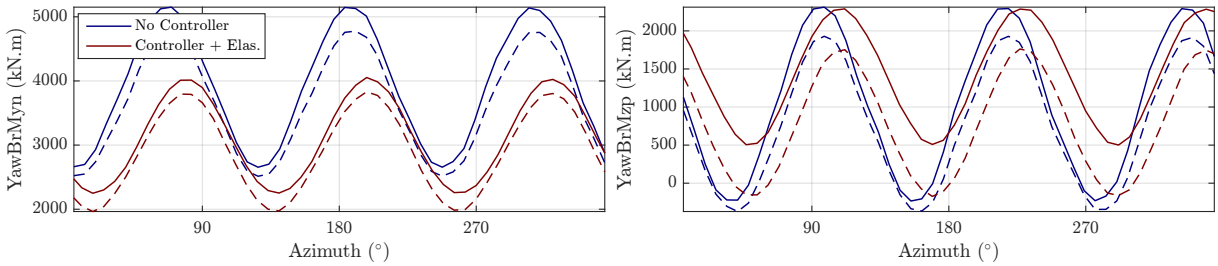

(b) Fore/aft (left) and yaw (right) RNA moments

Figure 4.39: Comparison between ARDEMA (full line) and AeroDyn (dashed) with and without controller and elasticity - Yaw -40° - $V = 25m/s$

from 270° to 90° (from 90° to 270° for the bottom half disk). For the yaw moment, the left half disk goes from 0° to 180° and the right from 180° to 0°. Based on the coordinate system from Fig. 4.36, a positive Fore/Aft moment corresponds to a nose up moment, which means that the top half disk is more loaded than the bottom half disk. A positive yaw moment implies that the left half disk is more loaded than the right half disk. For Fig. 4.41, a spanwise position of 90% has been chosen as the moment generated by a force is higher if it is far from the moment axis, and thus a force located at such spanwise position has a large impact on the total tower top moments. Both AoA, relative velocity and axial force have been plotted in order to reveal the impact of both relative velocity and AoA on the axial force. Indeed, the axial force is supposed to increase (when AoA is lower than stall angle) when AoA and

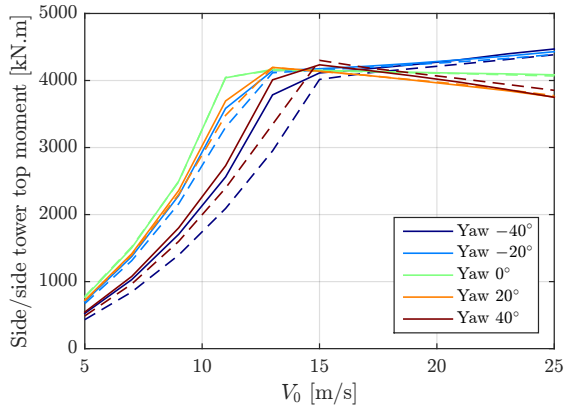

(a) Side/side moment - With skewed wake model

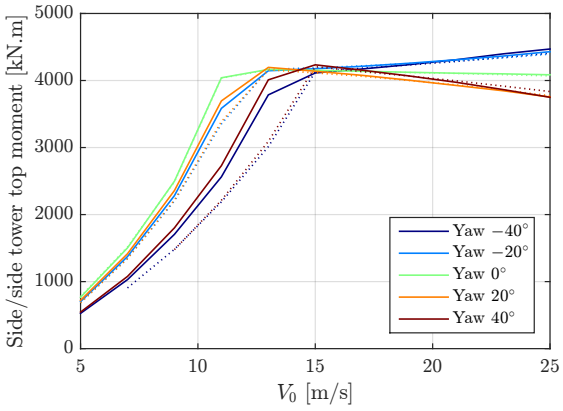

(b) Side/side moment - Without skewed wake model

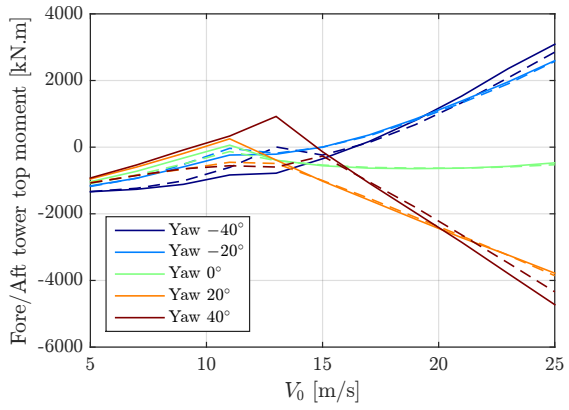

(c) Fore/aft moment - With skewed wake model

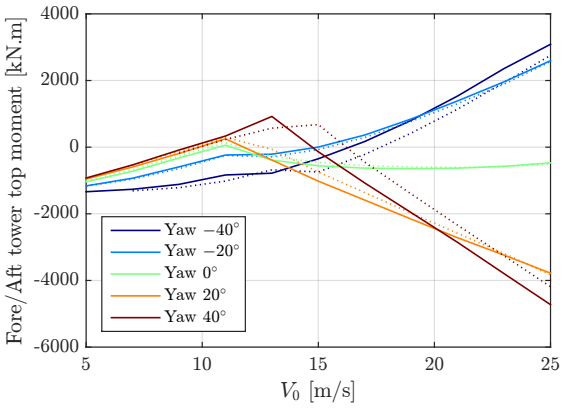

(d) Fore/aft moment - Without skewed wake model

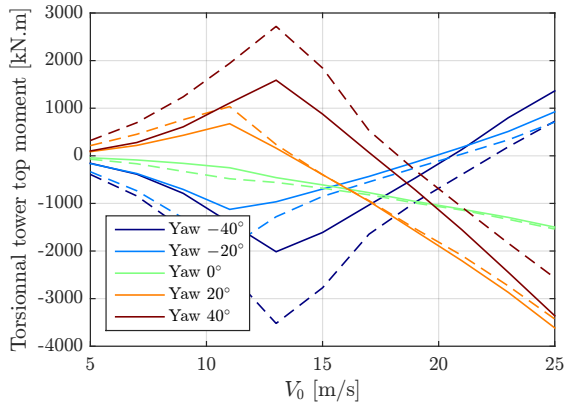

(e) Yaw moment - With skewed wake model

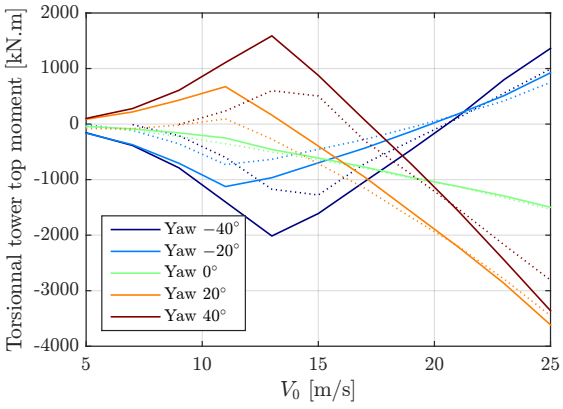

(f) Yaw moment - Without skewed wake model

Figure 4.40: Comparison between ARDEMA (full) and AeroDyn (dashed)- Mean RNA moments - Elastic cases with controller - Uniform wind

lift coefficient increase. However, the axial force is also proportional to the square of velocity. As it appears clearly that AoA and velocity are not in phase for both figures, the resulting axial force phase changes depending on both AoA and velocity phases. A maximum axial force reached around 0° or 180° creates a large disequilibrium between top and bottom rotor disks, implying large positive or negative fore/aft RNA moments respectively. This is clearly represented in the bottom figure from Fig. 4.41, representative of the high fore/aft tower top moments observed at high wind speed in Fig. 4.40. For yaw

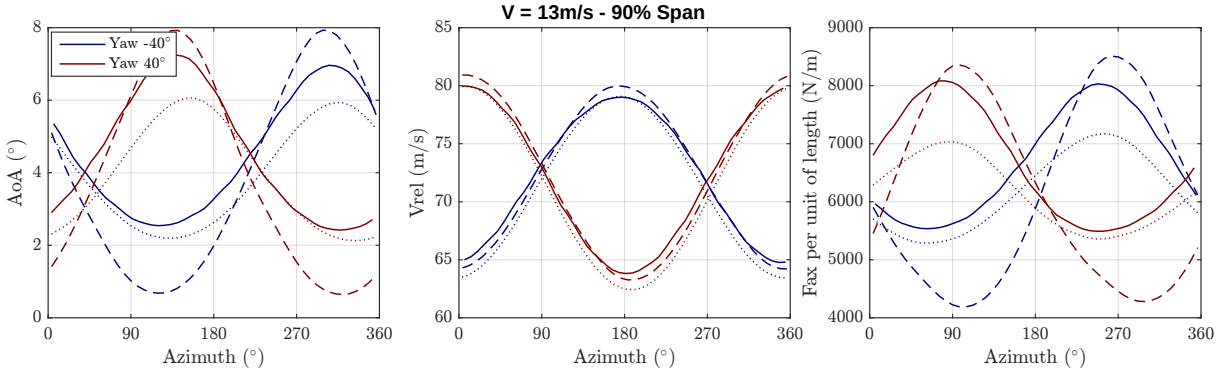

(a) $V = 13m/s$

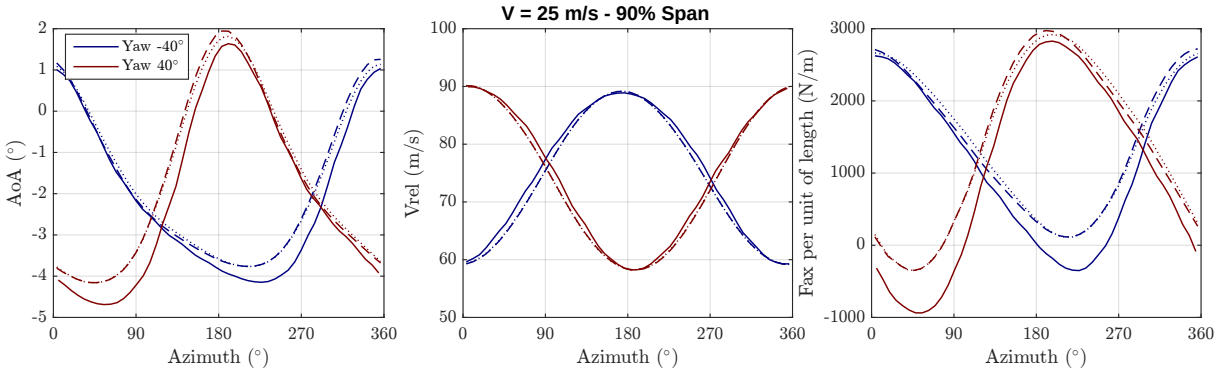

(b) $V = 25m/s$

Figure 4.41: Comparison of AoA, relative velocity and axial force per unit length - ARDEMA (full line), BEMT (dashed line) and BEMT without skewed wake model (dotted line) - Elastic cases with controller - Uniform wind

RNA moment, a maximum axial force reached around 90° or 270° is responsible for large positive or negative moments respectively. This is observed in the top figure from Fig. 4.41, representative of the peak observed around 13m/s in Fig. 4.40. The amplitude of the variations in axial force is also correlated with the tower top moments. Thus, at 13m/s the amplitude of the BEMT with skewed wake model is much larger than without skewed wake model. The imbalance between left and right rotor disks is then greater when using the skewed wake model, resulting in increased torsion as noticed in Fig. 4.40. It also appears clearly that there is a direct correlation between the variations in AoA and the variations in axial force, and despite the fact that the mean forces over one period are close, the mean yaw moment is impacted by this difference in amplitude of AoA. The same conclusion can be made for the fore/aft moment. Thus both amplitude and phase of the AoA variations over one period have a strong impact on tower top moments. Slight variations of both can change totally the resulting moments.
It appears clearly that the skewed wake model modifies the RNA moments, and that large differences are observed between panel method and BEMT with and without skewed wake model. In the next sections, all AeroDyn simulations are performed with the skewed wake model while the sensitivity of the same load channels to DS model is analyzed.

4.4.1.2 Sensitivity to dynamic stall model

The DS model is known to have an impact on RNA moments, as Hansen as shown by changing constants in Gormont DS model [79]. In this section, the sensitivity of Beddoes-Leishman model to the time constants T_p and T_f (see section 3.1.2 and Appendix A) is investigated. The different tested configurations are presented in Table 4.11. The recommended values are either multiplied or divided by a factor 2.
The T_b time constant was not changed mainly because of coding issues: this time constant is hard-coded

Table 4.11: DS parameters for sensitivity study

Case	Tp	Tf	Tb	Unsteady attached
Tp/Tf x1	1.7	3.0	3.93	Yes
Tp/Tf x0.5	0.85	1.5	3.93	Yes
Tp/Tf x2	3.4	6.0	3.93	Yes
No DS	-	-	-	AeroDyn: No / ARDEMA: Yes

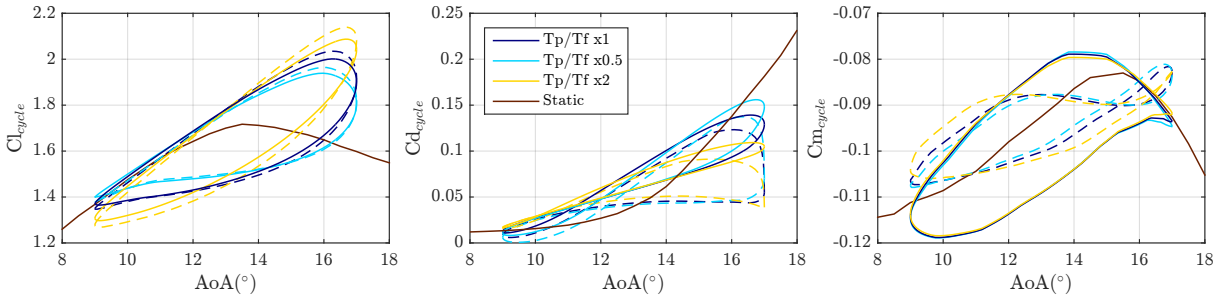

Figure 4.42: Sensitivity of DS model in a 2-D case - ARDEMA (full line) and AeroDyn (dashed line) DS models - DU35-A17 profile - $\alpha_{\text{mean}} = 13.0°$ - $\alpha_{\text{amp}} = 4.0°$ - $k = 0.10$

in FAST source code, and changing it requires to recompile the code for the 3 time constant values, then changing the call to FAST executable when performing sensitivity studies. This was considered to be a possible source of manual mistakes, and thus has not been considered here. From a scientific point-of-view, the purpose of the study was to investigate if some changes in the 2-D dynamic loops resulted in significant changes in the turbine loads. Modifying T_p and T_f time constant proved to change the 2-D hysteresis loops enough to investigate this point. Furthermore, most of B-L models does not include the second pressure lag. The 2-D hysteresis loops presented in 4.42 are plotted for both ARDEMA and AeroDyn DS models, showing similar behavior. Higher time constants reduce the width of the hysteresis lift and drag loops but increase the stall delay with a higher maximum lift. In ARDEMA, no changes are observed on moment coefficient loops as the separation module is not affecting unsteady moment calculation. When the DS model is not used in ARDEMA the hysteresis caused by the wake dynamic (equivalent to the attached module from B-L model) is still included has the unsteady induction can not be dissociated from the mean induction. In AeroDyn, deactivating the DS module implies that all 2-D unsteadiness is removed, including unsteady attached flow behavior.

Fig. 4.43 shows that at higher winds speeds the AoA variations for a yaw angle of -40° are much greater. Based on observations from section 4.3.2.2 mid chord sections are the ones creating the more loads at $V = 25m/s$. In the opposite, at lower wind speeds, the tip sections create more loads, but AoA

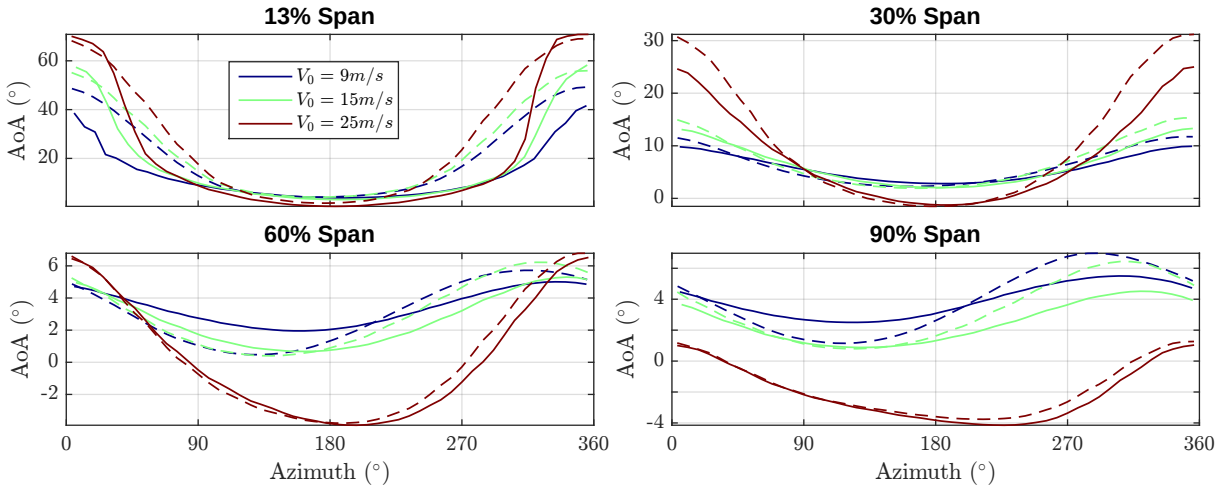

Figure 4.43: Variations of AoA for several wind speeds - Comparison between ARDEMA (solid lines) and AeroDyn (dashed lines) - Yaw -40° - Controller and elasticity enabled

variations have a smaller amplitude. At $V = 25m/s$, stall angle is reached on a large span of the blade and thus the impact of DS model is greater. Furthermore at high winds speed, tower top moments reach high values when there is yaw, implying that for such cases the impact of DS on RNA moments should be the greatest. For these reasons, this wind speed is chosen to assess the sensibility of RNA moments to DS.

In Table 4.12 the cases investigated on the NREL 5MW with yaw misalignment are presented. Both ARDEMA and AeroDyn are compared in order to assess whether both code have a different response to DS model. The impact of including DS model in the wake reduction is also investigated in rigid cases

Table 4.12: DS study cases - Uniform wind with no shear - Wind 25m/s - Yaw -40°

DS in wake reduction	Controller	Elasticity	DS cases
Yes	No	Rigid	Tp/Tf x1, Tp/Tf x0.5, Tp/Tf x2, No DS
No	No	Rigid	Tp/Tf x1, Tp/Tf x0.5, Tp/Tf x2, No DS
Yes	Yes	Elastic	Tp/Tf x1, Tp/Tf x0.5, Tp/Tf x2, No DS

without controller. The inclusion of controller and elasticity is then compared to rigid cases without controller.

The spanwise location of 30% is chosen for the next comparisons as the AoA reaches values much higher than stall angle, implying that dynamic stall occurs at this spanwise location. However, for this spanwise location, large difference can be observed between ARDEMA and AeroDyn caused by the differences between sections and elements and the polar interpolation in ARDEMA. These differences are limited when the lift coefficient is in the linear attached region, but static or dynamic stall can create much larger differences because of the large differences in lift coefficient between two sections at such angles. In Fig.4.44, the values of AoA are higher in AeroDyn for the considered section compared to ARDEMA. However because of the differences in the polar interpolation, it appears that the lift in ARDEMA is higher. For both the stall delay and lift overshoot caused by the DS model is observed, enhanced by higher time constants like in the 2-D cases. It is also interesting to notice the small phase

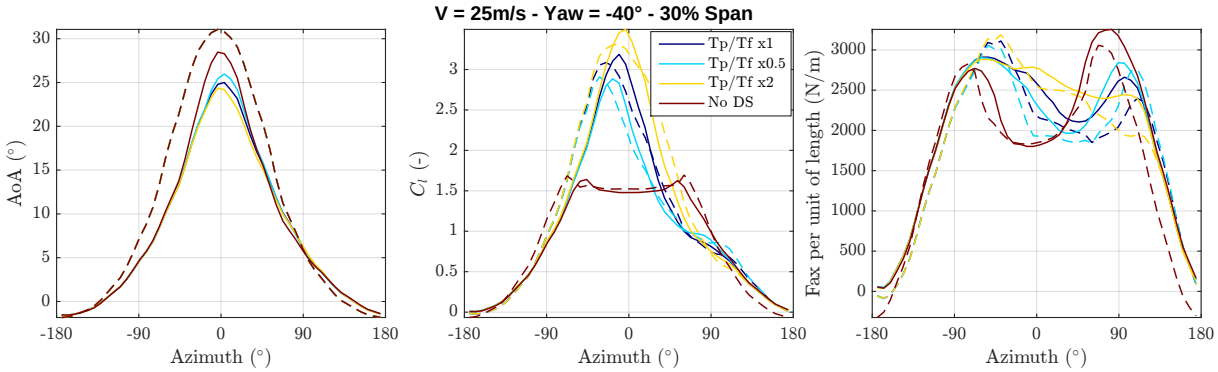

(a) Rigid case without controller - With DS in wake reduction

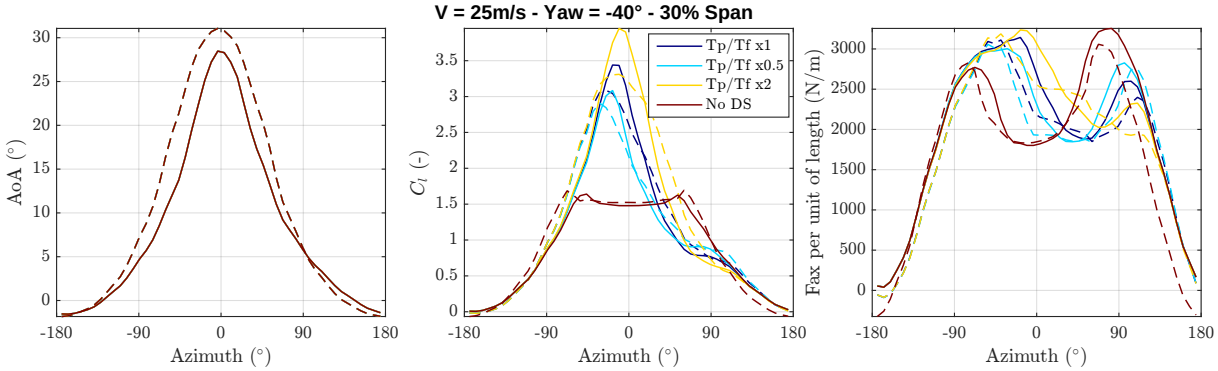

(b) Rigid case without controller - Without DS in wake reduction

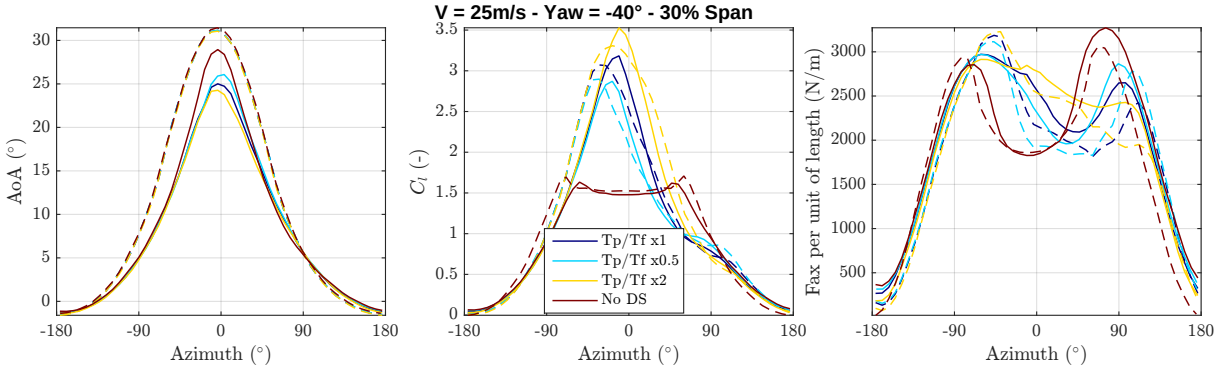

(c) Elastic case with controller - With DS in wake reduction

Figure 4.44: Variations of AoA, lift coefficient and axial force per unit length - DS sensitivity study - Comparison between ARDEMA (solid lines) and AeroDyn (dashed lines) - Uniform wind

shift observed for both solvers: AeroDyn lift is in advance compared to ARDEMA. The axial forces, with a phase resulting in the combination of the relative velocity phase and the AoA phase, are then also modified. This results in a high axial force peak for AeroDyn at around -45°, which is not visible in ARDEMA. The phase differences observed for the different time constants also affect the axial force, in particular after the maximum lift. For lower time constants, stall is more pronounced. This strongly modifies the balance of the forces acting on the rotor for certain azimuthal positions.

Including the DS in wake reduction reduces the maximum lift values observed on ARDEMA. The higher the Cl, the more axial induction is created locally and thus the AoA decreases, compensating slightly the stall delay caused by DS model. On the opposite, when DS is not included in the wake reduction, the

AoA is constant whatever DS is used for force calculations, enhancing the stall delay and overshoot. This reveals the importance of including a retroaction of DS in the wake. For a BEMT solver, it is often considered that dynamic effects on a 2-D sections have a much smaller time scale than dynamic induction over the full rotor, and thus both can be dissociated [170]. In the present cases it is observed that including DS in the wake does modify the local AoA, and thus rotor induction.
No major difference is observed for the cases with controller and elasticity compared to the rigid case without controller, both including DS in the wake correction. A small change in AeroDyn AoAs is to notice for the different DS configurations. The rotor efficiency is slightly modified by the DS, which is handled by the controller by slightly changing the pitch angles for each configuration. The influence of

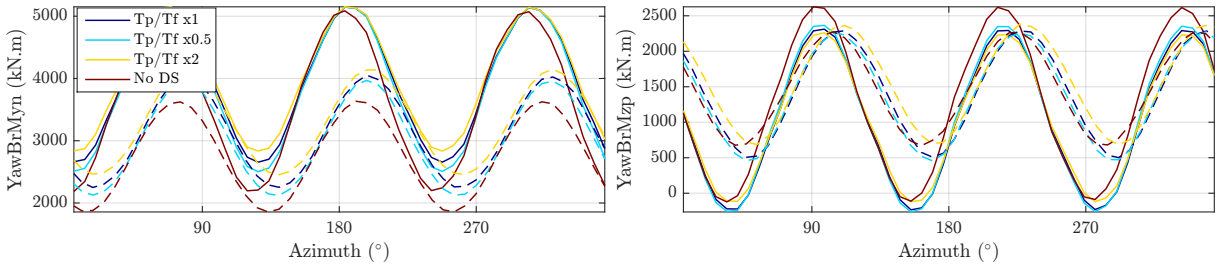

(a) ARDEMA

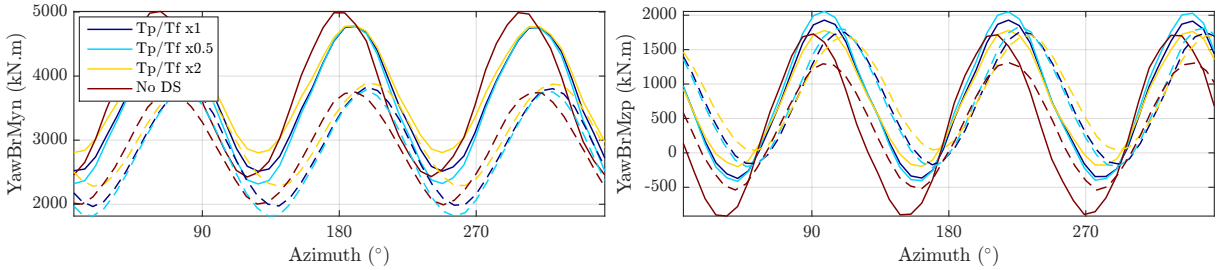

(b) AeroDyn

Figure 4.45: Variations of fore/aft (left) and yaw moments (right) - DS sensitivity study - Comparison between rigid cases without controller (solid lines) and elastic cases with controller (dashed lines) - Uniform wind - $V = 25m/s$ - Yaw -40°

DS on RNA moments is plotted in Fig. 4.45 where it appears that the impact of DS on fore/aft and yaw moments is restrained to some azimuthal positions. In the rigid case, maximum fore/aft and yaw moment are not affected. Only the minimum values are strongly changed. This is not the case when elasticity and controller are enabled, where both minimum and maximum values are changed. RNA moments in AeroDyn appears to be slightly more affected by DS than in ARDEMA, probably because of the retroaction of DS in the wake.
To conclude, it is thus clear that by changing the DS time constants the local force coefficients are modified. However this does not seem to have an impact on maximum fore/aft moment in the rigid cases. However, for elastic cases with controller small difference are observed, implying that a coupled code modifies the impact of the DS model compared to a purely aerodynamic method. These observations are made on unrealistic wind conditions, and the next sections will thus investigate the impact of more realistic turbulent wind conditions on such observations.

4.4.2 Turbulent wind

In the previous sections, uniform wind speed in space and time has been used for the simulations. In reality, the rotor experiences a non-uniform wind speed which varies in time. Furthermore, the wind is lower close to the ground because of the boundary layer effect. Turbulence intensity (TI), which is the adimensional standard deviation of wind speed, is used to quantify the distribution of velocities over time. A wind shear profile is used for the mean vertical wind distribution. Other modifications to the uniform flow field can be observed in reality such as veer or wake of other turbines. In the present study, only turbulence and wind shear will be accounted for. The choice of both of these parameters is known to affect turbine loads [186]. The purpose of this study is thus to be as close as possible to real engineering loads study and check if the observations for uniform winds from previous section are still valid in realistic wind conditions. In order to be consistent with the previous results in uniform wind, several aspects are investigated. Cases with BEMT and panel method are thus conducted in yawed cases with turbulent wind. The influence of wind shear is detailed in a specific section as no wind shear was included in uniform wind cases while wind shear is considered in the turbulent wind cases. The impact of turbulent wind versus uniform wind on RNA loads is also introduced. The specificity of turbulent wind simulations is the random aspect of the pre-generated turbulent wind field. The impact of two different wind fields on the comparison between ARDEMA and AeroDyn is thus also presented in a specific section. The last section then focuses on the different DS configurations in turbulent wind conditions.

4.4.2.1 Comparison between aerodynamics solvers

The investigated turbulent cases are presented in Table 4.13. The chosen wind conditions are based on real environmental values used for loads assessment in the North Sea.

Standard 10-min wind conditions are generated with TurbSim [98] in a 150x150m box surrounding

Table 4.13: Yaw misalignment cases - Turbulent wind with controller and elasticity

Wind vel.	Shear Coefficient	Turbulence	Turbulent seeds	Yaw angle
11.4 m/s	No	8.7%	1	-40°,-20°,0°,20°,40°
11.4 m/s	0.13	8.7%	1	-40°,-20°,0°,20°,40°
15 m/s	0.13	8.7%	1	-40°,-20°,0°
25 m/s	0.13	8.5%	9	-40°,-20°

the rotor discretized in 50x50 points, with a time step of 0.02s. The Kaimal turbulence model is used, with the TI and shear defined in Table 4.13. To maintain the aleatory and chaotic aspect of turbulence, a random parameter defined here as *turbulent seed* is used in TurbSim to generate different wind time series with the same statistics regarding turbulence. Different turbulent seeds thus are thus different time series of a turbulent wind with given properties. In TurbSim, the statistics of this wind simulations such as mean wind speed or turbulence intensity are based on the full simulation length. For cases with a controller, around 200s of simulated time are needed in order to start the turbine. In order to have correct statistics for the 10 min of simulated time, the first time step of the simulated wind is repeated over the 200s needed for the startup of the machine and added at the beginning of the wind file. The simulations are then 800s long. The main issue with this process is that the first time step is aleatory generated and is different from one seed to another, which means that the turbines are not exactly at the

same operating conditions when the 10 min data of turbulent wind begins. In ARDEMA, the wake is also different depending on this initialization. However, this was considered as the best option to obtain correct statistics over 10 min simulations.
In uniform wind, after a certain number of rotations, the simulations can be considered as converged and for each rotation, the wind turbine variables are the same. In turbulent wind, as the wind changes from one rotation to the other, variables must be averaged over all rotations of the 10 min wind data to be plotted along azimuthal position. In the next plots, maximum values and/or standard deviation are thus often plotted with the mean values per azimuthal position. In Fig. 4.46, the mean fore/aft

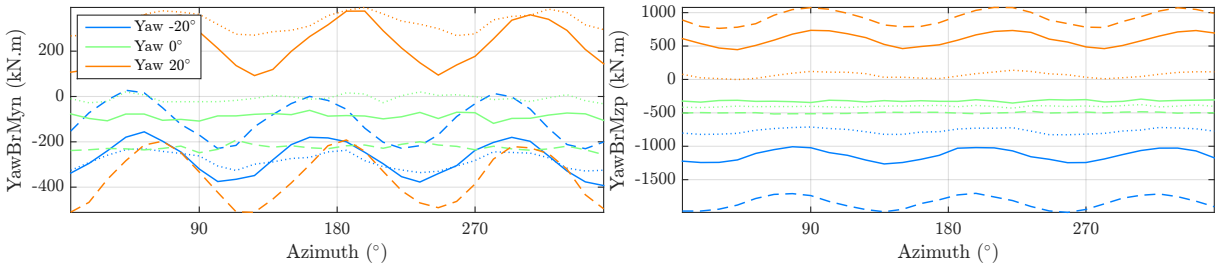

(a) Yaw -20°, 0°, 20°

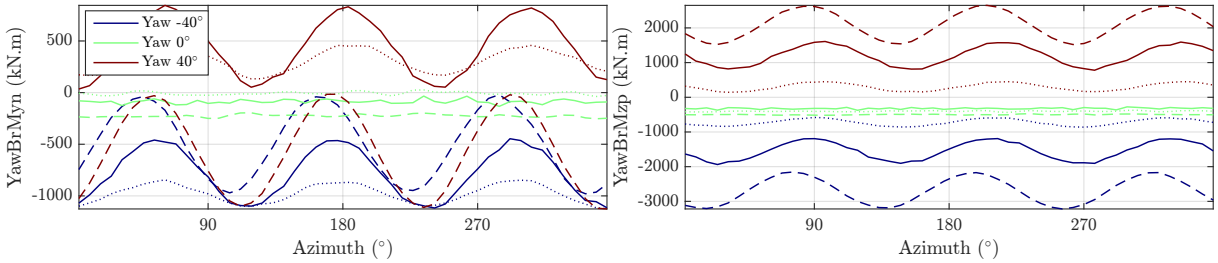

(b) Yaw -40°, 0°, 40°

Figure 4.46: Fore/aft (left) and yaw (right) moments - ARDEMA (full line), AeroDyn with (dashed line) and without (dotted line) skewed wake model - Turbulent wind - $V = 11.4m/s$ - Controller and elasticity enabled

and yaw RNA moments per azimuthal positions are plotted for the five different yaw values, at a wind speed of $11.4m/s$. The same trends than in uniform wind are observed. The 3-p period dominates the variations. the skewed wake model in AeroDyn increases the amplitude of variations and the mean values of fore/aft RNA moment are poorly predicted. However, without skewed wake model the variations for both moments are underpredicted compared to ARDEMA, and the mean yaw moment is also too low. Like in uniform wind (see Fig. 4.40), in ARDEMA at $11.4m/s$, positive yaw moments are obtained for positive yaw angles, and negative yaw moments are obtained for negative yaw angles.

4.4.2.2 Influence of shear

The influence of shear is investigated in Fig. 4.47 and 4.48 by comparing two turbulent wind cases at $V = 11.4m/s$. The trends predicted in the geometrical AoA analysis from section 2.3.3 are observed, in particular the difference between positive and negative yaw. Indeed, when yaw misalignment is combined with wind shear it appears that the amplitude of AoA variations increases as it is observed in Fig. 4.47. The negative yaw cases should thus be more impacted by dynamic stall.
Fig. 4.48 reveals that applying shear shifts up fore/aft and yaw moments, in positive and negative yaw

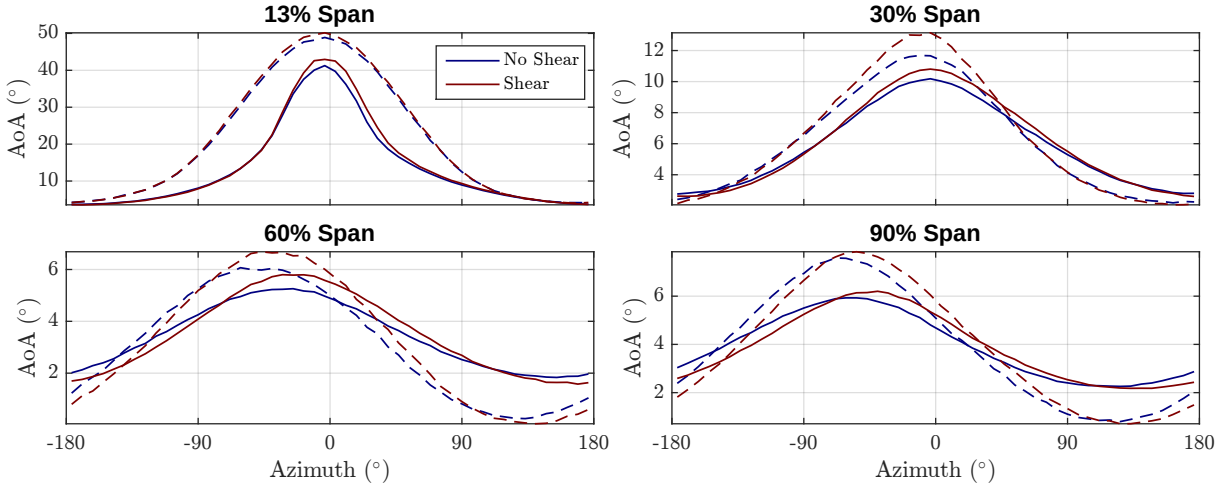

(a) Yaw -40°

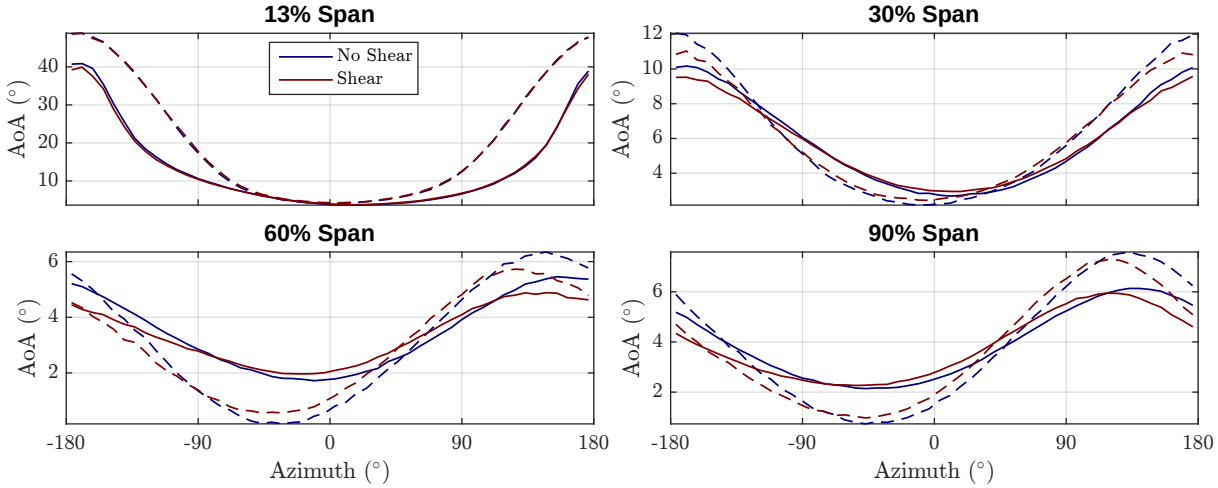

(b) Yaw +40°

Figure 4.47: AoA variations for several spanwise positions - Influence of shear - ARDEMA (full line) and AeroDyn (dashed line) - Turbulent wind - $V = 11.4m/s$ - Controller and elasticity enabled

angles for both solvers. For the fore/aft RNA moment, it is easy to understand that as the wind is lower close to the ground, the loads are lower on the bottom half rotor disk creating a nose-up pitching moment. At negative yaw angle, the amplitude of both moments is higher with shear, in particular with ARDEMA.

4.4.2.3 Comparison between turbulent and uniform flow

In the present section, a comparison is made between simulations with turbulent and uniform winds. In Fig. 4.49, the AoA and axial force per unit length are plotted against azimuthal position for several spanwise locations, for a wind speed $V = 25m/s$ and a yaw angle of -40°. For the turbulent case, the mean values per azimuthal positions are plotted, with error bars corresponding to the standard deviation for a given azimuthal position. This is not needed in uniform cases for which very little variations are observed from one rotation to another, caused only by the structural deformations. The turbulent case include a shear with a coefficient of 0.13, not considered in the uniform wind case. As noticed in the

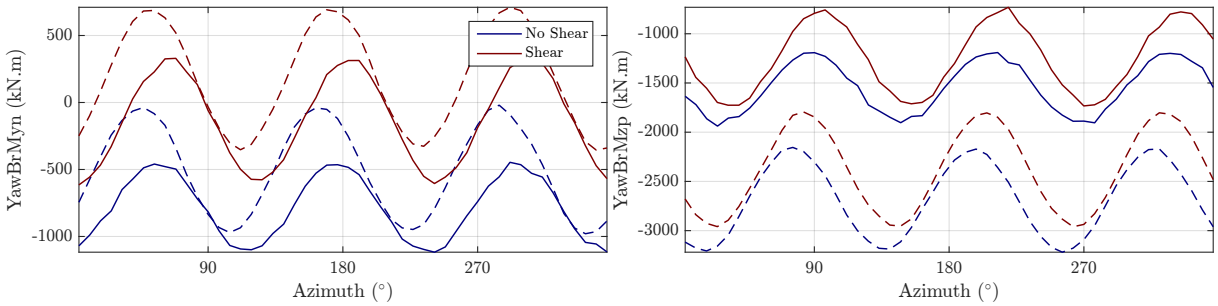

(a) Yaw -40°

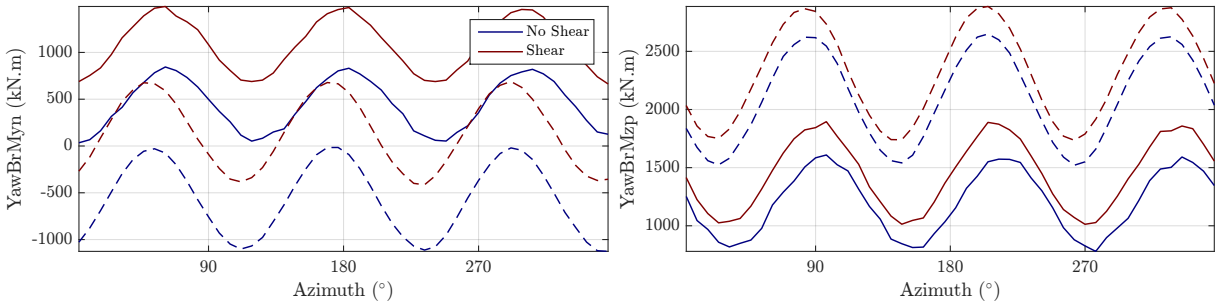

(b) Yaw +40°

Figure 4.48: Fore/aft (left) and yaw (right) moments variations - Influence of shear - ARDEMA (full line) and AeroDyn (dashed line) - Turbulent wind - $V = 11.4m/s$ - Controller and elasticity enabled

previous section, this is responsible for a higher amplitude of the mean AoA for both solvers. The maximum standard deviation is noticed for an azimuthal position of 0° for sections close to the root while it is more uniformly distributed at the tip. At this azimuthal position, the relative wind speed is also the lowest and the axial force does not follow the same trend. Standard deviation for both solvers is very close.

In Fig. 4.50, maximum and minimum values of fore/aft and yaw RNA moments are also plotted for the turbulent case. The difference between maximum and minimum values for a given azimuthal position can reach nearly twice the mean value and the order of magnitude of standard deviation is the same as the amplitude of the 3-p variations of the mean value. Turbulence thus as a large impact on the RNA moments. The shift between turbulent and uniform cases is caused by shear, as observed in previous section. It is also interesting to notice that the standard deviation and the maximum values are very close for both solvers. This confirms the predominance of turbulence on both moments.

The maximum and minimum values follow the 3-p frequency, but with a more chaotic behavior. Indeed, while the standard deviation and the mean RNA moment values are the same for the three periods included during one rotation, high differences from one period to another is observed for minimum and maximum values. A random combination of wind conditions and azimuthal position is responsible for this behavior. Lets consider a gust responsible for high loads in the generated wind field. If the gust reaches the turbine for an azimuthal position where a given RNA moment is low, then the maximum load is not reached. On the opposite, a combination of gust and high load azimuthal position results in maximal loading. In order to smooth this phenomenon, several calculations must be performed with different wind fields.

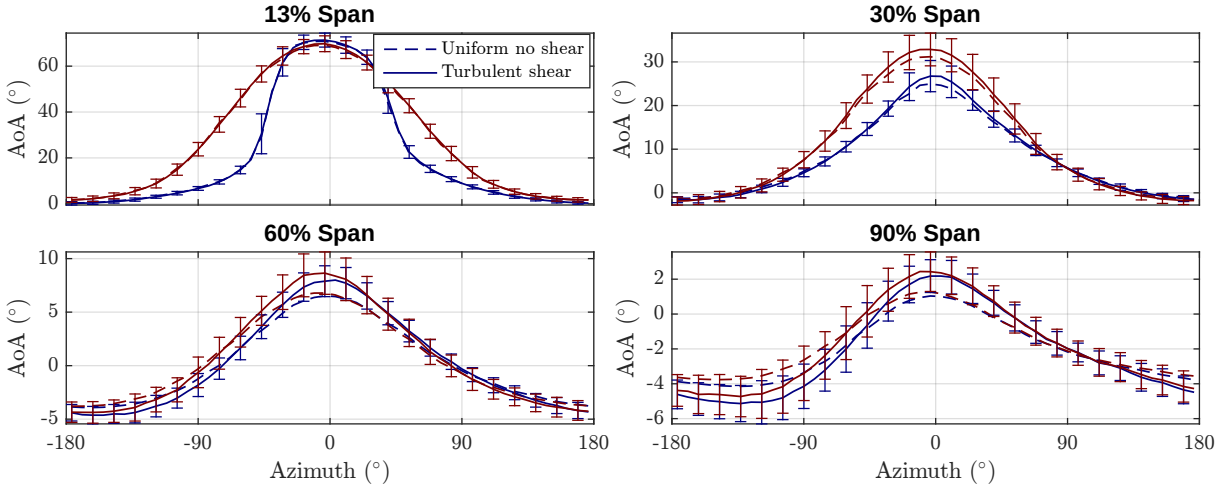

(a) AoA

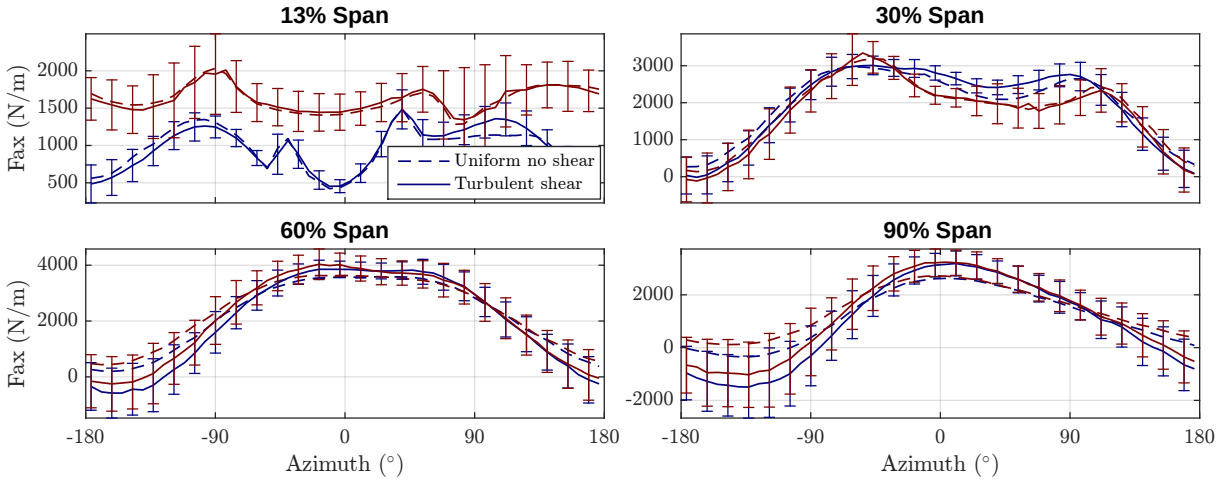

(b) Axial force per unit length

Figure 4.49: Influence of turbulence - ARDEMA (blue line) and AeroDyn (red line) - $V = 25m/s$ - Controller and elasticity enabled

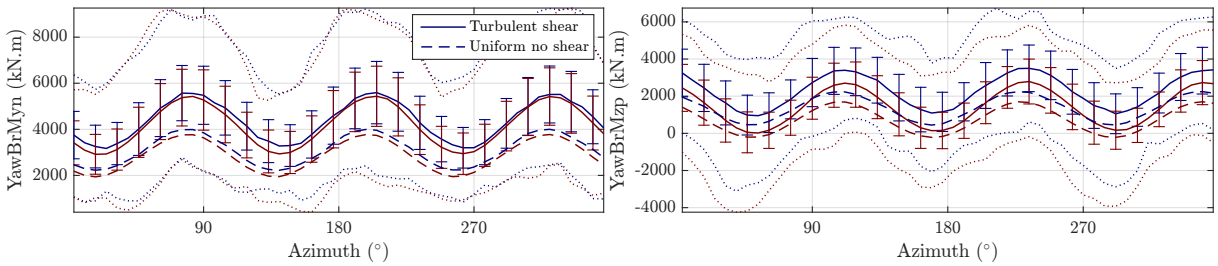

Figure 4.50: Fore/aft (left) and yaw (right) moments variations - Influence of turbulence - ARDEMA (full line) and AeroDyn (dashed line) - $V = 25m/s$ - Controller and elasticity enabled

4.4.2.4 Influence of turbulent seed

The turbulent wind fields generated by TurbSim are based on turbulence spectra and random phase wind speeds. This random phase is determined by a *seed* number introduced in TurbSim input files. In order to smooth the variations observed over one rotation of the maximum and minimum values, several turbulent seeds must be used. In usual engineering process, more than 20 seeds can be used in order to have correct statistics of the extreme loads.

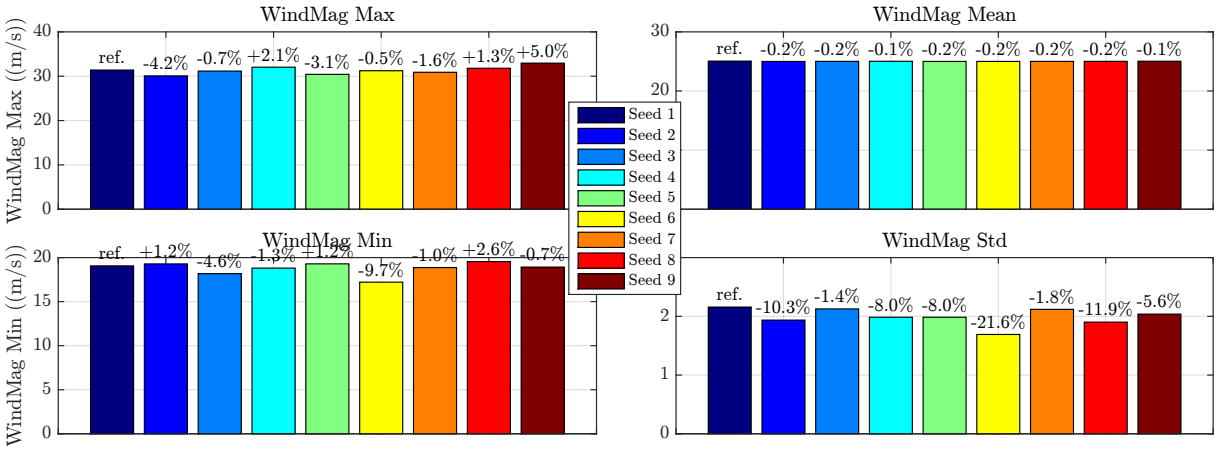

Figure 4.51: Statistics of several 10-min turbulent wind seeds - Mean wind speed $V = 25m/s$ - TI 8.5% - Wind shear coefficient of 0.13

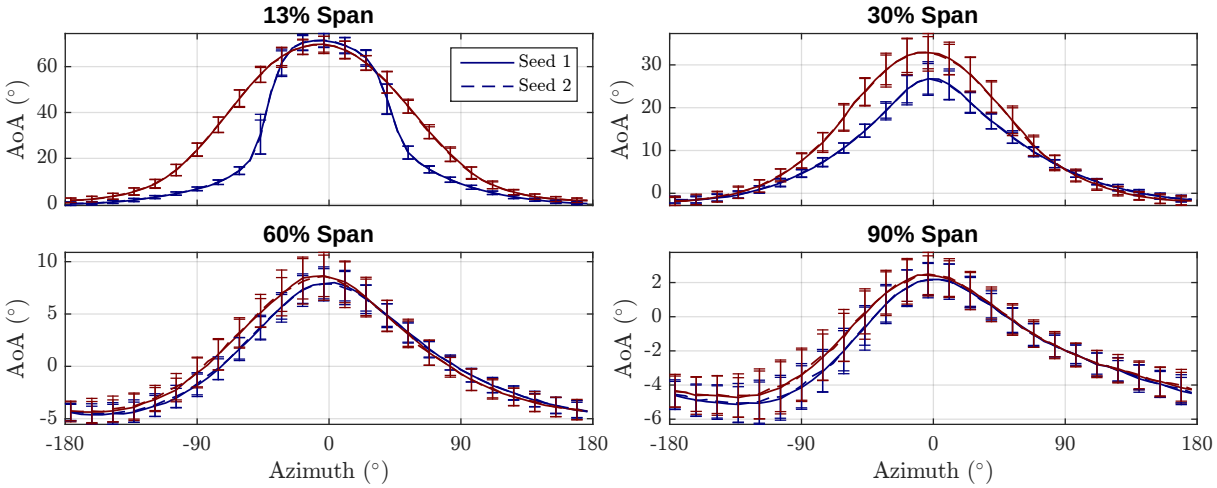

Figure 4.52: AoA variations for several spanwise positions - Influence of turbulence seed - ARDEMA (blue line) and AeroDyn (red line) - Turbulent wind - $V = 25m/s$ - Controller and elasticity enabled

In the present study, 9 seeds have been used because of computational time limitations. Fig. 4.51 show the 10 min statistics of these wind fields at one point located at hub height. Small variations are observed on the mean wind speed, while larger variations are observed on the standard deviation that does not match the input TI. This is a known issue caused by the IEC Kaimal spectra (see TurbSim manual [98]). The maximum and minimum values can reach 10% difference from one seed to another,

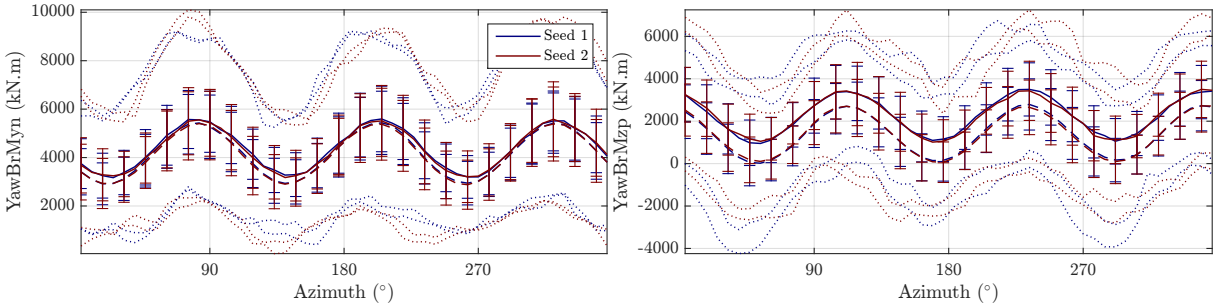

Figure 4.53: Fore/aft (left) and yaw (right) moments variations - Influence of turbulence seed - ARDEMA (full line) and AeroDyn (dashed line) - Turbulent wind - $V = 25m/s$ - Controller and elasticity enabled

which is why several seeds must be used and loads results must be averaged.
The mean AoA and standard deviations are plotted in Fig. 4.52 for two different turbulent seeds. The mean value and standard deviations are not affected by the differences between both seeds. In Fig. 4.53, the fore/aft and yaw RNA moments are plotted for the two seeds. For both ARDEMA and AeroDyn, the mean values and standard deviation predicted are in very good agreement. However, this is not the case for maximum and minimum values. Seed 2 is responsible for a maximum value of the fore/aft RNA moment around 10% higher than the maximum value for seed 1. The minimum value is also lower for seed 1. For the yaw RNA moment, a maximum negative yaw moment is obtained with seed 1.

4.4.2.5 Sensitivity to dynamic stall model

The sensitivity of loads to the DS model is assess in this section, for the extreme case with a large yaw error of -40° and a wind speed of $25m/s$. The investigated cases are presented in Table 4.14.

The mean AoAs, lift coefficient and axial force per unit length for a spanwise position of 30% are

Table 4.14: DS study cases - Turbulent wind with shear - Controller and elasticity enabled

Wind vel.	Shear coeff.	Yaw	Turbulent seeds	DS cases
25m/s	0.13	-40°	9	Tp/Tf x1, Tp/Tf x0.5, Tp/Tf x2, No DS

plotted in Fig. 4.54 against the azimuthal position for the different DS configuration, and for the same turbulent seed. The lift over shoot and stall delay can clearly be observed as well as the DS parameters dependency. No major difference can be noticed compared to the uniform wind cases. This observation is also valid for the RNA moments plotted in Fig. 4.55. Maximum and minimum values of the RNA moment appear to be more complex to analyze for just one turbulent seed. For example, the maximum yaw moment in ARDEMA is reached for the configuration without DS for an azimuthal position around 200°. It does not reflect the fact that the maximum mean value appears for the *Tp/Tf x2* configuration. In order to assess whether this maximum value is reached because of the model or because of the specific seed, an averaging over several seeds must be done.

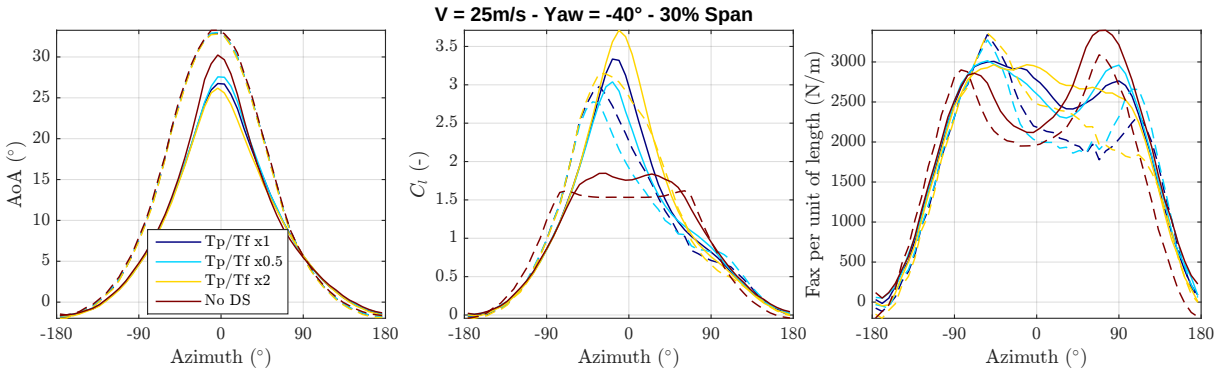

Figure 4.54: Variations of AoA, lift coefficient and axial force per unit length - DS sensitivity study - Comparison between ARDEMA (solid lines) and AeroDyn (dashed lines) - Turbulent wind

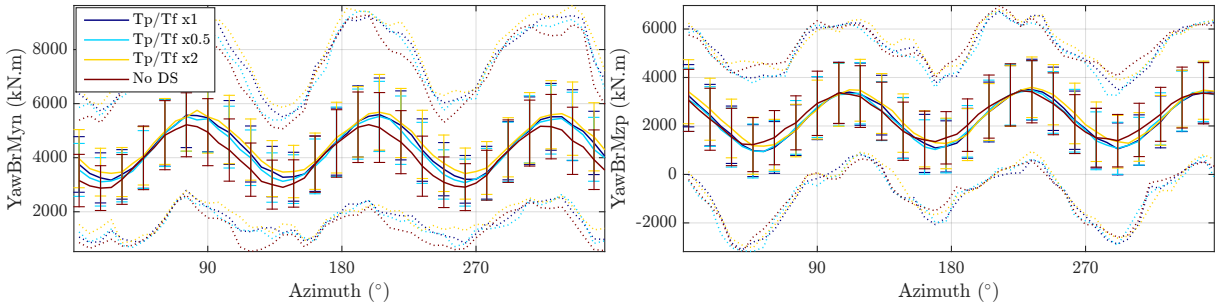

(a) ARDEMA

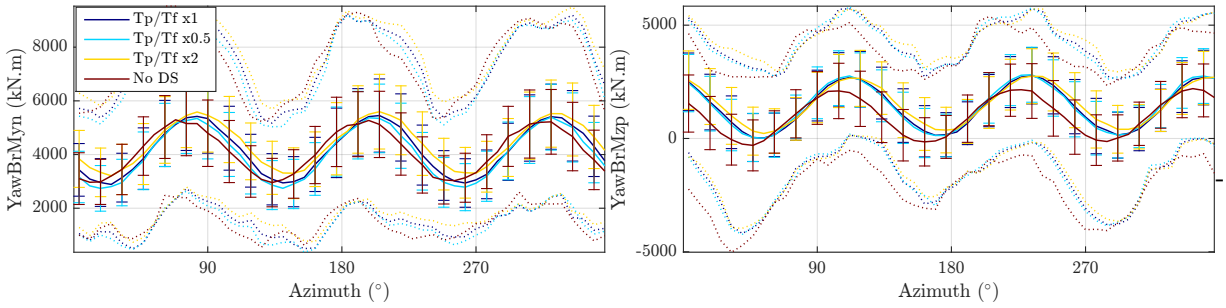

(b) AeroDyn

Figure 4.55: Fore/aft (left) and yaw (right) moments comparison - DS sensitivity study - Mean value (solid line), standard deviation (error bars) and min/max values (dotted lines) - $V = 25m/s$ - Controller and elasticity enabled

4.4.3 Loads analysis

In this section, the impact of DS model for both ARDEMA and AeroDyn in the cases with $V = 25m/s$ and a yaw angle of -40° is investigated by analysing the mean, standard deviation, maximal and minimal values of several loads channels: the fore/aft RNA moment *YawBrMyn*, the yaw RNA moment *YawBrMzp*, the blade root edgewise moment *RootMxb1* and the blade root flapwise moment *RootMyb1*. Uniform case without controller nor elasticity are compared to uniform case with controller and elasticity, and to turbulent cases with controller and elasticity. For the turbulent cases, the results are averaged by taking the mean value of the 9 simulated turbulent seeds.

4.4.3.1 Loads statistics

The fore/aft RNA moment statistics are plotted in Fig. 4.56. For all cases the maximum values are higher in ARDEMA. This difference is reduced when controller and elasticity are enabled. The three different configurations of DS do not change the maximum value in the case without controller, whereas a correlation can be observe for the cases with elasticity and control: nearly 5% difference in ARDEMA for the uniform case between the two extrem DS configurations. This difference is smoothed out for turbulent cases where the maximum values are twice higher than in uniform wind. For all cases, not using the DS can result in underestimating the maximum load, up to 7% for the turbulent case.

For the yaw RNA moment in Fig. 4.57, ARDEMA also shows higher maximum values. For the uniform cases, the different DS configurations reach 5% difference which is not the case with turbulent wind. For such case, the impact of DS is negligible in ARDEMA and AeroDyn, except for the AeroDyn case without DS. This does not reflect the impact of DS on the mean values of the yaw moment with up to 6% of difference between the two extrem DS configurations.

The maximum edgewise root loads are higher in ARDEMA for all configurations as plotted in Fig. 4.58. The maximum and minimum loads are both critical for the edgewise blade root moment as both have approximately the same absolute value. The mean value is close to 0 and large relative difference can thus be observed. DS configurations have little impact on the maximum load but reaches around 4% for the minimum value on the turbulent cases with ARDEMA.

In Fig. 4.59, the flapwise blade root moment statistics show that for the rigid uniform case, the maximum values are higher in ARDEMA while the mean values are higher in AeroDyn. This can be explained by a higher amplitude of variations in ARDEMA, confirmed by the higher standard deviation. Differences of around 3/4% are observed between the maximum values with the different DS configuration in turbulent wind.

4.4.3.2 Fatigue loads

Equivalent loads are computed for the same cases than in the previous sections, based on a rainflow counting methodology [186] [165]. A Wölher exponent of 10 is used. The equivalent loads for the uniform rigid cases, uniform elastic cases with controller and turbulent cases are plotted in Fig. 4.60. For the fore/aft RNA moment, up to 20% difference can be observed for the different DS configuration. These differences are larger in AeroDyn than in ARDEMA. This is not the case anymore for the cases with turbulence where no difference is observed for ARDEMA, and less than 2-% for AeroDyn. Both solvers then give very similar results. This is also the case for the yaw RNA moment. For the blade root moments, small differences are observed in uniform wind cases, except for the flapwise root moment where more than 7% of differences are observed between the two extreme DS configurations in ARDEMA. These observations hold for the turbulent case with around 5% difference in ARDEMA. For fatigue analysis, the flapwise root moment is thus the only variable investigated in this study that is affected significantly by different DS parameters in turbulent conditions.

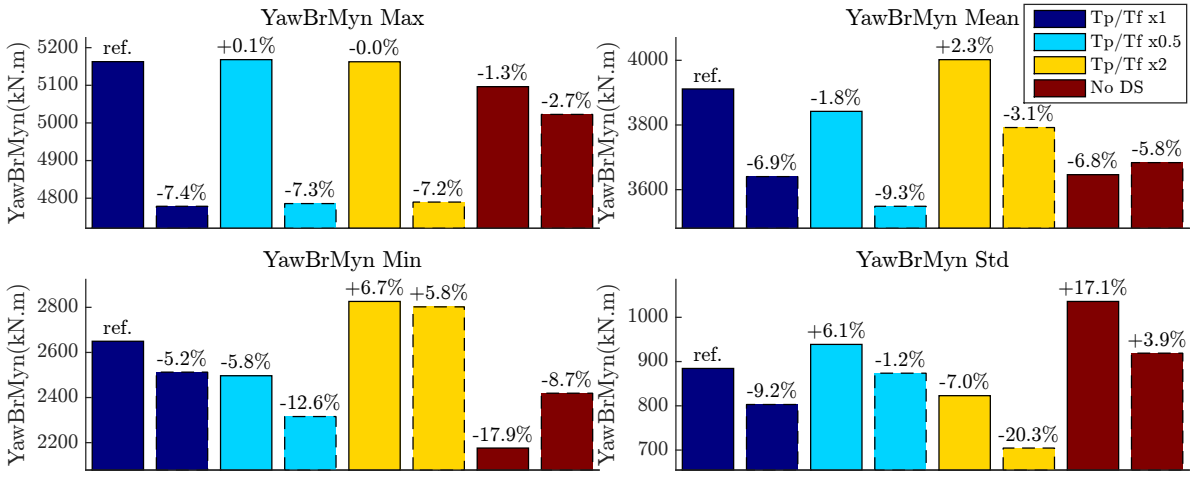

(a) Uniform wind - Rigid case without controller

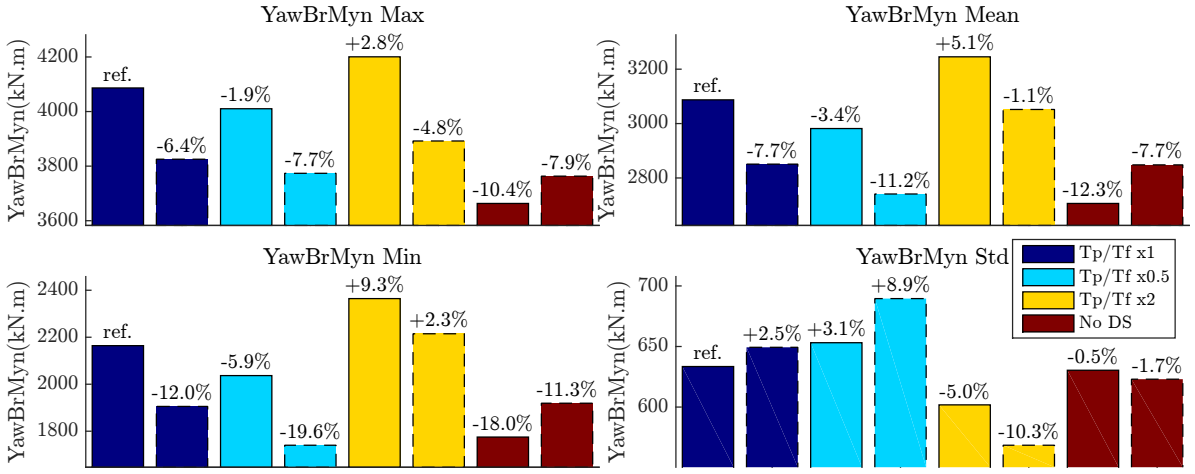

(b) Uniform wind - Controller and elasticity enabled

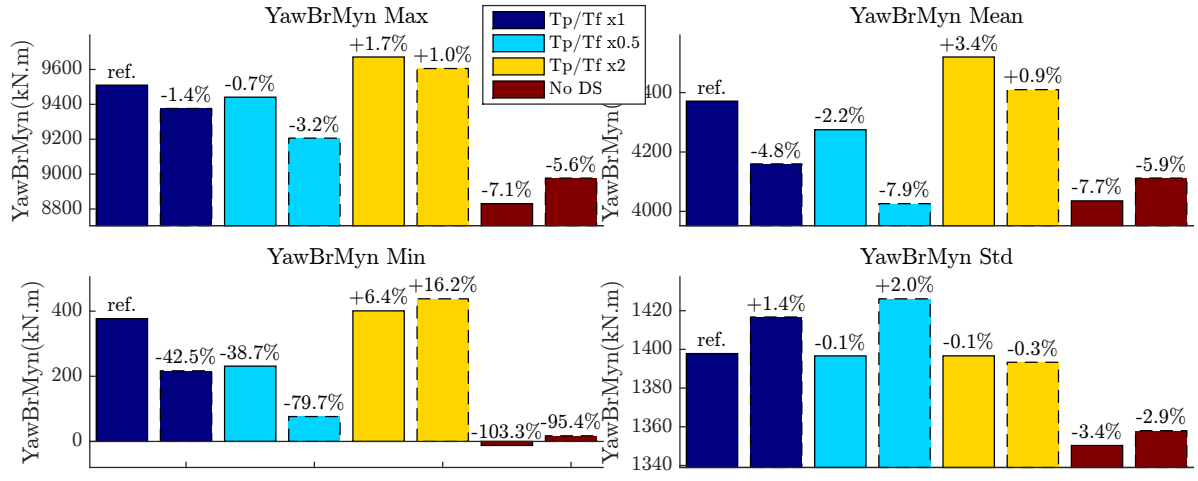

(c) Averaged values for 9 turbulent wind seeds - Controller and elasticity enabled

Figure 4.56: Fore/aft RNA moment statistics - Maximum (top left), minimum (bottom left), mean (top right) and standard deviation (top bottom) - Comparison between ARDEMA (solid lines) and AeroDyn (dashed lines) for several DS parameters - $V = 25m/s$ - Yaw -40°

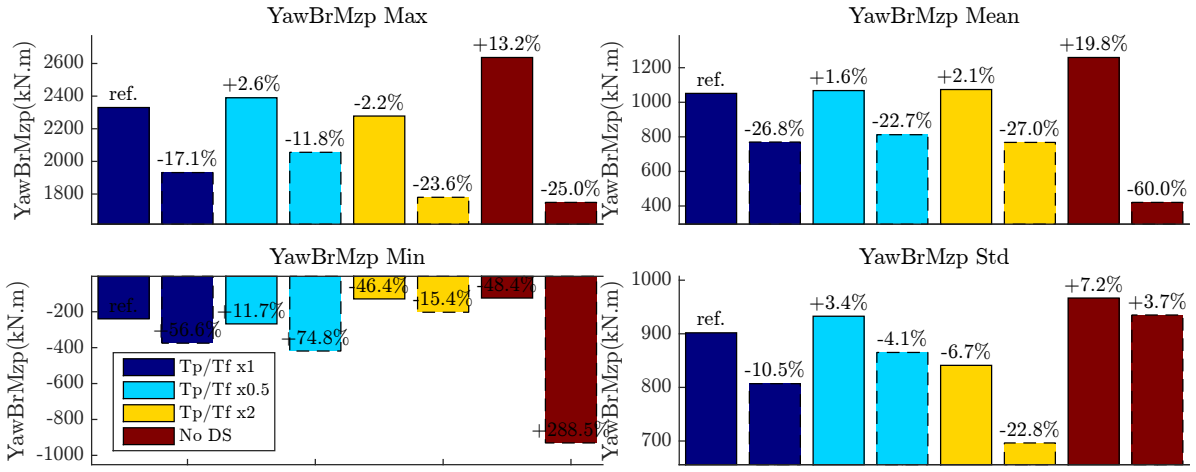

(a) Uniform wind - Rigid case without controller

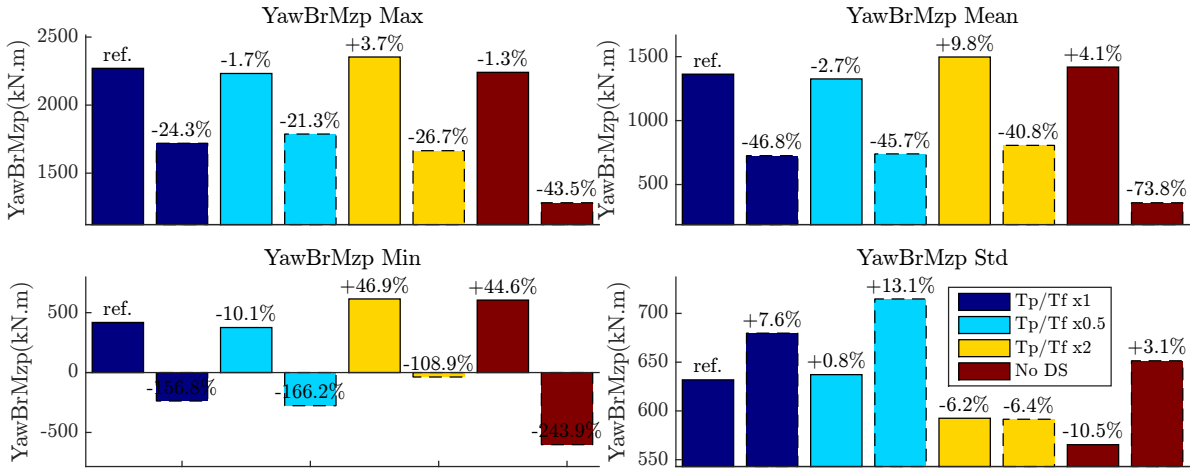

(b) Uniform wind - Controller and elasticity enabled

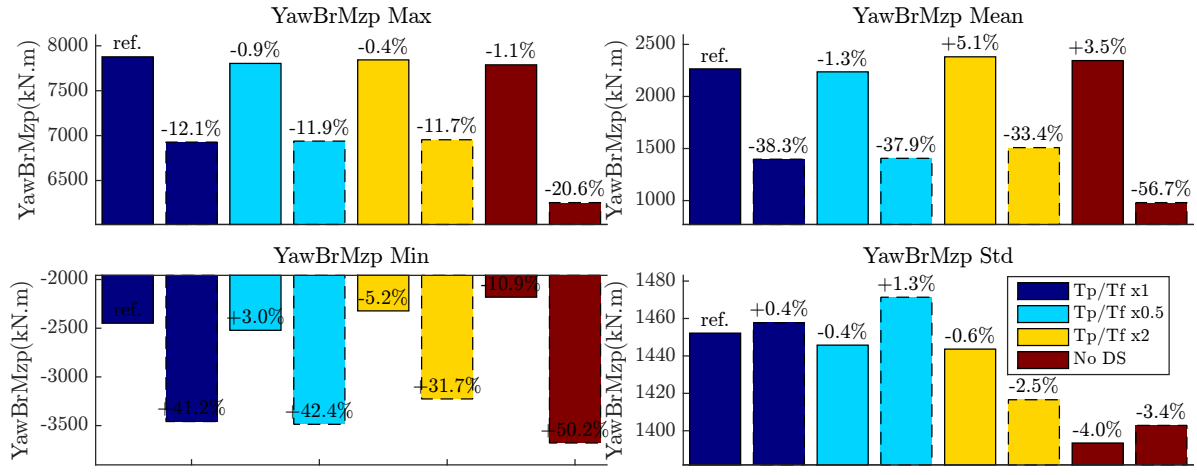

(c) Averaged values for 9 turbulent wind seeds - Controller and elasticity enabled

Figure 4.57: Yaw RNA moment statistics - Maximum (top left), minimum (bottom left), mean (top right) and standard deviation (top bottom) - Comparison between ARDEMA (solid lines) and AeroDyn (dashed lines) for several DS parameters - $V = 25m/s$ - Yaw -40°

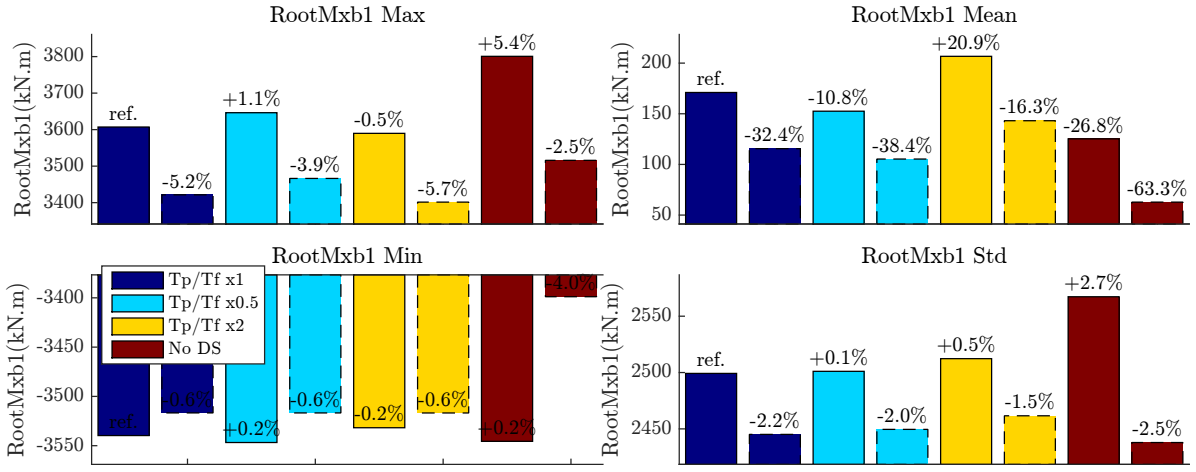

(a) Uniform wind - Rigid case without controller

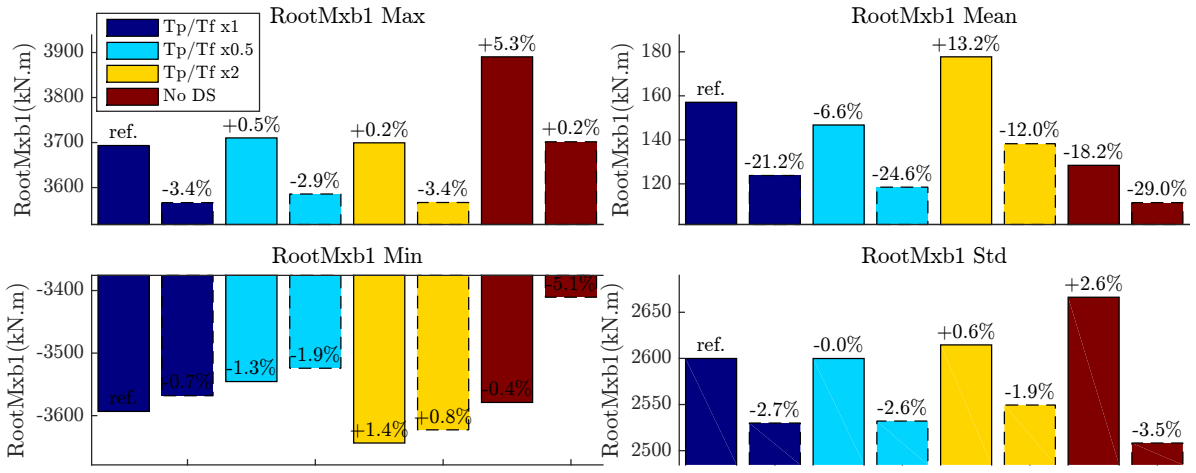

(b) Uniform wind - Controller and elasticity enabled

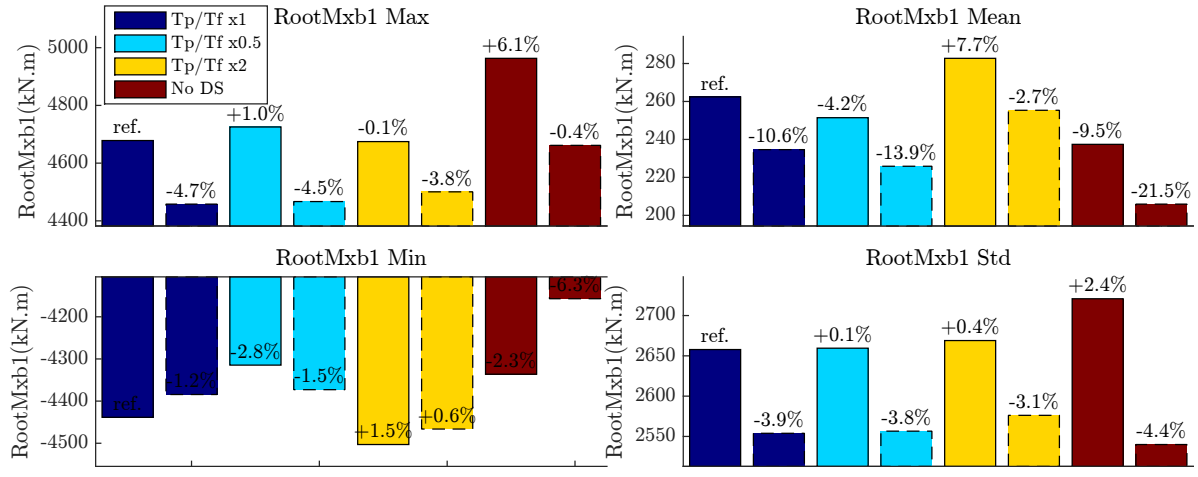

(c) Averaged values for 9 turbulent wind seeds - Controller and elasticity enabled

Figure 4.58: Blade root edgewise moment statistics - Maximum (top left), minimum (bottom left), mean (top right) and standard deviation (top bottom) - Comparison between ARDEMA (solid lines) and AeroDyn (dashed lines) for several DS parameters - $V = 25m/s$ - Yaw -40°

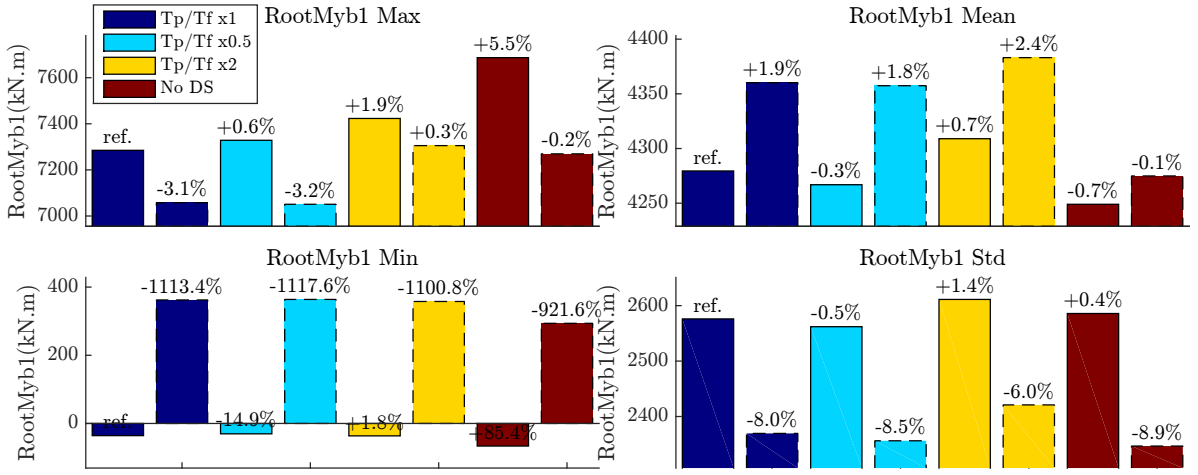

(a) Uniform wind - Rigid case without controller

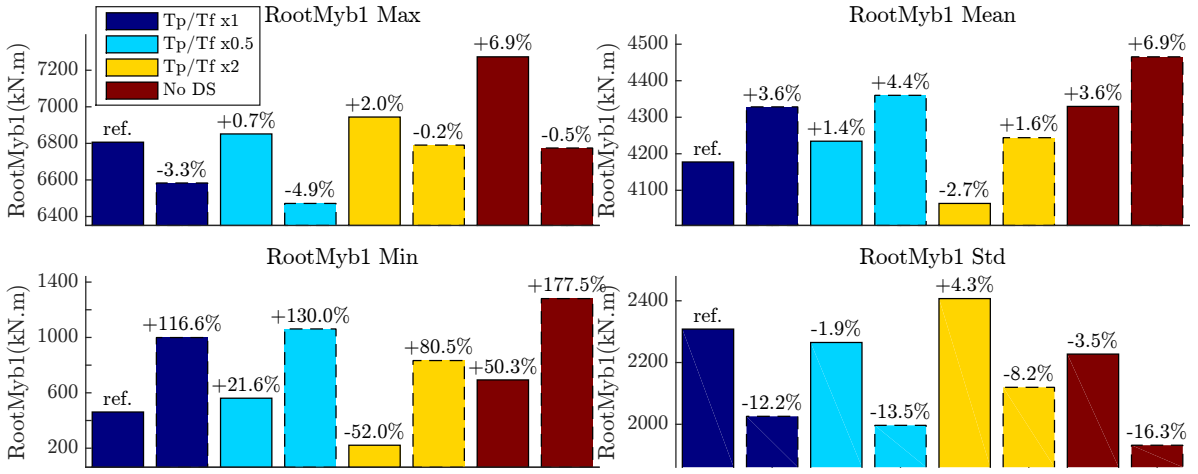

(b) Uniform wind - Controller and elasticity enabled

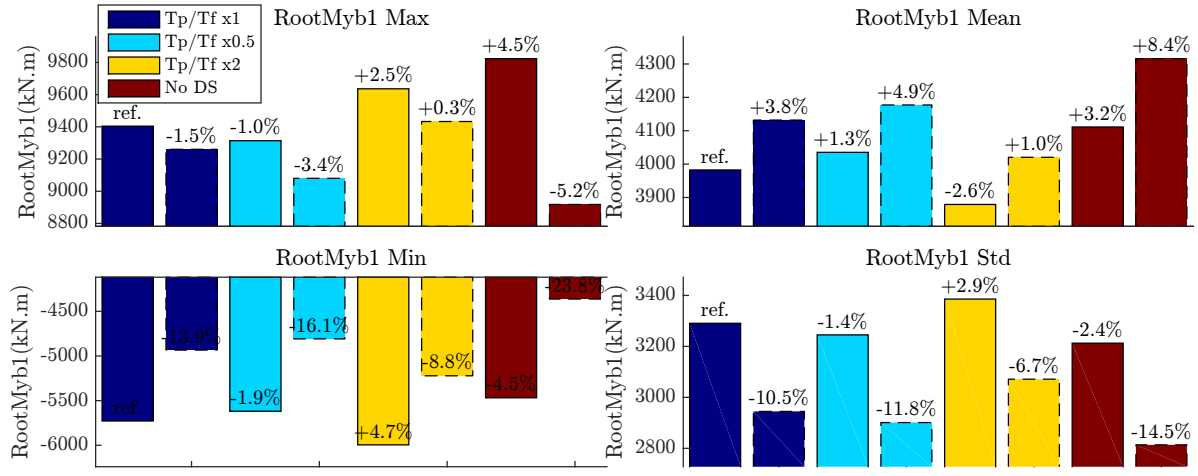

(c) Averaged values for 9 turbulent wind seeds - Controller and elasticity enabled

Figure 4.59: Blade root flapwise moment statistics - Maximum (top left), minimum (bottom left), mean (top right) and standard deviation (top bottom) - Comparison between ARDEMA (solid lines) and AeroDyn (dashed lines) for several DS parameters - $V = 25m/s$ - Yaw -40°

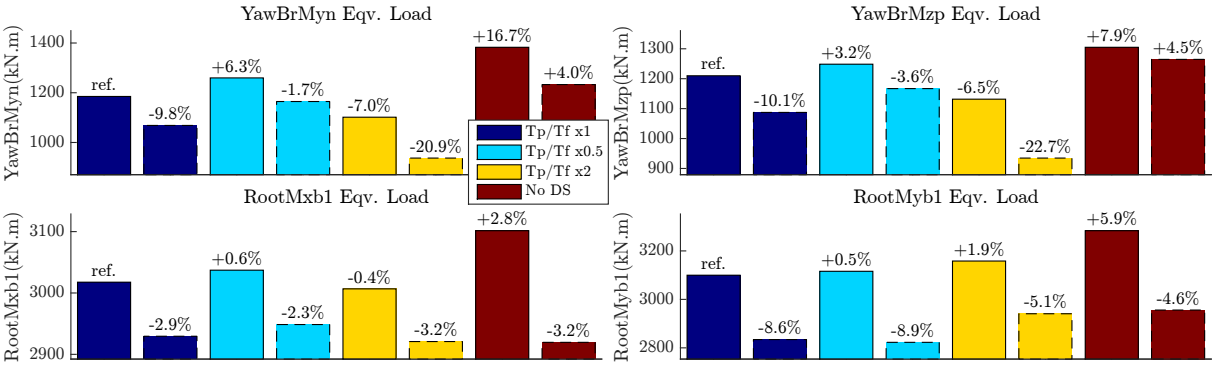

(a) Uniform wind - Rigid case without controller

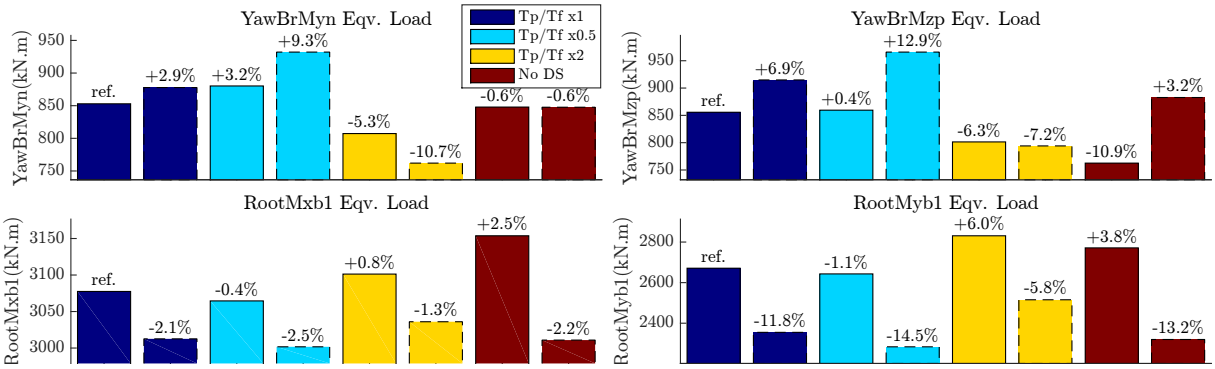

(b) Uniform wind - Controller and elasticity enabled

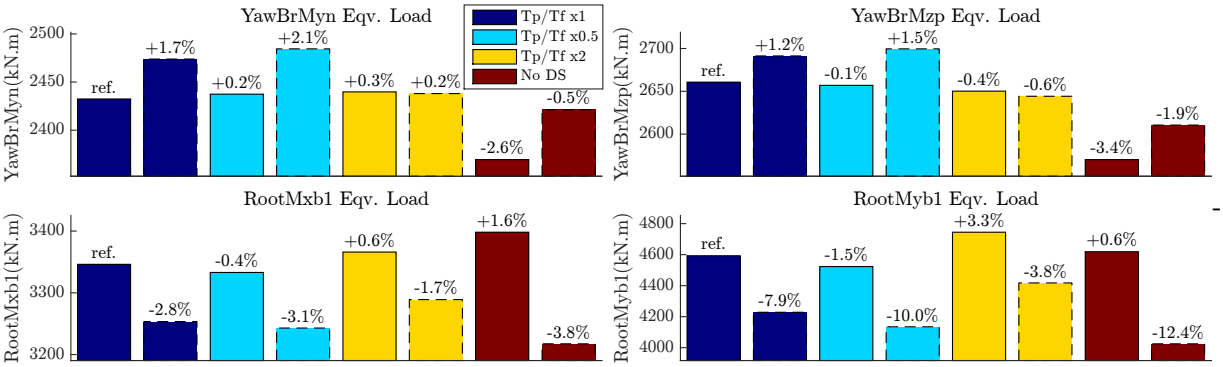

(c) Averaged values for 9 turbulent wind seeds - Controller and elasticity enabled

Figure 4.60: Equivalent loads for fore/aft RNA moment (top left), yaw RNA moment (top right), edge-wise blade root moment (bottom left) and flapwise blade root moment(bottom right) - Comparison between ARDEMA (solid lines) and AeroDyn (dashed lines) for several DS parameters - $V = 25m/s$ - Yaw -40°

Chapter 5

Aerodynamic at section level: Large Eddy Simulation

Contents

The hypothesis of inviscid flow can give a good approximation of aerodynamic forces on airfoils at low CPU cost as long as the boundary layer is fully attached on the airfoil surface. As presented in the previous chapter, once separation is reached the assumption does not stand and other models or corrections must be used. Computational fluid dynamics methods such as RANS and LES theoretically have the capacity to predict such flows. However, it clearly appears from literature that it is not an easy task to obtain a correct estimation of unsteady forces in stalled cases. For this reason, experimental results are still mostly used despite the high costs of wind tunnel measurements. For unsteady inflow conditions, measurements are even more costly as the number of cases is increased. Furthermore, the 3-D nature of stalled flows implies that investigating 2-D sections will by insufficient in a near future. But as the wind turbine blades are increasing in size, full scale experimental measurements will be impossible. CFD could then be the only available tool to predict correctly the aerodynamic forces. 3-D RANS simulations appear to give very good results for attached flows, but struggle with highly separated

flows. Strangfeld [188] investigates the 3-D flow over a pitching NACA0018 airfoil with URANS. The results are promising for attached flows, but stall is not captured correctly. Indeed, the unsteady nature of shear flows around stalled airfoils is not suited to RANS methods orginally developed for steady flows. LES and hybrid methods such as DES are very promising due to their ability to capture much more scales of the turbulent flow in the separated region. However, for high Reynolds numbers these methods are very CPU time consuming. In order to perform such LES with realistic CPU time, a Wall-Modeled LES (WMLES) strategy is considered in the present chapter. Recent investigations from Calafell [31] [30] with such methodology show promising results on wind turbine dedicated airfoils. The purpose of the present chapter is to validate a Wall-Modeled LES methodology for massively separated flows over an airfoil at high Reynolds number, focusing on periodic inflow conditions. Academic wind tunnel experiments and numerical investigations are few on such thick wind turbines airfoils. The methodology is then applied to deep-stall cases in order to understand the transition from lifting to bluff body. Highly unsteady flows are also investigated for assessing the validity of the panel code presented in the previous chapter.

5.1 Presentation of the LES solver YALES2

Calculations are performed using the parallel LES finite-volume YALES2 code [138]. The code solves the incompressible Navier-Stokes equations with central 4th-order schemes and specific domain decomposition that allows very good performances on large super-computers. The time step is handled by respecting a maximum local Courant Friedrichs Lewy (CFL) number of 0.9. The WALE turbulence model is used [143], which focuses on complex wall bounded flows (see Chapt.3.3.3). Depending on the mesh resolution, two wall models have been tested (see Chapt.3.3.4): a classical log-law model [27] and the Duprat wall-law model [49] implemented in the tabulated formulation from Maheu [122] to improve speed. Both models can be classified as *wall shear stress* models according to the classification from Larsson [108]. The Duprat model has been chosen due to its capability of taking into account the streamwise pressure gradient dp/dx. In theory, this can help the prediction of separation point. Fig. 5.1

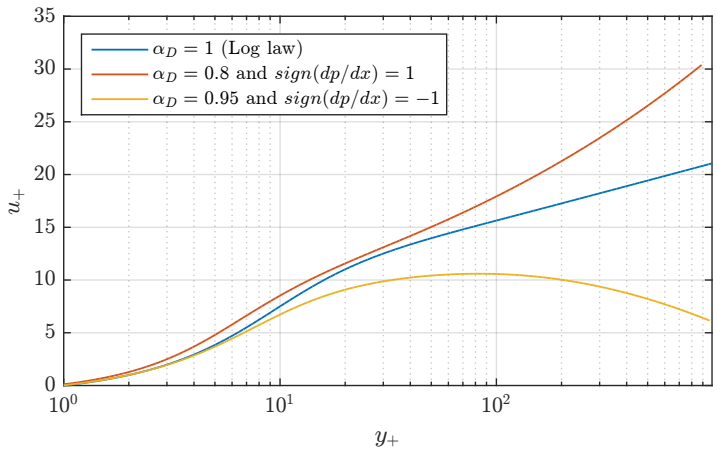

Figure 5.1: Duprat wall law for several values of α_D and pressure gradient

presents the dimensionless velocity u^+ as a function of y^+ according to the Duprat wall law, for different values of α_D, which quantifies the influence of the pressure gradient on the wall velocity. For $\alpha_D = 1$

the streamwise pressure gradient is negligible and the Duprat wall law has the same formulation as the log law. For smaller values of α_D, the pressure gradient has some impact.
For the oscillating cases, the moving frame strategy is chosen in order to model the airfoil motion: Coriolis and acceleration forces are taken into account by adding velocity source terms in the momentum transport equation, keeping fixed connectivity and metrics. The following rotating frame forces are added to Eq. 3.32:

$$\overrightarrow{f}_{rf} = -2\rho\overrightarrow{\omega} \times \overrightarrow{u} - \rho\overrightarrow{\omega}^2 \times \overrightarrow{x} - \rho\frac{d\overrightarrow{\omega}}{dt} \times \overrightarrow{x} \tag{5.1}$$

with $\overrightarrow{\omega}$ the angular velocity vector and $\overrightarrow{x}$ the distance vector between the center of rotation and a given location.
Post-processing functions based on level-set methodology have also been used to obtain the flow data at a given distance from the airfoil surface, which is not trivial in the case of unstructured meshes.

5.2 Geometry and meshes

Considering the airfoil chord c, the 3D computational domain is modeled as a circle of radius $15c$ extruded in spanwise direction, the airfoil being located in the center. Periodic conditions are applied spanwise. The spanwise length convergence is tested in static conditions with values from $0.25c$ to $4c$. These values are based on the observations from Fukumoto [61] who performed LES on a NACA0015 airfoil for attached and detached flows, static and and dynamic cases with a spanwise length up to $5c$. The FFA-W3-241 profile is used in most of the cases investigated in this study. This choice was based on the fact that experimental data for static and dynamic cases are available and that the profile is used on the open-source DTU 10MW reference wind turbine [13] blades.
According to Choi and Moin [38], the number of grid points needed for performing a wall-modeled LES of the flow around an airfoil without separation at $Re = 1.0 \cdot 10^6$ is approximately $3.63 \cdot 10^6$. This order of magnitude is to keep in mind when considering the number of grid points used in the present simulations. However, this number is underestimated in the case of separated flow for which the refinement must be greater in order to capture correctly the thickening of the boundary layer until separation. Furthermore, the methodology of computation is more suited to structured grid for which the size of grid cells in the spanwise direction can be much larger than in the other directions. In the present cases, five unstructured hybrid meshes with different refinement levels defined in Table 5.1 are used for a target Reynolds number $Re = 1.6 \cdot 10^6$. Prism layers are generated around the airfoil, with an aspect ratio between 10 to 15 on the wall and a growth rate of 1.25 (Fig. 5.2). The size of cells in streamwise and spanwise directions is thus the same. The global growth rate for tetrahedra is 1.10. The minimum prism cell height goes from $3 \cdot 10^{-4}c$ (mesh M1) to $1.0 \cdot 10^{-5}c$ (mesh M5) close to the leading edge airfoil whereas the maximum tetrahedron cell size is around $0.1c$ in the whole domain.

The unstructured meshes have been generated with the purpose to reduce as much as possible the number of cells without missing main flow features. Thus, the cell height of the first prism layer is not constant along the chord: the leading edge has been more refined considering that the boundary layer is the thinnest in this region and a poor resolution will trigger perturbations that will modify the downstream flow. The second half of the airfoil close to the trailing edge is meshed with a coarser resolution. This property can be observed in Fig. 5.3 with the y^+ values obtained for a static attached case. Discontinuities in y^+ can be observed close to the leading edge for meshes M1 to M3, while mesh M4 has a constant prism height up to 65% of the chord length to ensure that transition will not be triggered by any mesh discontinuities. For M5 mesh with a mean y^+ below 1, the same prism height has been used over all

Table 5.1: Mesh characteristics

Mesh	Control volumes[a]	Spanwise Length	Mean y^+	Mean x^+,z^+	Wall model	CPU time[a,b] for $25U_0t/c$
M1	7.5 M	0.25c - 4c	25	250	Duprat	0.5 kHrs
M2	17 M	0.25c - 2c	9	100	Duprat	3 kHrs
M3	80 M	0.25c - 1c	3	40	Duprat	50 kHrs
M4	220 M	0.25c	1.5	20	Duprat	1000 kHrs
M5	750 M	0.25c	1	10	-	10000 kHrs

[a] Span = 0.25c [b] Steady attached cases, Intel Xeon Broadwell 2.30Ghz cores

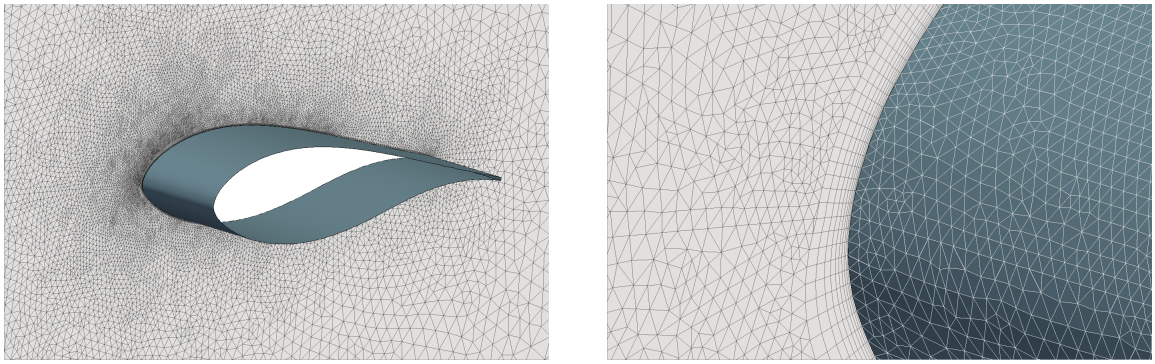

(a) FFA-W3-241 airfoil (b) Detailed mesh view: wall meshing

Figure 5.2: Mesh M1

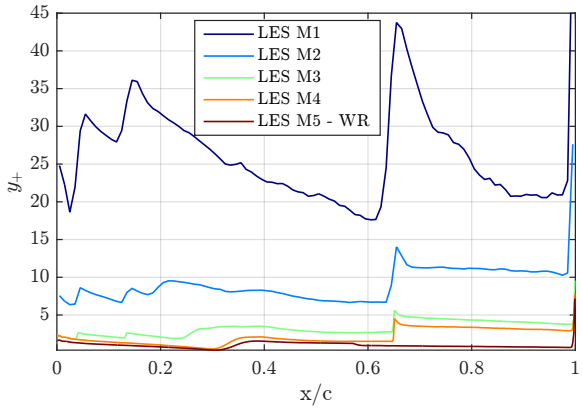

Figure 5.3: y^+ along chord for AoA = 4° and all meshes

suction side of the airfoil in the same purpose. A small bump in y^+ is still observed after mid-chord probably caused by the discontinuity in x^+ and z^+.

5.3 Validation

Steady cases have been performed first to determine the mesh resolution and the correct numerical parameters. Attached cases correspond to small AoAs, for which the flows remains attached to the airfoil,

with constant aerodynamic forces. Detached flows appear at high AoAs, creating large vortical structures and unsteady forces on the profile. Several cases presented in Table 5.2 are investigated in order to validate the computational methodology. These cases have been chosen based on the experimental data measurements from Fuglsang [58].

Table 5.2: Cases for static validation of LES methodology

AoA	Spanwise length	C_l LES	C_l Rfoil	C_l Expe.
4°	$0.25c$	0.85	0.87	0.79
8.8°	$0.25c$	1.42	1.44	1.24
12.6°	$0.25c$	1.84	1.69	1.31
16.4°	$1c$	1.60	1.40	1.25
23.2°	$2c$	1.35	1.32	1.09

The calculations are performed on 128 to 4096 Intel Xeon Broadwell 2.30Ghz cores. Considering the non-dimensional distance traveled by airfoil in chords $U_0 t/c$, with U_0 the fluid velocity at inlet, and t the physical time, around $25U_0 t/c$ are needed for flow convergence in attached flow cases. Because of the unsteady nature of separated flows, stalled cases need around $100U_0 t/c$ to obtain correct statistics of aerodynamic forces.

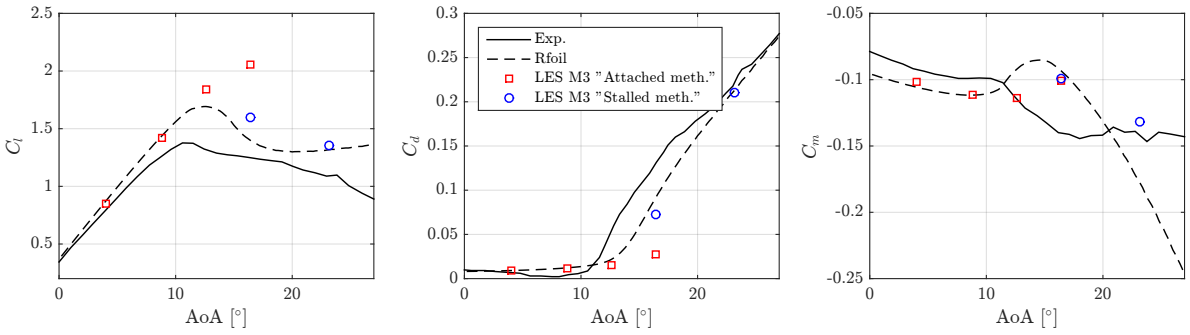

Figure 5.4: Aerodynamic coefficients comparison - M3 mesh resolution - $Re = 1.6 \cdot 10^6$

Results from the steady cases are compared with measurements performed at the VELUX open jet wind tunnel [58]. The Xfoil [46] and Rfoil [201] codes have been used for comparison. Xfoil is an open source code based on a panel method with boundary layer formulations able to compute polars and steady flow features as long as the flow remains attached. Rfoil is a modified version of Xfoil with specific treatment of separated flows. The code to code comparison between LES and Rfoil of integrated forces in Fig. 5.4 shows around 2% difference on the lift coefficient in attached cases, and less than 10% difference in stalled cases. Stall is however stronger in experimental data. The maximum lift coefficient is much higher in numerical cases than what has been observed experimentally and stall appears to be delayed. The VELUX wind tunnel has an estimated background turbulence intensity of 1% which could be responsible for these large discrepancies around stall, as mentionned by van Rooij [202]. 2-D RANS numerical simulations have been conducted with Ellypsis on the FFA-W3-241 and presented in the experimental report from Fuglsang [58], revealing a maximum lift coefficent of 1.8 for and AoA around 16°, quite far from experimental values. Other 2-D RANS simulations have been conducted more

recently on Ellypsis at a much higher Reynolds number $Re = 12.0 \cdot 10^6$ in order to assess the polars for the DTU10MW generic wind turbine [13] as illustrated in Fig.5.5. The maximum C_l is still around 1.8 considering either a fully turbulent boundary layer or a boundary layer transition with 0.1% turbulence, but it could be justified by the much higher Reynolds number. An early transition could be responsible for a turbulent boundary layer more developed, delaying stall.

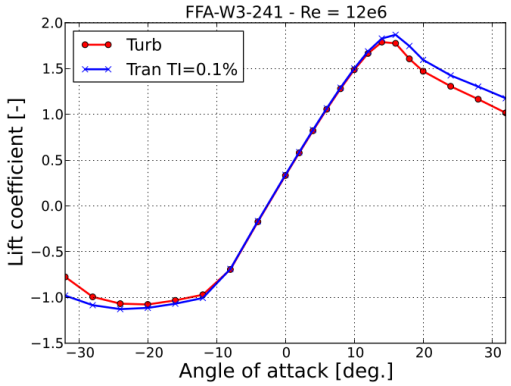

Figure 5.5: Lift coefficient of the FFA-W3-241 obtained with 2-D RANS at $Re = 12.0 \cdot 10^6$ - [13]

A specific methodology appeared to be necessary for stalled cases as illustrated in Fig. 5.4. A wider spanwise length and artificial viscosity must be added in order to obtain a correct prediction of separation considering the same mesh resolutions and numerical procedure than for attached cases. This is detailed in next sections.

5.3.1 Results for attached flows

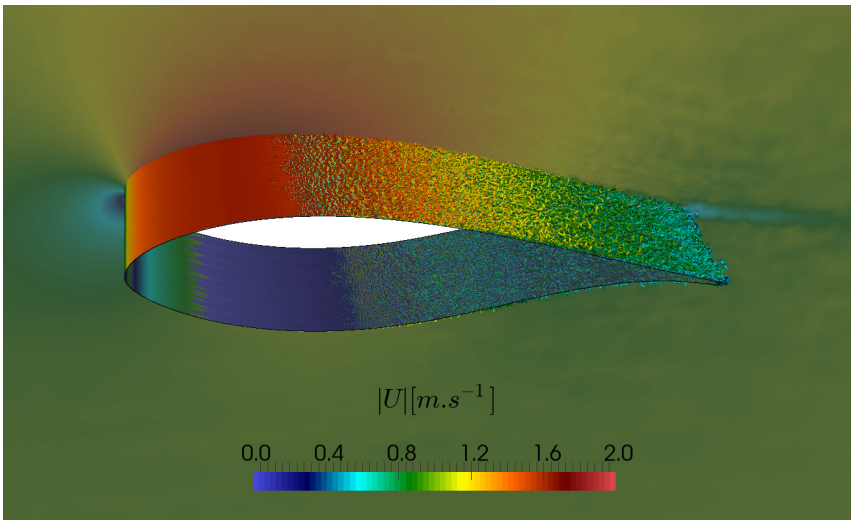

Figure 5.6: Angle of attack 4° - M3 mesh - Isosurface for Q-criterion $Q = 1000s^{-2}$ and instantaneous velocity field

Main flow features can be observed in Fig. 5.6 for an attached case (AoA = 4°). Isosurface of Q-criterion colored by velocity reveals for that the transition zone is located at around 25% of the chord

length, generating small vortices propagating downstream close to the airfoil as the flow remains attached. In order to understand more accurately the differences observed on integrated forces over the

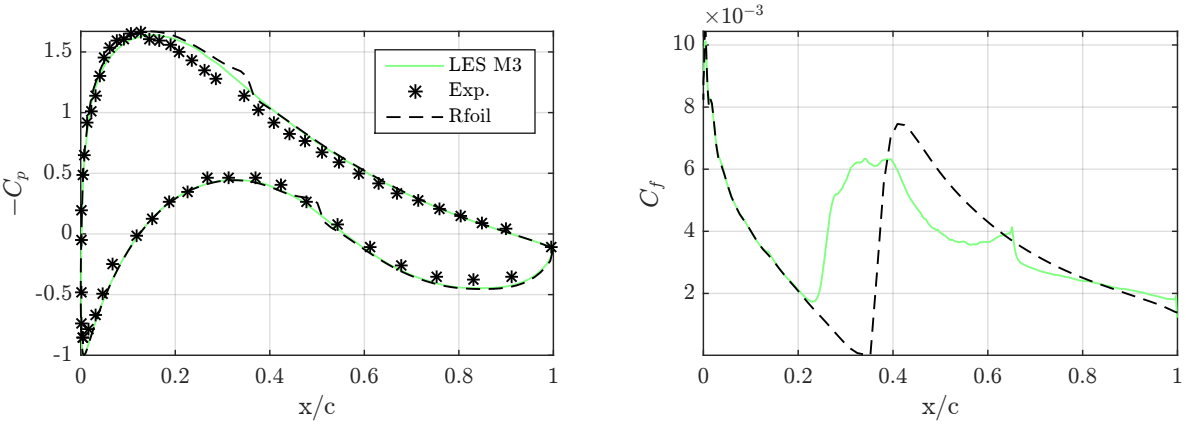

Figure 5.7: Pressure and friction coefficients comparison for AoA = 4° - Mesh M3

airfoil surface, the pressure and friction coefficients (C_p and C_f respectively) are mostly used. They are related to the local pressure and shear stress (see Fig. 2.9) with the following formulas:

$$C_p = \frac{p - p_0}{\frac{1}{2}\rho V_0^2}, \qquad C_f = \frac{\tau_w}{\frac{1}{2}\rho V_0^2} \tag{5.2}$$

with p the local pressure, p_0 the pressure far upstream, τ_w the local wall shear stress, ρ the fluid density and V_0 the upstream velocity. Fig. 5.7 shows very good correlation of the pressure coefficient between experiment, LES results on M3 mesh and Rfoil code. The small pressure bump observed on Rfoil around transition zone is not obtained with experimental data and LES. The VELUX wind tunnel has an estimated background turbulence intensity of 1%, which can create an early transition. The M3 mesh seems also to destabilize the laminar boundary layer, triggering early transition. This behavior appears clearly on the suction side friction coefficient C_f. Indeed, the comparison of C_f between LES and Rfoil reveals that both match perfectly when the boundary layer is laminar, but then separation appears too early on LES at around $x/c = 0.25$ while for Rfoil it appears later at around $x/c = 0.35$. However, this does not seem to impact lift and drag coefficients as they are still predicted correctly.

A more accurate comparison of the boundary layer in attached case is also performed between the Xfoil code and LES. Fig. 5.8 compares Xfoil and LES boundary layer characteristics along the profile curvilinear abscissa z, starting at trailing edge directed to pressure side. The edge velocity U_e, defined as the velocity on the outer edge of the boundary layer, and the displacement thicknesses [172] $\delta^\star$ are variables computed in Xfoil. The displacement thickness is defined by Schlichting [172] :

$$\delta^\star = \frac{1}{U}\int_0^\infty (U - u)dy \tag{5.3}$$

with U the tangential velocity of the inviscid flow out of the boundary layer, u the local tangential velocity and y the direction normal to the airfoil surface. The edge velocity for LES is considered here as the maximum tangential velocity in streamwise direction obtained along the normal, up to y^+ values of 2000. The displacement thickness is then computed integrating the tangential velocity profiles along the airfoil surface normals. Both the edge velocity and displacement thickness comparisons show very good correlation. The suction side transition can be clearly identified, around $z/z_{max} = 0.7$ in Xfoil and $z/z_{max} = 0.65$ for LES.

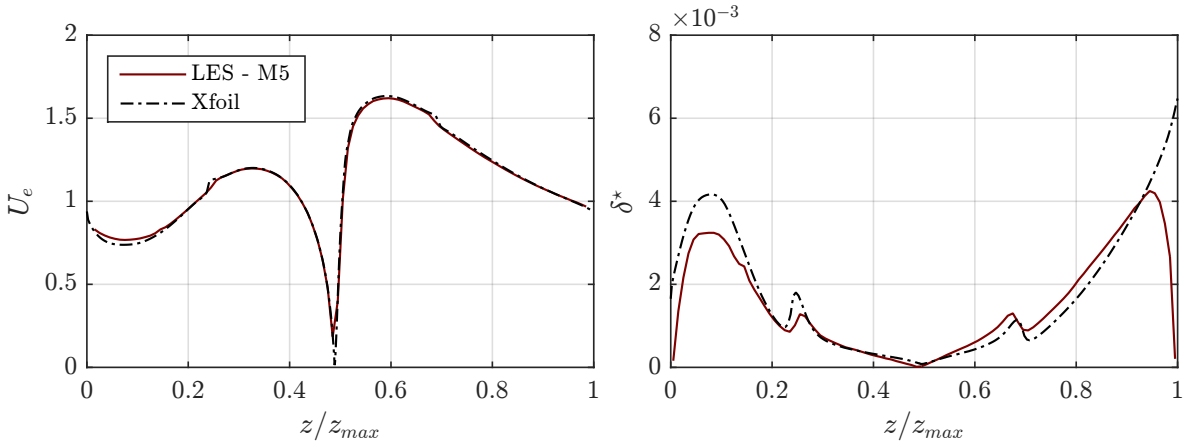

Figure 5.8: Edge velocity (left) and displacement thickness (right) along curvilinear abscissa for AoA = 4° - Mesh M5

5.3.2 Results for separated flows

This section focuses on the validation of separated flow cases. It clearly appears from literature that this cases are much more challenging, as most of the hypothesis of wall laws are not valid anymore when the flow starts to separate. In the present study, it appeared that the methodology used for attached cases is not satisfying for stalled angles, leading to unrealistically high lift values. This issue was overcome by extending the span length to at least $1c$ and by adding artificial viscosity. This artificial viscosity is introduced because in the stalled case, the separated boundary layer may cross the prism/tetrahedron transition, a region where the central finite-volume schemes need stabilization. Two methodologies for attached and stalled cases are thus defined regarding spanwise length and use of artificial viscosity. Less than 10% difference with Rfoil in stalled cases are then obtained. The experimental data have been obtained with an estimated background turbulence intensity of 1%, which can justify the lower measured lift coefficient as no turbulence is injected in the LES simulation.

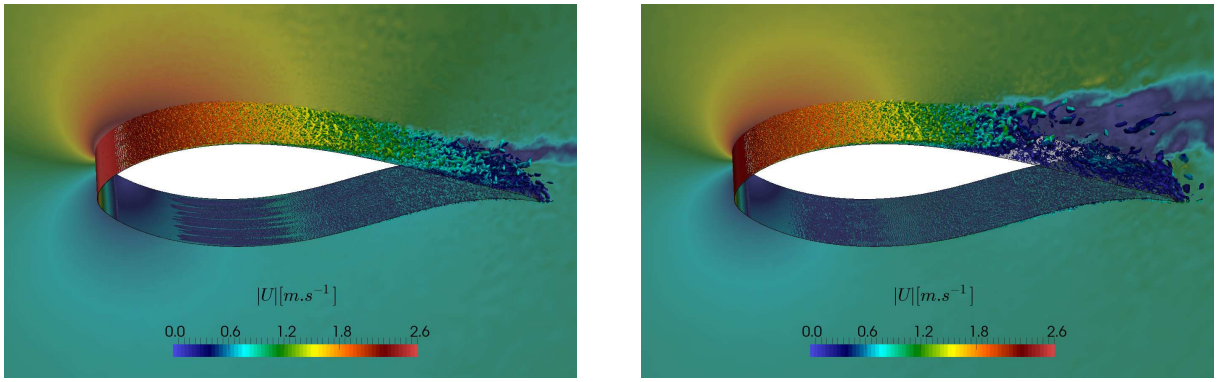

Figure 5.9: AoA = 16.4° without (left) and with (right) artificial viscosity - M3 mesh - Isosurface for Q-criterion $Q = 1000s^{-2}$ and instantaneous velocity field

Main flow features can be observed in Fig. 5.9 for a separated case (AoA = 16.4°). The transition is triggered much closer to the leading edge. The vortices then grow in size and become detached from the airfoil surface, creating a separated flow with chaotic structures around the mi-chord of the suction side.

The left figure represents the flow without artificial viscosity (with artificial viscosity for the right figure respectively), and the flow separation is much lighter in this case.

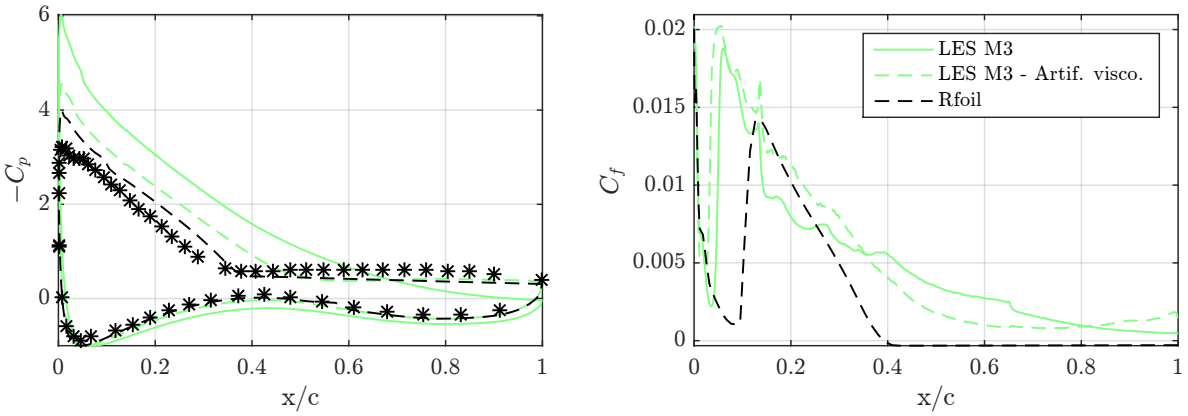

Figure 5.10: Pressure and friction coefficients comparison for AoA = 16.4°

Figure 5.10 shows very good correlation of the pressure coefficient between experiment, LES results and Rfoil code when artificial viscosity is used. The light stall observed with no artificial viscosity also appears on pressure coefficient. It can also be noticed that the flat pressure zone at around 50% of the blade chord, which corresponds to the separated zone, is larger in the experimental case which is in line with the lower lift coefficient observed in experimental data compared to numerical data. The transition does not seem to be better predicted with artificial viscosity. As in the attached case, transition appears too early compared to Rfoil. Introducing artificial viscosity is even worse for transition as the transition zone is shifted to the leading edge. Because of computational limitations it was not possible to use M4 and M5 meshes on separated cases: the wider span and longer simulation time needed for stalled cases would require too many CPU hours.

In order to check that the amount of artificial viscosity introduced in the simulations is not excessive, the ratio between artificial viscosity and the sum of turbulent and molecular viscosity is plotted in Fig. 5.11. Oscillations in the flow close to transition zone are not well captured by the mesh, triggering locally artificial viscosity with the same order of magnitude than physically modeled viscosity. The sensitivity of separation point prediction to the amount of artificial viscosity introduced appeared to be low after several trials, raising questions regarding the difficulty to capture it correctly without it. The most probable interpretation is that the separation process is based on a balance between the kinetic energy of the

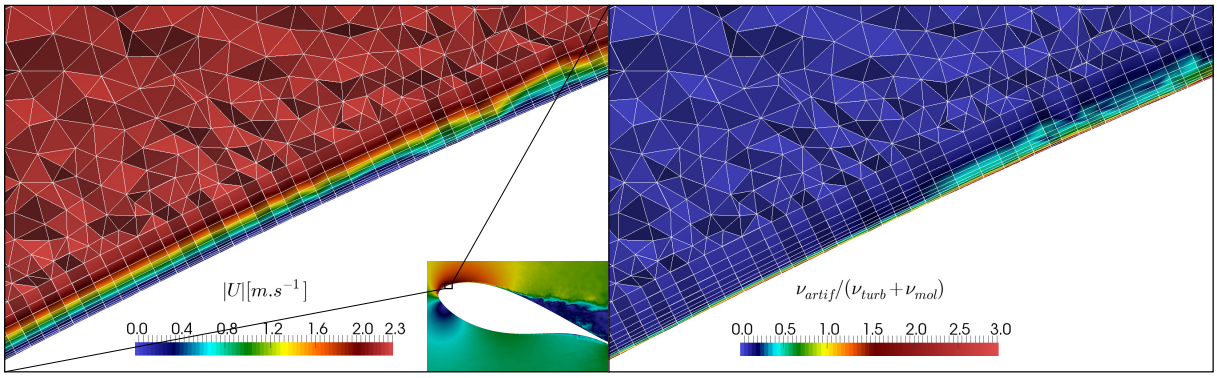

Figure 5.11: Velocity and artificial viscosity near transition zone - AoA = 16.4° - M3 mesh

boundary layer and the pressure gradient. By adding artificial viscosity, the kinetic energy is lowered and the pressure gradient is large enough to create separation. As the meshes M1 to M3 are not refined enough to capture correctly all the turbulent structures of the boundary layer, the balance is not well predicted. Furthermore, both wall law and turbulence models are not accurate enough to predict such phenomenon when the mesh is too coarse. The methodology used here is not perfect from a physical point of view as a non-physical model is introduced. The boundary layer development for example is poorly predicted. But the main flow features such as separation point and local forces are much improved. By keeping a given level of artificial viscosity for a given mesh, these flow features can be reproduced over several flow conditions, giving a good insight of the flow at a relatively low CPU cost. In order to prevent a strong impact on the flow, the smallest values of artificial viscosity needed to trigger separation are used depending on the mesh.

5.3.3 Grid convergence study

Several meshes are used as presented in the previous sections. The present section aims at understanding which mesh refinement is needed to obtain specific data from the flow. The cases investigated are presented in Table 5.3, with the obtained lift coefficient.

Table 5.3: Mesh convergence study for attached and detached cases

Mesh Span	C_l for AoA = 4° $0.25c$	C_l for AoA = 16.4° [a] $1c$	C_l for AoA = 23.2° [a] $2c$
M1	0.78	2.35	1.35
M2	0.85	2.25	1.35
M3	0.85	1.60	1.40 [b]
M4	0.85	-	-
M5	0.85	-	-

[a] With artificial viscosity [b] With spanwise length of $1c$

From these results, it appears than in attached cases, the coarsest mesh M1 shows 10% of difference in the lift coefficient compared to the other meshes. The detached case at 16.4° is the most challenging: even with artificial viscosity, only mesh M3 is able to obtain a correct prediction of separation. By introducing more artificial viscosity in meshes M1 to M2, it appeared that the boundary layer was fully detaching from the surface. On the opposite, at 23.2° and with a relatively low amount of artificial viscosity, the separation prediction is much easily predicted with meshes M1 and M2. In such cases, a factor of 10 in the artificial viscosity constant revealed no changes in the prediction of separation point, and thus in the prediction of lift coefficient. As a conclusion, near stall cases (angle of attacks between 12° and 16°) are proven to be much more complex to obtain than attached and stall cases, for which coarse meshes give satisfying results despite the poor prediction of transition. Despite these relatively good estimations of the forces coefficients in such cases, it must be clear that the very coarse mesh M1 is not predicting correctly the boundary layer behavior as represented in Fig. 5.12. The large turbulent structures are not representative of real flow structures for mesh M1. Mesh M3 and M5 reveal much thinner turbulent boundary layer. In mesh M5, 2-D waves can be observed, representative of the transition process. For the attached case, Fig. 5.13 reveals that the coarsest LES meshes are not able to

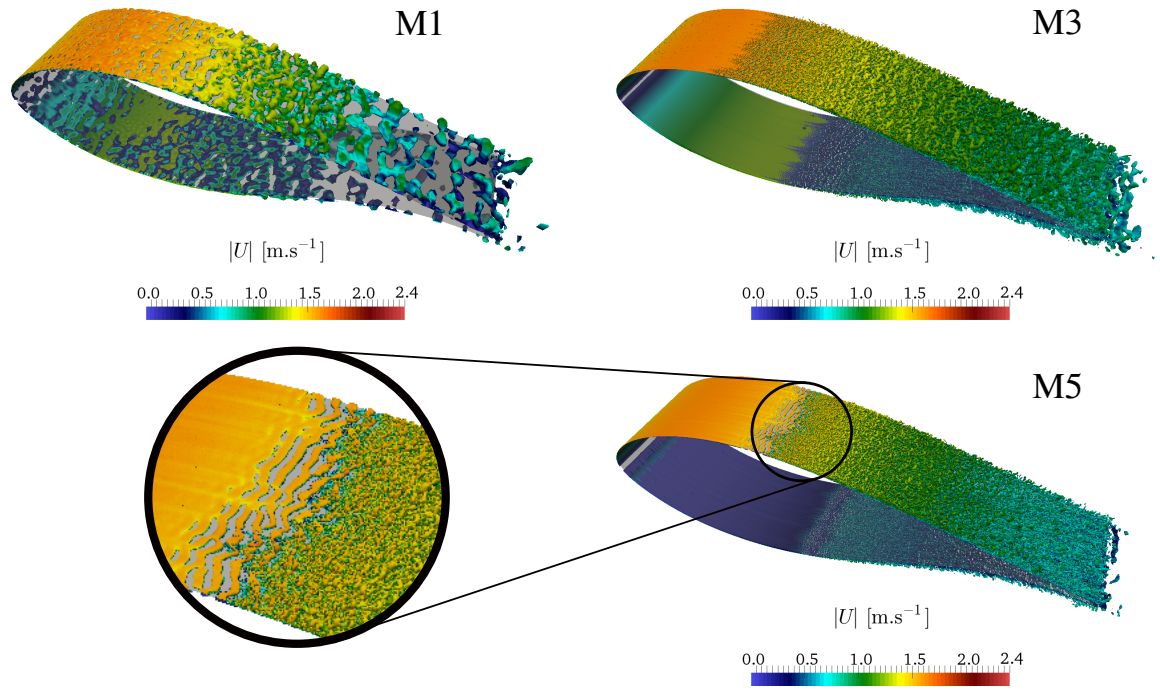

Figure 5.12: Isosurface of Q-criterion and several mesh refinements - AoA = 4°

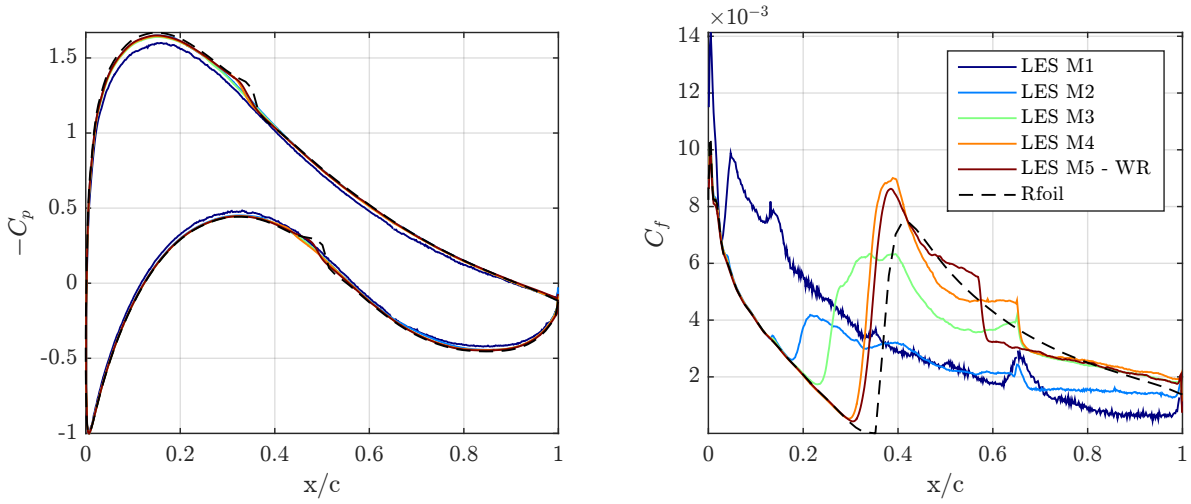

Figure 5.13: Pressure and friction coefficients comparison for AoA = 4°

capture the pressure bump observed in Rfoil while mesh M5 reveals a thickening of the boundary layer before transition similar to the one observed in Rfoil. The coarse meshes destabilize laminar boundary layer, triggering early transition. This behavior appears clearly on the suction side friction coefficient, with a transition point getting closer to Rfoil results as the mesh resolution increases. The transition is better predicted with finer meshes but without significant consequences on pressure coefficient.

Fig. 5.14 to 5.17 represent comparisons of u^+ profiles between LES, Xfoil plotted with Duprat and logarithmic wall laws. Meshes M1, M3 and M5 are used for comparison. For Duprat's law, the α_D parameter that takes into account the pressure gradient is computed based on the pressure coefficient along

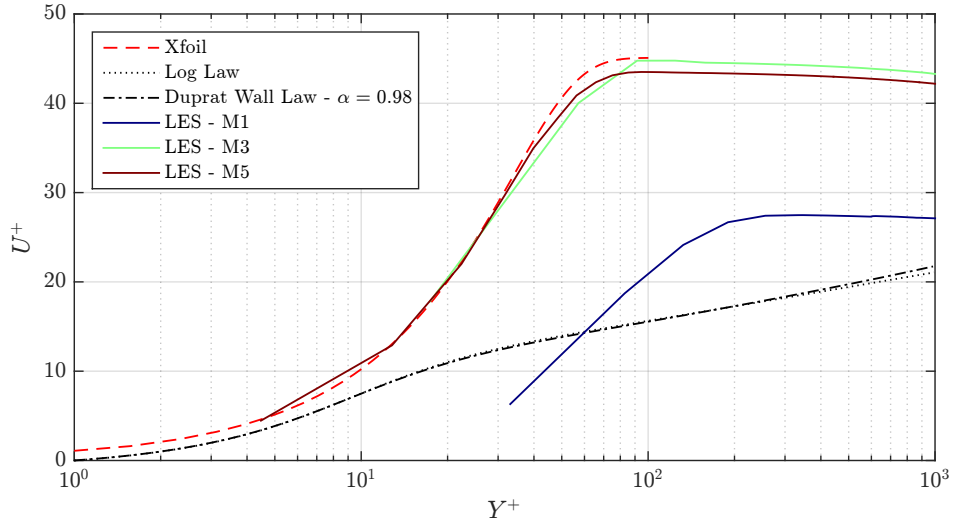

Figure 5.14: Velocity profile comparison for AoA = 4° - $x/x_{max} = 0.6$

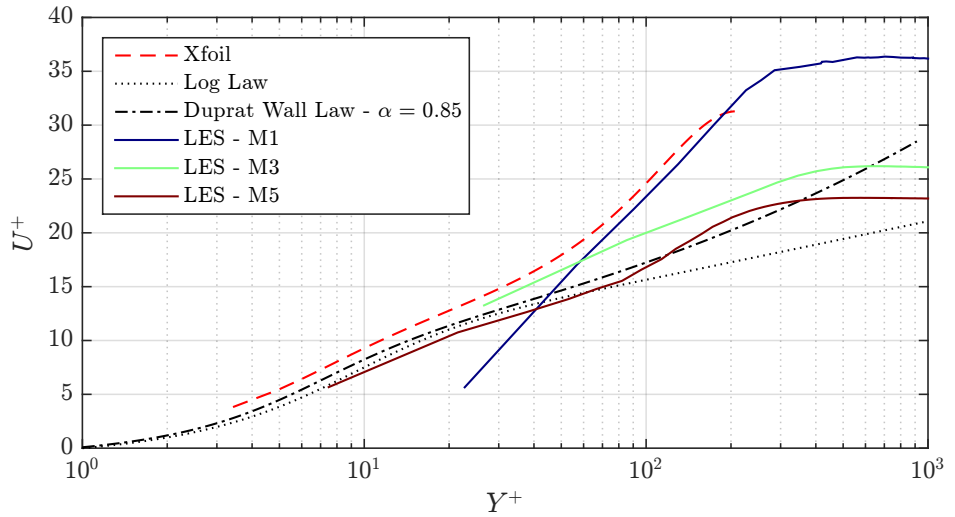

Figure 5.15: Velocity profile comparison for AoA = 4° - $x/x_{max} = 0.7$

the streamwise position on the airfoil suction side x. Fig. 5.14 is located at $x/x_{max} = 0.6$, before transition for both codes. Correlation is good for meshes M3 and M5, but with very high difference compared to Duprat and logarithmic laws. This can be explained by the fact that these laws are representative of turbulent boundary layers, while this zone is laminar. Mesh M1 is not matching with these results as the transition on this coarse mesh is predicted far too early. Furthermore, the Duprat wall law can not predict correctly the shear stress in this laminar region. For Fig. 5.15, LES velocity profile is close to Duprat wall law as transition has already occurred, which is not the case for Xfoil. Both codes are then close to wall laws for Fig. 5.16 and 5.17 as the boundary layers are turbulent for such coordinates. It can also be noticed that the wall resolved LES from M5 and Xfoil results are much closer to the Duprat wall law than to classical log law, revealing the applicability of this law when pressure gradients are observed. It also appears that mesh M1 is not predicting accurately the velocity profile.

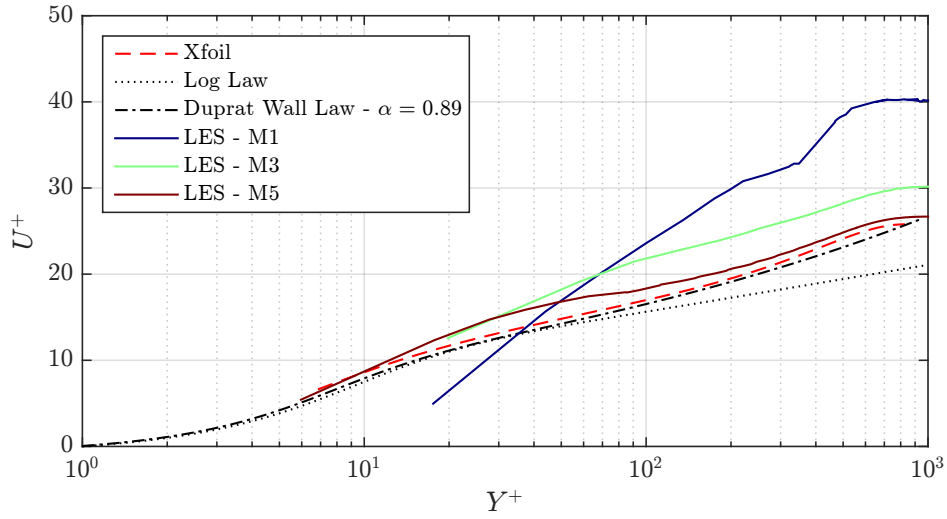

Figure 5.16: Velocity profile comparison for AoA = 4° - $x/x_{max} = 0.8$

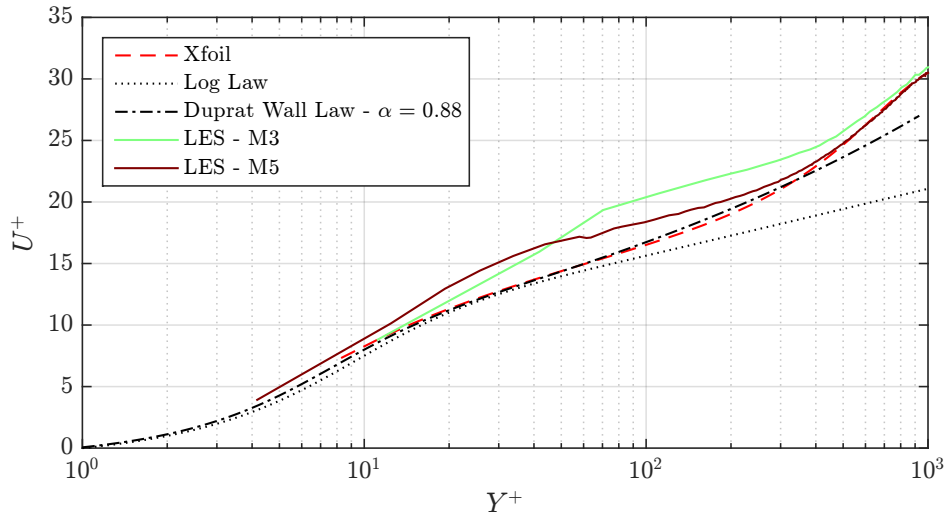

Figure 5.17: Velocity profile comparison for AoA = 4° - $x/x_{max} = 0.95$

5.3.4 Spanwise length

Several spanwise lengths are tested for both attached and detached cases with results presented in Table 5.4. In the case of unstructured meshes, the size of the mesh is directly proportional to the spanwise length for a given grid resolution, and it is a critical question when trying to reduce the number of required CPU hours. In the case of structured grids, cells are most often stretched in the spanwise direction as it is considered that the flow is mostly streamwise. This helps reducing the number of cells but can prevent from capturing 3-D stall turbulent structures. No difference is noticed in the prediction of lift coefficient for the attached case, implying that such span length is enough for attached cases. However, for stalled cases, a short spanwise length is not giving good results. The predicted lift coefficients are too high for spanwise length below $1c$. The temporal lift signals represented in Fig.5.18 reveal that if the spanwise length is lower than $1c$, aerodynamic forces undergo strong variations corresponding to the presence of large 2D vortices. With spanwise length over $1c$, the behaviour seems less obvious, but mean

Table 5.4: Spanwise length convergence study for attached and detached cases

Span Mesh	C_l for AoA = 4° M1	C_l for AoA = 23.2° [a] M1
$0.25c$	0.78	1.55
$0.5c$	-	1.48
$1c$	-	1.38
$2c$	0.78	1.35
$4c$	-	1.32

[a] With artificial viscosity

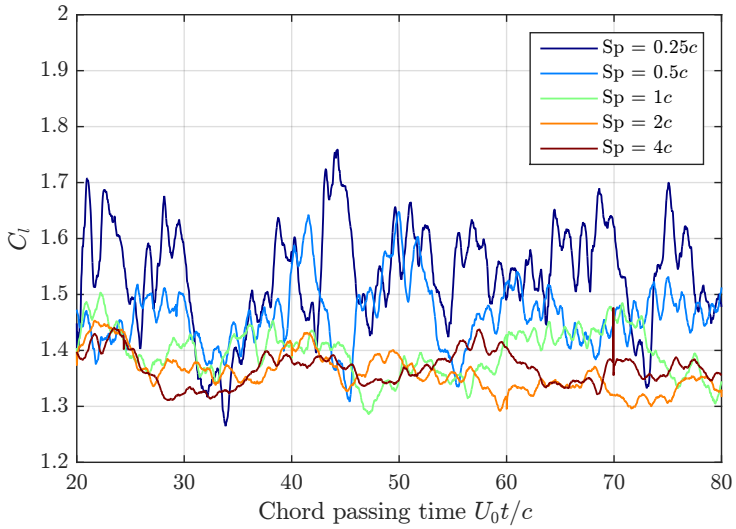

Figure 5.18: Convergence study of lift signal on spanwise length - M1 mesh - AoA = 23.2°

aerodynamic forces still appear to evolve when comparing with the $2c$ spanwise length. No significant difference is observed between the $2c$ and the $4c$ which seems to prove that convergence is reached.

A spanwise length of $0.25c$ is enough to capture correctly the 3D behaviour of small vortices created after transition zone. However this length is not enough to capture correctly the larger vortices that appear in stalled conditions, creating unrealistically stable 2-D vortices which do not evolve to 3-D vortices and thus prevent the airfoil to stall correctly as can be observed in Fig.5.19. This is in line with the observations of Fukuomoto [61].

5.3.5 Unsteady inflow conditions

5.3.5.1 Presentation of cases

Pitching cases both in attached and detached flow conditions are then studied. Few studies on such configurations have been conducted with LES, most at lower Reynolds number and for thin airfoils [105] [207] [119]. The main issue is that such cases focus on the creation and dynamics of the leading edge vortex and its characteristic massive stall. The flow behavior is very different for the thick FFA-W3-241

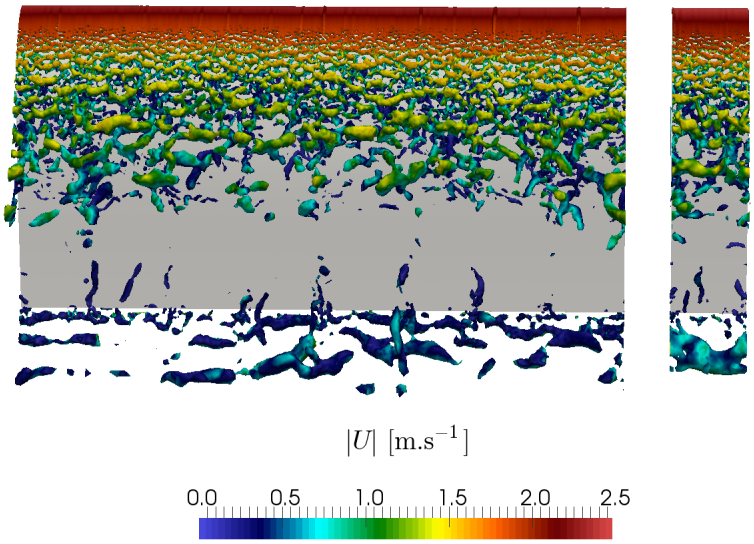

Figure 5.19: Isosurface of Q-criterion for several spanwise lengths - M1 mesh - AoA = 23.2°

airfoil characterized by a smooth trailing edge separation. Two cases have been studied here and defined in Table 5.5, based on the available experimental data from Fulgsang [58]. The reduced frequency k is defined as $k = \pi f c/U_0$, with f the pitching frequency. The parameters α_{mean} and α_{amp} are respectively the mean and amplitude values of angle of attacks, with the following motion of the angle of attack : $\alpha(t) = \alpha_{\text{mean}} + \alpha_{\text{amp}} * sin(2kU_0t/c)$. The center of rotation is located at $x/c = 0.4$, with x the position of the rotation center along the chord.

Table 5.5: Dynamic cases caracteristics

Case	α_{mean}	α_{amp}	k	Mesh	Spanwise length
Attached	3.8°	1.4°	0.093	M2	$0.25c$
Stalled	24.6°	1.9°	0.093	M1	$2c$

The mean cycle values for aerodynamic forces can be obtained with less than 5 cycles in attached cases, which represent around $150U_0t/c$ in our cases. However, dynamic stall cases imply to have much more cycles: at least 20 cycles (around $700U_0t/c$) to obtain correct mean values. These values give an order of magnitude of the CPU time needed to perform dynamic stall calculations once steady simulations have been performed successfully.

The temporal signals of lift and drag coefficients in dynamic stall cases reveal the complexity of the flow, as shown in Fig. 5.20. To obtain correct cycle average values in stalled cases, at least 20 cycles are needed, which leads to very high CPU time even with the coarsest mesh M1. Temporal signals for attached cases however reveal a good cycle to cycle correlation.

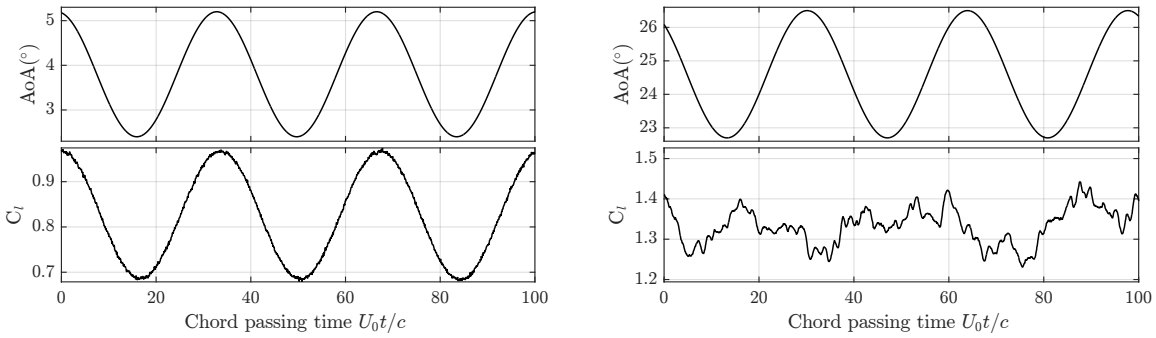

(a) Attached case (b) Stalled case

Figure 5.20: Temporals signals of AoA and C_l for attached and stalled oscillating cases.

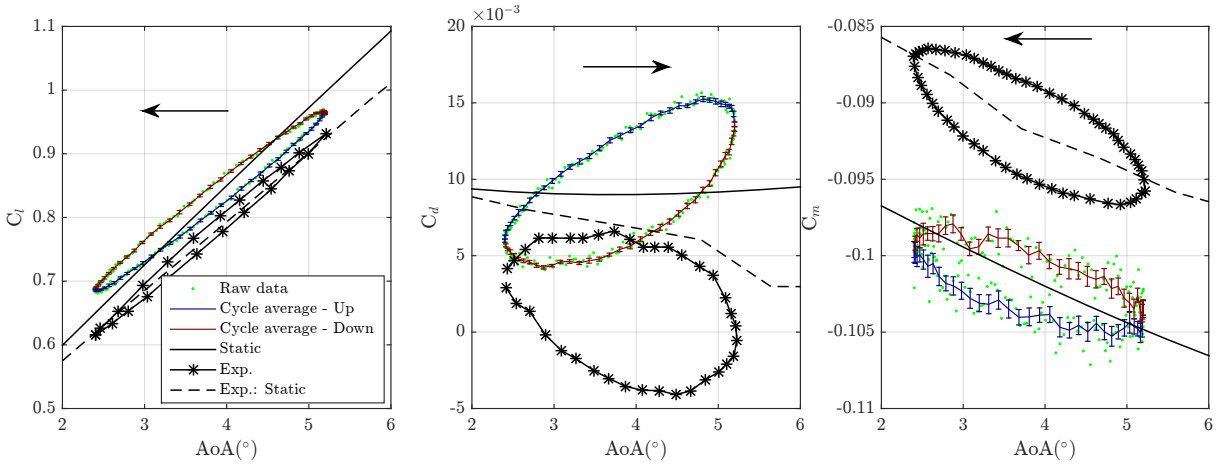

Figure 5.21: Average cycle values force coefficients - Dynamic attached case

5.3.5.2 Cycle averaged analysis

Fig. 5.21 and 5.22 compare cycle averaged force coefficients obtained in the current study with the experimental results. The plotted error bars have a total length corresponding to the standard deviation σ for binned AoA values, based on the raw data of the several simulated cycles. The hysteresis loop is correctly captured, but the shift observed in steady cases between experimental and numerical results is still present. The standard deviation is much larger for the separated case which is expected when observing the temporal signals, and appears to be slightly more important in the descending phase than the ascending phase, because of the chaotic reattachment process. It is quite remarkable to notice such behavior on the force coefficients despite the very poor modeling of the near wall flow with mesh M1.
The hysteresis loops for all three force coefficients observed in the separated oscillating case do not reveal the presence of specific peaks caused by a leading edge vortex. From these observations, it can be assumed that removing the leading edge vortex module from the Beddoes-Leishman dynamic stall model is a valid assumption for thick airfoils in such conditions. The hysteresis loop is then mainly caused by the delay on separation point. The next section focuses on the conditions for the apparition of vortex shedding on thick airfoils.

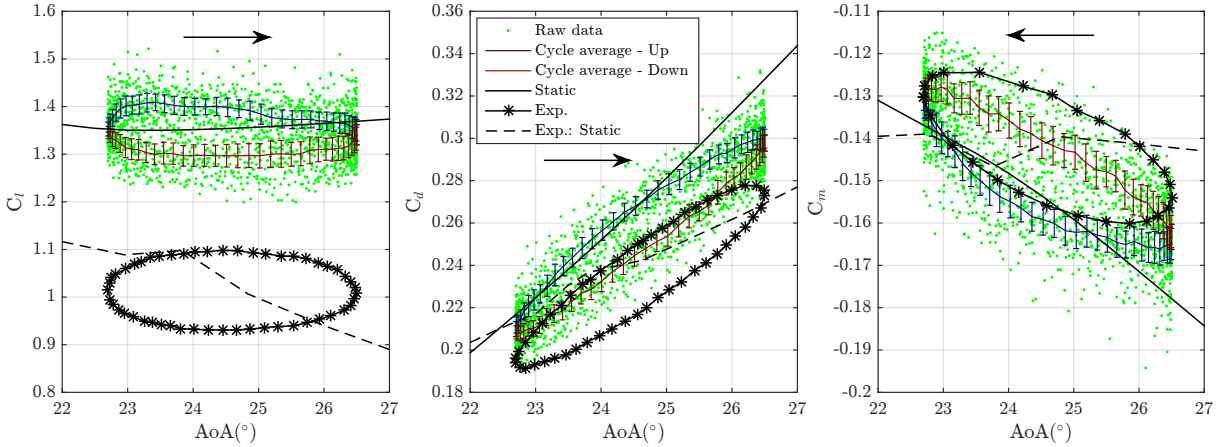

Figure 5.22: Average cycle values of force coefficients - Dynamic stall case

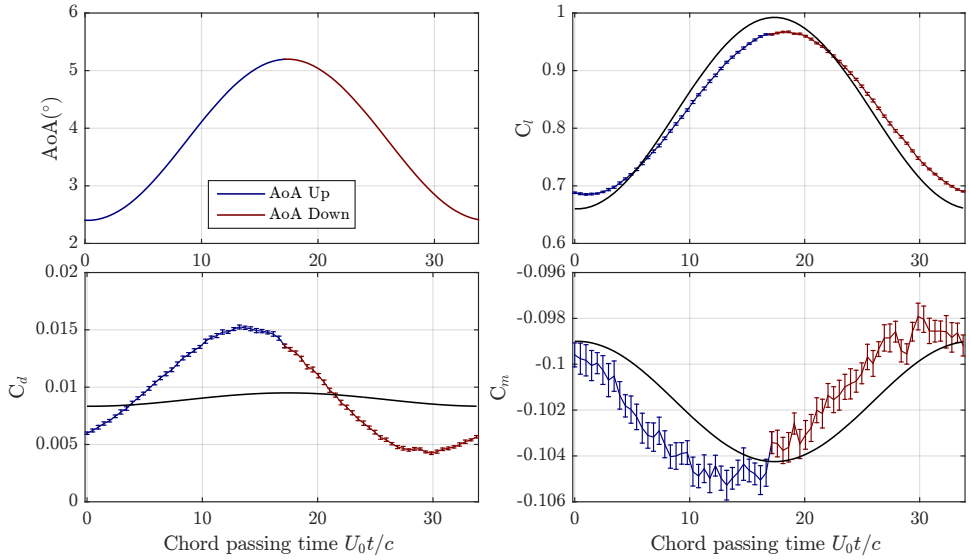

Figure 5.23: Average periodic values force coefficients - Dynamic attached case

5.4 Application to deepstall cases - AoA from $23.2°$ to $90°$

In several DLCs, the AoA can significantly exceed the stall angle and get as high as $90°$ on the whole blade in standstill conditions. The aerodynamic behavior is totally different in such massively separated cases, and is known to act like a *bluff body*. The most famous case of bluff body is the cylinder, and the study of the flow over a cylinder is still a challenge. The main difference with the flow around an airfoil is the appearance of large vortices emitted periodically on each side of the cylinder, a phenomenon referred to as the Karman vortex street. The flow around an airfoil acts in the same way when the angle of attack is high enough: most studies have been performed for many years investigating the shedding frequency of flat plates [37]. It appears that for thin airfoils with leading edge vortex stall, this behavior is observed as soon as stall occurs and that the boundary layer is fully detached on the suction side. For thicker airfoils with trailing edge stall, no massive separation occurs at stall angle and the shedding does

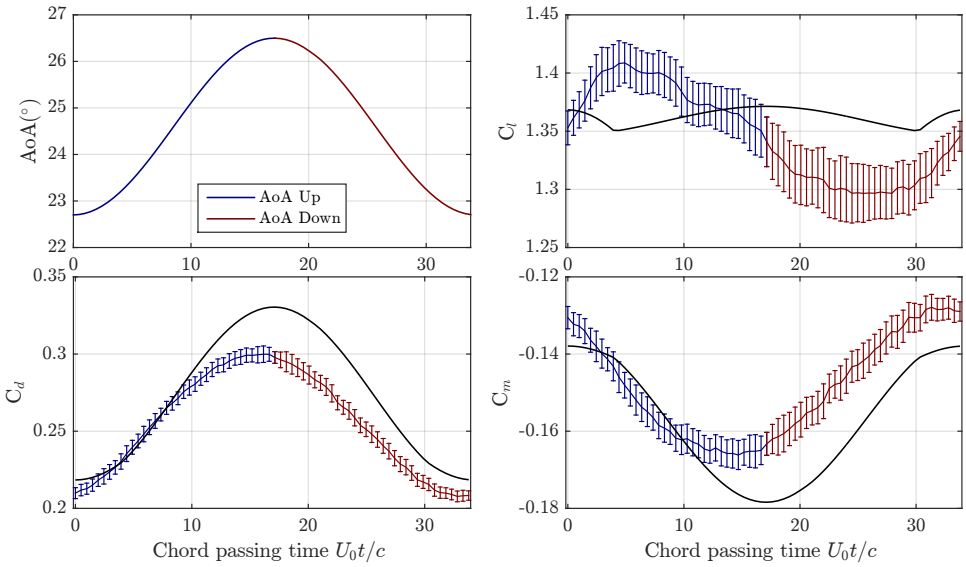

Figure 5.24: Average periodic values force coefficients - Dynamic stall case

not appear clearly. At the maximum angle of attack of 23.2° investigated during the validation, the flow on the suction side of the airfoil is not totally detached. According to the definitions that could be found in litterature [195] [127], deep stall is characterized by a fully detached boundary layer on suction side and massive detachment of vortices. In the present study, it is thus considered that the deep stall angle is reached when the boundary layer is fully detached on the suction side. The purpose of this study is then to identify at which angle the flow behavior changes from light stall to deep stall, and characterize the force coefficients.

Investigating such cases is highly relevant as engineering models are poorly predicting aerodynamic forces at such angles. Some dynamic stall models are used to predict the self excitation of the aerodynamic forces, such as Snel or ONERA BH models (see section 3.1.2). However, when used in oscillating inflow conditions, Stettner [187] noticed large discrepancies in aerodynamic damping provided by several engineering models at deep stall angle and higher. The main issue for such cases is to predict correctly the mean aerodynamic cyclic forces, in order to assess the aeroelastic stability of the blade. As the forces are highly unsteady, the mean cycle values are in fact poorly representative of the real temporal forces. Other models have been developed to focus only on the stochastic aspect of stall and deep stall, such as the models proposed by Bertagnolio [17] and Hansen [81], but independantly from the dynamic stall models. To validate such models, DES has been used in preference to RANS due to its capacity to capture a larger spectrum of turbulent structures. The studies from DTU Risø based on EllipSys code by Skrzypiński [178] [179] reveal the better capablities of DES for such flows. Xu [206] used DDES to simulate the flow over a s809 airfoil up to 90° AoA and compared the results to RANS calculations. The conclusions are the same regarding the difficulties to capture correctly the shedding vortices with RANS. Heinz [87] also performed full aeroelastic blade simulation in standstill condition with DES in order to assess the stability of a blade. Pellegrino [148] and Meskell [131] investigated the capabilities of unsteady RANS for such applications. Very few experimental data and analysis of the flow in such conditions are available. The experimental studies from Lind [117] [118] give a good insight of the flow behavior at very large angle of attack and in reverse flows.

5.4.1 Flow analysis

The first purpose of this study is to determine the critical deep stall AoA for which the boundary layer fully detaches from the airfoil, and to understand the apparition of vortex shedding. Two "quasi-static" cases are investigated and described in table 5.6.

Table 5.6: Quasi-static cases caracteristics

Case	α_{init}	α_{fin}	k	Mesh	Spanwise length
Case 1	23.2°	40°	0.01	M1	$2c$
Case 2	40°	90°	0.003	M1	$2c$

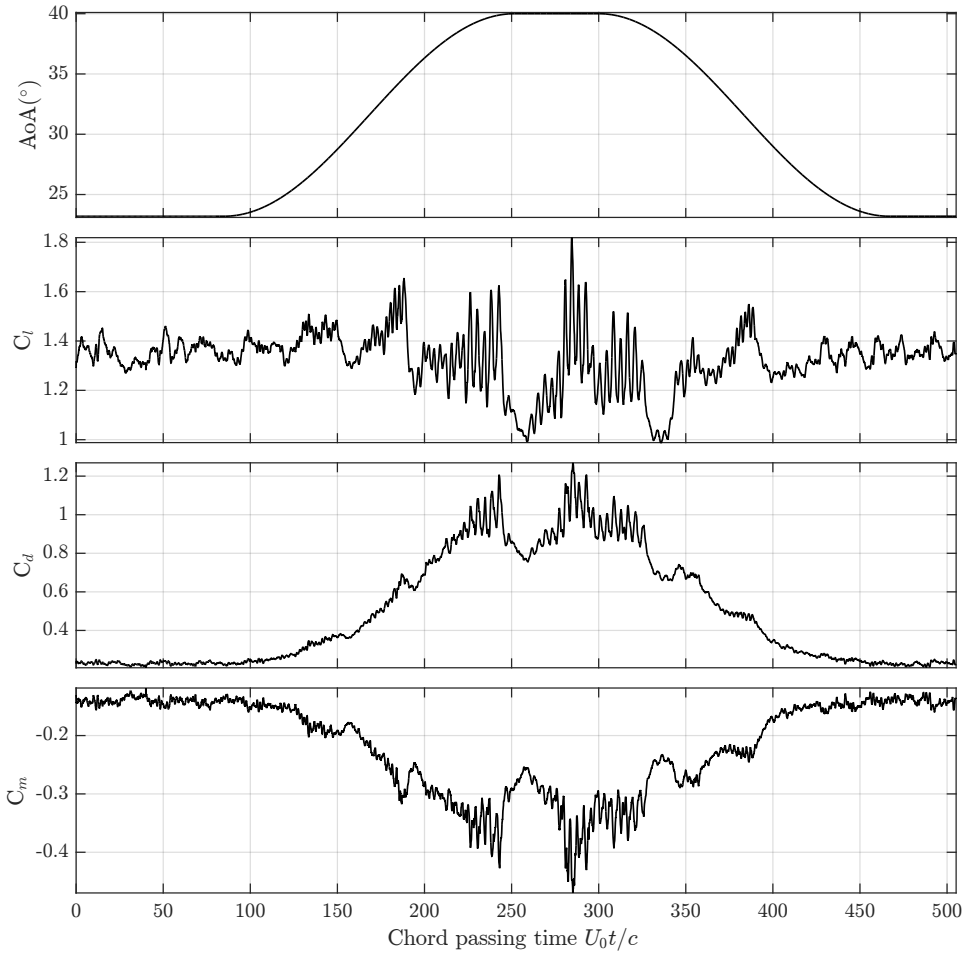

Figure 5.25: Temporals signals of AoA and force coefficients for quasi-static deepstall case - AoA from 23.2° to 40°

A dynamic case with a very low reduced frequency of 0.01 is first investigated based on the previous static simulations performed at $23.2°$. This reduced frequency has been chosen based on the proposition from Leishman [109] to consider 0.01 as the limit between static and unsteady cases. The AoA evolves from $23.2°$ to $40°$ in a sinusoidal motion. The angle of $40°$ is maintained for around 50 flow passing times

and then moves back from $40°$ to $23.2°$. The evolution of the AoA, lift, drag and moment coefficients is given in Fig. 5.25.

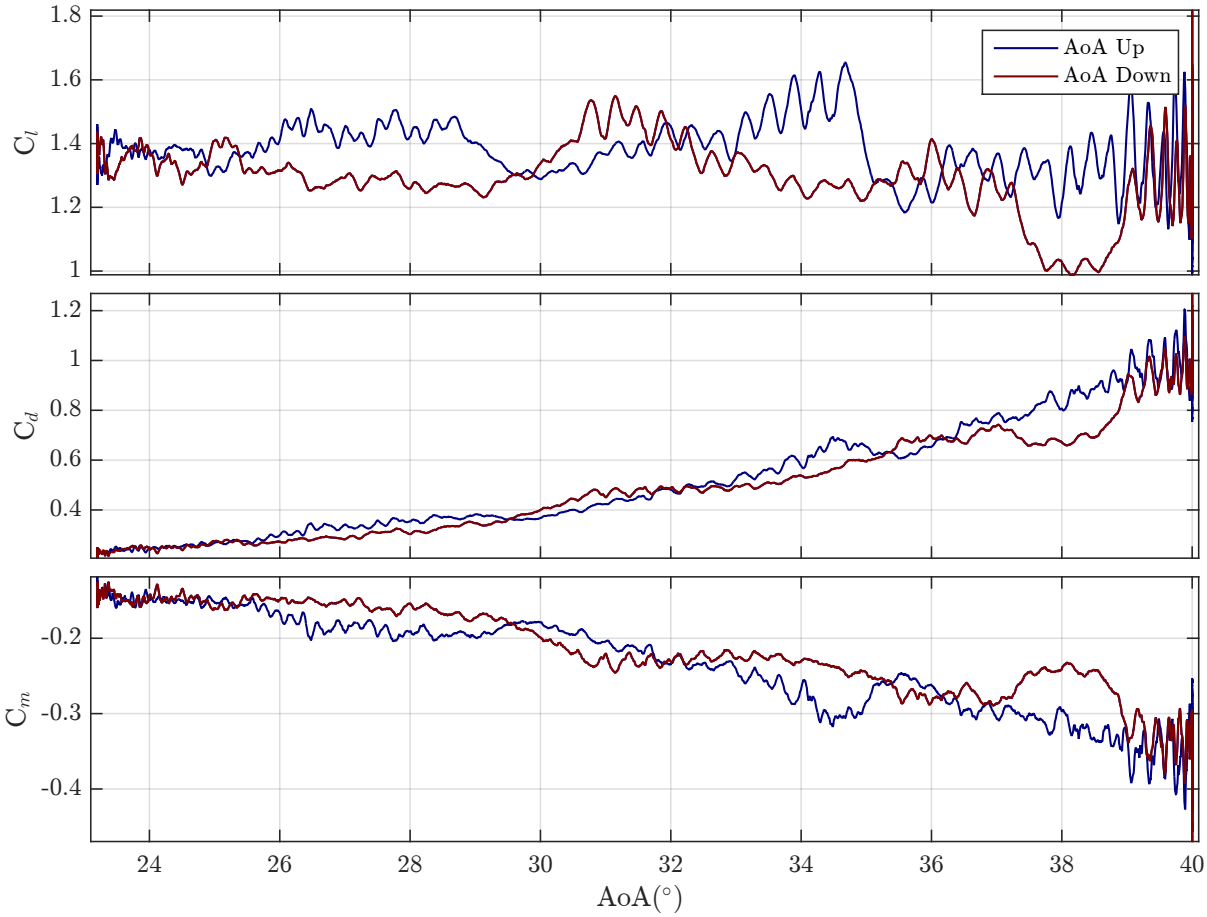

Figure 5.26: Ascending and descending phases for quasi-static case with $k = 0.01$ - AoA from $23.2°$ to $40°$

It appears that the mean value of lift coefficient does not change a lot over this range of AoA. However the drag coefficient increases from 0.25 to around 1.00 showing that the stalling process is getting stronger. The moment coefficient also changes, decreasing from -0.15 to -0.35. An important feature to notice is the switch from a very stochastic behavior up to $30°$ to a more organized and cycling aspect afterwards. The stochastic behavior seems to be in line with the observations and models from Bertagnolio [17] and Hansen [81]. It is not the cases for higher angles of attack were the signals are dominated by specific frequencies: the shedding frequency. For AoAs above $30°$, it is interesting to notice that two distinct behaviors can be observed:

- Strong periodicity, high lift and drag
- Aperiodic signal, low lift and drag

Those two behaviors switch regularly from one to the other progressively.
In order to check that the hypothesis of static flow is respected, the force coefficients in the ascending and

descending phase are plotted in Fig. 5.26. It appears clearly that the succession of periodic and aperiodic phases are not linked to specific AoA values. However, the main trends of the flow behavior are not the same when the AoA increases or decreases: the strong periodicity appears or disappears around $25°$ and $30°$ respectively. The periodicity of the signal is thus stronger when the AoA increases. This figure also reveals that the force coefficients are different in the ascending and descending phases. Thus, the hypothesis of steady flow is not respected. However this might not be caused by the reduced frequency, but by the fact that the flow behavior for a given angle of attack is strongly dependant of the precedent state: for the ascending phase, it is highly probable that the flow goes from a more attached state to a more detached state, while it is the opposite in the descending phase, whatever the reduced frequency can be. This is in line with the observations from Timmer [193] and Lind [118] who give two values of static forces coefficients at deep stall angle depending on the history of the AoA. In the present case, the mean value of C_l for ascending and descending phases between $23°$ and $40°$ are 1.37 and 1.30 respectively. For C_d, the values are 0.54 and 0.50 and for C_m, -0.24 and -0.22.

Timmer [193] proposed to relate the deep stall angle with the leading edge radius with the formula $\alpha_{deep-stall} = 1114(y/c)$ with y the ordinate of the airfoil upper surface for the abscissa $x = 0.0125$ along the chord c. According to this formula, the deep stall angle should be reached around $35°$ for the FFA-W3-241 airfoil. Based on the flow observed in the quasi-static case, three static cases have been investigated with AoAs of $30°$, $34°$ and $37°$ in addition to the static values obtained at $23.2°$ and $40°$. Fig. 5.27 shows the mean velocity magnitude for these five static cases, revealing that the fully separated state is reached between $34°$ and $37°$, which is in good agreement with the prediction from Timmer.

It appears that the separation moves gradually from the trailing edge to the leading edge from $23.2°$ to

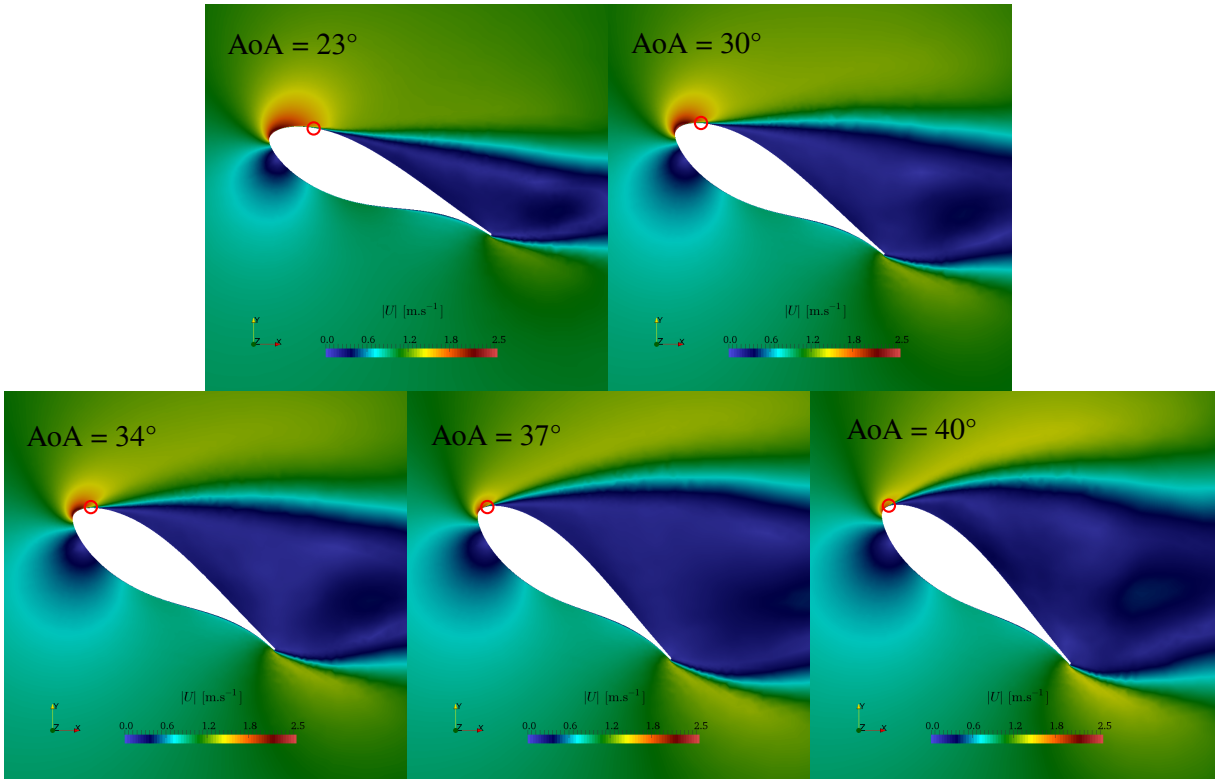

Figure 5.27: Mean velocity magnitude at 5 different AoA: identification of deepstall angle

34°. Then it seems that a jump on the separation can be observed to reach the leading edge at 37°. It can also be observed that the curvature of the separation line between the fast undisturbed flow and the slow detached flow is much higher when the fully separated state is reached. This observation can be related to the experiments of Chen and Fang [37] on flat plates with bevel angle: for a given angle of attack (around 40°), the separation point switches from the rear lip to the front lip of the flat plate leading edge, resulting in a increase of separation angle.

It is also interesting to notice that the Kirchhoff theory used in the B-L dynamic stall model to compute

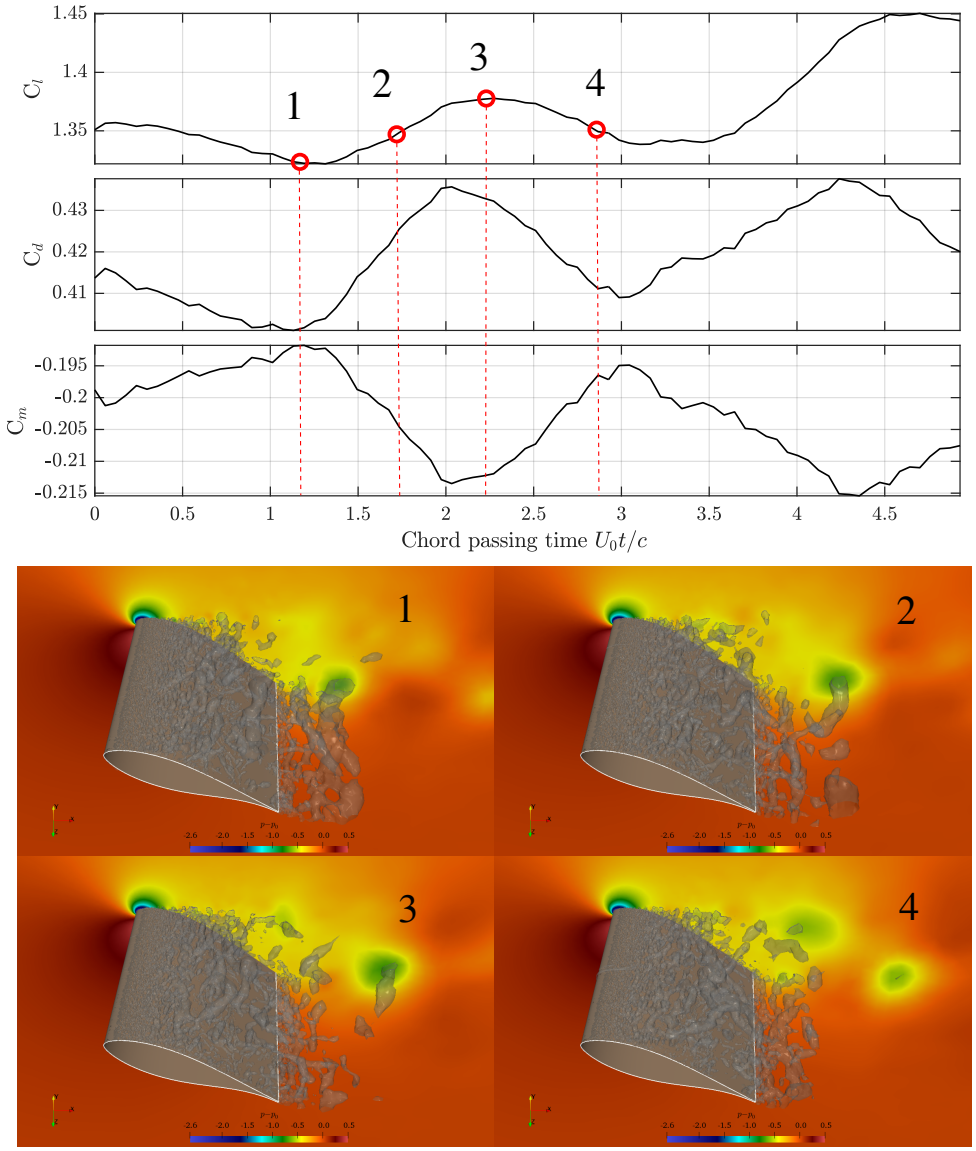

Figure 5.28: Force coefficients and shedding process at AoA = 30°.

the position of separation point is quite robust even for high angle of attack. Indeed, according to the formula used in the ARDEMA code presented earlier, the fully separated state is reached when the linear fully attached lift is four times larger than the real viscous lift. For the FFA-W3-241, the fully separated state is reached at around 30° (see Fig. 4.1).

The shedding process at an AoA of 30° is presented in Fig. 5.28, showing snapshots of flow behavior

during one period of the lift oscillating signal. The instantaneous pressure field is presented on a slice plane at a given spanwise position, as well as iso-surface of Q-criterion for $Q = 30$. First, it is important to notice that the lift, drag and moment coefficients have the same frequency. The drag and moment coefficients are in phase while the lift coefficient is slightly delayed. The roll-up of the trailing edge vortex soon after detaching from the airfoil appears on snapshot 1. The lift, drag and moment coefficients

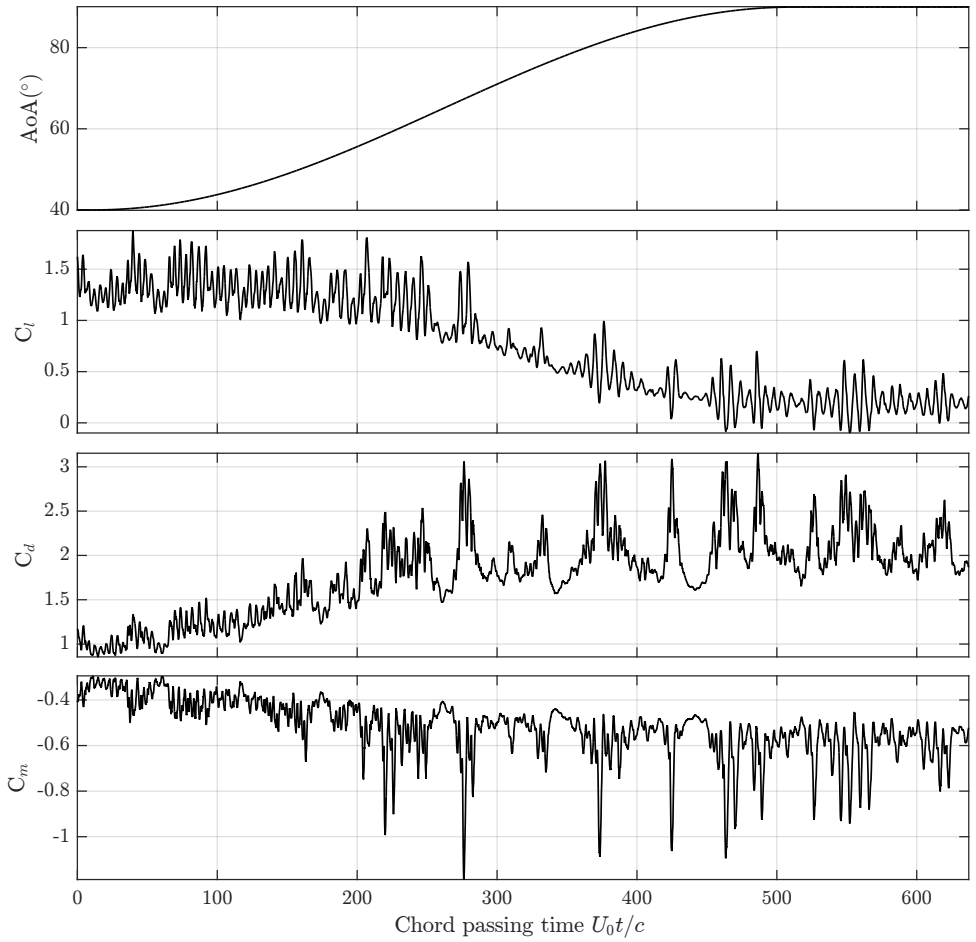

Figure 5.29: Temporals signals of AoA and force coefficients for quasi-static deepstall case - AoA from $40°$ to $90°$

are at the lower value of the cycle. While the trailing edge vortex is convected downstream in the next snapshots, another more diffuse vortex appears behind the separation point on snapshot 3: the maximum values of force coefficients are reached when this vortex passes over the trailing edge. On snapshot 4, a new trailing edge vortex is created while the separation point vortex is convected downstream. The creation of the separation point vortex seems driven by the trailing edge vortex. A succession of high frequency small vortices appear at the separation point constantly, but when the trailing edge vortex appears these small vortices accumulate to create a large and diffuse vortex, weaker than the trailing edge vortex but passing over the airfoil surface and creating a suction peak periodically.

A second quasi-static case is then simulated from $40°$ to $90°$ with the same sinusoidal motion than previously but with a lower reduced frequency $k = 0.003$ in order to have approximately the same maximum pitch rate than in the previous case. The temporal force coefficients are presented in Fig. 5.29.

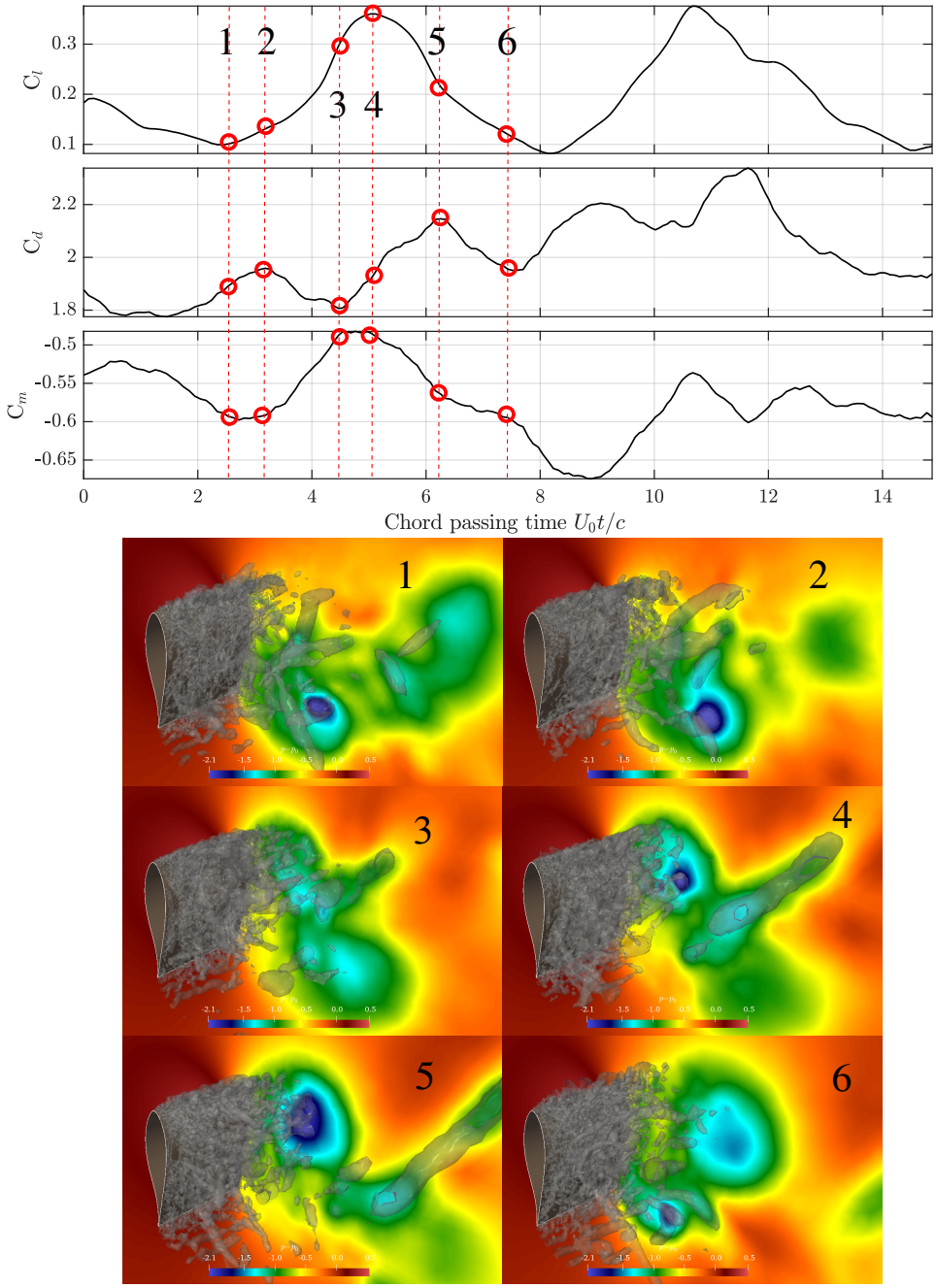

Figure 5.30: Force coefficients and shedding process at AoA = 90°.

The lift coefficient starts decreasing between 50° and 60° up to 90°. On the opposite, drag and moment coefficients are mostly constant after 70°. The trends observed previously regarding the succession of strongly periodic and aperiodic phases can be noticed in the present case too. At 90°, it appears that the switch from one phase to another might be linked to the creation of the shedding vortices: during the aperiodic phases, the large trailing and leading edge vortices are increasing in strength at a greater distance from the airfoil than in the periodic phases. Their influence on the pressure at the suction side of the airfoil is then reduced: the pressure increase on the suction side, without being influenced by the

vortices. When the vortices accumulate strength closer to the airfoil surface, their influence is easily identified on the force coefficients. Fig. 5.30 show the succession of events during an oscillation of the lift coefficient. First, it appears clearly that the frequency of drag and moment coefficients are twice the frequency of lift coefficient. Furthermore, the peaks of lift are slightly delayed while drag and moment are in phase. Both leading and trailing edge vortices are created alternatively. In contrast to what is observed at $30°$, the leading edge vortex is created close to the airfoil suction in the same way than the trailing edge vortex, rolling up from the separation point. In snapshot 1, the lift is at his lowest value, drag is still increasing and moment is at his maximum negative value. The leading edge vortex is far from the airfoil surface while the trailing edge vortex suction is strong: the pitching moment is increased by the trailing edge vortex suction. In snapshot 2, the strength of trailing edge vortex covers a large area of the suction side, implying a large drag and moment. In snapshots 3 and 4, the leading edge vortex starts rolling up, increasing in strength. Because of its location slightly above the airfoil, the suction force creates lift and decreases the nose down pitching moment. On the opposite, drag is at its lowest value as the strength of both vortices is quite low. The leading edge vortex then detaches from the surface in snapshot 5, covering a large part of the suction side and increasing drag to its maximum value. A new small and weak trailing edge vortex begins to accumulate at the trailing edge in snapshot 6, implying a low drag value. It is remarkable that the trailing edge vortex create suctions down while leading edge vortex creates suction up, implying that the frequency of the lift signal will then be twice lower than the frequency of drag and moment that will react to each vortex creation and convection.

To summarize the values of force coefficients obtained from $0°$ to $90°$, Fig. 5.31 compares the results

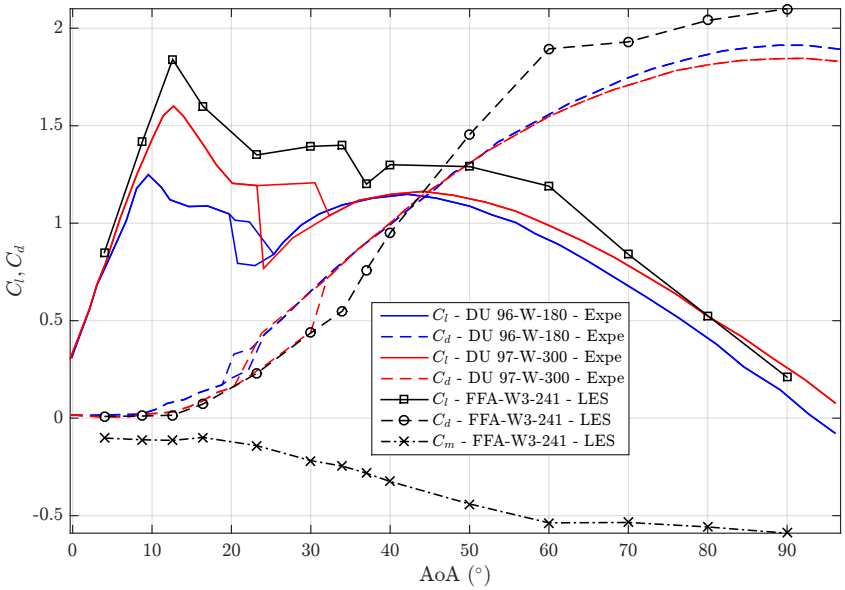

Figure 5.31: Comparison of force coefficients from $0°$ to $90°$ with experimental results from Timmer [193]

obtained with the current methodology with experimentals results from Timmer [193]. In the current simulations, the Reynolds number is $Re = 1.6 \cdot 10^6$ while Timmer experiments are conducted at $Re = 1.0 \cdot 10^6$. The profiles used by Timmer are the DU-96-W-180 and DU-97-W-300 wind turbine dedicated profiles with relative thickness of 18% and 30% respectively. The FFA-W3-241 profile is quite similar to such profiles and results can be compared to have an idea about their validity. It thus appears that

the maximum drag value $C_d = 2.1$ obtained with LES at $90°$ is too high compared to the results from Timmer. He proposed a correlation for the maximum drag coefficient in the same form than the one for the deep stall angle presented above: $C_{d,max} = 1.994 - 5.4375(y/c)$ with y the ordinate of the airfoil upper surface for the abscissa $x = 0.0125$ along the chord c. According to this formula, the maximum drag coefficient for the FFA-W3-241 airfoil should be $C_{d,max} = 1.82$.

5.4.2 Shedding frequencies

A critical aspect regarding the force signals obtained near and after deep stall angle is the frequency and amplitude of the self excited oscillations. Indeed, the periodic forces are responsible for increased fatigue loading on the blades, in particular when the shedding frequency is close to the blade (or tower) natural frequency. Few experimental studies are available at high Reynolds number as the blockage effects in a wind tunnel are significant when reaching high angles of attack, increasing the difficulty to reach high wind tunnel flow velocity in comparison to small AoA cases. Some numerical investigations have been performed for such flows that combine the difficulty to obtain a correct description of the boundary layer at high Reynolds number and the necessity to capture a large spectrum of turbulent structures. Skrzypinski [178] and Xu [206] investigated such cases with RANS and DES of wind turbine dedicated airfoils and realistic Reynolds numbers, and it clearly appears that RANS does not capture enough turbulent structures, creating artificially large shedding vortices not perturbed by the smaller ones observed in DES. The shedding frequency is thus much smaller than the ones obtained with DES, due to the correlation between the vortex size and energy and its shedding frequency. The amplitude of the force coefficient also appears to be too large for RANS cases. The same observations can be extrapolated to the RANS study from Pellegrino [148] on a s809 profile at $Re = 1.0 \cdot 10^6$. The Strouhal number $St = fc/U$ obtained with RANS calculations appears to be around 0.13 for an airfoil at a $90°$ AoA, while experimental and DES analysis predict a Strouhal number between 0.15 and 0.16. Lind and Jones [118] investigated the Strouhal number of five bluff bodies with AoA varying from $0°$ to $180°$: a NACA0012,a NACA0024, a 24% relative thickness ellipse and a 26% relative thickness ellipse. Several number Reynolds up to $Re = 1.0 \cdot 10^6$ are presented in Lind PhD thesis manuscript [116], revealing the independence of Strouhal number towards Reynolds number. However, the different airfoils seem to have different Strouhal numbers: a higher curvature radius at leading and/or trailing edge will be characterized by a higher Strouhal number. The NACA0024 and the cambered ellipse should then be the closest to the FFA-W3-241 airfoil.

Fig. 5.32 and 5.33 plot the spectra of the quasi-static cases force coefficients. The full temporal length of the simulations are used (just removing the initialization phase). In the first case (AoA from $23°$ to $40°$), three distinct peaks appear at 0.25, 0.4 and 0.5, while in the second case (AoA from $40°$ to $90°$) the Strouhal range from 0.15 to 0.25 for the lift coefficient is covered. The Strouhal peaks are the same for the three force coefficients in the first case, whereas the analysis is more complex in the second case. The drag coefficient appears to have a higher frequency range than lift coefficient, while moment coefficient contains the frequency range of both lift and drag coefficients. In order to investigate more accurately the Strouhal number for a given AoA range, the spectra are calculated over several AoA ranges and plotted in next figures. In Fig. 5.35 and 5.35, the spectra of the ascending and descending phases of the first quasi-static case are computed around four different AoA ranges. The several peaks observed on the spectra of the full temporal signals are observed distinctly. A very weak peak around $St = 0.5$ is observed at the lowest range from $23.2°$ to $26°$. Then the Strouhal number decreases as the AoA increases. A secondary peak at twice the frequency of the first peak is observed for the AoA

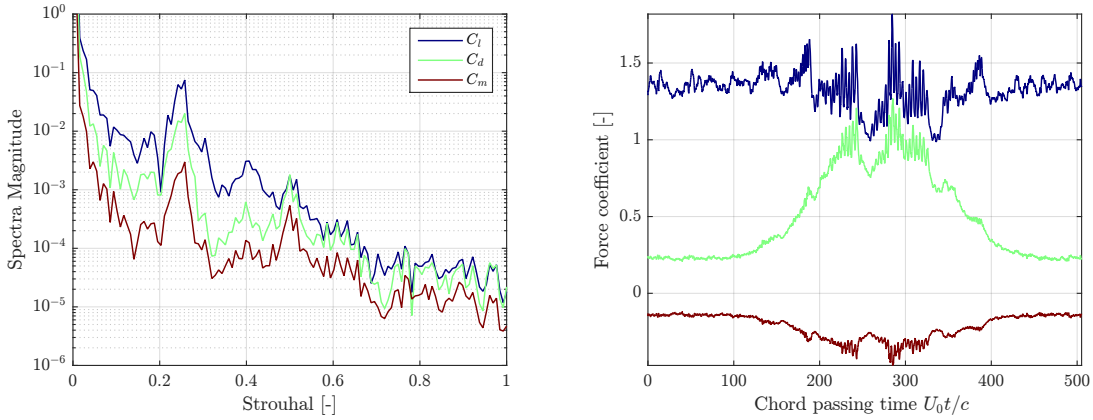

Figure 5.32: Normalized spectra for quasi-static case and associated temporal signals - AoA from 23° to 40°

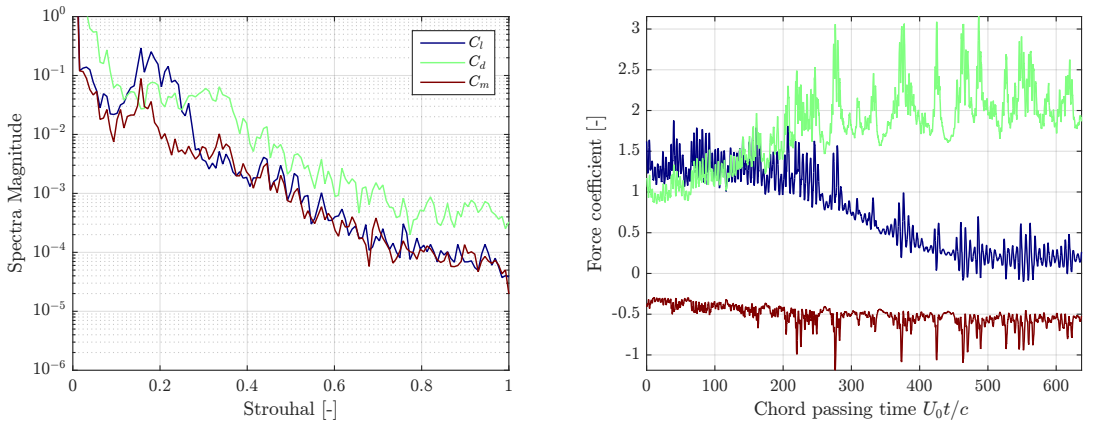

Figure 5.33: Normalized spectra for quasi-static case and associated temporal signals - AoA from 40° to 90°

ranges from 32° to 38° and 38° to 40°. It is interesting to notice that the frequency observed during the ascending and descending phase are not the same: during ascending phase, the Strouhal number between 26° and 32° is $St = 0.5$ while for the descending phase $St = 0.4$. This is also observed for the AoA range from 32° and 38° with $St = 0.4$ and $St = 0.3$ respectively. This phenomenon can be explained by considering that a time delay is needed for the shedding process to reach a stable state.

In order to analyse more accurately the frequency range around deep stall angle, the spectra of the three static cases at AoA values of 30°, 34° and 37° are plotted in Fig. 5.36. The Strouhal number at 30° and 34° is very close, between 0.38 and 0.4. At 37°, a jump is observed in the Strouhal number that decreases to 0.25. This behavior has been observed on flat plates with bevel angle by Chen [37], caused by the jump of the separation point from the front lip to the rear lip of the leading edge. This seems to be in line with the observation from the previous section regarding the jump of the separation point to the leading edge between 34° and 37°.

The same process is conducted to investigate the Strouhal number for several AoA ranges of the second quasi-static from 40° and 90°, and presented in Fig. 5.37. The Strouhal decreases as the AoA increases in a continuous way. The presence of a secondar peak at twice the main frequency is more visible, specif-

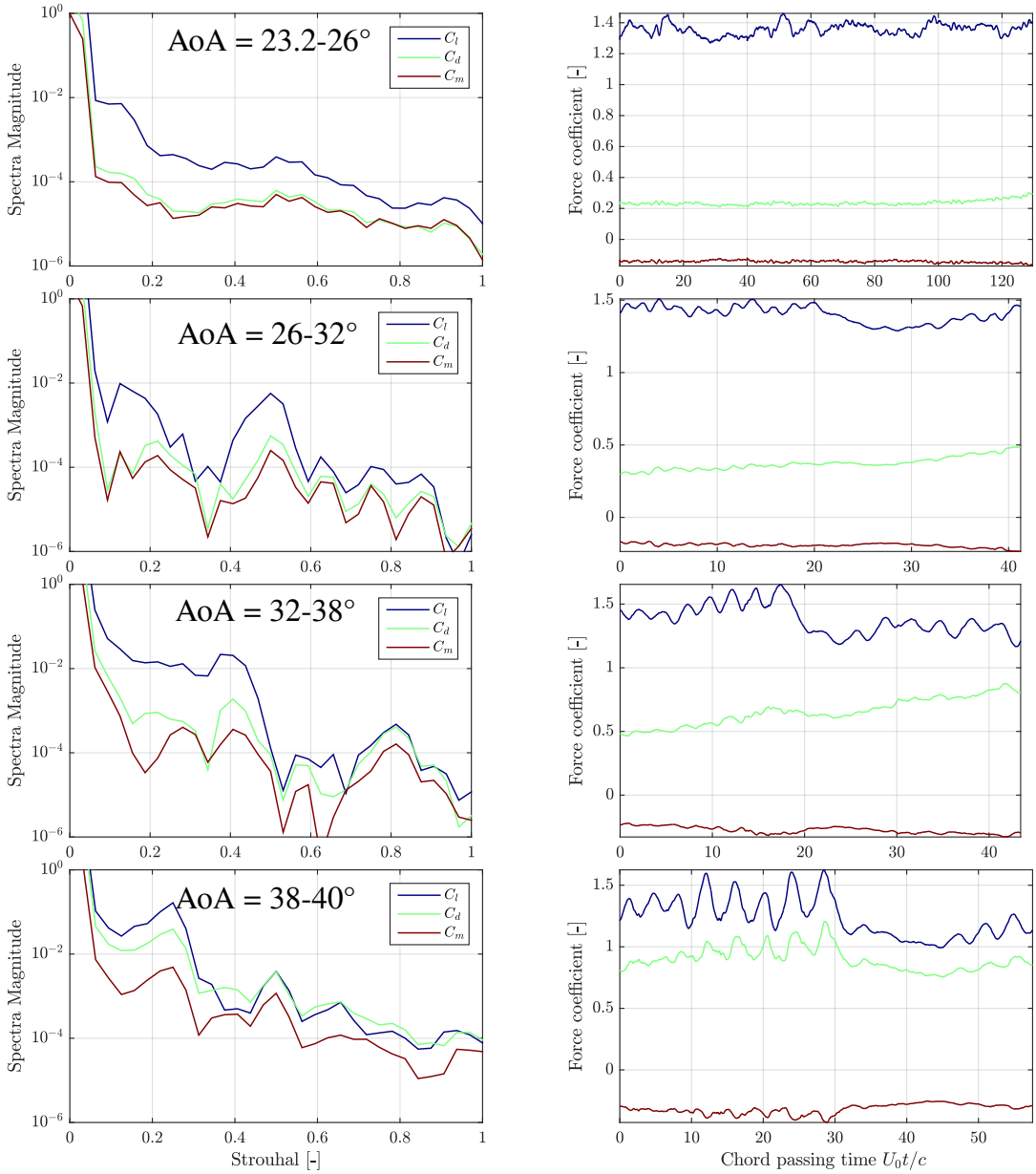

Figure 5.34: Normalized spectra for quasi-static case and associated temporal signals - Several AoA ranges from 23° to 40°, ascending phase

ically on the drag and moment coefficients. At 90°, the main peak at $St = 0.157$ for the lift coefficient does not appear on the drag coefficient, but is replaced by the double frequency. This phenomenon has also been observed by Zou [211] or Pellegrino [148]. This is in line with the flow observations presented in the previous section based on Fig. 5.30. It implies that the time period defining the Strouhal number is the time between the creation of two leading (or trailing) edge vortices.

The projected chord $c_{proj} = c.sin(AoA)$ is often used to define the Strouhal number instead of the chord length. In the figures presented above, the full chord is used, revealing a constantly decreasing Strouhal for increasing AoA. In Fig. 5.38, it appears that the Strouhal number based on projected chord is constant from deep stall angle to 90°. The results obtained in this study are compared with several

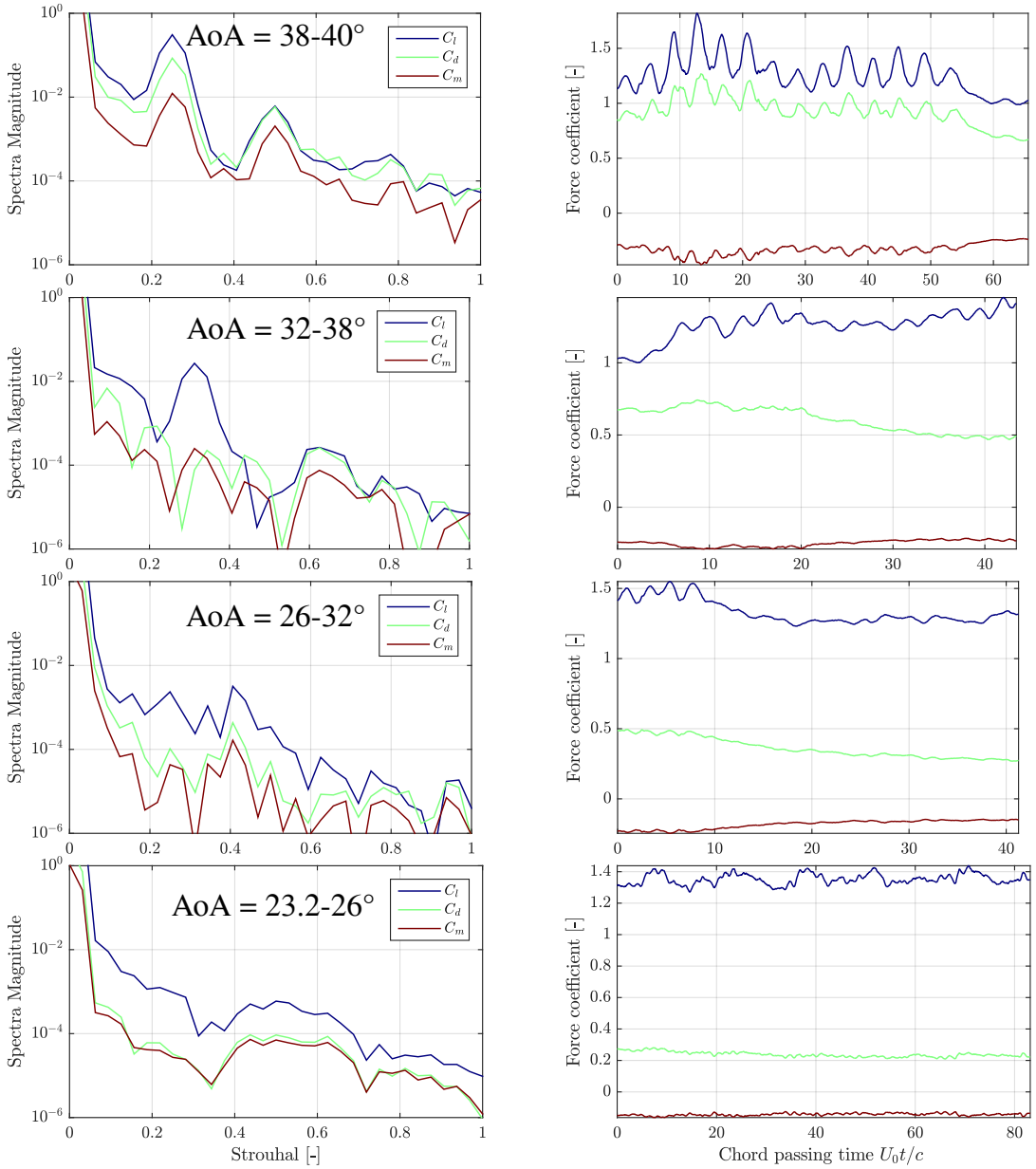

Figure 5.35: Normalized spectra for quasi-static case and associated temporal signals - Several AoA ranges from 23° to 40°, descending phase

data from literature based on the projected chord. The experimental results from Lind are presented for $Re = 6.6 \cdot 10^5$ and two airfoils shapes. For both, the Strouhal are slightly above the present results with a Strouhal number around 0.18 at 90° (0.157 for the present LES). The hook shape of the Strouhal number at low AoAs is also observed by Lind and Jones [116] on several airfoils but at lower AoAs than for the present simulations. The present results match perfectly with the simulations from Skrzypinski [178] at 90°, performed with DES at a Reynolds number of $Re = 2.0 \cdot 10^6$ on an 18% relative thickness airfoil. As mentionned earlier, the results from Pellegrino [148] obtained with RANS on a s809 profil at $Re = 1.0 \cdot 10^6$ are lower than the present ones, with a projected chord Strouhal of 0.13. The standard deviation of lift and tangential forces coefficients are also presented and compared with the data from

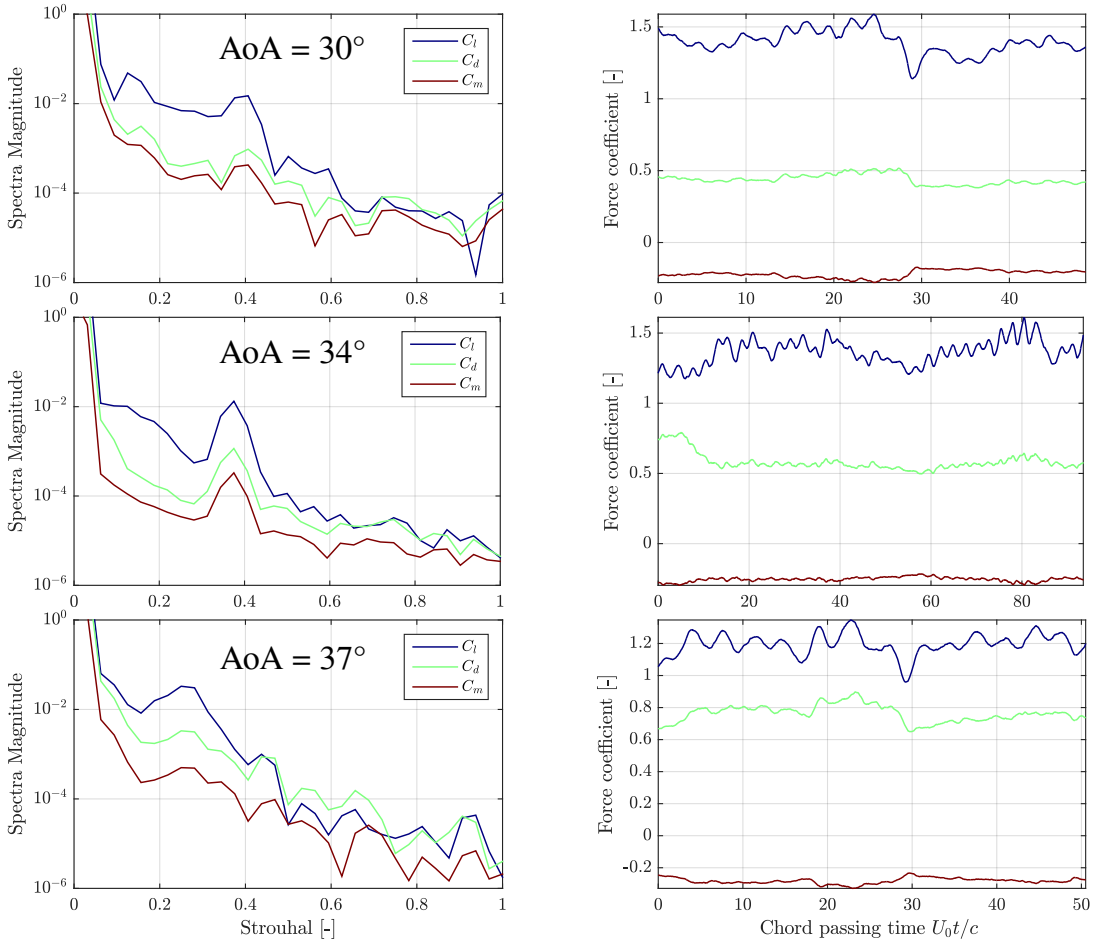

Figure 5.36: Normalized spectra and associated temporal signals for three static cases near deep stall angle

Lind and Jones [118] on lift coefficient. The standard deviation gives an order of magnitude of the mean amplitude of the oscillations caused by the vortex shedding. In the present simulations, the standard deviation on C_l reaches a maximum value of 0.23 at 60° and decreases up to 90°. The same observation is made by Lind on the curved ellipse but with a maximum value reached at a lower AoA of 45°. The standard deviation on C_t appears to be almost constant between 60° and 90°. When considering vortex induced vibrations of blades, C_t is the critical parameter to analyse. Indeed, the force oscillations in the normal directions are aerodynamically damped as any motion in such direction creates a strong opposite drag. On the opposite, a motion in the tangential direction is not damped. The edgewise natural frequency of the blade must then be different from the Strouhal number. However the most critical AoAs are for the maximum amplitude of the oscillations. Based on the results obtained in the present study, it appears that AoA from 60° to 90° have large amplitudes of oscillations on C_t, with chord based Strouhal numbers varying from around 0.16 to 0.19.

5.4.3 Oscillating airfoil in deepstall conditions

Two oscillating cases described in Chapt. 5.7 have been simulated in order to assess the flow behavior at higher AoAs than the validation cases. No experimental data are available for these ranges, but it

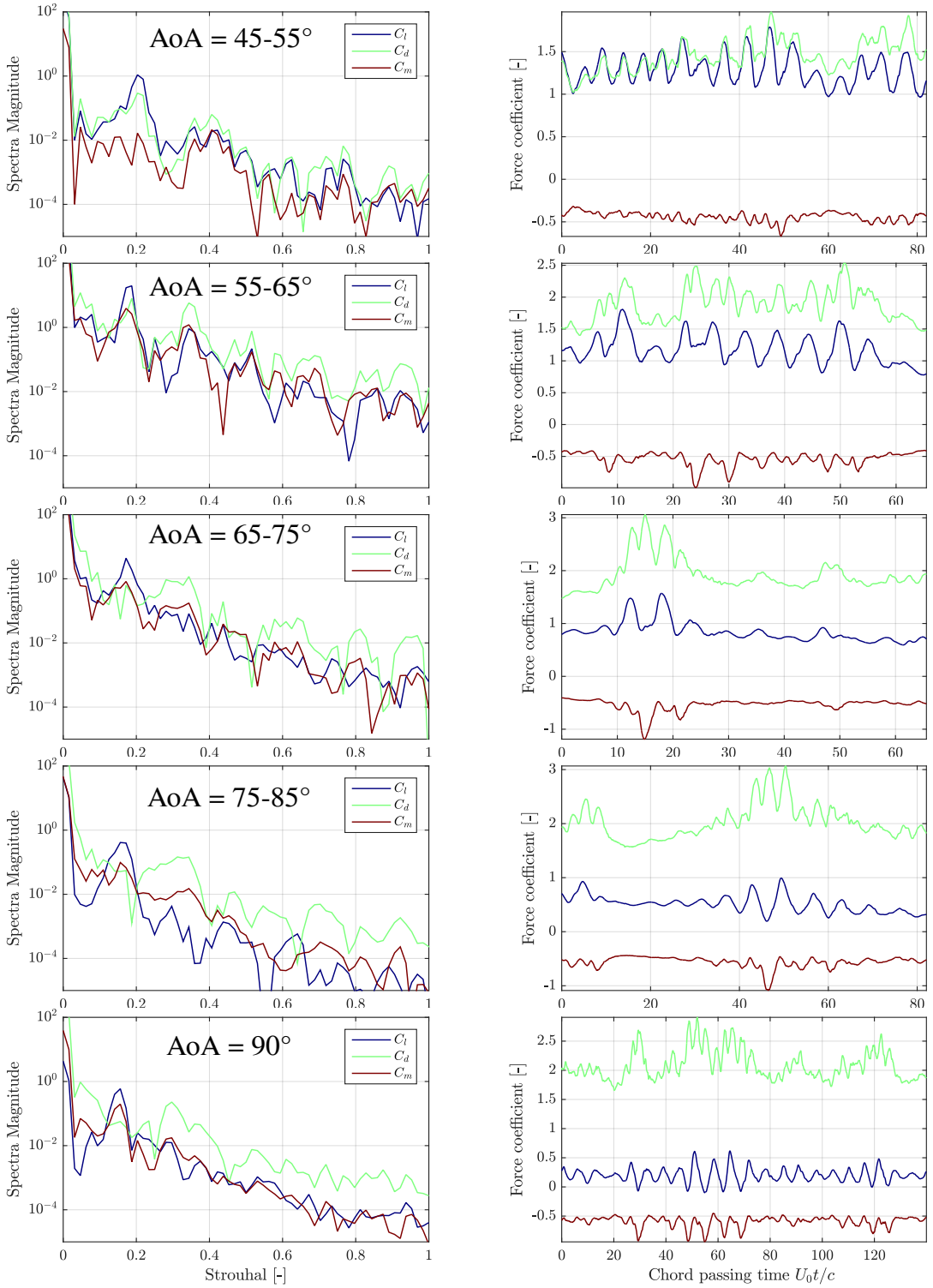

Figure 5.37: Normalized spectra for quasi-static case and associated temporal signals - Several AoA ranges from 40° to 90°

is supposed that considering the good results obtained in static cases, the dynamic cases could provide valuable information. The reduced frequency, amplitude and mean angle investigated in the present cases

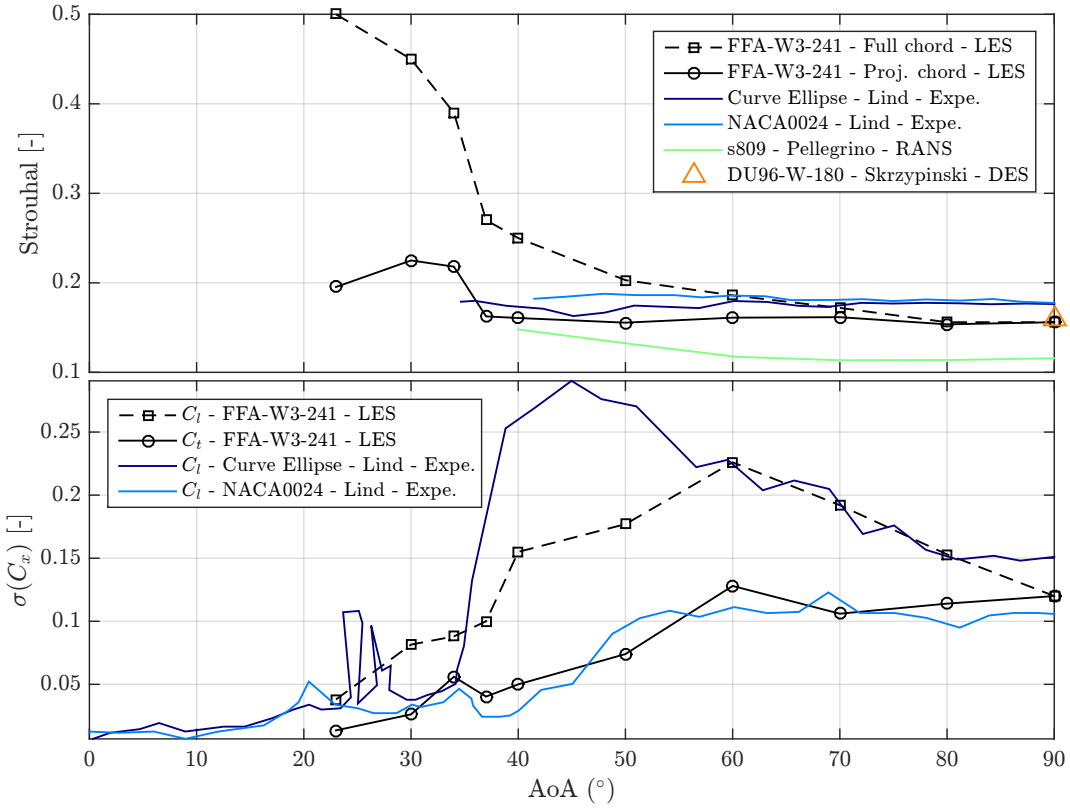

Figure 5.38: Comparison of Strouhal number (top) and standard deviation (bottom) of force coefficients - AoA from 0° to 90°

-

Table 5.7: Dynamic cases caracteristics

Case	α_{mean}	α_{amp}	k	Mesh	Spanwise length
Near deep stall	30°	5°	0.1	M1	$2c$
Deep stall	40°	5°	0.1	M1	$2c$

correspond to typical values observed on wind turbine blades operating in yaw condition (see Chap. 2.3.3) for thick sections between the root and the mid-span of the blade. Most studies investigating such AoAs are focused on vortex induced vibrations which could appear in standstill conditions. In such cases, a motion is applied to the blade close to the shedding frequency in order to assess whether the flow is giving or receiving energy to the blade. Depending on the result, the blade is stable or unstable for given flow conditions. Meskell and Pellegrino [131] worked over lock-in phenomena that appear with vortex induced vibration: the blade natural frequencies are close to the shedding frequence and resonance can appear. The airfoil then starts to move at the shedding frequency, and then the AOA changes due to heaving motion (or pitching and combined pitching/heaving depending on which natural frequency is investigated). It then appears that the vortex shedding frequency shifts to the exact natural frequency of the blade, enhancing the phenomenon. In the present case, the pitching frequency is one order of magnitude lower than the shedding frequency and no lock-in phenomenon is to expect. The first case

has a mean AoA below the deep stall angle and reaches a maximum AoA of $35°$ close to the deepstall angle. The second case has a mean AoA above deep stall angle but with a minimum value around deep stall angle.

Fig. 5.39 and 5.40 reveal the temporal signals of force coefficients for both cases. It appears

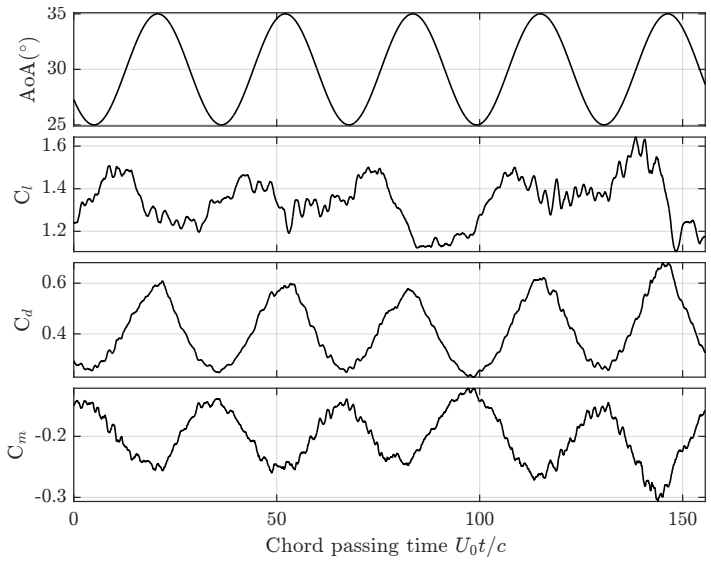

Figure 5.39: Temporal signals of AoA and force coefficients for near deep stall dynamic case - $\alpha_{\text{mean}} = 30°$

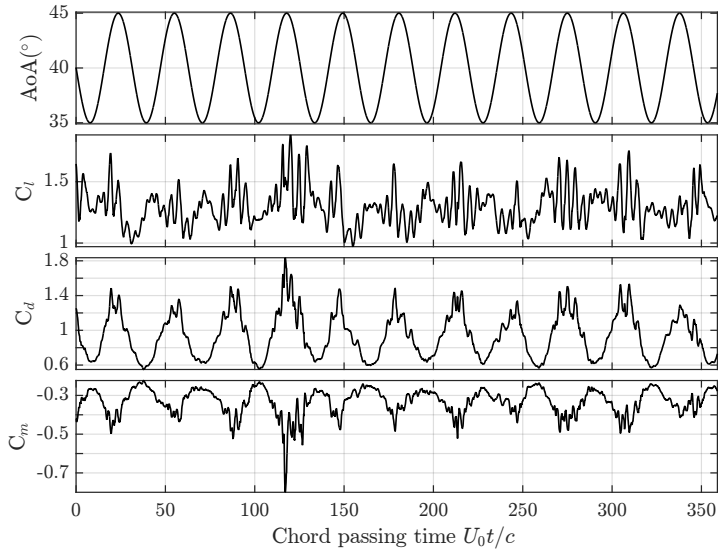

Figure 5.40: Temporals signals of AoA and force coefficients for deep stall dynamic case - $\alpha_{\text{mean}} = 40°$

that the large shedding oscillations are visible on the whole deep stall case range, but enhanced at the larger AoAs. Only small oscillations can be observed on the near deep stall case. Five periods after an initialization of around 50 chord passing time are simulated for the near deep stall case, and around ten periods for the deep stall case respectively. More simulated time could improve the statistics for

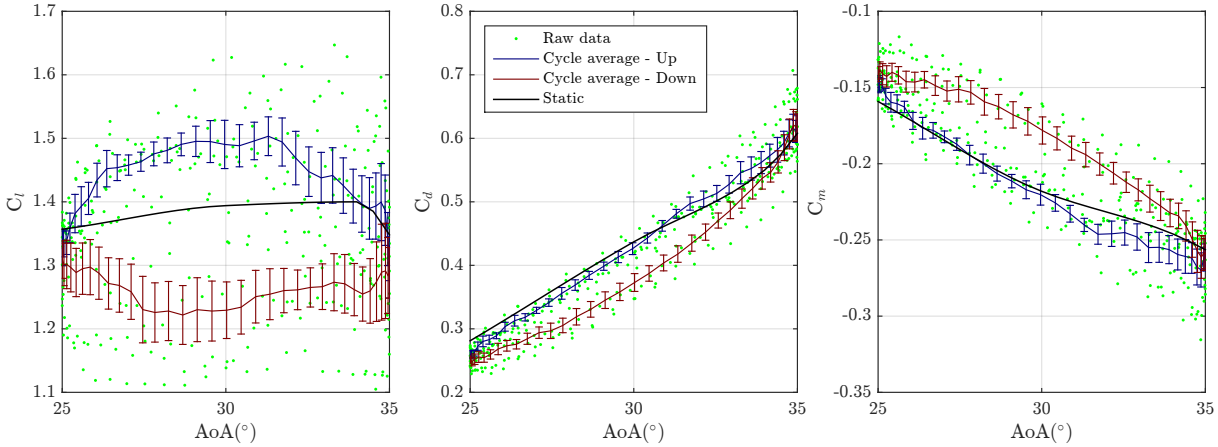

Figure 5.41: Cycle averaging of force coefficients - Near deep stall case

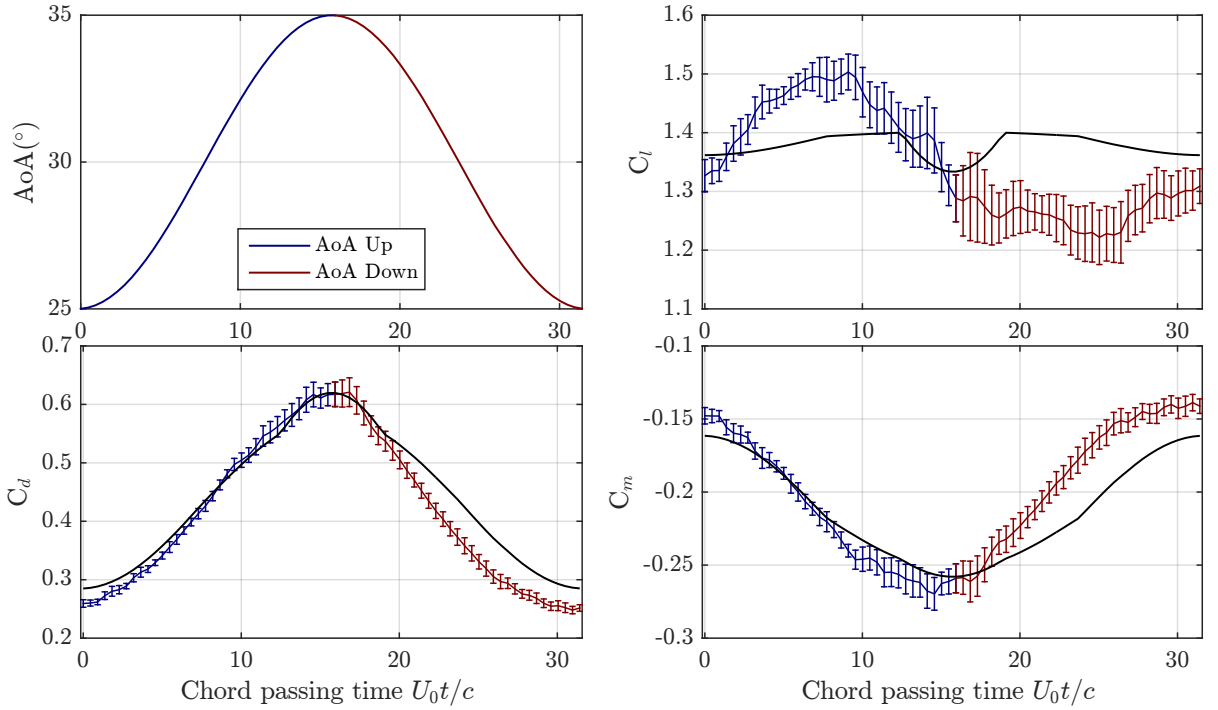

Figure 5.42: Period averaging of force coefficients - Near deep stall case

the cycle average, but because of limited CPU time it is chosen to double the number of periods on the deep stall case that faces larger variations than the near deep stall case. Indeed, it can be observed in Fig. 5.41 that a correct representation of the average values can be obtained with only five cycles in the near deep stall case. The comparison between the static (or quasi-static) values obtained with LES described in the previous section and the dynamic cyclic values reveals a strong hysteresis on the lift coefficient. This is in line with the observation that the trailing edge separation stall is still on going, and the hysteresis on the separation point implies an hysteresis on the lift. Loops are also observed on drag and moment coefficients. The error bars have a total length corresponding to the standard deviation

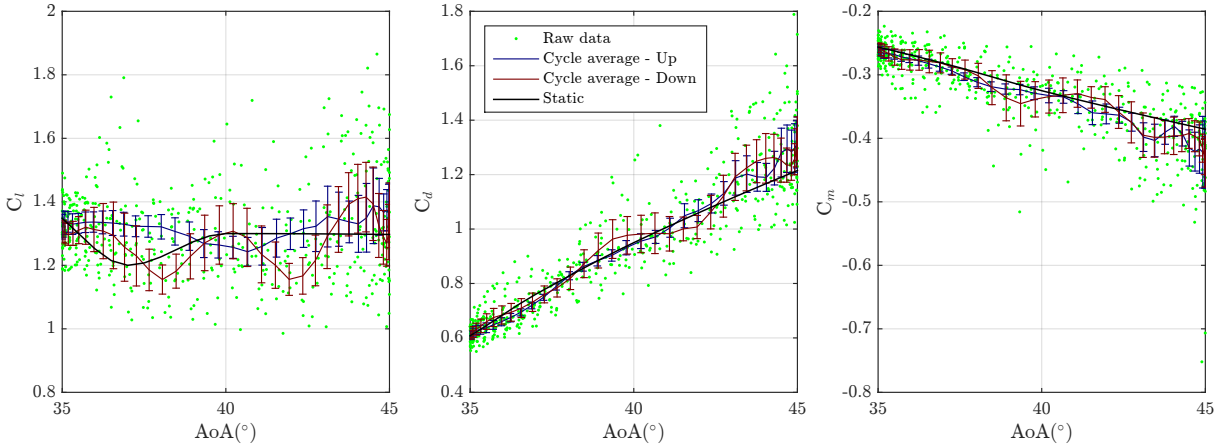

Figure 5.43: Cycle averaging of force coefficients - Deep stall case

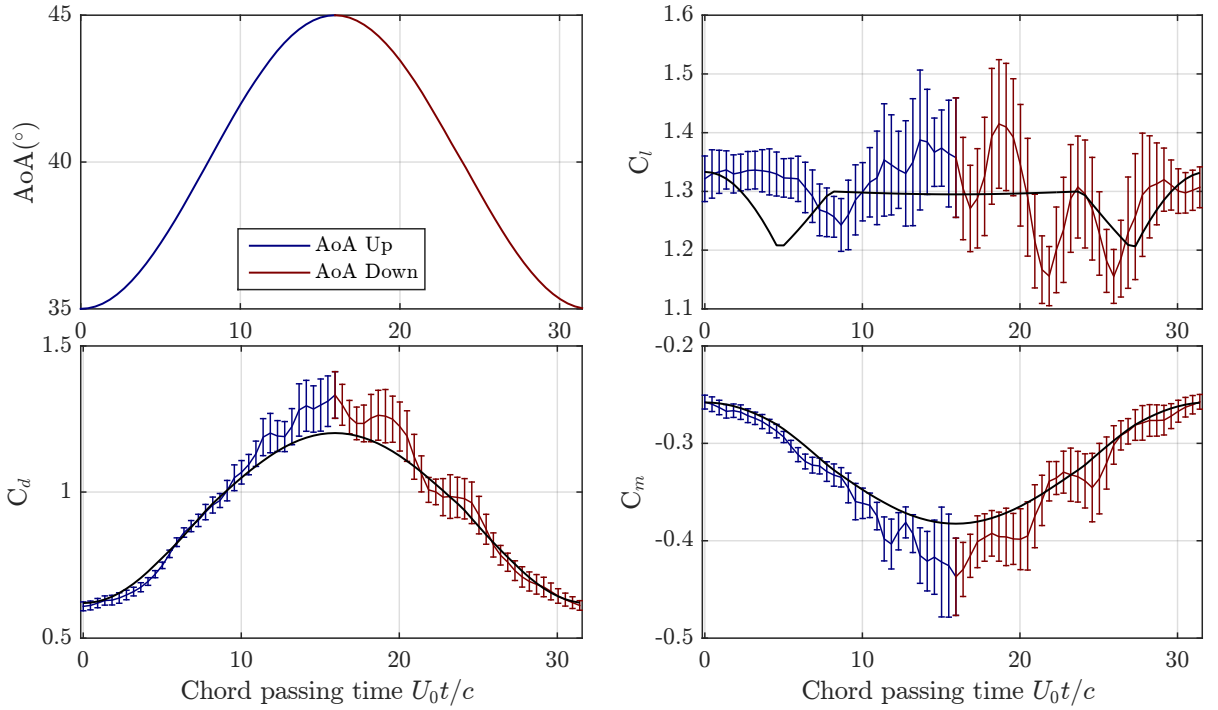

Figure 5.44: Period averaging of force coefficients - Deep stall case

σ for binned AoA values. Fig. 5.42 represents the same data but plotted over a time period, with the corresponding static values of the force coefficients. It appears clearly that the standard deviation is larger for the descending phase, so for the reattachment of the flow, than in the ascending phase. This is in line with the observations from Mulleners [139], Zanotti [210] or Kaufmann [103] on several airfoils. The reattachment process thus has a greater variability than the stall. Furthermore, it appears clearly on drag and moment coefficients that the dynamic signal is delayed compared to the static signal. Fig. 5.43 and 5.44 present the same results for the deep stall case. Fig. 5.43 reveals that there is only a very light hysteresis on all force coefficients. This could be explained by the fact that the separation point is fixed

at the leading edge for the whole range of AoAs, implying that the stall process is not anymore based on the position of the separation point. The standard deviation appears to be larger than in the near deep stall case, in particular at the maximum AoA for all forces. Oscillations are particularly visible on the descending phase. Considering the temporal force signals, it appears clearly that this is caused by the shedding of vortices in phase with the time where the maximum angle is reached. This can be linked to a leading edge dynamic stall behavior, but in a more gradual and smoother way as the shedding is occurring during both ascending and descending phases. The phasing of the vortex shedding with the oscillating motion is clearly visible in Fig. 5.44, where the average force coefficients over ten periods are clearly oscillating at a Strouhal around 0.2 just after the maximum AoA is reached. This is less visible on the ascending phase, which could prove the shedding is re-phasing with the motion at maximum AoA and then in the descending phase, while it is more chaotic in the ascending phase. Furthermore, both drag and moment experience an overshoot at the maximum AoA and no delay in comparison to the static forces. Fig. 5.45 represents the spectra of drag coefficient for both cases, but splitting ascending and

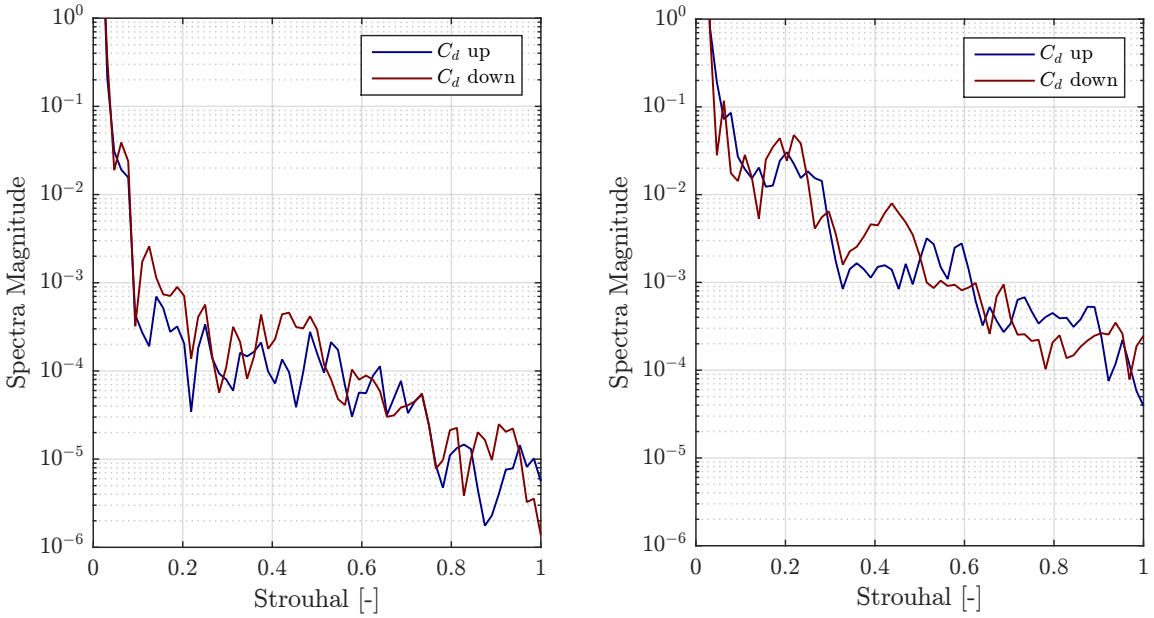

(a) Near deep stall case

(b) Deep stall case

Figure 5.45: Comparison between ascending and descending phases - C_d spectra.

descending phases. The signals for both ascending and descending phases have been reconstructed in continuous signals conserving the derivatives of the original signal. It appears that the Strouhal number of descending phases is lower than for ascending phases, confirming the observations made on the quasi-static case 1 on the delayed shedding frequency. Furthermore, the spectra magnitude at the shedding frequency is larger for descending phases, showing that for both cases the shedding process is enhanced when the maximum angle is reached.

5.5 Application to highly unsteady inflow conditions

5.5.1 Flow analysis

The next investigated cases presented in Table 5.8 focus on high values of reduced pitch rate, in the same order of magnitude than the values observed for turbulent winds (see 2.3.3). The maximum reduced pitch rates (see Eq. 2.18) have been computed based on a sinusoidal motion, an airfoil chord of 1 m and a freestream velocity of 1 m/s. The airfoil used in these simulations is a 21% relative thickness generic airfoil provided by Siemens Gamesa Renewable Energy. The mesh used has an equivalent refinement than the M1 mesh used previously, with a spanwise length of $2c$. The Reynolds number is $Re = 1.6 \cdot 10^6$ and the y^+ values are the same than the ones obtained with M1 mesh presented earlier.

Table 5.8: High frequency cases caracteristics

Case	α_{mean}	α_{amp}	k	Max AoA reduced pitch rate
Case 1	12.5°	22.5°	0.220	5.0
Case 2	12.5°	22.5°	0.439	9.9
Case 3	12.5°	22.5°	1.099	24.7

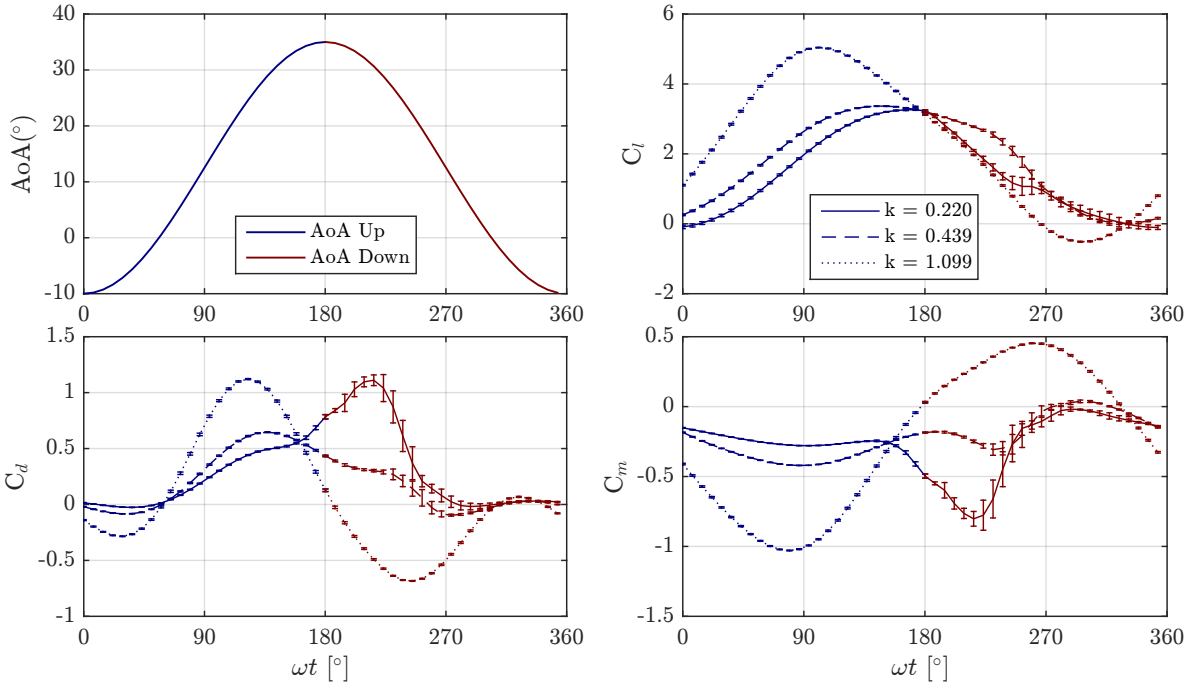

Figure 5.46: Period averaged force coefficients for three different reduced frequencies.

The period averaged forces coefficients presented in Fig. 5.46 for the three cases reveal strong discrepancies. The forces are plotted against the phase angle ωt with $\omega = 2kU/c$, and the error bars are twice the standard deviation of the signals. For the three cases, the force coefficients have the same sinusoidal trend than the AoA, but with a more or less significant lag. The largest lag is obtained for Case 3 with the highest reduced pitch rate, with a phase delay of around 90°. The lag is slightly different

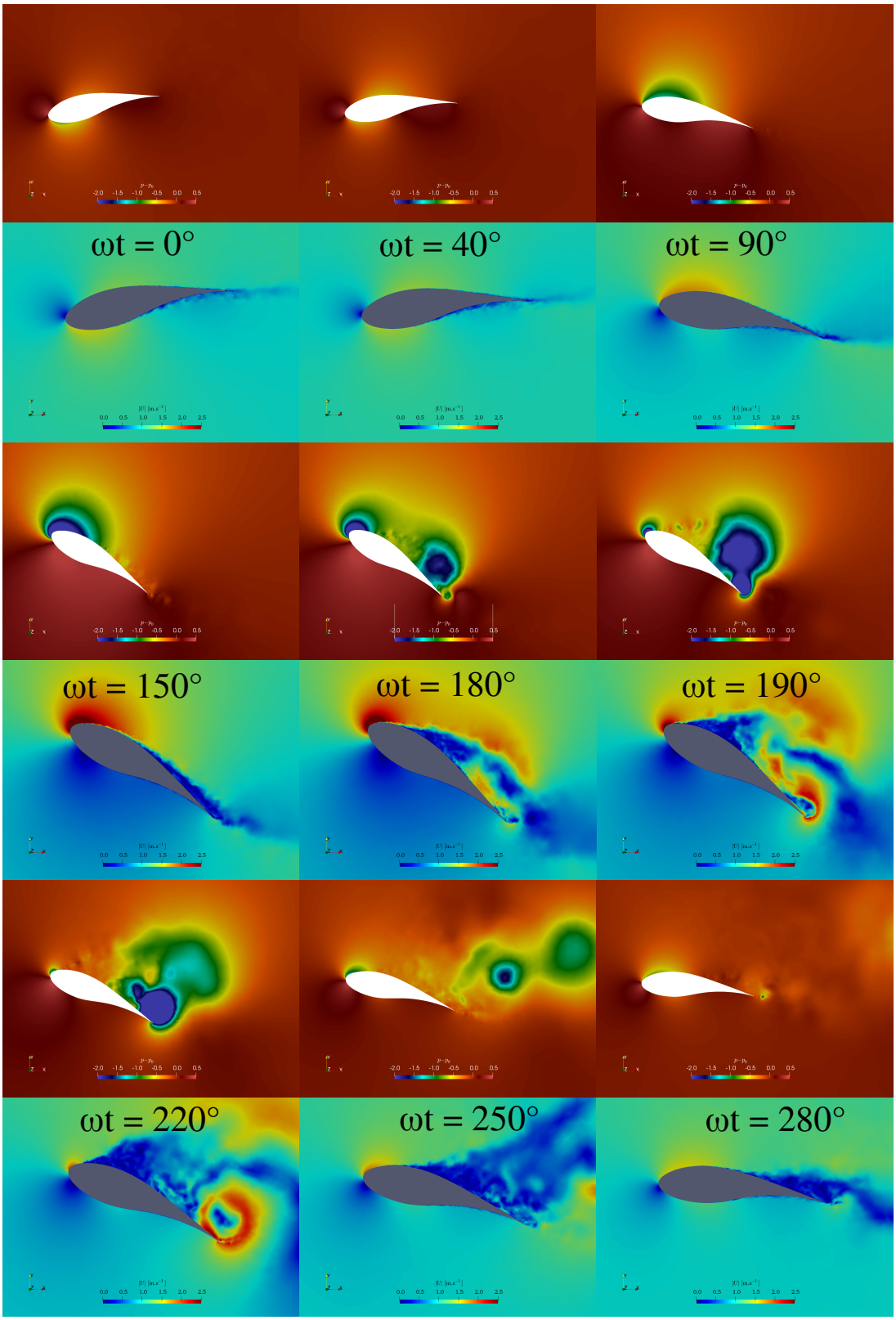

Figure 5.47: Instantaneous velocity (top) and pressure (bottom) for several phase angle - $k = 0.220$

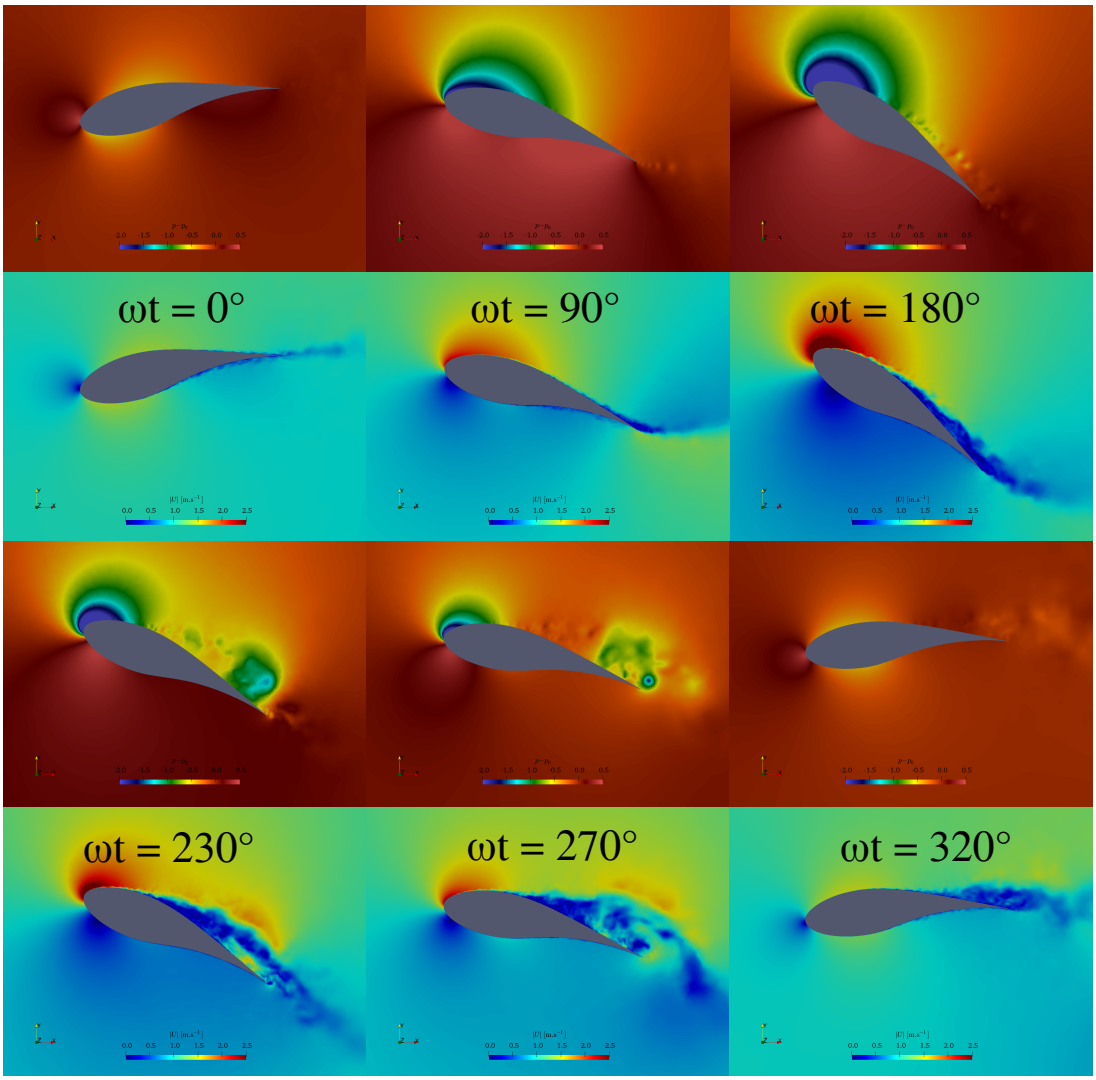

Figure 5.48: Instantaneous velocity (top) and pressure (bottom) for several phase angle - $k = 0.439$

for the three force coefficients. In addition to the sinusoidal response, other peaks are observed on the force signals. Case 1 with the lowest reduced pitch rate reveals a peak at around $\omega t = 220°$, and Case 2 around $250°$ respectively. No other peak is observed for Case 3. The standard deviation around the peaks is much higher than for other phase angles.

The instantaneous pressure and velocity magnitude at several phase angles for a given spanwise position on the airfoil are presented in Fig. 5.47 to 5.49, revealing the main flow features for the three cases. For Case 1, large vortices are emitted from the suction side and trailing edge. The vortex formation appears to be in line with the observation from Mulleners [140]: the boundary layer starts detaching over a large part of the airfoil suction side while the angle of attack increases. Several small rolling up vortices appear on the separation line, increasing the height of the separated flow. The vortices accumulate, creating a large vortex that is convected downstream. In the present case, the boundary layer starts to detach at around $150°$. The separation point then moves to the leading but remains on the suction side for the whole range of AoAs. The clockwise large separation vortex reaches the trailing edge at $180°$, when the AoA is the highest. A counter-clockwise trailing edge vortex then starts to roll-up. The separated flow zone increases

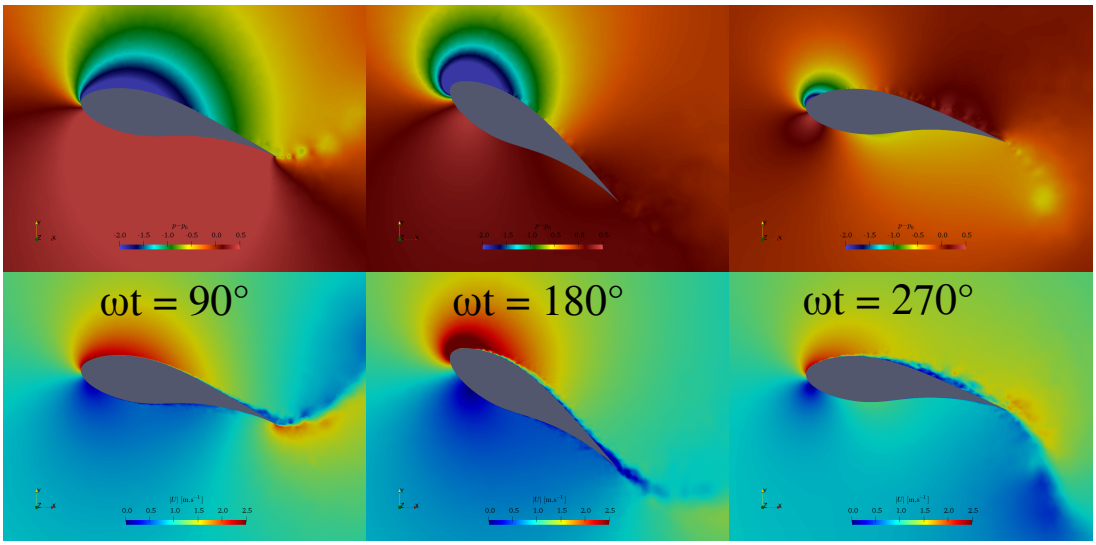

Figure 5.49: Instantaneous velocity (top) and pressure (bottom) for several phase angle - $k = 1.099$

in height as the separation vortex is pushed away for the airfoil by the trailing edge vortex. Both vortices grow in strength, and are convected downstream for $\omega t = 220°$. Smaller vortices are then emitted while the boundary layer slowly re-attaches. The dynamics of these large vortices are responsible for the peaks observed in force coefficients. The flow visualization from Melius [130] on a thick wind turbine airfoil is very similar to this case. For Case 2 presented in Fig. 5.48, the same trends are observed except that because of the faster oscillating motion the vortices are created at a higher phase angle, when the AoA decreases. The vortices are then weaker and smaller because the time of accumulation of vorticity is reduced, which is responsible of the smaller and delayed peaks on force coefficients compared to Case 1. The boundary layer is also less detached. For Case 3, no large vortices are observed. The boundary layer does not detach, and only small vortices are emitted from the trailing edge all along the motion. These observations are comparable to the ones from Gharali [66] who investigates the effects of several high reduced frequencies on a s809 airfoil with unsteady RANS simulations. The Reynolds numbers investigated are one or two order of magnitude lower than in the present cases, and the AoA variations are based on oscillating horizontal and vertical freestream velocities. However the observations are very close to the present cases: a very high reduced frequency prevents the boundary layer to detach fully and the emitted vortices have a much higher frequency and lower impact on the force coefficients.

5.5.2 Cross comparison: LES, panel method and Theodorsen theory

The results obtained with LES are then compared with simulations from the panel method presented in Chapter 4, that includes viscous corrections and a dynamic stall model. These results are also compared to Theodorsen theory, using the formulation presented in Annex B. The dynamic stall model from the panel method does not include any model for the apparition of large vortices, while Theodorsen theory only considers fully attached flow. The cycle average force coefficients for the three methods and the three cases are presented in Fig. 5.51. The panel method results are roughly discretized due to some time stepping limitations in the code: the rolling-up of the wake panels can creates instabilities if the panels are too close to strong vorticity gradients. Despite the differences in the modelling approach, a good correlation is observed on the hysteresis loops of the three methods. For Case 1, the detachment

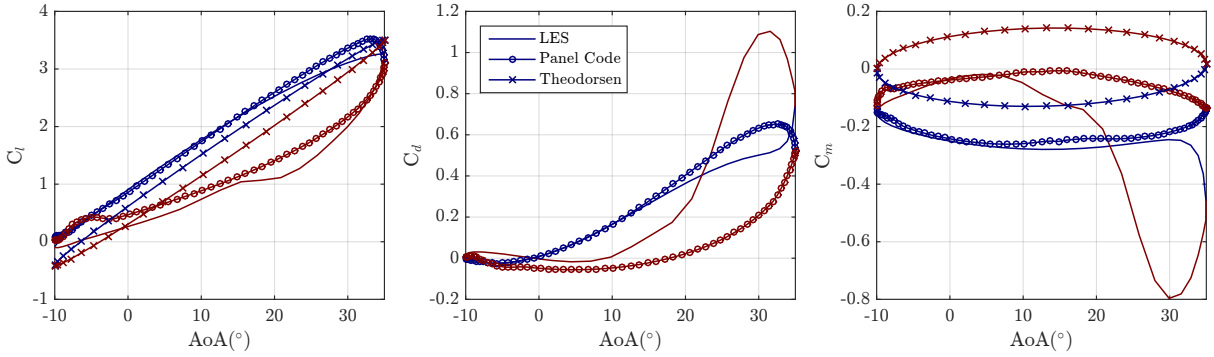

(a) Case 1 - $k = 0.220$

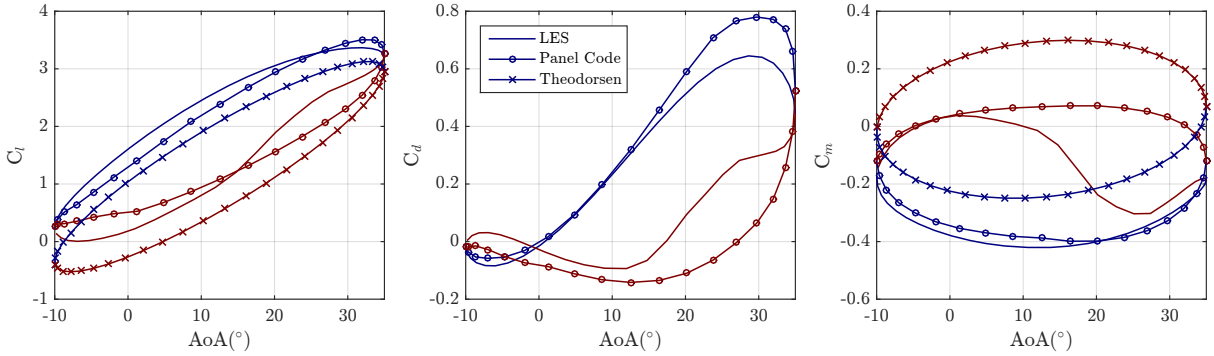

(b) Case 2 - $k = 0.439$

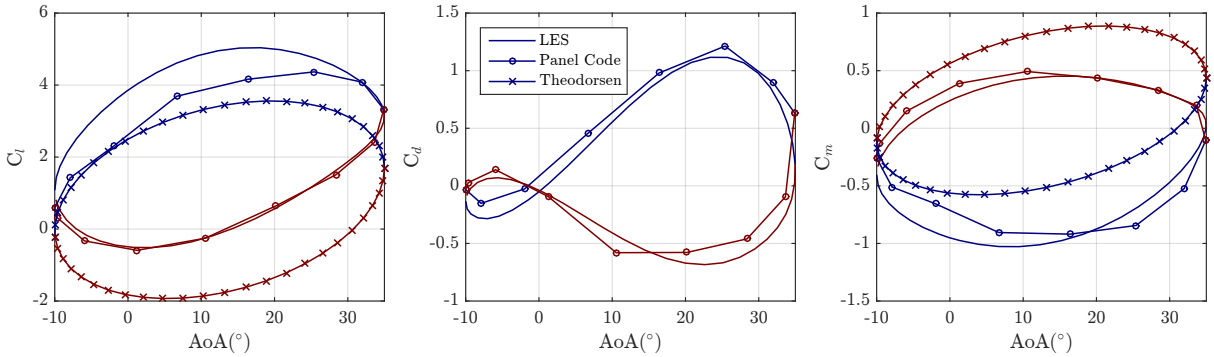

(c) Case 3 - $k = 1.099$

Figure 5.50: Comparison of cycle averaged forces coefficients obtained with LES, panel method with dynamic stall model and Theodorsen theory.

and reattachment of the boundary layer is not considered by Theodorsen theory, explaining the strong difference in the lift loop. The impact of the vortex emission is clearly observed with LES on drag and moment coefficients, but not predicted by the two other methods. Apart from the AoA ranges for which the influence of the vortices is large, the different methods are in agreement. For Case 2, the results are very close for the three methods as the impact of flow separation and vortex emission is reduced. LES is still able to capture some important features causes by the vortices. For Case 3, the hysteresis loops and trends are the same for the three methods: the flow is dominated by inviscid unsteadiness very well predicted by the simple Theodorsen theory. More specifically, the balance between impulsive and circulatory components appears to be well taken into account. Fig. 5.51 presents the added mass (impulsive lift) and circulatory lifts as well as the total lift predicted by Theodorsen theory. The phase

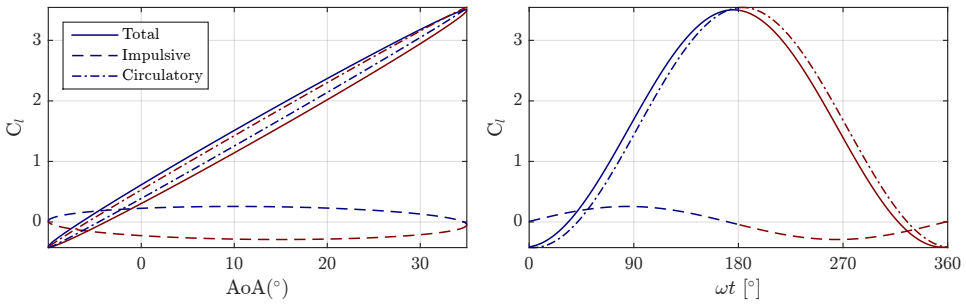

(a) Case 1 - $k = 0.220$

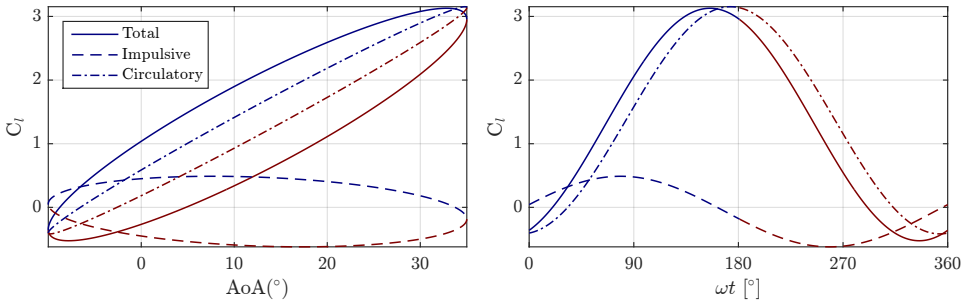

(b) Case 2 - $k = 0.439$

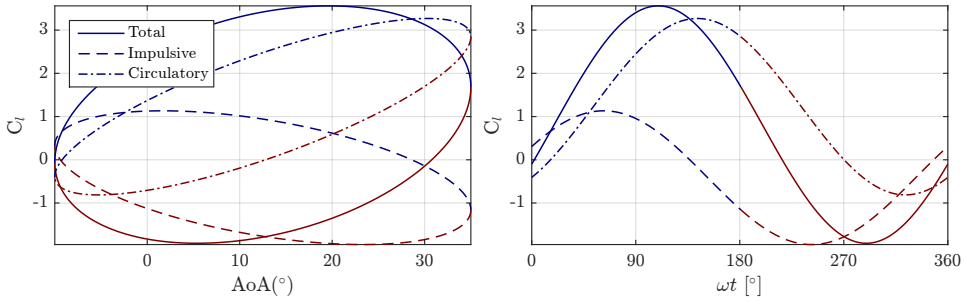

(c) Case 3 - $k = 1.099$

Figure 5.51: Comparison between impulsive, circulatory and total lift from Theodorsen theory as a function of AoA (left) and angular value (right)

delay for the three cases observed in LES is predicted by the balance between added mass and ciculatory components. The impulsive lift formulation from the B-L dynamic stall module has also been tested but is not presented here. The results obtained were not consistent with the other methods, with unrealistically high values of lift coefficients.

It appears clearly that for specific pitching conditions, a leading edge vortex can appear even on thick airfoils. However, it has also been noted in previous chapter that the leading edge vortex module from the B-L model can give unrealistic results if the trigger conditions are not perfectly known. This observation raises interests in the development of engineering models more suited to deep stall conditions.

Chapter 6

Conclusions and perspectives

Contents

6.1 Conclusions on advanced aerodynamic models

The main objective of this study is the investigation of advanced aerodynamic models influence on the loads of aero-servo-elasto coupled simulations. In this thesis, two advanced aerodynamic models are mostly investigated: a panel method with a specific methodology that takes into account viscous effects, and a Wall-Modeled LES (WMLES) code used on cases for which other models do not consider enough flow physics to be accurate. The panel method code purpose is to capture rotor level specific flow features such as variable induction and tip effects, using sectional viscous data to correct the inviscid flow. These sectional data are originally defined for 2-D steady flows, but by correcting these data with semi-empirical models more realistic aerodynamic forces are obtained. However, such models are not perfect and calibrated with experimental data. These data are costly to obtain and with limitations for low-Mach Reynolds numbers which are the common operational ranges of large OWTs. The WMLES offers a promising alternative to experiments at realistic CPU time for unsteady flows as it provides realistic information on the flow structures without fully resolving the boundary layer flow.
The summary of this thesis approach is thus to use advanced models such as WMLES and panel methods to assess the limits and possibly improve engineering models. WMLES in this context is considered as a *numerical wind tunnel* for 2-D sections aerodynamics, while the panel method code offers a better confidence for 3-D unsteady flows than standard BEMT tools. Viscous 3-D effects such as stall delay for rotational flow can not be captured which is the main limitation of such methodology compared to full CFD rotor simulations. However, unsteady RANS simulations are known to have limited capacity

for unsteady flows despite reasonable CPU time, while using DES or WMLES for realistic engineering load cases is not yet a viable option because of the large CPU time required.

6.1.1 Panel method: improve knowledge of critical DLCs

A panel method code coupled to a servo-elasto code is investigated in this study. Panel methods solve inviscid flows and in order to obtain realistic loads, a viscous correction method is introduced and compared against BEMT. The implementation of a Beddoes-Leishman type dynamic stall model in the panel method is also validated against experimental data. No leading edge vortex module is implemented which seems to be more robust for thick airfoils despite some discrepancies for thinner airfoils with leading edge vortex behavior. The unsteady attached flow model in particular is based on the calculation of AoAs and velocities on the rotor plane. By using the lifting-line theory in an incomplete form, the velocities are assumed to contain tip effects and unsteadiness. The wake strength is corrected by applying reduction factors to the inviscid wake. These reduction factors are computed with viscous polars. Then the calculation of AoAs based on the blade pressure integration adds the impulsive terms to the forces. The reduction factors applied on both forces and wake include the dynamic stall corrections. This methodology applied to oscillating sections gives good results when compared to experimental data and standard unsteady attached flow modules based on Theodorsen theory. For finite wings with dynamic stall bevahior, the 3-D stall interactions can not be captured by such methodology. However, the 3-D lift polars reveal that tip effects are captured. For full rotor simulations, the distribution of axial and tangential forces show some discrepancies between the panel method and BEMT with less than 10% difference in power and thrust between both codes at several TSRs, revealing differences in the induction fields. When elasticity is considered, the load distribution is significantly modified at high TSRs where the blade deflection is the largest. Indeed, the panel method appears to modify differently the induction fields compared to BEMT as the influence of each section onto the other is taken into account. Including a controller also changes significantly the code-to-code comparison as the operational point of the wind turbine is modified depending on the power output of each method. Below rated power, a change in performance will imply a change in rotationnal speed while after rated the pitch angle handles the difference in power. The power sensitivity to pitch is significant and implies that the power differences will be compensated by the pitch difference without modifying significantly the aerodynamic force projections. However, it means that loads related to power (such as side/side tower top moment or tangential blade root force) are closer when a controller is used while the loads related to thrust (such as fore/aft and yaw moment or axial blade root moment) can be much different. To conclude, the differences observed between aerodynamic models on structural loads can lead to very different conclusions if rigid cases or elastic cases with controller are conducted.

Both panel method and BEMT method are compared in yawed cases which are characterized by periodic variations of AoA and induced velocities. The impact of wind shear and turbulence are investigated. From a modeling point of view, the skewed wake model from BEMT and the DS module effects on loads are assessed. Several parametrizations of the B-L DS model are tested by changing the time constants for separation point and leading edge pressure dynamics. It appears that in full rotor simulations, including the DS in the wake reduction mitigates the local lift force on spanwise location close to the root. Skewed wake model in yaw cases introduce a phase shift on the induced velocities. This phase shift appears clearly when comparing AoA in BEMT simulations with and without the skewed wake model with the panel method. However, no clear improvement on the loads is noticed except for the yaw RNA moment

which is underpredicted when no skewed wake model is used. The BEMT code does not include any dynamic wake model in addition to the skewed wake model, which could explain the large differences noticed between both BEMT and Panel Method. The fore/aft and yaw RNA moments signal during one rotation in yawed cases are dependent on the phase of the axial blade forces, which itself is related to the lift coefficient and local velocity phases. By modifying the induced velocities phase, the skewed wake model changes the magnitude of RNA moments. The dynamic stall model also modifies the phase of the lift coefficient, and the impact on mean RNA moment is not negligible.
The cases for which the more DS events are observed are high wind cases (low TSR) with a large yaw misalignment. For such cases, it is noticed that the loads impacted by the DS module are not the same for rigid cases without controller than when the elasto-servo coupling is included. This also demonstrates the necessity to perform coupled simulations in order to assess whether a given engineering model impacts the loads or not. For the fatigue loading, it appears that including turbulence decreases the code-to-code comparison as turbulence is responsible for most of the fatigue loading. However, the flap blade root moment still shows some significant differences between BEMT and panel method, and for several DS parametrizations.

6.1.2 Wall-Modeled LES: a validated tool for exploring highly unsteady flow behavior

Wall-Modeled Large Eddy Simulations are performed on static wind turbine airfoil cases at a Reynolds number of $1.6 \cdot 10^6$, with correct prediction of aerodynamic force coefficients when compared to state-of-the-art numerical tools that are proven to be efficient in such conditions. Pressure coefficients show a very good correlation with both experimental and numerical data. However, a correct prediction of transition with realistic CPU time still seems a challenge despite the use of a wall law model adapted to boundary layers with pressure gradient and augmented with a sub-grid scale model handling turbulence near solid walls. The turbulent boundary layer is then poorly estimated and the separation point prediction is incorrect with coarse meshes. Thus it appears that attached flows and fully separated flows are the easier to predict as the positions of separation points are clearly defined at the leading and/or trailing edge. The stall process, in particular close to the stall angle, is much more difficult to predict and requires fine meshes. Despite this difficulty, the hysteresis observed on force coefficients in oscillating detached cases are close to the experimental hysteresis loops.

Investigation on deep stall angle reveals that the methodology validated against experimental data up to an AoA of $24°$ gives realistic results up to an AoA of $90°$, with a correct prediction of the deep stall angle at around $35°$. The observed force coefficients and shedding frequency are in line with the observations on similar airfoils. It appears that the shedding behavior is important around and beyond deep stall angle. It also appears clearly that dynamic stall model such as B-L model does not model properly the complexity of such phenomenon: the leading edge vortex behavior of the B-L model only appears when the airfoil is pitching and does not consider the self exciting lift, which is dominant around and after deep stall angle. Furthermore only one Strouhal frequency is considered whereas it is observed in the present simulations that it changes with the AoA. It appears that before deep stall angle the shedding frequency decreases quickly with AoA up to deep stall angle. After deep stall angle, the shedding frequency decreases in a way that the projected chord Strouhal is constant around 0.15. Oscillating cases close to deep stall angle also reveal several interesting features. First, it appears that before deep stall angle, the separation point dynamics is still responsible of hysteresis on force coefficients while after deep stall the hysteresis is negligible. On the other hand, it appears that after deep stall a small lift over-

shoot and a phasing of the shedding lift with the oscillating motion are observed. This behavior is close to the typical dynamic stall vortex observed on thinner airfoils at lower AoAs. A shift in the shedding frequencies is also observed during the ascending and descending phases, revealing the need for more complex modeling of shedding frequencies in engineering models for such AoA.
Investigations on high reduced frequency pitching cases also revealed the transition from flows dominated by viscous effects at medium reduced frequency of 0.220 to flows dominated by unsteady inviscid effets at a higher reduced frequency of 1.099. The lift coefficient phasing for oscillating cases is the combination of circulatory and impulsive lift phases, and a good agreement is found between Theodorsen theory and WMLES for the highest reduced frequency.
Based on these different observations, WMLES shows promising results for very specific conditions: either flows for airfoils with high inflow variations or airfoils at very high AoAs around and after deep-stall. Their is no absolute evidence that the first conditions can be met for large offshore turbines: despite equivalent pitching rate, the amplitude and reduced frequency of the inflow variations on wind turbine blades might not reach such challenging values as the ones tested in this thesis. The second conditions on the other hand can be met on severe yaw misalignment cases such as the ones investigated in the present work. Other operating conditions not investigated here can result in very large AoAs.

6.2 Perspectives

6.2.1 Panel methods for more complex flows

One of the main limitation of the present panel method is the lack of appropriate models for very large yaw errors. Indeed, it was observed that for yaw errors higher than $40°$ with turbulent wind, instabilities were observed in the wake. A possible explanation for this issue is the poor discretization of the vorticity distribution. The use of vortex lines with constant vorticity implies that there is a large jump in vorticity from one time step to another (because of turbulence and large AoA variations). This might be responsible for numerical instability, and could be improved by using a continuous vorticity distribution (surface vorticity ditribution) and higher order panels: piece-wise linear panels instead of piece-wise constant panels for example. These limitations could also be responsible for instabilities in the wake when the time step is reduced. For this issue, changing the advection scheme by a higher order scheme could also improve the results.
Other complex inflow situations have been simulated by several authors with panel methods such as half-wake situations (turbine in the wake of another turbine) or pitch default on one blade. For these situations, the BEMT hypothesis of an annular uniform induced velocity field is not respected and the present panel method should also improve the loads predictions. The impact of the ground on the wake shape could also be investigated has it modifies the induced velocity field and can not be taken into account by BEMT. For large modern wind turbines, one of the main issue is the lack of experimental data that could help validate new models. Indeed, no wind tunnel measurements can be performed at realistic Reynolds number on such large rotors. The open air measurements performed on real wind turbines offer the best alternative to get realistic data but with no control on the inflow conditions. Comparing the present model with such data should be one of the next steps of this work.

6.2.2 Perspectives on LES for wind tubine applications

The present simulations performed with WMLES have shown that even coarse meshes are able to capture main flow features at very high AoA and Reynolds number of $1.6 \cdot 10^6$. For large wind turbines in operation the Reynolds number can reach values around 10^7, and it is known that stall angle and maximum lift coefficient still evolve at these Reynolds numbers. One of the perspective would be to investigate these higher Reynolds number with the present methodology. However it has been observed that the present wall-law model can not capture efficiently the stall angle. Future work could include the implementation of more complex wall laws based on the review from Bodart [21].
Despite these clear limitations at low and moderate AoA, the fully separated flow analysis has shown that even without a proper modeling or solving of boundary layer, WMLES is able to obtain an estimation of the flow where no other models can. The application of WMLES for wind turbines should then focus on such cases. In the present study, only extruded geometries have been investigated and 3-D geometrical effects have thus not been considered. The analysis of the flow around a full blade in fully separated conditions would require a mesh of around 500 millions cells, which is still feasible considering the performances of YALES2 code and the capacity of modern super-computers. The flow around nacelle and tower/blade interactions also appears to be well suited to WMLES with unstructured meshes.

6.2.3 Advanced models for idling wind turbines

For all dynamic stall models, it appears that the handling of the leading edge vortex is the most complex phenomenon to capture. While it is often considered that for thick wind turbine airfoils such model is not necessary, it appears clearly that for all airfoils vortex shedding is observed after a certain angle. However, the classical B-L model is not really suited for such conditions and is most often deactivated when such AoAs are reached. Investigating less known dynamic stall models such as Snel or ONERA-BH models that contain the self exciting shedding phenomenon could be the next steps of this work, using WMLES to understand more accurately the shedding process. Idling or stopped wind turbines can indeed suffer very large yaw misalignment (for example if the connection to the electrical grid is not operational and the nacelle orientation fixed), and the periodic shedding can generate vortex induced vibrations when the shedding frequency is close to the blade or tower natural frequencies. In order to predict these events, coupling WMLES with an elastic solver could help understanding the phenomenon, and provide data for proper engineering modeling.

Appendix A

Implementation of the dynamic stall model in ARDEMA code

The dynamic stall modele implemented in ARDEMA is based on the work of Beaudet [15].

A.1 Zero lift angle and lift coefficient slope

The angle of attack with zero lift α_0 and the slope of the normal coefficient around α_0 is needed for the dynamic stall model. As α_0 is usually a small angle value, it has been considered that the normal coefficient slope is equal to the lift coefficient slope, and will be noted $C_{l,slope}$.

The function ClAlfa0Slope from Ardema3DAeroSection class computes both α_0 and $C_{l,slope}$.

α_0 is computed thanks to the secant method up to 1e-5 accuracy based on input viscous polars. The resulting lift, very close to 0, is noted C_{l,α_0} .

$C_{l,slope}$ is the maximum slope between any lift coefficient values between -20 and +20 degrees (1 degree step) and C_{l,α_0}

A.2 Attached flow module

Based on [15] it has been considered that when using a free wake method the attached flow module from the original Beddoes-Leishman model can be omitted using directly the effective angle of attack : α_e obtained from the flow solver. This angle can be computed in different ways (see 4) :

- Angle of attack from the velocity vector on a specific point. The velocity vector considers the induced velocities from the wake and the body.
- Angle of attack from the bound circulation using the inviscid polar and the lift coefficient from the bound circulation.
- Angle of attack from the pressure integration using the inviscid polar and the lift coefficient from the pressure integration.

It is recommended to use the angle obtained from pressure integration as input to the dynamic stall module. This angle α_e is then used to compute the normal and tangential force coefficients in attached flow with correction for large angles of attacks:

$$C_N^P = C_{l,slope} * sin(\alpha_e - \alpha_0) \tag{A.1}$$

$$C_T^P = \eta C_{l,slope} * sin(\alpha_e - \alpha_0) tan(\alpha_e) \tag{A.2}$$

With η a constant equal to 0.95.

A.3 Separation point calculation

This section focuses on the computation of the separation points based on Kirchhoff theory.

The Kirchhoff theory for flat plates extended to thick airfoils give the following relations: plot the separation point function for a given polar in order to determine the angle for which it is fully separated.

$$C_N = C_{l,slope} * sin(\alpha_e - \alpha_0) \left(\frac{1+\sqrt{f}}{2} \right)^2 = C_N^P * \left(\frac{1+\sqrt{f}}{2} \right)^2 \tag{A.3}$$

$$C_T = \eta C_{l,slope} * sin(\alpha_e - \alpha_0) tan(\alpha_e) \sqrt{f} = C_T^P * \sqrt{f} \tag{A.4}$$

With f the separation point location on the airfoil chord. f is between 0 (fully separated flow) and 1 (attached flow).

These relations can be reversed to obtain the separation point based on angles. Following [15], two separations points are calculated in the current implementation, one based on normal force and the other one on tangential force:

$$z_N = 2 * \sqrt{\frac{C_N}{C_{l,slope} * sin(\alpha_e - \alpha_0)}} - 1 \tag{A.5}$$

$$z_T = \frac{C_T}{Slope_{C_{l,slope}} * (\alpha_e - \alpha_0) * sin(\alpha_e - \alpha_0)} \tag{A.6}$$

and then :

$$f_N = sign(z_N) * (z_N)^2 \tag{A.7}$$

$$f_T = sign(z_T) * (z_T)^2 \tag{A.8}$$

In order to avoid α_e singularities in 0 and α_0 , threshold are applied on α_e :

- In α_0 : if $|\alpha_e - \alpha_0| < \epsilon$ then $\alpha_e = sign(\alpha_e) * \epsilon$
- In 0 : if $|\alpha_e| < |\alpha_0/4| + \epsilon$ then $\alpha_e = sign(\alpha_e) * (|\alpha_0/4| + \epsilon)$

With $\epsilon = 0.5$.

Both separation points values are saturated at +/- 1. In the formula above, the force coefficients are obtained through the following formula:

$$C_N = cos(\alpha_e) * (C_{l,\alpha_e} - C_{l,\alpha_0}) + sin(\alpha_e) * (C_{d,\alpha_e} - C_{d,\alpha_0}) \tag{A.9}$$

$$C_T = sin(\alpha_e) * (C_{l,\alpha_e} - C_{l,\alpha_0}) - cos(\alpha_e) * (C_{d,\alpha_e} - C_{d,\alpha_0}) \tag{A.10}$$

C_{l,α_e} and C_{d,α_e} are obtained thanks to viscous polars data.

A.4 Separated flow module

The purpose of this function is then to apply several lag functions to both forces coefficients and separation points. Each of this lag function is defined by a time constant determined experimentally or from bibliography. A non-dimensional time variable is used for defining a time step :

$$\Delta s = \frac{2U_r}{c}\Delta t \tag{A.11}$$

With U_r the relative fluid velocity, c the airfoil chord, and Δt the time step.

All the following formula are presented for the normal coefficient: the same formula are used for tangential coefficient.

A first pressure lag (time constant $T_p = 1.7$) is applied to the force coefficient $C^P_{N,k}$ obtained from the attached flow module, in discretized form (time step k):

$$C'_{N,k} = C^P_{N,k} - D_{p,k} \tag{A.12}$$

$$D_{p,k} = D_{p,k-1}e^{-\Delta s/T_p} + (C^P_{N,k} - C^P_{N,k-1})e^{-\Delta s/2T_p} \tag{A.13}$$

A second pressure lag (time constant $T_b = 3.0$) is then applied on the resulting coefficients:

$$C''_{N,k} = C'_{N,k} - D_{b,k} \tag{A.14}$$

$$D_{b,k} = D_{b,k-1}e^{-\Delta s/T_b} + (C'_{N,k} - C'_{N,k-1})e^{-\Delta s/2T_b} \tag{A.15}$$

The resulting coefficients are then used to compute a delayed angle of attack based on the formula for attached flows:

$$\alpha_{delayed,k} = arcsin\left(\frac{C''_{N,k}}{C_{l,slope}}\right) + \alpha_0 \tag{A.16}$$

A third lag function (time constant $T_f = 3.93$) is then applied to the resulting separation points $f'_{N,k}$ (for normal force coefficient) and $f'_{T,k}$ (for tangential force coefficient) :

$$f''_{N,k} = f'_{N,k} - D_{f_N,k} \tag{A.17}$$

$$D_{f_N,k} = D_{f_N,k-1}e^{-\Delta s/T_f} + (f'_{N,k} - f'_{N,k-1})e^{-\Delta s/2T_f} \tag{A.18}$$

Then applying Kirchhoff formula we obtain the dynamic force coefficients:

$$C^{dyn}_{N,k} = C^P_N * \left(\frac{1 + sign(f''_{N,k})\sqrt{|f''_{N,k}|}}{2}\right)^2 \tag{A.19}$$

$$C^{dyn}_{T,k} = C^P_T * sign(f''_{T,k})\sqrt{|f''_{T,k}|} \tag{A.20}$$

A.5 Leading edge vortex module

No leading edge vortex module has been implemented yet in ARDEMA. For horizontal wind turbines, common airfoils are over 20% thickness. For such airfoils, no leading edge vortex is observed.

A.6 Stored variables

The following data are stored at each time step, then used in the next time step and overwritten:

- $\alpha_{e,k}$
- $D_{p,k}$
- $D_{b,k}$
- $\alpha_{delayed,k}$
- $D_{f_N,k}$
- $D_{f_T,k}$

Appendix B

Theodorsen function

These section is derived from the analytical development of Theodorsen presented in Leishman book [110]. The theory has been developed for a flat plate (i.e. thin airfoil represented by a vortex sheet) subject to small disturbances (wake is assumed to be a planar surface of vortex sheet extending from the trailing edge downstream to infinity, convected at the freestream velocity). From this theory and for a pure oscillatory oscillation in angle of attack, lift and moment coefficients (along the pitch axis, or attachment point in this case) can be expressed as the sum of added mass and circulatory terms:

$$C_L = \underbrace{\pi b\left(\frac{\dot{\alpha}}{V} - \frac{ba\ddot{\alpha}}{V^2}\right)}_{\text{Added mass}} + \underbrace{\overbrace{2\pi\left[\alpha + b\left(\frac{1}{2} - a\right)\frac{\dot{\alpha}}{V}\right]}^{\text{Quasi-steady}} \overbrace{C(k)}^{\text{Theodorsen}}}_{\text{Circulatory}} \tag{B.1}$$

$$C_M = \underbrace{-\frac{\pi}{2}\left[\frac{b^2}{V^2}\left(\frac{1}{8} + a^2\right)\ddot{\alpha}\right]}_{\text{Added mass}} + \underbrace{\overbrace{\pi\left(a + \frac{1}{2}\right)\left[\alpha + b\left(\frac{1}{2} - a\right)\frac{\dot{\alpha}}{V}\right]}^{\text{Quasi-steady}} \overbrace{C(k)}^{\text{Theodorsen}} - \frac{\pi}{2}\left[\left(\frac{1}{2} - a\right)\frac{b\dot{\alpha}}{V}\right]}_{\text{Circulatory}} \tag{B.2}$$

Where:

- b is the semi-chord
- a is the dimensionless (with regard to semi-chord) pitch axis location relative to the mid-chord of the airfoil
- V is the magnitude of the steady flow velocity
- α, $\dot{\alpha}$ and $\ddot{\alpha}$ are respectively the angle of attack, the derivative of the angle of attack and the second derivative of the angle of attack with respect to time
- $C(k)$ is a complex valued transfer function known as "Theodorsen's function" which accounts for the circulatory effects of the shed wake on the unsteady airloads. The complex notation enables to account for the change in the amplitude (absolute value) and the phase lag (argument)
- k is the reduced frequency $k = \frac{b\omega}{V}$ where ω is the pulsation

Note that the moment coefficient is the moment coefficient along the attachment point $x_a tt$. To transfer the moment coefficient to another point, namely x, such as the quarter chord point, one can use the relation involving the normal force coefficient C_n (or the lift coefficient for small angles):

$$C_m = C_{m_{att}} + C_n\left(\frac{x}{c} - \frac{x_{att}}{c}\right) \approx C_{m_{att}} + C_l\left(\frac{x}{c} - \frac{x_{att}}{c}\right) \quad \text{for small angles} \tag{B.3}$$

As in this case, the variation of the angle of attack is pure harmonically oscillatory, the angle of attack can be expressed as $\alpha = \bar{\alpha}e^{i\omega t}$, and consequently, $\dot{\alpha} = i\omega\alpha$ and $\ddot{\alpha} = -\omega^2\alpha$. With the same assumption on the motion, the Theodorsen's function can be expressed in terms of Hessel functions of the first and second kinds. A practical approximation is used here:

$$C(k) = 1 - \frac{0.165}{1 - 0.0455\frac{i}{k}} - \frac{0.335}{1 - 0.3\frac{i}{k}} \tag{B.4}$$

Lift and moment coefficients are driven by the effects of the reduced frequency k, the pitch axis location (i.e. attachment point) a and the amplitude $\bar{\alpha}$ of the oscillation.

For pure harmonically oscillations, the lift and moment coefficients are supposed to be also harmonic responses, so to study the effect of the reduced frequency, the comparisons of the amplitude and the phase lags are in principle sufficient.

List of Figures

List of Tables

Bibliography

[1] AVATAR: Home.

[2] European Commission - Energy. Accessed : 2019-01-02.

[3] Innwind.eu.

[4] UNFCCC - Process. Accessed : 2019-01-02.

[5] WindEurope - the voice of the wind energy industry. Accessed : 2019-01-02.

[6] X. Amandolese and E. Szechenyi. Experimental study of the effect of turbulence on a section model blade oscillating in stall. *Wind Energy*, 7(4):267–282, 2004.

[7] T. Ashuri, J. R. R. A. Martins, M. B. Zaaijer, G. A. M. van Kuik, and G. J. W. van Bussel. Aeroservoelastic design definition of a 20 MW common research wind turbine model: A 20 MW common research wind turbine model. *Wind Energy*, 19(11):2071–2087, November 2016.

[8] T. Ashuri, M.B. Zaaijer, J.R.R.A. Martins, G.J.W. van Bussel, and G.A.M. van Kuik. Multidisciplinary design optimization of offshore wind turbines for minimum levelized cost of energy. *Renewable Energy*, 68:893–905, August 2014.

[9] Turaj Ashuri, Michiel B. Zaaijer, Joaquim R.R.A. Martins, and Jie Zhang. Multidisciplinary design optimization of large wind turbines—Technical, economic, and design challenges. *Energy Conversion and Management*, 123:56–70, September 2016.

[10] C. Bak. Three-Dimensional Corrections of Airfoil Characteristics Based on Pressure Distributions. In *European Wind Energy Conference & Exhibition (EWEC)*, Athens, Greece, 2006.

[11] Christian Bak, Peter Fuglsang, Jeppe Johansen, Ioannis Antoniou, and Forsøgsanlæg Risø. *Wind tunnel tests of the NACA 63-415 and a modified NACA63-415 airfoil*. Forsøgsanlæg Risø, Roskilde, 2000. OCLC: 771094727.

[12] Christian Bak, Niels Troldborg, and Helge Aagaard Madsen. DAN-AERO MW: Measured airfoil characteristics for a MW rotor in atmospheric conditions. page 10, 2011.

[13] Christian Bak, F. Zahle, R. Bitsche, T. Kim, A. Yde, L. C. Henriksen, M. H. Hansen, JPAA Blasques, M. Gaunaa, and A. Natarajan. The DTU 10-MW reference wind turbine. *Danish wind power research*, 2013.

[14] Elias Balaras, Carlo Benocci, and Ugo Piomelli. Two-layer approximate boundary conditions for large-eddy simulations. *AIAA Journal*, 34(6):1111–1119, June 1996.

[15] Laurent Beaudet. *Etude expérimentale et numérique du décrochage dynamique sur une éolienne à axe vertical de forte solidité*. PhD thesis, Université de Poitiers, 2014.

[16] F. Bertagnolio, N.N. Sørensen, J. Johansen, and P. Fuglsang. *Wind Turbine Airfoil Catalogue*. Risoe National Laboratory, Roskilde, Denmark, August 2001.

[17] Franck Bertagnolio, Flemming Rasmussen, Niels Sørensen, Jeppe Johansen, and Helge Madsen. A Stochastic Static Stall Model Applied to a Wind Turbine Blade. In *26th AIAA Applied Aerodynamics Conference*, Honolulu, Hawaii, August 2008. American Institute of Aeronautics and Astronautics.

[18] Anders Björck. Coordinates and Calculations for the FFA-W1-xxx, FFA-W2-xxx and FFA-W3-xxx Series of Airfoils for Horizontal Axis Wind Turbines. Technical Report FFA TN 1990-15, The Aeronautical Research Institue of Sweden, 1990.

[19] Sébastien Bocquet. *Modélisation de paroi et injection de turbulence pariétale pour la Simulation des Grandes Echelles des écoulements aérothermiques*. PhD thesis, Université de Toulouse, 2013.

[20] J. Bodart and J. Larsson. Wall-modeled large eddy simulation in complex geometries with application to high-lift devices. *Center for Turbulence Research Annual Research Briefs*, pages 37–48, 2011.

[21] Julien Bodart, Johan Larsson, and Parviz Moin. Large eddy simulation of high-lift devices. American Institute of Aeronautics and Astronautics, June 2013.

[22] K. Boorsma, M. Hartvelt, and L.M. Orsi. Application of the lifting line vortex wake method to dynamic load case simulations. *Journal of Physics: Conference Series*, 753:022030, September 2016.

[23] C. L. Bottasso, F. Campagnolo, and A. Croce. Multi-disciplinary constrained optimization of wind turbines. *Multibody System Dynamics*, 27(1):21–53, January 2012.

[24] Emmanuel Branlard. *Wind turbine tip-loss corrections - Review, implementation and investigation of new models*. PhD thesis, DTU Risoe, 2011.

[25] Emmanuel Branlard. *Wind Turbine Aerodynamics and Vorticity-Based Methods*, volume 7 of *Research Topics in Wind Energy*. Springer International Publishing, Cham, 2017.

[26] Simon-Philippe Breton, Frank N. Coton, and Geir Moe. A study on rotational effects and different stall delay models using a prescribed wake vortex scheme and NREL phase VI experiment data. *Wind Energy*, 11(5):459–482, September 2008.

[27] W. Cabot. Near-wall models in large eddy simulations of flow behind a backward-facing step. *Center for Turbulence Research Annual Research Briefs*, 1996.

[28] W. Cabot and P. Moin. Approximate wall boundary conditions in the large-eddy simulation of high Reynolds number flow. *Flow, Turbulence and Combustion*, 63(1-4):269–291, 2000.

[29] I. Cafarelli. A survey of the latest developments in dynamic stall and optimization of rotating structures. 1999.

[30] J Calafell, O Lehmkuhl, A Carmona, C D Pérez-Segarra, and A Oliva. A dynamic wall model for Large-Eddy simulations of wind turbine dedicated airfoils. *Journal of Physics: Conference Series*, 524:012147, June 2014.

[31] J. Calafell, O. Lehmkuhl, I. Rodriguez, and A. Oliva. On the Large-Eddy Simulation modelling of wind turbine dedicated airfoils at high Reynolds numbers. In *Proceeding of THMT-12. Proceedings of the Seventh International Symposium On Turbulence, Heat and Mass Transfer Palermo, Italy, 24-27 September, 2012*, page 12, Antalya, Turkey, 2012. Begellhouse.

[32] Lawrence W. Carr. Progress in analysis and prediction of dynamic stall. *Journal of Aircraft*, 25(1):6–17, January 1988.

[33] Lawrence W. Carr, Kenneth W. McAlister, and William J. McCroskey. Analysis of the development of dynamic stall based on oscillating airfoil experiments. 1977.

[34] F. O. Carta. A comparison of the pitching and plunging response of an oscillating airfoil. Technical Report NASA-CR-3172, NASA, 1979.

[35] P. K. Chaviaropoulos and M. O. L. Hansen. Investigating Three-Dimensional and Rotational Effects on Wind Turbine Blades by Means of a Quasi-3d Navier-Stokes Solver. *Journal of Fluids Engineering*, 122(2):330, 2000.

[36] Adam Chehouri, Rafic Younes, Adrian Ilinca, and Jean Perron. Review of performance optimization techniques applied to wind turbines. *Applied Energy*, 142:361–388, March 2015.

[37] Jerry M. Chen and Yuan-Cheng Fang. Strouhal numbers of inclined flat plates. *Journal of Wind Engineering and Industrial Aerodynamics*, 61(2-3):99–112, July 1996.

[38] Haecheon Choi and Parviz Moin. Grid-point requirements for large eddy simulation: Chapman's estimates revisited. *Physics of Fluids*, 24(1):011702, January 2012.

[39] F. N. Coton and R. A. McD. Galbraith. An experimental study of dynamic stall on a finite wing. *The Aeronautical Journal*, 103(1023):229–236, May 1999.

[40] Frank N. Coton, Tongguang Wang, and Roderick A. McD Galbraith. An examination of key aerodynamic modelling issues raised by the NREL blind comparison. *Wind Energy*, 5(2-3):199–212, 2002.

[41] Hugh D. Currin, Frank N. Coton, and Byard Wood. Dynamic Prescribed Vortex Wake Model for AERODYN/FAST. *Journal of Solar Energy Engineering*, 130(3):031007, 2008.

[42] R. R. Damiani and G. J. Hayman. The Dynamic Stall Module for FAST 8. Technical report, NREL, 2016.

[43] Rick Damiani, Greg Hayman, Qi Wang, and Jason M. Jonkman. Development and Validation of a New Unsteady Airfoil Aerodynamics Model Within AeroDyn. American Institute of Aeronautics and Astronautics, January 2016.

[44] K.R. Dixon. *The Near Wake Structure of a Vertical Axis Wind Turbine*. PhD thesis, TU Delft, April 2008.

[45] DNV GL. Energy Transition Outlook 2018, 2018.

[46] Mark Drela. XFOIL: An analysis and design system for low Reynolds number airfoils. In *Low Reynolds number aerodynamics*, pages 1–12. Springer, MIT, 1989.

[47] Zhaohui Du and Michael Selig. A 3-D stall-delay model for horizontal axis wind turbine performance prediction. In *1998 ASME Wind Energy Symposium*, Reno,NV,U.S.A., January 1998. American Institute of Aeronautics and Astronautics.

[48] H. Dumitrescu and V. Cardoş. Predictions of unsteady hawt aerodynamics by lifting line theory. *Mathematical and Computer Modelling*, 33(4-5):469–481, February 2001.

[49] C. Duprat, G. Balarac, O. Métais, P. M. Congedo, and O. Brugière. A wall-layer model for large-eddy simulations of turbulent flows without pressure gradient. *Physics of Fluids*, 23(1):015101, 2011.

[50] William Frederick Durand. *Aerodynamic Theory*. Springer Berlin Heidelberg, Berlin, Heidelberg, 1935.

[51] Moutaz Elgammi and Tonio Sant. Integrating a new flow separation model and the effects of the vortex shedding for improved dynamic stall predictions using the Beddoes-Leishman method: An improved method for dynamic stall prediction. *Wind Energy*, pages n/a–n/a, 2016.

[52] European Commission. Renewable Energy Road Map Renewable energies in the 21st century: building a more sustainable future, 2007.

[53] European Commission. Energy 2020 A strategy for competitive, sustainable and secure energy, 2010.

[54] Mark Faber. *A comparison of dynamic stall models and their effect on instabilities*. PhD thesis, 2018.

[55] Joel H. Ferziger and M. Perić. *Computational methods for fluid dynamics*. Springer, Berlin ; New York, 3rd, rev. ed edition, 2002.

[56] Paul Fleming, Jennifer Annoni, Jigar J. Shah, Linpeng Wang, Shreyas Ananthan, Zhijun Zhang, Kyle Hutchings, Peng Wang, Weiguo Chen, and Lin Chen. Field test of wake steering at an offshore wind farm. *Wind Energy Science*, 2(1):229–239, May 2017.

[57] P. Fuglsang, C. Bak, J. G. Schepers, B. Bulder, T. T. Cockerill, P. Claiden, A. Olesen, and R. van Rossen. Site-specific Design Optimization of Wind Turbines. *Wind Energy*, 5(4):261–279, October 2002.

[58] Peter Fuglsang, editor. *Wind tunnel tests of the FFA-W3-241, FFA-W3-301 and NACA 63-430 airfoils*. Number 1041 in Risø-R. Risø National Laboratory, Roskilde, 1998.

[59] Peter Fuglsang, Christian Bak, Mac Gaunaa, and Ioannis Antoniou. *Wind Tunnel Tests of Risø-B1-18 and Risø-B1-24*. 2003.

[60] Peter Fuglsang, Kristian S. Dahl, and Ioannis Antoniou. *Wind tunnel tests of the Risø-A1-18, Risø-A1-21 and Risø-A1-24 airfoils*. Number 1112 in Risø-R. Risø National Laboratory, Roskilde, 1999. OCLC: 247470171.

[61] Hiroaki Fukumoto, Hikaru Aono, Taku Nonomura, Akira Oyama, and Kozo Fujii. Significance of Computational Spanwise Domain Length on LES for the Flowfield with Large Vortex Structure. American Institute of Aeronautics and Astronautics, January 2016.

[62] Evan M. Gaertner. Modeling dynamic stall for a free vortex wake model of a floating offshore wind turbine. Master's thesis, University of Massachusetts Amherst, 2014.

[63] Arne Van Garrel. Development of a Wind Turbine Aerodynamics Simulation Module. 2003.

[64] Donald E. Gault. A correlation of low-speed, airfoil-section stalling characterisitcs with Reynolds number and airfoil geometry. Technical report, National Advisory Committee for Aeronautics, 1957.

[65] Massimo Germano, Ugo Piomelli, Parviz Moin, and William H. Cabot. A dynamic subgrid-scale eddy viscosity model. *Physics of Fluids A: Fluid Dynamics*, 3(7):1760–1765, July 1991.

[66] Kobra Gharali and David A. Johnson. Numerical modeling of an S809 airfoil under dynamic stall, erosion and high reduced frequencies. *Applied Energy*, 93:45–52, May 2012.

[67] M. Goman and A. Khrabrov. State-space representation of aerodynamic characteristics of an aircraft at high angles of attack. *Journal of Aircraft*, 31(5):1109–1115, September 1994.

[68] A. Gonzalez and X. Munduate. Unsteady modelling of the oscillating S809 aerofoil and NREL phase VI parked blade using the Beddoes-Leishman dynamic stall model. *Journal of Physics: Conference Series*, 75:012020, July 2007.

[69] R. E Gormont. A Mathematical Model of Unsteady Aerodynamics and Radial Flow for Application to Helicopter Rotors. Technical Report USAAMRDL TECHNICAL REPORT 72-67, Boeing Vertol Company, 1973.

[70] F. Grasso. Development of Thick Airfoils for Wind Turbines. *Journal of Aircraft*, 50(3):975–981, May 2013.

[71] Francesco Grasso and Ozlem Ceyhan. Non-conventional flat back thick airfoils for very large offshore wind turbines. In *33rd Wind Energy Symposium*, Kissimmee, Florida, January 2015. American Institute of Aeronautics and Astronautics.

[72] S Guntur and N N Sørensen. An evaluation of several methods of determining the local angle of attack on wind turbine blades. *Journal of Physics: Conference Series*, 555:012045, December 2014.

[73] S. Guntur and N. N. Sørensen. A study on rotational augmentation using CFD analysis of flow in the inboard region of the MEXICO rotor blades: A study on rotational augmentation by CFD analysis of the MEXICO rotor. *Wind Energy*, 18(4):745–756, April 2015.

[74] Srinivas Guntur, Jason Jonkman, Ryan Sievers, Michael A. Sprague, Scott Schreck, and Qi Wang. A Validation and Code-to-Code Verification of FAST for a Megawatt-ScaleWind Turbine with Aeroelastically Tailored Blades. *Wind Energy Science Discussions*, pages 1–38, March 2017.

[75] Srinivas Guntur, Niels N. Sørensen, and Scott Schreck. Dynamic Stall on Rotating Airfoils: A Look at the N-Sequence Data from the NREL Phase VI Experiment. *Key Engineering Materials*, 569-570:611–619, July 2013.

[76] Srinivas Guntur, Niels N. Sørensen, Scott Schreck, and Leonardo Bergami. Modeling dynamic stall on wind turbine blades under rotationally augmented flow fields: Modeling dynamic stall on wind turbine blades under rotationally augmented flow fields. *Wind Energy*, 19(3):383–397, March 2016.

[77] Rohit Gupta and Phillip J. Ansell. Investigation of the Effects of Reynolds Number on the Unsteady Flow Physics of Airfoil Dynamic Stall. American Institute of Aeronautics and Astronautics, January 2018.

[78] S. Gupta and J. G. Leishman. Dynamic stall modelling of the S809 aerofoil and comparison with experiments. *Wind Energy*, 9(6):521–547, November 2006.

[79] A. C. Hansen, C. P. Butterfield, and X. Cui. Yaw Loads and Motions of a Horizontal Axis Wind Turbine. *Journal of Solar Energy Engineering*, 112(4):310, 1990.

[80] A.C. Hansen. Yaw dynamics of horizontal axis wind turbines. Final report. Technical Report NREL/TP–442-4822, 10144778, May 1992.

[81] M. H. Hansen. Stall-induced vibrations of a blade section in deep-stall. In *Research in aeroelasticity EFP-2007-II*, pages 114–121. Danmarks Tekniske Universitet, Risø Nationallaboratoriet for Bæredygtig Energi, Roskilde, t. buhl edition, 2009. OCLC: 761004033.

[82] Martin O. L. Hansen. *Aerodynamics of wind turbines*. Routledge, New York, NY, third edition edition, 2015.

[83] M.H. Hansen, M. Gaunaa, and H.A. Madsen. A Beddoes-Leishman type dynamic stall model in sate-space and indicial formulations. Technical report, Risoe, 2004.

[84] M.O.L. Hansen, J.N. Sørensen, S. Voutsinas, N. Sørensen, and H.Aa. Madsen. State of the art in wind turbine aerodynamics and aeroelasticity. *Progress in Aerospace Sciences*, 42(4):285–330, June 2006.

[85] Martin Hartvelt and Rotor Design Track-Aerodynamics. *Comparison of the Aeroelastic Free Vortex Wake Code AWSM with Conventional BEM Based Codes on 10MW+ Wind Turbines*. PhD thesis, ECN, 2016.

[86] S Hauptmann, M Bülk, L Schön, S Erbslöh, K Boorsma, F Grasso, M Kühn, and P W Cheng. Comparison of the lifting-line free vortex wake method and the blade-element-momentum theory regarding the simulated loads of multi-MW wind turbines. *Journal of Physics: Conference Series*, 555:012050, December 2014.

[87] Joachim C. Heinz, Niels N. Sørensen, Frederik Zahle, and Witold Skrzypiński. Vortex-induced vibrations on a modern wind turbine blade: Vortex-induced vibrations on a modern wind turbine blade. *Wind Energy*, 19(11):2041–2051, November 2016.

[88] I. Herráez, B. Akay, G. J. W. van Bussel, J. Peinke, and B. Stoevesandt. Detailed Analysis of the Blade Root Flow of a Horizontal Axis Wind Turbine. *Wind Energy Science Discussions*, pages 1–33, January 2016.

[89] Iván Herráez, Elia Daniele, and J. Gerard Schepers. Extraction of the wake induction and angle of attack on rotating wind turbine blades from PIV and CFD results. *Wind Energy Science*, 3(1):1–9, January 2018.

[90] J.G. Holierhoek, J.B. de Vaal, A.H. van Zuijlen, and H. Bijl. Comparing different dynamic stall models: Comparing different dynamic stall models. *Wind Energy*, 16(1):139–158, January 2013.

[91] IEA. Renewables Information, 2018.

[92] Internation Electrotechnical Commission. *IEC 61400-1 Ed.4.0 - International Standard - Wind energy generation systems - Part 1 : Design requirements*. 2019.

[93] IRENA. Renewable power generation costs in 2017. page 160, 2017.

[94] Thomas Jaravel. *Prediction of pollutants in gas turbines using large eddy simulation*. PhD Thesis, Institut National Polytechnique de Toulouse, 2016.

[95] Min-Soo Jeong, Sang-Woo Kim, In Lee, Seung-Jae Yoo, and K.C. Park. The impact of yaw error on aeroelastic characteristics of a horizontal axis wind turbine blade. *Renewable Energy*, 60:256–268, December 2013.

[96] Ángel Jiménez, Antonio Crespo, and Emilio Migoya. Application of a LES technique to characterize the wake deflection of a wind turbine in yaw. *Wind Energy*, 13(6):559–572, December 2009.

[97] B. J. Jonkman and J. M. Jonkman. *FAST v8.15.00a-bjj*. National Renewable Energy Laboratory, April 2016.

[98] B. J. Jonkman and L. Kilcher. Turbsim User's Guide: Version 1.06.00. Technical report, 2012.

[99] Jason Jonkman, G. J. Hayman, Bonnie Jonkman, and R. R. Damiani. AeroDyn v15 User's Guide and Theory Manual. Technical report, NREL, 2017.

[100] Jason M. Jonkman and Marshall L. Buhl Jr. *FAST user's guide*. 2005.

[101] Jason Mark Jonkman, Sandy Butterfield, Walter Musial, and George Scott. *Definition of a 5-MW reference wind turbine for offshore system development*. National Renewable Energy Laboratory Golden, CO, 2009.

[102] Joseph Katz and Allen Plotkin. *Low-speed aerodynamics: from wing theory to panel methods*. McGraw-Hill series in aeronautical and aerospace engineering. McGraw-Hill, New York, 1991.

[103] Kurt Kaufmann, Michel Costes, Francois Richez, and Anthony D Gardner. Numerical investigation of three-dimensional dynamic stall on an oscillating finite wing. page 13, 2014.

[104] M. A. Khan. *Dynamic Stall Modeling for Wind Turbines*. PhD thesis, TU Delft, 2018.

[105] Yusik Kim and Zheng-Tong Xie. Modelling the effect of freestream turbulence on dynamic stall of wind turbine blades. *Computers & Fluids*, 129:53–66, April 2016.

[106] R. Lanzafame, S. Mauro, and M. Messina. Evaluation of the Radial Flow Effects on Micro HAWTs through the Use of a Transition CFD 3d Model – part I: State of the Art and Numerical Model Review. *Energy Procedia*, 82:156–163, December 2015.

[107] J.W. Larsen, S.R.K. Nielsen, and S. Krenk. Dynamic stall model for wind turbine airfoils. *Journal of Fluids and Structures*, 23(7):959–982, October 2007.

[108] Johan Larsson, Soshi Kawai, Julien Bodart, and Ivan Bermejo-Moreno. Large eddy simulation with modeled wall-stress: recent progress and future directions. *Mechanical Engineering Reviews*, 3(1):15–00418, 2016.

[109] J. G. Leishman. Challenges in Modeling the Unsteady Aerodynamics of Wind Turbines. volume 5, pages 85–132, Reno, NV, USA, 2002.

[110] J. G. Leishman. *Principles of Helicopter Aerodynamics*. Cambridge University Press, 2nd edition edition, 2006.

[111] J. G. Leishman and T. S. Beddoes. A generalized model for airfoil unsteady aerodynamic behavior and dynamic stall using the indicial method. 1986.

[112] J. G. Leishman and T. S. Beddoes. A Semi-Empirical Model for Dynamic Stall. *Journal of the American Helicopter society*, 34(3):3–17, 1989.

[113] J.G. Leishman and G. L. Crouse. State-space model for unsteady airfoil behavior and dynamic stall. American Institute of Aeronautics and Astronautics, April 1989.

[114] M. Liebreich. Bloomberg New Energy Finance, 2017.

[115] Douglas K. Lilly. A proposed modification of the Germano subgrid-scale closure method. *Physics of Fluids A: Fluid Dynamics*, 4(3):633–635, 1992.

[116] A.H. Lind. *An experimental study of static and oscillating rotor blade sections in reverse flow.* PhD Thesis, Faculty of the Graduate School of the University of Maryland, 2015.

[117] Andrew H. Lind and Anya R. Jones. Vortex Shedding from Airfoils in Reverse Flow. *AIAA Journal*, 53(9):2621–2633, September 2015.

[118] Andrew H. Lind and Anya R. Jones. Unsteady airloads on static airfoils through high angles of attack and in reverse flow. *Journal of Fluids and Structures*, 63:259–279, May 2016.

[119] Jian Liu, Wenqing Zhu, Zhixiang Xiao, Haisheng Sun, Yong Huang, and Zhitao Liu. DDES with adaptive coefficient for stalled flows past a wind turbine airfoil. *Energy*, 161:846–858, October 2018.

[120] E Llorente, A Gorostidi, M Jacobs, W A Timmer, X Munduate, and O Pires. Wind Tunnel Tests of Wind Turbine Airfoils at High Reynolds Numbers. *Journal of Physics: Conference Series*, 524:012012, June 2014.

[121] Helge Aagaard Madsen. New airfoils for high rotational speed wind turbines. Technical report, 2015.

[122] N. Maheu, V. Moureau, P. Domingo, F. Duchaine, and G. Balarac. Large-eddy simulations of flow and heat transfer around a low-Mach number turbine blade. In *Proceedings of the Summer Program 2012*, Center for Turbulence Research, 2012.

[123] Luca Manni, Takafumi Nishino, and Pierre-Luc Delafin. Numerical study of airfoil stall cells using a very wide computational domain. *Computers & Fluids*, 140:260–269, November 2016.

[124] Marinos Manolesos, Georgios Papadakis, and Spyros G. Voutsinas. Experimental and computational analysis of stall cells on rectangular wings: Experimental and CFD analysis of stall cells. *Wind Energy*, 17(6):939–955, June 2014.

[125] S. Mauro, R. Lanzafame, and M. Messina. An Insight into the Rotational Augmentation on HAWTs by means of CFD Simulations – Part I: State of the Art and Numerical Results. *International Journal of Applied Engineering Research*, 12(21):10491–10504, 2017.

[126] W. J. Mccroskey. The phenomenon of dynamic stall.[vortex shedding phenomenon on oscillating airfoils. 1981.

[127] W J McCroskey. Unsteady Airfoils. *Annual Review of Fluid Mechanics*, 14(1):285–311, January 1982.

[128] W. J. McCroskey, K. W. McAlister, L. W. Carr, S. L. Pucci, O. Lambert, and R. F. Indergrand. Dynamic Stall on Advanced Airfoil Sections. *Journal of the American Helicopter Society*, 26(3):40–50, July 1981.

[129] W.J. McCroskey, L.W. Carr, and K.W. McAlister. Dynamic Stall Experiments on Oscillating Airfoils. *AIAA Journal*, 14(1):57–63, January 1976.

[130] Matthew Melius, Raúl Bayoán Cal, and Karen Mulleners. Dynamic stall of an experimental wind turbine blade. *Physics of Fluids*, 28(3):034103, March 2016.

[131] Craig Meskell and Alberto Pellegrino. Vortex Shedding Lock-In due to Pitching Oscillation of a Wind Turbine Blade Section at High Angles of Attack. *International Journal of Aerospace Engineering*, 2019:1–12, March 2019.

[132] Ministère de l'environnement de l'énergie et de la mer. Programmation pluriannuelle de l'énergie, 2016.

[133] J.E. Minnema. *Pitching moment predictions on wind turbine blades using the Beddoes-Leishman model for unsteady aerodynamics and dynamic stall*. PhD thesis, The University of Utah, 1998.

[134] R. Modarres. *Semi-Empirical Modeling of Two-Dimensional and Three-Dimensional Dynamic Stall*. PhD thesis, Washington University in St. Louis, 2016.

[135] B. Montgomerie. Dynamic stall model called SIMPLE. Technical report, Netherlands Energy Research Foundation ECN, 1996.

[136] B. Montgomerie. Methods for Root Effects, Tips Effects and Extending the AoA Range to +-180 deg, with Application to Aerodynamics for Blades on WT and Propellers. Technical Report FOI-R-1305-SE, Swedish Defence Research Agency, Stockholm, June 2004.

[137] Patrick J. Moriarty and A. Craig Hansen. *AeroDyn theory manual*. Citeseer, 2005.

[138] Vincent Moureau, Pascale Domingo, and Luc Vervisch. Design of a massively parallel CFD code for complex geometries. *Comptes Rendus Mécanique*, 339(2-3):141–148, February 2011.

[139] Karen Mulleners and Markus Raffel. The onset of dynamic stall revisited. *Experiments in Fluids*, 52(3):779–793, March 2012.

[140] Karen Mulleners and Markus Raffel. Dynamic stall development. *Experiments in Fluids*, 54(2), February 2013.

[141] H. Müller-Vahl, C. Strangfeld, C. N. Nayeri, C. O. Paschereit, and D. Greenblatt. Thick Airfoil Deep Dynamic Stall. In *Wind energy - impact of turbulence*, number volume 2 in Research topics in wind energy. Springer, Heidelberg, 2014.

[142] Hanns Friedrich Müller-Vahl, Georgios Pechlivanoglou, Christian Navid Nayeri, Christian Oliver Paschereit, and David Greenblatt. Matched pitch rate extensions to dynamic stall on rotor blades. *Renewable Energy*, 105:505–519, May 2017.

[143] Franck Nicoud and Frédéric Ducros. Subgrid-scale stress modelling based on the square of the velocity gradient tensor. *Flow, turbulence and Combustion*, 62(3):183–200, 1999.

[144] Andrew Ning. AirfoilPrep.py, 2019.

[145] Andrew Ning, Gregory Hayman, Rick Damiani, and Jason M. Jonkman. Development and Validation of a New Blade Element Momentum Skewed-Wake Model within AeroDyn. In *33rd Wind Energy Symposium*, Kissimmee, Florida, January 2015. American Institute of Aeronautics and Astronautics.

[146] A J Niven and R A McD Galbraith. Modelling dynamic stall vortex inception at low Mach numbers. page 10, 1997.

[147] Stig Oye. Dynamic stall simulated as time lag of separation. Technical Report, Technical University of Denmark, 1991.

[148] Alberto Pellegrino and Craig Meskell. Vortex shedding from a wind turbine blade section at high angles of attack. *Journal of Wind Engineering and Industrial Aerodynamics*, 121:131–137, October 2013.

[149] Ricardo Pereira, Gerard Schepers, and Marilena D. Pavel. Validation of the Beddoes-Leishman dynamic stall model for horizontal axis wind turbines using MEXICO data: Validation of the Beddoes-Leishman. *Wind Energy*, 16(2):207–219, March 2013.

[150] D. Petot. Modélisation du décrochage dynamique par équations différentielles. *La Recherche Aérospatiale*, n°5:59–72, 1989.

[151] Kirk Gee Pierce. *Wind turbine load prediction using the Beddoes-Leishman model for unsteady aerodynamics and dynamic stall*. PhD thesis, The University of Utah, 1996.

[152] O Pires, X Munduate, O Ceyhan, M Jacobs, and H Snel. Analysis of high Reynolds numbers effects on a wind turbine airfoil using 2d wind tunnel test data. *Journal of Physics: Conference Series*, 753:022047, September 2016.

[153] R. A. Piziali. 2-D and 3-D oscillating wing aerodynamics for a range of angles of attack including stall. 1994.

[154] S. B. Pope. *Turbulent flows*. Cambridge University Press, Cambridge ; New York, 2000.

[155] Thomas Prässler and Jan Schaechtele. Comparison of the financial attractiveness among prospective offshore wind parks in selected European countries. *Energy Policy*, 45:86–101, June 2012.

[156] Yong-Xing Qiu, Xiao-Dong Wang, Shun Kang, Ming Zhao, and Jun-Yu Liang. Predictions of unsteady HAWT aerodynamics in yawing and pitching using the free vortex method. *Renewable Energy*, 70:93–106, October 2014.

[157] R. Reuss Ramsay, M. J. Hoffmann, and G. M. Gregorek. Effects of Grit Roughness and Pitch Oscillations on the S809 Airfoil. 1995.

[158] Daniele Ragni and Carlos Ferreira. Effect of 3d stall-cells on the pressure distribution of a laminar NACA64-418 wing. *Experiments in Fluids*, 57(8), August 2016.

[159] H. Rahimi, J.G. Schepers, W.Z. Shen, N. Ramos García, M.S. Schneider, D. Micallef, C.J. Simao Ferreira, E. Jost, L. Klein, and I. Herráez. Evaluation of different methods for determining the angle of attack on wind turbine blades with CFD results under axial inflow conditions. *Renewable Energy*, 125:866–876, September 2018.

[160] Giridhar Ramanujam and Huseyin Ozdemir. Improving Airfoil Lift Prediction. In *35th Wind Energy Symposium*, Grapevine, Texas, January 2017. American Institute of Aeronautics and Astronautics.

[161] N Ramos-García. *Unsteady viscous-inviscid interaction technique for wind turbine airfoils*. PhD thesis, Ph. D. thesis, Technical university of Denmark, 2011.

[162] Néstor Ramos-García, Jens Nørkaer Sørensen, and Wen Zhong Shen. A strong viscous-inviscid interaction model for rotating airfoils: A strong viscous-inviscid interaction model for rotating airfoils. *Wind Energy*, 17(12):1957–1984, December 2014.

[163] Néstor Ramos-García, Jens Nørkær Sørensen, and Wen Zhong Shen. Validation of a three-dimensional viscous–inviscid interactive solver for wind turbine rotors. *Renewable Energy*, 70:78–92, October 2014.

[164] Marc Rapin and Biel Ortun. 3d rotational correction in ONERA aeroelastic predictions of NREL wind turbine. In *45th AIAA Aerospace Sciences Meeting and Exhibit*, page 213, 2007.

[165] Abdolrahim Rezaeiha, Ricardo Pereira, and Marios Kotsonis. Fluctuations of angle of attack and lift coefficient and the resultant fatigue loads for a large Horizontal Axis Wind turbine. *Renewable Energy*, 114:904–916, December 2017.

[166] Vasilis A. Riziotis and Spyros G. Voutsinas. Dynamic stall modelling on airfoils based on strong viscous–inviscid interaction coupling. *International Journal for Numerical Methods in Fluids*, 56(2):185–208, January 2008.

[167] S. Rodrigues, C. Restrepo, E. Kontos, R. Teixeira Pinto, and P. Bauer. Trends of offshore wind projects. *Renewable and Sustainable Energy Reviews*, 49:1114–1135, September 2015.

[168] Joeri Rogelj, Drew Shindell, Kejun Jiang, Solomone Fifita, Piers Forster, Veronika Ginzburg, Collins Handa, Shigeki Kobayashi, Elmar Kriegler, Luis Mundaca, Roland Séférian, and Maria Virginia Vilariño. Mitigation Pathways Compatible with 1.5°C in the Context of Sustainable Development. In *Global warming of 1.5°C. An IPCC Special Report on the impacts of global warming of 1.5°C above pre-industrial levels and related global greenhouse gas emission pathways, in the context of strengthening the global response to the threat of climate change, sustainable development, and efforts to eradicate poverty*, pages 93–174. 2018.

[169] Tonio Sant. *Improving BEM-based aerodynamic models in wind turbine design codes.* PhD thesis, DUWIND Delft University Wind Energy Research Institute, Delft, 2007. OCLC: 905870415.

[170] G Schepers. *Engineering models in wind energy aerodynamics : development, implementation and analysis using dedicated aerodynamic measurements*. PhD thesis, Techische Universiteit Delft, Delft, 2012. OCLC: 820570607.

[171] J. Schepers. An engineering model for yawed conditions, developed on basis of wind tunnel measurements. In *37th Aerospace Sciences Meeting and Exhibit*, Reno,NV,U.S.A., January 1999. American Institute of Aeronautics and Astronautics.

[172] Hermann Schlichting and Klaus Gersten. *Boundary-Layer Theory*. Springer Berlin Heidelberg, Berlin, Heidelberg, 2017.

[173] W. R. Sears and D. P. Telionis. Boundary-layer separation in unsteady flow. *SIAM Journal on Applied Mathematics*, 28(1):215–235, 1975.

[174] Thomas Sebastian. *The Aerodynamics and Near Wake of an Offshore Floating Horizontal Axis Wind Turbine*. PhD Thesis, University of Massachusetts Amherst, 2012.

[175] W. Sheng, R. A. McD. Galbraith, and F. N. Coton. A New Stall-Onset Criterion for Low Speed Dynamic-Stall. *Journal of Solar Energy Engineering*, 128(4):461, 2006.

[176] W. Sheng, R. A. McD. Galbraith, and F. N. Coton. A Modified Dynamic Stall Model for Low Mach Numbers. *Journal of Solar Energy Engineering*, 130(3):031013, 2008.

[177] Wanan Sheng, Roderick A. McD. Galbraith, and Frank N. Coton. On the S809 airfoil's unsteady aerodynamic characteristics. *Wind Energy*, 12(8):752–767, November 2009.

[178] Witold Skrzypiński, Mac Gaunaa, Niels Sørensen, Frederik Zahle, and Joachim Heinz. Vortex-induced vibrations of a DU96-W-180 airfoil at 90deg angle of attack: Vortex-induced vibrations of a DU96-W-180 airfoil at 90deg AOA. *Wind Energy*, 17(10):1495–1514, October 2014.

[179] Witold Robert Skrzypiński, Mac Gaunaa, Niels Sørensen, Frederik Zahle, and Joachim Heinz. Self-induced vibrations of a DU96-W-180 airfoil in stall: Self-induced vibrations of a DU96-W-180 airfoil in stall. *Wind Energy*, 17(4):641–655, April 2014.

[180] J Smagorinsky. General Circulation Experiments with the Primitive Equations. *Monthly Weather Review*, 1963.

[181] H. Snel. Sectional Prediction of Lift Coefficients on rotating wind turbine blades in stall. 1994.

[182] H. Snel. Heuristic modelling of dynamic stall characteristics. pages 429–433, Dublin Castle, Ireland, 1997.

[183] H. Snel and J. G. Schepers. Joint investigation of dynamic inflow effects and implementation of an engineering method. Technical report, ECN, 1995.

[184] Philippe R. Spalart, W-H. Jou, M. Strelets, and S. R. Allmaras. Comments on the feasibility of LES for wings, and on a hybrid RANS/LES approach. In *Advances in DNS/LES*, Louisiana Tech University, 1997.

[185] David A. Spera. Models of lift and drag coefficients of stalled and unstalled airfoils in wind turbines and wind tunnels. 2008.

[186] Henrik Stensgaard Toft, Lasse Svenningsen, Wolfgang Moser, John Dalsgaard Sørensen, and Morten Lybech Thøgersen. Wind Climate Parameters for Wind Turbine Fatigue Load Assessment. *Journal of Solar Energy Engineering*, 138(3):031010, April 2016.

[187] M Stettner, M J Reijerkerk, A Lünenschloß, V Riziotis, A Croce, L Sartori, R Riva, and J M Peeringa. Stall-Induced Vibrations of the AVATAR Rotor Blade. *Journal of Physics: Conference Series*, 753:042019, September 2016.

[188] C. Strangfeld, C. L. Rumsey, H. Müller-Vahl, D. Greenblatt, C. Nayeri, and C. O. Paschereit. Unsteady Thick Airfoil Aerodynamics: Experiments, Computation, and Theory. American Institute of Aeronautics and Astronautics, June 2015.

[189] J. N. Sørensen. *General Momentum Theory for Horizontal Axis Wind Turbines*, volume 4 of *Research Topics in Wind Energy*. Springer International Publishing, Cham, 2016.

[190] J.L. Tangler and D.M. Somers. NREL Airfoil Families for HAWTS. Technical Report NREL/TP-442-7109, NREL, 1995.

[191] F. J. Tarzanin. Prediction of Control Loads Due to Blade Stall. *Journal of the American Helicopter Society*, 17(2):33–46, April 1972.

[192] Theodore Theodorsen. General Theory of Aerodynamic Instability and the Mechanism of Flutter, 1935. f.

[193] W A Timmer. Aerodynamic characteristics of wind turbine blade airfoils at high angles-of-attack. page 8, Crete, Greece, 2010.

[194] W. A. Timmer and R. P. J. O. M. van Rooij. Summary of the Delft University Wind Turbine Dedicated Airfoils. *Journal of Solar Energy Engineering*, 125(4):488, 2003.

[195] W.A. Timmer and C. Bak. Aerodynamic characteristics of wind turbine blade airfoils. In *Advances in Wind Turbine Blade Design and Materials*, pages 109–149. Elsevier, 2013.

[196] C. T. Tran and D. Petot. Semi-empirical model for the dynamic stall of airfoils in view of the application to the calculation of responses of a helicopter blade in forward flights. page 24, Bristol, England, 1980.

[197] Niels Troldborg, Christian Bak, Niels N Sørensen, Helge A Madsen, Pierre-Elouan Rethore, Frederik Zahle, and Srinivas Guntur. Experimental and numerical investigation of 3d aerofoil characteristics on a MW wind turbine. In *Proceedings of the European Wind Energy Association (EWEA) 2013*, page 11, Vienna, February 2013.

[198] V. K. Truong. A 2-D Dynamic stall model based on a Hopf bifurcation. 1993.

[199] V. K. Truong. Prediction of helicopter rotor airloads based on physical modelling of 3d unsteady aerodynamics. page 14, 1996.

[200] Rajesh Vaithiyanathasamy. *Double wake model for separated flows over airfoils*. PhD thesis, University of Twente, 2017.

[201] R. P. J. O. M. van Rooij. Modification of the Boundary Layer Calculation in RFOIL for Improved Airfoil Stall Prediction. Technical Report IW-96087R, TU Delft, Delft, the Netherlands, 1996.

[202] R. P. J. O. M. van Rooij and W. A. Timmer. Roughness Sensitivity Considerations for Thick Rotor Blade Airfoils. *Journal of Solar Energy Engineering*, 125(4):468, 2003.

[203] L A Viterna and D C Janetzke. Theoretical and experimental power from large horizontal-axis wind turbines. Technical Report DOE/NASA/20320-41, NASA-TM-82944, 6763041, September 1982.

[204] Kai Wang, Vasilis A. Riziotis, and Spyros G. Voutsinas. Aeroelastic stability of idling wind turbines. *Wind Energy Science*, 2(2):415–437, August 2017.

[205] A.E. Winkelmann. On the occurrence of mushroom shaped stall cells in spearated flow. In *16th Fluid and Plasmadynamics Conference*, Danvers,MA,U.S.A., July 1983. American Institute of Aeronautics and Astronautics.

[206] He-Yong Xu, Chen-Liang Qiao, Hui-Qiang Yang, and Zheng-Yin Ye. Delayed detached eddy simulation of the wind turbine airfoil S809 for angles of attack up to 90 degrees. *Energy*, 118:1090–1109, January 2017.

[207] D. You and W. Bromby. Large-eddy simulation of unsteady separation over a pitching airfoil at high Reynolds number. In *Seventh International Conference on Computational Fluid Dynamics (ICCFD7), Big Island, Hawaii*, 2012.

[208] Frederik Zahle, Carlo Tibaldi, David R. Verelst, Robert Bitche, and Christian Bak. Aero-Elastic Optimization of a 10 MW Wind Turbine. American Institute of Aeronautics and Astronautics, January 2015.

[209] Alessandro Zanon, Pietro Giannattasio, and Carlos J. Simão Ferreira. A vortex panel model for the simulation of the wake flow past a vertical axis wind turbine in dynamic stall: A vortex panel model for VAWT in dynamic stall. *Wind Energy*, 16(5):661–680, July 2013.

[210] A. Zanotti, R. Nilifard, G. Gibertini, A. Guardone, and G. Quaranta. Assessment of 2d/3d numerical modeling for deep dynamic stall experiments. *Journal of Fluids and Structures*, 51:97–115, November 2014.

[211] F. Zou, V. A. Riziotis, S. G. Voutsinas, and J. Wang. Analysis of vortex-induced and stall-induced vibrations at standstill conditions using a free wake aerodynamic code: Analysis of vortex-induced and stall-induced vibrations at standstill. *Wind Energy*, 18(12):2145–2169, December 2015.